

Doctoral Thesis

Thesis Title

Study on Improvement of Microwave Non-
destructive Testing Technology for Inspection
of Piping Systems with Bends

Department of Quantum Science and Energy Engineering

Graduate school of Engineering,

TOHOKU UNIVERSITY

CHEN GUANREN

Advising Professor at Tohoku Univ.	Professor <u>Hidetoshi, Hashizume</u>
Research Advisor at Tohoku Univ.	
Dissertation Committee Members Name marked with “○” is the Chair of the Committee	○ <u>Prof. Hidetoshi, Hashizume</u> 1 <u>Prof. Tetsuya, Uchimoto</u> 2 <u>Prof. Kenji, Tobita</u> 3 <u>Associate Prof. Notitaka, Yusa</u>

TOHOKU UNIVERSITY
Graduate School of Engineering

Study on Improvement of Microwave Non-destructive Testing Technology for Inspection of
Piping Systems with Bends

(曲がり部を有する配管に対する電磁波非破壊検査手法の高度化に関する研究)

A dissertation submitted for the degree of Doctor of Philosophy (Engineering)

Department of Quantum Science and Energy Engineering

by

Guanren CHEN

August 3, 2020

Study on Improvement of Microwave Non-destructive Testing Technology for Inspection of Piping Systems with Bends

Guanren CHEN

Abstract

Metal pipes are extensively employed in various industrial facilities for substance transportation. During pipe operation, degradations occur on account for fatigue, corrosion, etc., which may result in pipe failure and thus cause catastrophic consequences. Conventional non-destructive testing (NDT) methods such as ultrasonic testing and eddy current testing are of high precision but request probe scans or surface preparations, which are time&labor consuming. Ergo, an NDT technology using microwave has been proposed to implement rapid and long-range pipe inspection. Microwaves are propagated inside a pipe as guided waves, while reflection from a flaw is measured and its time-of-flight is evaluated for location.

Former studies have demonstrated that flaws such as pipe wall thinning and cracks can be detected and located at a long distance. Nevertheless, these studies mainly focused on inspection of straight pipes, while the application to bent pipes, which are also widely used, has not been studied deeply. This study targets the inspection of piping systems with bends using microwave NDT, and three aspects of works are carried out: 1. Clarify the effect of a bend on microwave transmission and reflection; 2. Develop a crack-detection method using a TE₁₁ mode microwave probe for inspection of bent pipes with open-end; 3. Design a dual-port, side-incident microwave probe for directional inspection of closed piping systems. This thesis is organized as below:

Chapter 1 gives basic introductions to the background, former studies, and objective of this study;

Chapter 2 introduces the research methods, including the theory of microwave in a circular waveguide, numerical simulation method, experimental equipment, and signal-processing method.

Chapter 3 investigates the effect of a bend on microwave transmission and reflection. The factors affecting the mode conversion of microwaves due to a bend were studied theoretically and verified by numerical simulation. Both theoretical and numerical results reveal that the mode conversion at a bend depends on the three factors: the frequency normalized by the cut-off frequency of an arbitrary mode (f/f_c), the ratio of the curvature radius to the inner diameter of the pipe (r/D) and the bend angle (α). Moreover, the polarization of non-axisymmetric mode like TE₁₁ mode also influences the mode conversion, while the polarization itself is not affected by the bend. Experiment was performed to evaluate the effect of a bend microwave reflection, by quantitatively comparing the reflection signals from pipe wall thinning in a straight pipe with those in a bent pipe. The results show that the presence of a bend leads to a decrease in the reflection signal behind the bend, and the extent of decrease is also correlated with the mode conversion at the bend, i.e., r/D , α and f/f_c . Furthermore, the flaw size does not noticeably influence the decrease in reflection signal when the bend's dimensions are certain. To two bends with different inner diameters D but identical or similar r/D and α , given the same range of f/f_c , the effects of them on reflection are also consistent.

Chapter 4 presents a crack-detection approach using a TE₁₁ mode microwave probe. The linearly-polarized TE₁₁ mode is proved to be sensitive to both axial and circumferential cracks in the light of the analysis on surface current density. A systematic method was proposed to design a TE₁₁ mode microwave probe (comprising a TEM-TM₀₁ and a dual-bend TM₀₁-TE₁₁ mode converter) for an arbitrary inner pipe diameter D using theoretical and numerical analysis. A 3.5 GHz working bandwidth was achieved for $D = 23$ mm. Experimental verification was conducted by detecting an axial and a circumferential slit situated at different longitudinal and circumferential positions in a

7 m long stainless-steel pipe. The results show that both axial and circumferential slits were detected at arbitrary positions in a pipe by jointly analyzing the reflection signals of TE_{11} mode under horizontal and vertical polarizations. Subsequently, this method was applied for detecting cracks in a bent pipe. The results show that: given the impact of TE_{11} mode's polarization on mode conversion at the bend, the detectability against axial crack was still significant, whereas that against circumferential crack could be largely influenced if the bend imposes too much effect. The problem can be addressed by utilizing the TM_{01} mode 'integrated' in the probe to detect circumferential cracks. Moreover, the application to long-range detection and multiple inner pipe diameters has also been validated experimentally, and a detection range up to 15 – 24 m for $D = 11, 19,$ and 39 mm has been confirmed. Besides, an improved TE_{11} mode microwave probe design was proposed to achieve wide working bandwidth and apply to larger pipe diameters. In addition, this method was applied for inspecting bend-region cracks. The detection capability has been preliminarily confirmed, as both axial and circumferential slits at variant angular positions of a bend were successfully detected, with positional information specified by the peak locations of reflections. Finally, additional tests were made to examine the detectability of TE_{11} mode microwaves towards pipe wall thinning and non-penetrant slit.

Chapter 5 proposes a dual-port, side-incident microwave probe that realizes directional pipe inspections of closed piping systems. Two types of side-incident probes (LJ and JL) are proposed to transmit TM_{01} or TM_{02} mode microwaves into the pipe under test, and each type of probe has two ports utilized for inspections of two opposite directions. Numerical simulations were conducted to study the dimensional parameters affecting the transmission characteristic of the probe and thus optimize the probe to obtain better mode purity and transmission directivity. The simulation results also suggest that the optimal probe dimensions for one inner pipe diameter can be applied to another diameter according to the proportional relationship between the optimal dimensional parameters of the probe and the pipe diameter. Two LJ-type, side-incident probes with an inner diameter of 19 or 39 mm, were fabricated based on the simulation results. The experimental verification was subsequently carried out to test the detection directivity of the probes by detecting the pipe wall thinning situated on both sides of each probe. The results show that the proposed dual-port, side-incident microwave probes can effectively detect the pipe wall thinning on either side of each probe using the corresponding port, and thereby realize the directional pipe inspection. Furthermore, this method shows the prospect of being applied to various inner pipe diameters.

Chapter 6 summarizes the works carried out in this study and proposes some future tasks for further improvement and practical use of this technique.

Contents

- Chapter 1 Introduction..... 1
 - 1.1 Pipe failures..... 1
 - 1.2 Microwaves nondestructive testing (NDT) and pipe inspection 3
 - 1.2.1 Introduction to microwave NDT 3
 - 1.2.2 Conventional NDT methods for pipe inspection..... 4
 - 1.2.3 Microwave NDT for pipe inspection..... 4
 - 1.2.4 Bent pipe inspection using microwave NDT..... 5
 - 1.3 Objective 7
- Chapter 2 Research Methodologies..... 8
 - 2.1 Theory of microwaves in circular waveguide 8
 - 2.1.1 Electromagnetic wave basics [116,117]..... 8
 - 2.1.2 Microwave guided wave..... 10
 - 2.1.3 Velocity and wavelength of guided waves 13
 - 2.1.4 Circular waveguide..... 14
 - 2.1.5 Microwave loss..... 18
 - 2.2 Numerical simulation for microwave NDT..... 19
 - 2.3 Experimental apparatus 21
 - 2.3.1 Microwave generation..... 21
 - 2.3.2 Flexible cable 21
 - 2.3.3 Semi-rigid cable and connector 22
 - 2.4 Signal-processing method 23
 - 2.4.1 Fourier and inverse Fourier transform..... 23
 - 2.4.2 Dispersion compensation..... 24
- Chapter 3 The effect of a bend on microwave transmission and reflection 25
 - 3.1 Overview of microwave propagation in a bent pipe 25
 - 3.2 Theoretical derivation of the mode conversion due to a bend..... 26
 - 3.3 Numerical simulation on mode conversion..... 29
 - 3.4 Experiment 33
 - 3.4.1 Experimental system 33
 - 3.4.2 Experiment results 39

3.5 Summary	49
Chapter 4 Crack detection in open-ended bent pipes using a TE ₁₁ mode microwave probe.....	50
4.1 Theoretical basis of using TE ₁₁ mode for crack detection.....	50
4.2 Design of TE ₁₁ mode microwave probe	52
4.2.1 Design of TEM-TM ₀₁ mode converter	53
4.2.2 Design of TM ₀₁ -TE ₁₁ mode converter	53
4.3 Experimental verification	57
4.3.1 Experimental setup	57
4.3.2 Results and discussions	59
4.4 Application to bent pipe	62
4.5 Applicability to multiple pipe diameter and long pipes	66
4.6 Bend-region crack detection.....	71
4.7 Supplementary discussions on TE ₁₁ mode	76
4.7.1 Detection of pipe wall thinning using TE ₁₁ mode	76
4.7.2 Detection of non-penetrant slit	78
4.8 Summary	80
Chapter 5 Side-incident probe design for directional inspection of closed piping systems	81
5.1 Side-incident method.....	81
5.2 Numerical simulation	82
5.2.1 Single-port, side-incident probe	82
5.2.2 Dual-port, side-incident probe.....	85
5.2.3 Applicability to other inner pipe diameters	89
5.3 Experimental verification	91
5.3.1 Experimental setup	91
5.3.2 Results and discussion.....	94
5.4 Summary	96
Chapter 6 Conclusion	98
6.1 Summary of this study.....	98
6.2 Future tasks	100
Acknowledgment	101
Appendix	103
A. Mathematical demonstrations for other three coupling coefficients:	103
A.1 TM _{mn} to TE _{m'n'} mode, C _{[m'n'](mn)}	103

A.2 TM_{mn} to $TM_{m'n'}$ mode, $C_{(m'n')(mn)}$	103
A.3 TE_{mn} to $TM_{m'n'}$ mode, $C_{(m'n')[mn]}$	104
B. Theoretical and numerical calculation of mode conversion of TM_{01} , TE_{01} , and TE_{11} mode (under horizontal and vertical polarizations) due to a bend.....	105
B.1. Mode conversion of TM_{01} mode for different r/D and α values.....	105
B.2. Mode conversion of TE_{01} mode for different r/D and α values.....	108
B.3. Mode conversion of TE_{11} mode under horizontal polarization for different r/D and α values	111
B.4. Mode conversion of TE_{11} mode under vertical polarization for different r/D and α values	115
C. Additional test of the dual-port, side-incident probe using partial pipe wall thinning	118
Reference.....	121
Statement of reuse of materials	129

Chapter 1 Introduction

1.1 Pipe failures

Pipeline is an efficient and economical way for substance transportation, while piping systems are crucial components in a variety of industrial facilities such as chemical plant, refinery, power plant, etc. During operations, pipes suffer from corrosion, stress, aging, and other degradations, which weaken the structural strength of pipes. These degradations may lead to pipe failures and eventually result in economic losses, environmental pollutions, and even casualties. In 2004, a piping rupture and steam eruption [1] occurred in the third-floor turbine hall of the Mihama No.3 reactor, which was under operation. The accident caused 5 deaths and 6 injuries, and was regarded as Japan's worst nuclear power accident before Fukushima nuclear power plant accident. In 2007, another pipe rupture and steam leakage accident [2] occurred in Onagawa nuclear power plant. An erosion hole was generated due to the liquid droplet impingement, which facilitates the rate of the pipe wall thinning. Ergo, considerable attention has been paid to technologies for pipe inspection and maintenance.

Pipe failures in bent pipes also have attracted extensive interest. For instance, Figure 1-1 illustrates the typical degradations of the U-shaped tubes in steam generators: they are denting, fatigue cracking, fretting, intergranular attack, stress corrosion cracking, pitting, tube wear, wastage, etc. [3,4] Most of steam generator tubes which have failed over the years have been mill-annealed Inconel Alloy 600 [5]. Figure 1-2 exhibits the number of the repaired steam generator tubes in America classified by degradation type from 1973 to 2011, and it is evident that the stress corrosion cracking (acronym 'SCC' in the figure) accounts for the major cause of the tube degradation since late 1980's. Although the Inconel Alloy 690 and Incoloy Alloy 800, manifesting good resistance to stress corrosion cracking, had been used to replace Inconel Alloy 600, the stress corrosion cracking may still occur under some circumstances (e.g., the thermal treatment was not properly performed or under Pb-containing caustic environment) [7-11]. And there are still a number of in-service steam generator units that are made of Inconel Alloy 600 [6], the maintenance of them is also necessary. In addition, the bent pipes, especially bends are subject to the flow-accelerated corrosion [12,13] and liquid droplet impingement [14,15], which may result in pipe leakage or even rupture. Based on the above discussions, it is imperative to develop an efficient and reliable method for inspections of bent pipes.

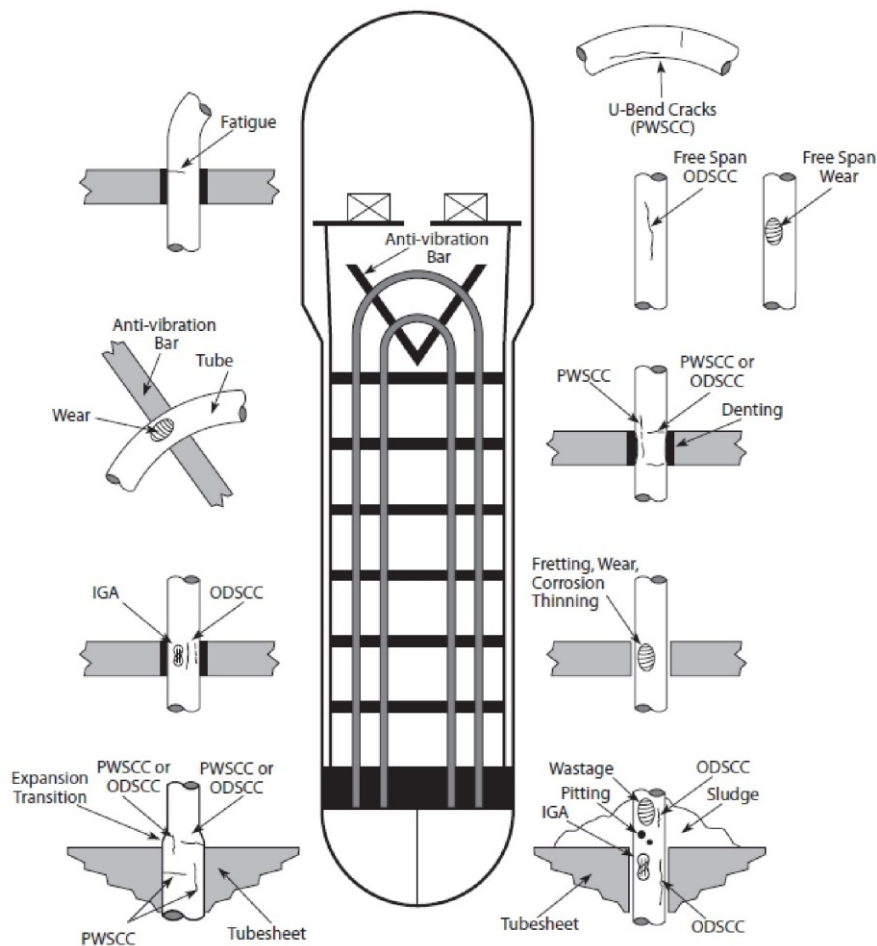


Fig. 1-1 Illustration of steam generator tube degradations. [3]

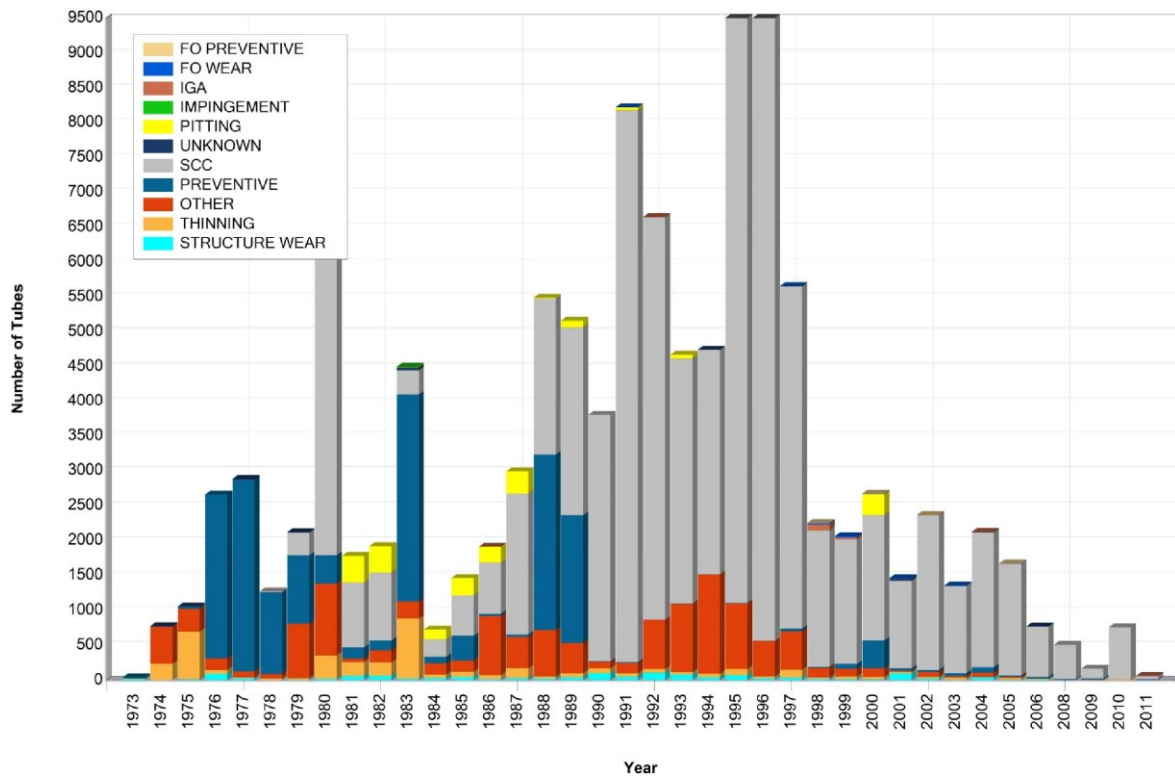


Fig. 1-2 Number of tubes repaired in American steam generators, classified by degradation mode for mill-annealed Inconel Alloy 600 (1973 to 2011). [6]

1.2 Microwaves nondestructive testing (NDT) and pipe inspection

1.2.1 Introduction to microwave NDT

Microwave is one kind of electromagnetic waves with frequency span ranging from 300 MHz to 300 GHz. Microwaves are widely used in the telecommunication realms, e.g., WiFi and 5G technologies. In terms of the characteristics and usages, the microwave band can be further divided into multiple sub-bands like X band and K band, as given in Table 1-1.

Table 1-1 Standard radar-frequency letter band nomenclature [16].

Band Designation	Nominal Frequency range
HF	3MHz – 30MHz
VHF	30MHz – 300MHz
UHF	300MHz – 1000MHz
L	1000MHz – 2000MHz
S	2000MHz – 4000MHz
C	4000MHz – 8000MHz
X	8000MHz – 12000MHz
K _u	12 GHz – 18 GHz
K	18 GHz – 27 GHz
K _a	27 GHz – 40 GHz
V	40 GHz – 75 GHz
W	75 GHz – 110 GHz
mm	110 GHz – 300 GHz

In addition to telecommunications, microwave has also been employed for non-destructive testing & evaluation [17,18]. For instance, Zoughi et al adopted microwaves to examine the material properties and status in cement and concrete, such as water-to-cement ratio [19], sand-to-cement ratio [20], cure state [21], chloride [22], alkali-silica reaction [23], etc. In fact, microwave is an effective tool for dielectric material characterization [24], such as timber [25], liquid [26], concrete mortar [27], and composites [28,29]. Sklarczyk et al used microwave imaging to detect concealed weapons [30-33] for safety inspection. Besides, microwaves can also be utilized for detecting crack and corrosion on metal surfaces [34-40], especially damages under coatings or corruptions [41,42]. Synthetic aperture radar (SAR) [43-47] technology is also applied to process the scanned reflection signals and to generate 3-D imaging or tomography. Also, some advanced probe structures [48-57] were proposed to improve the detection performance.

Recently, microwave NDT becomes very popular in composite material evaluation [58-61] and medical diagnosis. Li and Moll used open-end waveguide and horn-antenna system, respectively, to detect thickness variation [62], delamination [63] and other damages [64] in the wind turbine blade, which is made from glass fiber reinforced polymer (GFRP); Tian carried out experimental studies on the detection of impact damage [65] and holes [66] on carbon fiber reinforced polymers (CFRP) plates and pipes; Zoughi targeted the application of microwave NDT to carbon composites [67,68] such as carbon nanotubes. Regarding the medical usage, Udpa employed deformable reflector and time reversal method for breast imaging [69] and tumor detection [70]; Zoughi used Ka-band microwaves for assessing skin-burn injury [71] and evaluating the dielectric properties of skin [72]; Lin and Kim also applied microwaves and semi-conductor technology to detect human vital signs [73-75] like heartbeat and respiration. Furthermore, the latest studies also manifest that microwave NDT has a promising prospect in counterfeit leather [76] and integrated circuit identification [77], and food examination [78].

1.2.2 Conventional NDT methods for pipe inspection

In fact, many NDT methods have been developed and adopted for pipe inspection, including eddy current testing [79,80], ultrasonic testing [81,82], magnetic flux leakage [83,84], metal magnetic memory [85,86], and so on. However, these methods have some limitations when employed for rapid and long-range pipe inspection. For example, eddy current testing and ultrasonic testing are of high detection precision, but meanwhile they may also require surface preparations and probe scans, which lower the efficiency and restrict their use; magnetic flux leakage method employs a pipe inspection gauge moving inside the pipe like a piston, which is susceptible to pipe deformation and can be easily stuck inside the pipe. And this technology is usually utilized in very long-range oil/gas transportation (tens or hundreds of kilometers), and the pipe diameter is usually relatively big. On the other hand, the metal magnetic memory method does not require the magnetization device, but akin to the magnetic flux leakage method, it is only applicable to ferromagnetic materials.

In addition to the above mentioned NDT methods, the ultrasound guided-wave method [87,88] is also a method that can achieve long-range and high-speed pipe inspection. The ultrasound guided waves are excited from the pipe sidewall and propagated inside the pipe wall with some patterns, also known as modes [89]. There are torsional, longitudinal, and flexural modes, such as T(0,1), L(0,2), F(1,2), and F(1,3) modes, and they have been used for crack detection [90-92]. It should be noted that the ultrasound guided waves are equally susceptible to flaws on both internal and external surfaces of the pipe, while the internal and external mediums (e.g., sand and filled-fluid like water, respectively) influence the transmission of the guided waves [93,94]. Besides, mode conversion [95-98] occurs when ultrasound guided waves propagate in a bent pipe, and some high-order modes can be generated. Recently, a non-contact ultrasound guided-wave generation method was proposed by using electromagnetic acoustic transducer (EMAT) [99-101]. This technique does not require couplant or physical contact, and increases the inspection efficiency significantly. However, the propagation of ultrasound guide waves is sensitive to pipe joints or fittings, so the wave transmission can be interrupted by them and the detection range could be restricted.

1.2.3 Microwave NDT for pipe inspection

To realize a long-range, high speed, and non-destructive pipe inspection, an NDT method using microwaves has been proposed [102-104]. The principle is elucidated as follows: microwaves of specific mode(s) are emitted into a metallic pipe and propagated as guided waves at the speed close to the light speed. Since the energy of microwaves is basically confined within the pipe, the decay is very small and a long-range transmission can be achieved. Provided that there is a flaw located on the inner surface of the pipe, the transmission of microwaves will be perturbed, meanwhile a reflection will occur. Ergo, by measuring the reflection and analyzing the time-domain signal, we are able to detect and locate the flaw. The principle of microwave NDT for pipe inspection is illustrated in Fig. 1-3.

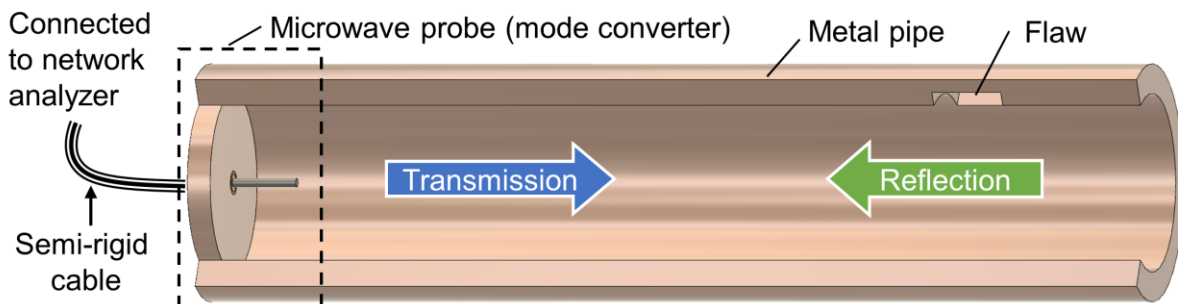


Fig. 1-3 Schematics of microwave NDT for pipe inspection.

The earlier studies have confirmed that this method works effectively in detecting pipe wall thinning [105,106], cracks [107,108], and corrosion under insulator [109]. Meanwhile, a detection range up to 26.5 m [110] has also been demonstrated. Furthermore, a side-incident probe [111] was developed to directionally transmit TM mode microwaves from sidewall into the pipe under test, implementing directional two-way pipe inspections.

Table 1-2 compares microwave NDT with other conventional NDT methods from the viewpoint of rapid and long-range pipe inspection. Among these methods, the ultrasound guided waves and microwave NDT manifest a promising prospect for rapid and long-range pipe inspection. Nonetheless, there are some also differences between them in excitations, usages, and other aspects. As for the ultrasound guided waves, since the guided waves are usually excited from the outer wall of the pipe, it can be used for the structural health monitoring of some crucial parts of the piping systems that has few pipe joints (e.g., seamless pipe) and accessible outer surface. On the other hand, microwave NDT focused on the inspection of the inner surface of pipe. Ergo, it is suitable for periodical maintenance or inspection of some piping systems whose sidewall is not easily accessible (e.g., immersed by water, covered by sand, or steam generator tube bunches fixed by tube sheet) but pipe-end is accessible. The pipe joint reflects the transmitted microwaves but does not cause noticeable signal decay. The mode conversion of microwaves also occurs at bend, and the details will be given in the latter sections. Just to be precise, the ultrasound guided waves can be excited from the pipe-end and inside of the pipe with a small diameter [100], while there is also a side-incident method [111] for microwave NDT to inspect pipes from the pipe’s sidewall.

Table 1-2 Comparison of different NDT methods in light of detection speed and range.

NDT method	Detection speed	Detection range	Features
Eddy current testing	Low	Small	High precision, quantitative evaluation of flaw characteristic, probe scan, local detection
Ultrasonic testing	Low	Small	High precision, quantitative evaluation of flaw characteristic probe scan and couplant, local detection
Magnetic flux leakage	Low	Very large	Extremely long detection range, suitable for oil/gas pipeline inspection, only applicable to ferromagnetic materials, easily stuck in pipe
metal magnetic memory	Low	Small	No need for strong magnetization, pipe buckling detection, only applicable to ferromagnetic materials.
Ultrasound guided waves	Fast	Large	Sensitive to flaws on both internal/external surfaces of pipe, wave propagation perturbed by pipe joints and inner and outer mediums.
Microwave NDT	Fast	Large	Sensitive to flaws inside pipes, filled fluid attenuates microwave wave transmission.

1.2.4 Bent pipe inspection using microwave NDT

Most previous studies focused on the inspections of straight pipes, while only few studies [112-114] were carried out for bent pipes, which are also widely used in various piping systems, such as steam

generators, heat exchangers, etc. Besides, as previously narrated, some pipe degradations tend to occur at the bend region such as flow-accelerated corrosion and liquid droplet impingement. In one former study [113], the detectability of this method against pipe wall thinning in bent pipes has been confirmed, while and the experimental setup and results are shown in Fig. 1-4. As we can see, compared with reflections ahead of the bend (e.g. point A), the reflections from pipe wall thinning behind the bend (e.g., point D) are smaller and dispersed. This is because the single-mode propagation was disrupted by the bend, while multiple modes were generated on account for the mode conversion at the bend. Ergo, when applying the current microwave NDT to bent pipe inspection, what effect a bend will have should be considered as well. This preliminary study only computed the mode conversion at several bends through numerical simulation, and only two bends were tested in the experiment. It did not offer a deep discussion on how microwave propagation is affected by the bend. Hence, it is worthwhile devoting much effort to insightfully investigate the practical influence of an arbitrary bend on microwave transmission and reflection by using a more efficient and general method. Furthermore, the detection object in that study was full-circumferential pipe wall thinning, which was dimensionally large and easy to detect. On the other hand, cracks are more difficult to detect owing to their relatively smaller size and complicated profile. The previous work also substantiated that the orientations of cracks significantly influence the detection sensitivity of the microwave NDT, and the sensitivity is also correlated with the microwave mode transmitted inside the pipe [115]. Therefore, crack detection in a bent pipe especially at the bent region ought to be further studied. Moreover, the earlier study was meant for inspecting bent pipes with open-end for probe insertion. However, there are also some closed piping systems which has no open-end for probe insertion. Moreover, there may be some orifices inside the pipes which perturbs the microwave transmission. Therefore, a side-incident method needs to be adopted, e.g., for periodic inspection or structural health monitoring of some crucial components in the pipe, like the bend suffering from flow-accelerated corrosion or liquid droplet impingement. However, the side-incident probe proposed in the previous study [111] was not adequately optimized and only applicable to a 19 mm inner pipe diameter. Therefore, many problems should be tackled for the side-incident method, such as: the dimensions of the probe need further optimization to improve the probe’s transmission characteristic; the applicability of the probe to other inner pipe diameters should also be resolved, etc. Anyway, additional endeavors should be made for the application to the inspection of closed piping system with bends.

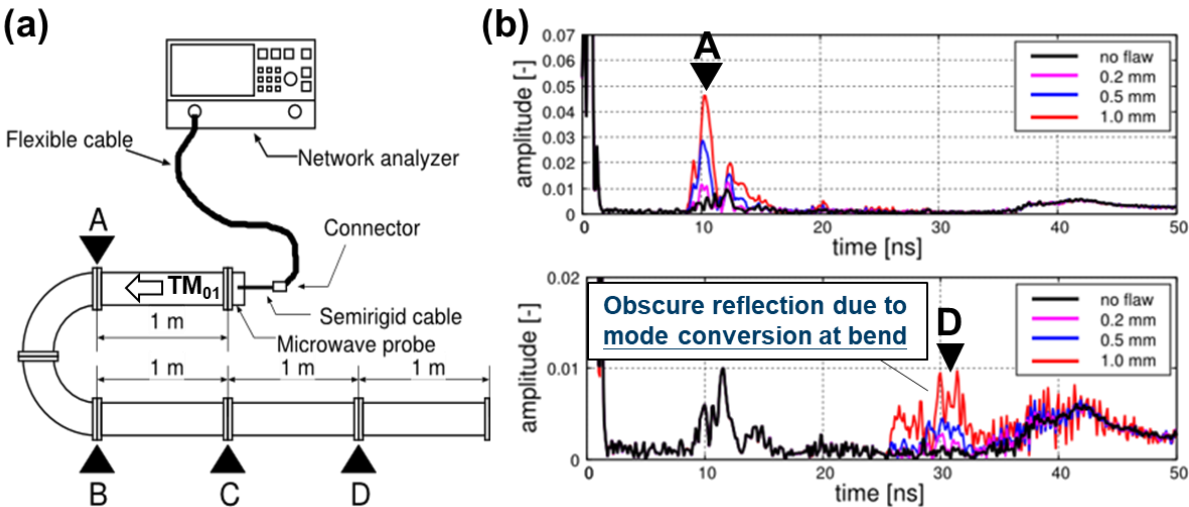


Fig. 1-4 Detection of pipe wall thinning in a bent pipe using TM_{01} mode microwaves [87], (a) experimental setup, (b) reflection signals.

1.3 Objective

This study is dedicated to the improvement of microwave NDT technology for inspection of piping systems with bends, to facilitate the use of this method for practical pipe inspection. Concretely, the following tasks shall be carried out:

- (1) investigate the effect of a bend on microwave transmission and reflection;
- (2) develop a crack detection method for inspection of bent pipe with open-end, including straight portion behind bend and bend-region;
- (3) improve the design of the side-incident microwave probe, realizing directional inspection in closed piping systems and applicability to different inner pipe diameters.

As shown in Fig. 1-5, wherein the task (1) aims to clarify and quantitatively evaluate microwave's behavior when propagating in a bent pipe; while based on the task (1), the tasks (2) and (3) were performed for the inspections of bent pipes with open-end and closed piping systems, respectively.

The rest of thesis is organized as follows: Chapter 2 presents the theoretical background and the technical approaches, including the microwave transmission inside a circular waveguide, Fourier transform/inverse Fourier transform, dispersion compensation, numerical simulation, and experimental instrument & specimens; Chapters 3 to 5 correspond to the aforementioned three major tasks (1)-(3); Chapter 6 summarizes the whole thesis and discusses future works.

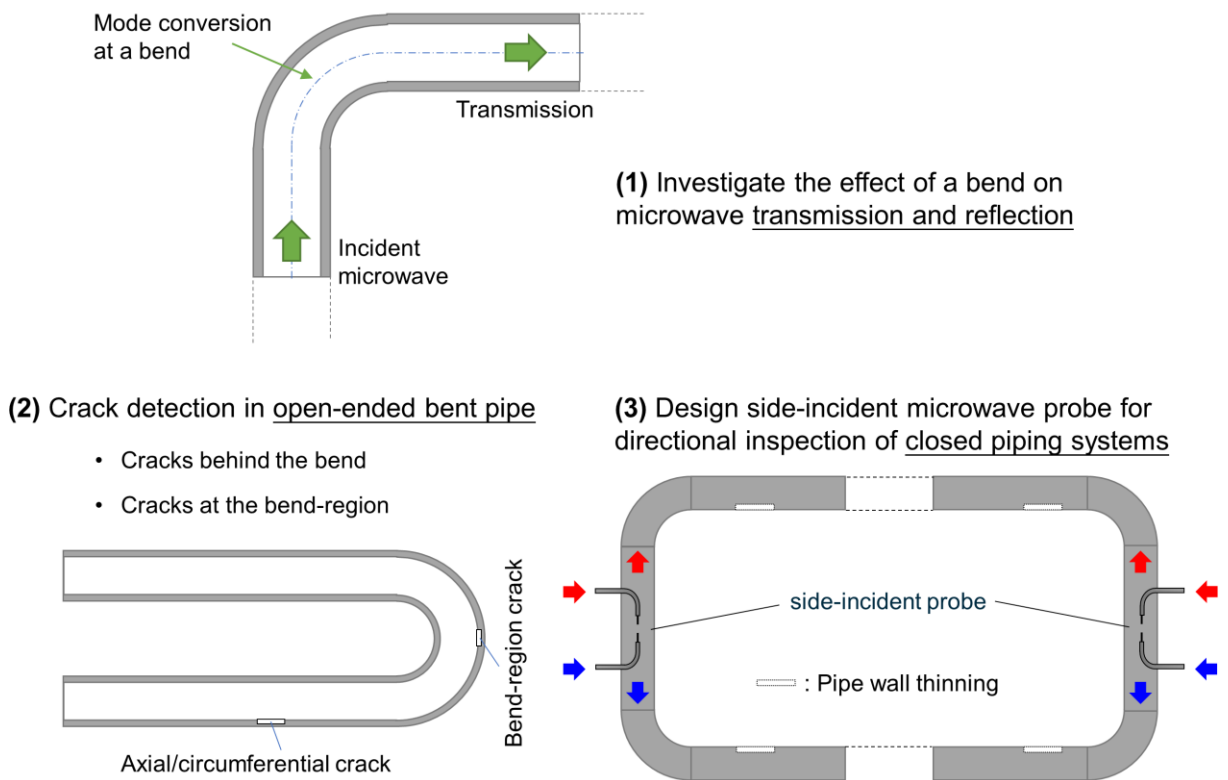


Fig. 1-5 Illustration of the three major tasks carried out in this thesis.

Chapter 2 Research Methodologies

2.1 Theory of microwaves in circular waveguide

2.1.1 Electromagnetic wave basics [116,117]

The electromagnetic waves in space are generally described by the time-varying Maxwell equations (differential form):

$$\nabla \times \mathbf{E} = -\frac{\partial \mathbf{B}}{\partial t}, \quad (2.1)$$

$$\nabla \times \mathbf{H} = \mathbf{J} + \frac{\partial \mathbf{D}}{\partial t}, \quad (2.2)$$

$$\nabla \cdot \mathbf{D} = \rho, \quad (2.3)$$

$$\nabla \cdot \mathbf{B} = 0, \quad (2.4)$$

wherein \mathbf{E} and \mathbf{H} are electric field and magnetic field intensities, respectively. The quantities \mathbf{B} and \mathbf{D} denote the magnetic and electric flux densities, and they are also called magnetic induction and electric displacement, respectively. The symbol ρ refers to volume charge density, while \mathbf{J} refers to the electric current density. These quantities are bound by the following relations

$$\mathbf{D} = \varepsilon \mathbf{E} = \varepsilon_0 \varepsilon_r \mathbf{E}, \quad (2.5)$$

$$\mathbf{B} = \mu \mathbf{H} = \mu_0 \mu_r \mathbf{H}, \quad (2.6)$$

$$\mathbf{J} = \sigma \mathbf{E}, \quad (2.7)$$

in which ε is permittivity, μ is permeability, and σ is conductivity. The symbols ε_0 and μ_0 are permittivity and permeability in a vacuum, respectively. Also, ε_r and μ_r are relative permittivity and relative permeability, respectively. Equations (2.5) – (2.7) are called constitutive relations. With these quantities, we can also determine the speed of light and intrinsic impedance in a specific material as

$$c = \frac{1}{\sqrt{\mu \varepsilon}}, \quad (2.8)$$

$$\eta = \sqrt{\frac{\mu}{\varepsilon}}. \quad (2.9)$$

Now we consider the microwave propagation in a metal pipe. As illustrated in Fig. 2-1, the direction of microwave propagation is set to Z -direction, which is also the axis of the metal pipe. So the electric field and magnetic field can be written as the following form

$$\mathbf{E} = \mathbf{E}_T(x, y) \exp(j\omega t - \gamma z), \quad (2.10)$$

$$\mathbf{H} = \mathbf{H}_T(x, y) \exp(j\omega t - \gamma z), \quad (2.11)$$

$$\gamma = \alpha + j\beta , \quad (2.12)$$

where \mathbf{E}_T and \mathbf{H}_T stand for the transverse electric and magnetic field, the symbol j is the complex unit, and ω is the angular frequency given by $\omega=2\pi f$ (f denotes the frequency). The notation γ is the propagation constant, composed of the phase constant β and the attenuation constant α . The microwave power per unit area flowing the past point z in the forward Z -direction is calculated as

$$P(z) = P(0)e^{-2\alpha z} , \quad (2.13)$$

the term $P(0)$ refers to the power per unit area at the point $z = 0$.

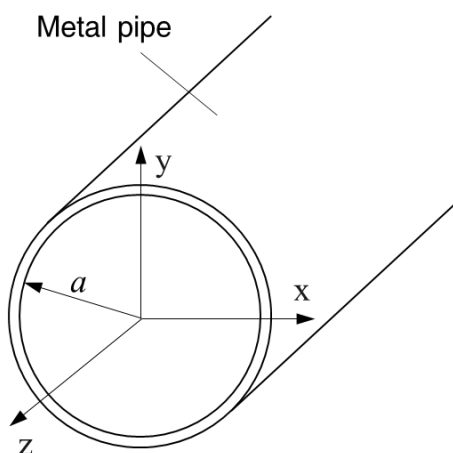


Fig. 2-1 Microwave propagation in a metal pipe with inner radius a .

Say we have a source-free, linear, isotropic, homogeneous region, so Eqs. (2.1) and (2.2) are

$$\nabla \times \mathbf{E} = -j\omega\mu\mathbf{H} , \quad (2.14)$$

$$\nabla \times \mathbf{H} = j\omega\varepsilon\mathbf{E} , \quad (2.15)$$

where there are two unknown variables and two equations. If we compute the curl on both sides of Eq. (2.14) as

$$\nabla \times \nabla \times \mathbf{E} = -j\omega\mu\nabla \times \mathbf{H} = \omega^2\mu\varepsilon\mathbf{E} , \quad (2.16)$$

and further obtain the equation for only \mathbf{E} ,

$$\nabla^2 \mathbf{E} + k^2 \mathbf{E} = 0 , \quad (2.17)$$

wherein

$$k = \omega\sqrt{\mu\varepsilon} . \quad (2.18)$$

Similarly, the equation for magnetic field can also be deduced in the same way:

$$\nabla^2 \mathbf{H} + k^2 \mathbf{H} = 0 . \quad (2.19)$$

Equation (2.17) or (2.19) is also known as Helmholtz equation, and parameter k is the wavenumber.

Now let us consider about the microwave energy. Also, consider a source-free field, the direction of microwave energy flux is also the propagation direction as $\mathbf{E} \times \mathbf{H}$, and a quantity has been proposed to depict microwave's energy flux

$$\mathbf{S} = \mathbf{E} \times \mathbf{H}^*, \quad (2.20)$$

which is known as Poynting vector. If we compute the divergence of \mathbf{S} and integrate it over a volume V , the result is

$$\begin{aligned} \int_V \nabla \cdot (\mathbf{E} \times \mathbf{H}^*) dv &= \oint_S \mathbf{E} \times \mathbf{H}^* ds \\ &= -\sigma \int_V |\mathbf{E}|^2 dv + j\omega \int_V (\varepsilon^* |\mathbf{E}|^2 + \mu |\mathbf{H}|^2) dv, \quad (2.21) \\ &= -\sigma \int_V |\mathbf{E}|^2 dv - \frac{\omega}{2} \int_V (\varepsilon'' |\mathbf{E}|^2 + \mu'' |\mathbf{H}|^2) dv - j \frac{\omega}{2} \int_V (\mu' |\mathbf{H}|^2 - \varepsilon' |\mathbf{E}|^2) dv \end{aligned}$$

wherein $\varepsilon = \varepsilon' + j\varepsilon''$, $\mu = \mu' + j\mu''$. The left side of the above equation represents the power flow out of the closed surface S , while the first and second terms at the right side of the equation are the power dissipation in the volume V due to conductivity, dielectric, and magnetic losses, respectively.

Moreover, say the microwave is vertically incident onto a good but not a perfect conductor, the propagation constant is thus written as

$$\gamma = \alpha + j\beta \approx j\omega\sqrt{\mu\varepsilon} \sqrt{\frac{\sigma}{j\omega\varepsilon}} = (1+j)\sqrt{\frac{\omega\mu\sigma}{2}}. \quad (2.22)$$

And here, the skin depth, referring to the depth of penetration into the conductor, is defined as

$$\delta = \frac{1}{\alpha} = \sqrt{\frac{2}{\omega\mu\sigma}} = \sqrt{\frac{1}{\pi f \mu\sigma}}. \quad (2.23)$$

For the good conductor (e.g. silver or gold), the skin depth δ could be very small at microwave frequency band, which is necessary for low-loss transmission.

2.1.2 Microwave guided wave

Provided that there is source-free and time-harmonic field in the waveguide, while the microwave transmission is along Z-direction in Fig. 2.1. The electric and magnetic fields can then be written as

$$\mathbf{E}(x, y, z) = [\mathbf{e}(x, y) + \hat{z}e_z(x, y)]e^{-\gamma z}, \quad (2.24)$$

$$\mathbf{H}(x, y, z) = [\mathbf{h}(x, y) + \hat{z}h_z(x, y)]e^{-\gamma z}, \quad (2.25)$$

wherein $\mathbf{e}(x,y)$ and $\mathbf{h}(x,y)$ denote the transverse components electric field and magnetic field, while e_z and h_z refer to the longitudinal components of the electric and magnetic field. Since we now consider the microwave transmission without any conductor and dielectric losses, the propagation constant $\gamma = j\beta$. Now we assume the field is source-free, so the electric field and magnetic field can be calculated from Eqs. (2.14) and (2.15), while their three components in each direction (x , y , and z) are expressed as

$$\frac{\partial E_z}{\partial y} + j\beta E_y = -j\omega\mu H_x, \quad (2.26a)$$

$$-j\beta E_x - \frac{\partial E_z}{\partial x} = -j\omega\mu H_y, \quad (2.26b)$$

$$\frac{\partial E_Y}{\partial x} - \frac{\partial E_X}{\partial y} = -j\omega\mu H_Z, \quad (2.26c)$$

$$\frac{\partial H_Z}{\partial y} + j\beta H_Y = j\omega\varepsilon E_X, \quad (2.26d)$$

$$-j\beta H_X - \frac{\partial H_Z}{\partial x} = j\omega\varepsilon E_Y, \quad (2.26e)$$

$$\frac{\partial H_Y}{\partial x} - \frac{\partial H_X}{\partial y} = j\omega\varepsilon E_Z. \quad (2.26f)$$

The above six equations can be further deduced for the four transverse components (E_X , E_Y , H_X and H_Y) with respect to the two longitudinal components (E_Z and H_Z), and reduced to four equations:

$$E_X = -\frac{j}{k_c^2} \left(\beta \frac{\partial E_Z}{\partial x} + \omega\mu \frac{\partial H_Z}{\partial y} \right), \quad (2.27a)$$

$$E_Y = \frac{j}{k_c^2} \left(-\beta \frac{\partial E_Z}{\partial y} + \omega\mu \frac{\partial H_Z}{\partial x} \right), \quad (2.27b)$$

$$H_X = \frac{j}{k_c^2} \left(\omega\varepsilon \frac{\partial E_Z}{\partial y} - \beta \frac{\partial H_Z}{\partial x} \right), \quad (2.27c)$$

$$H_Y = -\frac{j}{k_c^2} \left(\omega\varepsilon \frac{\partial E_Z}{\partial x} + \beta \frac{\partial H_Z}{\partial y} \right), \quad (2.27d)$$

wherein

$$k_c^2 = k^2 - \beta^2. \quad (2.28)$$

The parameter k_c is defined as the cut-off wavenumber, while β and k are the phase constant and wavenumber, respectively. To enable the propagation of microwave, the following condition must be fulfilled:

$$k > k_c. \quad (2.29)$$

Similarly, we have the following relations for the frequency and wavelength:

$$f > f_c = \frac{k_c}{2\pi\sqrt{\varepsilon\mu}}, \quad (2.30)$$

$$\lambda > \lambda_c = \frac{2\pi}{k_c} = \frac{1}{f_c\sqrt{\varepsilon\mu}}, \quad (2.31)$$

where f_c and λ_c are the cut-off frequency and cut-off wavelength, respectively. If $k < k_c$, β will become an imaginary number, so the propagation constant becomes a real number. In this case, the microwave will decay to zero immediately and exhibits a shut-down effect.

As discussed above, the transverse components of electric field and magnetic field can be expressed with the longitudinal components E_Z and H_Z . Therefore, in terms of different E_Z and H_Z , variant types of guided waves can be generated as given below.

(1) If $E_Z = 0$ and $H_Z = 0$, the transverse components will also be zero, so this kind of guided waves is called transverse electromagnetic (TEM) mode waves. The phase constant is calculated from Eqs. (2.26a) and (2.26e)

$$\beta = \omega \sqrt{\mu \varepsilon} = k. \quad (2.32)$$

It is obvious that the cut-off wavenumber k_c is zero. The wave impedance is

$$Z_{\text{TEM}} = \frac{E_X}{H_Y} = \frac{\omega \mu}{\beta} = \sqrt{\frac{\mu}{\varepsilon}} = \eta. \quad (2.33)$$

TEM mode guided waves usually exist within two or more conductors, e.g. the parallel plate waveguide, coaxial line, etc. In contrast, the closed conductor such as rectangular waveguide and circular waveguide, cannot support the TEM mode guided waves.

(2) If $H_Z = 0$, and $E_Z \neq 0$, this type of guided waves is referred to transverse magnetic (TM) mode, whose transverse field is given by

$$E_X = -\frac{j\beta}{k_c^2} \frac{\partial E_Z}{\partial x}, \quad (2.34a)$$

$$E_Y = -\frac{j\beta}{k_c^2} \frac{\partial E_Z}{\partial y}, \quad (2.34b)$$

$$H_X = \frac{j\omega\varepsilon}{k_c^2} \frac{\partial E_Z}{\partial y}, \quad (2.34c)$$

$$H_Y = -\frac{j\omega\varepsilon}{k_c^2} \frac{\partial E_Z}{\partial x}. \quad (2.34d)$$

In this case, the cut-off wavenumber k_c is not zero and usually dependent on the propagation mode and the dimensions/geometry of the waveguide. Meanwhile, the longitudinal electric field should be determined firstly, which can be solved with the Helmholtz equation

$$\left(\frac{\partial^2}{\partial x^2} + \frac{\partial^2}{\partial y^2} + \frac{\partial^2}{\partial z^2} + k^2\right)E_Z = 0. \quad (2.35)$$

Since $k_c^2 = k^2 - \beta^2$, the preceding equation is simplified to

$$\left(\frac{\partial^2}{\partial x^2} + \frac{\partial^2}{\partial y^2} + k_c^2\right)E_Z = 0. \quad (2.36)$$

In addition, the wave impedance of TM mode is solved as

$$Z_{\text{TM}} = \frac{E_X}{H_Y} = \frac{-E_Y}{H_X} = \frac{\beta}{\omega\varepsilon} = \frac{\beta\eta}{k}. \quad (2.37)$$

(3) If $E_Z = 0$, and $H_Z \neq 0$, this type of guided waves is defined as transverse electric (TE) mode, whose transverse components are solved as below

$$E_x = -\frac{j\omega\mu}{k_c^2} \frac{\partial H_z}{\partial y}, \quad (2.38a)$$

$$E_y = \frac{j\omega\mu}{k_c^2} \frac{\partial H_z}{\partial x}, \quad (2.38b)$$

$$H_x = -\frac{j\beta}{k_c^2} \frac{\partial H_z}{\partial x}, \quad (2.38c)$$

$$H_y = -\frac{j\beta}{k_c^2} \frac{\partial H_z}{\partial y}. \quad (2.38d)$$

Similar to TM mode, the longitudinal component of magnetic field H_z is solved as

$$\left(\frac{\partial^2}{\partial x^2} + \frac{\partial^2}{\partial y^2} + \frac{\partial^2}{\partial z^2} + k^2\right)H_z = 0, \quad (2.39)$$

and further simplified to

$$\left(\frac{\partial^2}{\partial x^2} + \frac{\partial^2}{\partial y^2} + k_c^2\right)H_z = 0. \quad (2.40)$$

And the wave impedance of TE mode is

$$Z_{TE} = \frac{E_x}{H_y} = \frac{-E_y}{H_x} = \frac{\omega\mu}{\beta} = \frac{k\eta}{\beta}. \quad (2.41)$$

It should be noted that the TM mode and TE mode are able to propagate inside either a closed conductor or multiple conductors.

2.1.3 Velocity and wavelength of guided waves

When the guided waves travel along the positive Z-direction, the velocity of the wave propagation is firstly defined as the phase velocity in that it is the velocity of a point with fixed phase ($\omega t - kz$) on the wave travels, and it is given by

$$v_p = \frac{dz}{dt} = \frac{\omega}{k} = \frac{1}{\sqrt{\epsilon\mu}}. \quad (2.42)$$

In a free-space and lossless media (e.g., vacuum), it is easy to get $v_p = 2.998 \times 10^8$ m/s, which is obviously the speed of light. Correspondingly, the wavelength of guided waves, which is defined as the interval between two adjacent peaks/valleys of a periodic signal, is expressed as

$$\lambda = \frac{2\pi}{k} = \frac{2\pi v_p}{\omega} = \frac{v_p}{f}. \quad (2.43)$$

When the phase velocity in a waveguide does not change with frequency, the phase of signal that contains multiple frequencies will not distort. If the signal is wideband containing multiple frequencies, meanwhile the phase velocity for different frequencies are different, the original phase relationship cannot be maintained and the signal distortion occurs. This phenomenon is called dispersion. In this sense, the phase velocity is calculated as

$$v_p = \frac{dz}{dt} = \frac{\omega}{\beta} = \frac{2\pi f}{\sqrt{k^2 - k_c^2}} = \frac{c}{\sqrt{1 - (f_c^2 / f^2)}}, \quad (2.44)$$

where c refers to the light speed in a vacuum.

If the bandwidth of the signal is not very large and the dispersion is not very severe, another parameter called group velocity can be defined to depict the velocity of microwave signal propagation, its expression is given below

$$v_g = \left(\frac{d\beta}{d\omega}\right)^{-1} = \frac{d\omega}{d\beta} = c \frac{\beta}{\sqrt{\beta^2 + k_c^2}} = c \sqrt{1 - \frac{f_c^2}{f^2}}. \quad (2.45)$$

In fact, the group velocity describes the velocity of a time-dependent envelope which modulates the magnitude of the original waveform, and it is apparent to see that $v_g < c < v_p$. Similarly, we can also define the group wavelength as

$$\lambda_g = \frac{2\pi}{\beta} = \frac{\lambda}{\sqrt{1 - \lambda^2 / \lambda_c^2}} = \frac{v_p}{f}, \quad (2.46)$$

which is larger than the wavelength in the free-space.

2.1.4 Circular waveguide

Microwaves can also propagate inside a hollow metal pipe, which serves as a circular waveguide and supports TM and TE modes. Figure 2-2 shows an illustration of the interior of a circular waveguide, with an inner radius of a . To simplify analysis and computation, cylindrical coordinates are used here. Equations (2.27a) to (2.27d) are thus rewritten as

$$E_\rho = \frac{-j}{k_c^2} \left(\beta \frac{\partial E_z}{\partial \rho} + \frac{\omega \mu}{\rho} \frac{\partial H_z}{\partial \phi} \right), \quad (2.47a)$$

$$E_\phi = \frac{-j}{k_c^2} \left(\frac{\beta}{\rho} \frac{\partial E_z}{\partial \phi} - \omega \mu \frac{\partial H_z}{\partial \rho} \right), \quad (2.47b)$$

$$H_\rho = \frac{j}{k_c^2} \left(\frac{\omega \varepsilon}{\rho} \frac{\partial E_z}{\partial \phi} - \beta \frac{\partial H_z}{\partial \rho} \right), \quad (2.47c)$$

$$H_\phi = \frac{-j}{k_c^2} \left(\omega \varepsilon \frac{\partial E_z}{\partial \rho} + \frac{\beta}{\rho} \frac{\partial H_z}{\partial \phi} \right), \quad (2.47d)$$

where $k_c^2 = k^2 + \gamma^2 = k^2 - \beta^2$, as the boundary is assumed to be perfectly conductive. The propagation is along the positive Z-direction ($e^{-j\beta z}$). The Z-direction electric field E_z and magnetic field H_z are respectively expressed as below

$$E_z(\rho, \phi, z) = e_z(\rho, \phi) \cdot e^{-j\beta z}, \quad (2.48)$$

$$H_z(\rho, \phi, z) = h_z(\rho, \phi) \cdot e^{-j\beta z}. \quad (2.49)$$

and they can be calculated from the Helmholtz equations

$$\nabla^2 E_z + k^2 E_z = 0, \quad (2.50)$$

$$\nabla^2 H_z + k^2 H_z = 0. \quad (2.51)$$

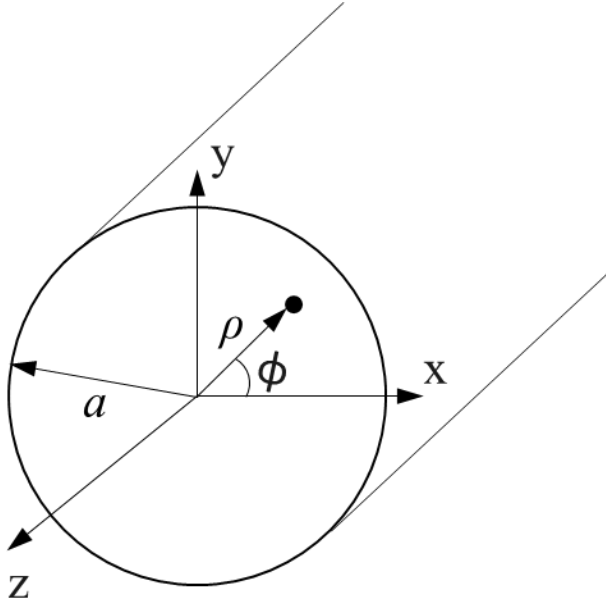


Fig. 2-2 Circular waveguide and cylindrical coordinate system.

Taking E_z as an example, Eq. (2.50) can be written in cylindrical coordinate:

$$\left(\frac{\partial^2}{\partial \rho^2} + \frac{1}{\rho} \frac{\partial}{\partial \rho} + \frac{1}{\rho^2} \frac{\partial^2}{\partial \phi^2} + k_c^2 \right) e_z(\rho, \phi) = 0. \quad (2.52)$$

If we employ the method of separation of variables and let

$$e_z = R(\rho) \cdot P(\phi), \quad (2.53)$$

we get the updated Eq. (2.52) as

$$\frac{\rho^2}{R} \frac{d^2 R}{d\rho^2} + \frac{\rho}{R} \frac{dR}{d\rho} + \rho^2 k_c^2 = \frac{-1}{P} \frac{d^2 P}{d\phi^2}. \quad (2.54)$$

It is apparent the left side of Eq. (2.54) only depends on ρ , while the right only depends on ϕ . Ergo, the two sides should be equal to one constant, which is set to m^2 hereafter. Note m is an integer as e_z must be periodic in ϕ . Then Eq. (2.54) is divided into two equations

$$\frac{d^2 P}{d\phi^2} + m^2 P = 0 \quad (2.55)$$

and

$$\rho^2 \frac{d^2 R}{d\rho^2} + \rho \frac{dR}{d\rho} + (\rho^2 k_c^2 - m^2) R = 0. \quad (2.56)$$

Equation (2.55) is a homogeneous differential equation, and its general solution is

$$P(\phi) = A \sin m\phi + B \cos m\phi, \quad (2.57)$$

where A and B are constants. On the other hand, Eq. (2.56) is recognized as Bessel's differential equation, and the solution is

$$R(\rho) = CJ_m(k_c\rho) + DY_m(k_c\rho), \quad (2.58)$$

where J_m and Y_m are the m -order first-kind and second-kind Bessel functions, respectively. Coefficients C and D are constants. Since the value of $Y_m(k_c\rho)$ becomes infinite at $\rho = 0$, which is physically irrational. Therefore, the coefficient D is set to 0 to make $DY_m(k_c\rho) = 0$. Consequently, the expression of e_z is as below

$$e_z(\rho, \phi) = (A \sin m\phi + B \cos m\phi)J_m(k_c\rho), \quad (2.59)$$

where the constant C is merged into A and B . Similarly, we can also derive the expression of h_z from Eq. (2.51) as

$$h_z(\rho, \phi) = (A \sin m\phi + B \cos m\phi)J_m(k_c\rho). \quad (2.60)$$

2.1.4.1 Circular TM modes

For circular TM modes, the longitudinal magnetic field $H_z = 0$, while the longitudinal electric field $E_z \neq 0$. Each components of the electric and magnetic fields are given below:

$$E_\rho = \frac{-j\beta}{k_c^2} (A \sin m\phi + B \cos m\phi)J_m'(k_c\rho)e^{-j\beta z}, \quad (2.61a)$$

$$E_\phi = \frac{-j\beta m}{k_c^2 \rho} (A \cos m\phi - B \sin m\phi)J_m(k_c\rho)e^{-j\beta z}, \quad (2.61b)$$

$$E_z = (A \sin m\phi + B \cos m\phi)J_m(k_c\rho)e^{-j\beta z}, \quad (2.61c)$$

$$H_\rho = \frac{-j\omega\epsilon m}{k_c^2 \rho} (A \cos m\phi - B \sin m\phi)J_m(k_c\rho)e^{-j\beta z}, \quad (2.61d)$$

$$H_\phi = \frac{-j\omega\epsilon}{k_c} (A \sin m\phi + B \cos m\phi)J_m'(k_c\rho)e^{-j\beta z}, \quad (2.61e)$$

$$H_z = 0. \quad (2.61f)$$

The boundary condition for TM modes is

$$E_z(\rho, \phi)|_{\rho=a} = 0. \quad (2.62)$$

To fulfill the above condition, the term $J_m(k_c\rho)$ in Eq. (2.61c) must be 0, namely

$$J_m(k_c a) = 0. \quad (2.63)$$

Here we define p_{mn} as the n -th root of m -order Bessel function J_m , so the cut-off wavenumber is

$$k_{cmm} = \frac{p_{mn}}{a}. \quad (2.64)$$

Table 2-1 summarizes the values of p_{mn} , wherein $m \geq 0$ and $n \geq 1$. The phase constant of TM_{mn} mode is

$$\beta_{mn} = \sqrt{k^2 - k_{c_{mn}}^2} = \sqrt{k^2 - \left(\frac{p_{mn}}{a}\right)^2}, \quad (2.65)$$

while the cut-off frequency can be calculated as

$$f_{c_{mn}} = \frac{k_c}{2\pi\sqrt{\epsilon\mu}} = \frac{p_{mn}}{2\pi a\sqrt{\epsilon\mu}}. \quad (2.66)$$

In addition, the wave impedance of TM_{01} mode is

$$Z_{\text{TM}} = \frac{E_\rho}{H_\phi} = -\frac{E_\phi}{H_\rho} = \frac{\beta}{\epsilon\omega} = \frac{\eta\beta}{k}, \quad (2.67)$$

where $\eta = \sqrt{\mu/\epsilon}$.

Table 2-1 Values of p_{mn} for circular TM modes.

m \ n	1	2	3	4	5
0	2.40482556	5.5200781	8.6537279	11.791534	14.930918
1	3.83170597	7.0155867	10.173468	13.323692	16.47063
2	5.1356223	8.4172441	11.619841	14.795952	17.959819
3	6.3801619	9.7610231	13.015201	16.223466	19.409415

2.1.4.2 Circular TE modes

To circular TE modes, the longitudinal electric field $E_z = 0$, while the longitudinal magnetic field is H_z is given by

$$H_z = (A \sin m\phi + B \cos m\phi)J_m(k_c\rho)e^{-j\beta z}. \quad (2.68)$$

Other components of E or H are derived as below

$$E_\rho = \frac{-j\omega\mu m}{k_c^2\rho}(A \cos m\phi - B \sin m\phi)J_m(k_c\rho)e^{-j\beta z}, \quad (2.69a)$$

$$E_\phi = \frac{j\omega\mu}{k_c}(A \sin m\phi + B \cos m\phi)J_m'(k_c\rho)e^{-j\beta z}, \quad (2.69b)$$

$$H_\rho = \frac{-j\beta}{k_c}(A \sin m\phi + B \cos m\phi)J_m'(k_c\rho)e^{-j\beta z}, \quad (2.69c)$$

$$H_\phi = \frac{-j\beta m}{k_c^2\rho}(A \cos m\phi - B \sin m\phi)J_m(k_c\rho)e^{-j\beta z}. \quad (2.69d)$$

The boundary condition for TE mode is

$$E_\phi(\rho, \phi)|_{\rho=a} = 0. \quad (2.70)$$

Hence, the term $J_m'(k_c\rho)$ in Eq. (2.69b) needs to be set to 0 as

$$J'_m(k_c a) = 0. \quad (2.71)$$

Similar to TM mode, we define a parameter p'_{mn} as the n -th root of the derivative of m -order Bessel function J'_m , determining the cut-off wavenumber

$$k_{c_{mn}} = \frac{p'_{mn}}{a}. \quad (2.72)$$

The values of p'_{mn} are summarized in Table 2-2. The phase constant and cut-off frequency are thus deduced as below:

$$\beta_{mn} = \sqrt{k^2 - k_{c_{mn}}^2} = \sqrt{k^2 - \left(\frac{p'_{mn}}{a}\right)^2}, \quad (2.73)$$

$$f_{c_{mn}} = \frac{k_c}{2\pi\sqrt{\epsilon\mu}} = \frac{p'_{mn}}{2\pi a\sqrt{\epsilon\mu}}. \quad (2.74)$$

The wave impedance of TE mode is

$$Z_{\text{TM}} = \frac{E_\rho}{H_\phi} = -\frac{E_\phi}{H_\rho} = \frac{\beta}{\epsilon\omega} = \frac{\eta\beta}{k}, \quad (2.75)$$

where $\eta = \sqrt{\mu/\epsilon}$.

Table 2-2 Values of p'_{mn} for circular TE modes.

m \ n	1	2	3	4	5
0	3.83170597	7.01558667	10.17346814	13.32369194	16.47063005
1	1.841183781	5.331442774	8.536316366	11.7060049	14.86358863
2	3.054236928	6.706133194	9.969467823	13.17037086	16.34752232
3	4.201188941	8.015236598	11.34592431	14.58584829	17.78874787

2.1.5 Microwave loss

In Section 2.1.4, we discussed the microwave propagation in a perfect conductor, in other words, no dissipation or energy loss. So the propagation constant $\gamma = j\beta$. But in reality, since the material of waveguide is imperfectly conductive, and the media inside the waveguide is not vacuum, the power losses inevitably occur. Especially for long-distance transmission, the attenuation is not negligible and needs to be taken into account. Therefore, the real part of propagation constant, i.e. the attenuation constant α , should be evaluated.

Usually, the attenuation in a waveguide results from two types of losses, the conductor loss and dielectric loss. The total attenuation is the summation of these two losses as

$$\alpha = \alpha_c + \alpha_d, \quad (2.76)$$

where α is the total attenuation constant, while α_c and α_d are the attenuation constants due to the conductor loss and dielectric loss, respectively.

For circular waveguide, the dielectric constant for TM and TE modes is identical. The derivation is given as follows. Firstly, the complex permittivity ϵ is expressed as below

$$\epsilon = \epsilon' - j\epsilon'' \tan \delta = \epsilon_0 \epsilon_r (1 - j \tan \delta), \quad (2.77)$$

where $\tan\delta$ is the loss tangent of the material. The propagation constant is thus given by

$$\begin{aligned}\gamma &= \sqrt{k_c^2 - k^2} = \sqrt{k_c^2 - \omega^2 \mu \epsilon (1 - j \tan \delta)} \\ &= \sqrt{-\beta^2 + j \omega^2 \mu \epsilon \tan \delta} \\ &\approx \frac{k^2 \tan \delta}{2\beta} + j\beta\end{aligned}\quad (2.78)$$

wherein the approximation was made in terms of Taylor expansion. From the above equation, we can see there is no change in the phase constant β , while the attenuation constant due to dielectric loss α_d for TM or TE mode is given by

$$\alpha_d = \frac{k^2 \tan \delta}{2\beta} \text{ Np/m}, \quad (2.79)$$

Moreover, Eq. (2.79) can also be applied to TEM mode by replacing β with k as

$$\alpha_d = \frac{k \tan \delta}{2} \text{ Np/m}. \quad (2.80)$$

In regard to the conductor loss, the expressions of the attenuation constants due to conductor loss for circular TM and TE modes are different and should be evaluated respectively. The results are presented directly here as Eqs. (2.81) and (2.82), while the detailed deductions can be found in [118], for TM_{mn} mode:

$$\alpha_c = \frac{a R_s \omega \epsilon k_c^2}{\beta p_{mn}^2} = \frac{k R_s}{\beta \eta a} \text{ Np/m}, \quad (2.81)$$

for TE_{mn} mode:

$$\alpha_c = \frac{R_s}{\beta k \eta a} \left[k_c^2 + \frac{m^2 k^2}{(p'_{mn})^2 - m^2} \right] \text{ Np/m}, \quad (2.82)$$

where R_s is the surface resistance of the conductor

$$R_s = \sqrt{\frac{\omega \mu}{2\sigma}} = \eta \sqrt{\frac{\omega \epsilon}{2\sigma}} = \frac{1}{\delta \sigma} \quad (\delta \text{ is skin depth}). \quad (2.83)$$

2.2 Numerical simulation for microwave NDT

Two/three-dimensional numerical simulations are adopted for analysis. A commercial software COMSOL Multiphysics in conjunction with its RF module [119] is employed for computation, and finite element method is used for field solution. The governing equation is given below

$$\nabla \times \mu_r^{-1} (\nabla \times \mathbf{E}) - k_0^2 [\epsilon_r - j \sigma / (\omega \epsilon_0)] \mathbf{E} = 0, \quad (2.84)$$

where $k_0 = \omega \sqrt{\epsilon_0 \mu_0}$ denotes the propagation constant in a vacuum, determined by the angular frequency ω as well as the permittivity ϵ_0 and permeability μ_0 in a vacuum. The values of ϵ_0 and μ_0 are 8.854×10^{-12} F/m and $4\pi \times 10^{-7}$ H/m, respectively. The electric field \mathbf{E} is solved in three-dimension, and σ denotes the conductivity. The parameters ϵ_r and μ_r in denote the relative permittivity and relative permeability, respectively. In the calculation, the values for ϵ_r , μ_r and σ are assigned to 1, 1, and 0 for the

media air. The boundary condition of the inner pipe surface is defined as perfect electric conductor, which is characterized by

$$\mathbf{n} \times \mathbf{E} = 0, \quad (2.85)$$

where \mathbf{n} is the outward normal vector on the inner surface of waveguide.

Say the microwaves propagate along the Z-direction, so the waves of electric field transmitted to the negative Z-direction is written as

$$\mathbf{E} = \mathbf{E}_T(r, \phi) \exp(j\omega t + j\beta z). \quad (2.86)$$

Since no microwave is transmitted to the positive Z-direction, the absorption condition is

$$\frac{1}{\beta} \frac{\partial \mathbf{E}}{\partial z} - \frac{1}{\omega} \frac{\partial \mathbf{E}}{\partial t} = 0. \quad (2.87)$$

If there exist microwaves transmitted to the positive Z-direction \mathbf{E}_0 as

$$\mathbf{E} = \mathbf{E}_T(r, \phi) \exp(j\omega t + j\beta z) + \mathbf{E}_{0T}(r, \phi) \exp(j\omega t - j\beta z), \quad (2.88)$$

so the absorption condition at the boundary is given by

$$\frac{1}{\beta} \frac{\partial \mathbf{E}}{\partial z} - \frac{1}{\omega} \frac{\partial \mathbf{E}}{\partial t} = -\frac{2}{\omega} \frac{\partial \mathbf{E}_0}{\partial t}. \quad (2.89)$$

The scattering parameter (S-parameter) [120] is used to evaluate the transmission and reflection characteristics of microwaves. Figure 2-3 exhibits a two-port (1 and 2) network, in which a_1/a_2 refers to the wave incident to port 1/2, while b_1/b_2 represents the wave reflected from port 1/2. The coefficient matrix \mathbf{S} between ports 1 and 2 is a mathematical construct quantifying the energy propagation between two ports, the correlation between a_1 , a_2 , b_1 , b_2 and \mathbf{S} is characterized by

$$\begin{pmatrix} b_1 \\ b_2 \end{pmatrix} = \begin{pmatrix} S_{11} & S_{12} \\ S_{21} & S_{22} \end{pmatrix} \times \begin{pmatrix} a_1 \\ a_2 \end{pmatrix}, \quad (2.90)$$

where S_{11} , S_{12} , S_{21} , and S_{22} are defined as S-parameters, and their summation suffices for the following equation

$$|S_{11}|^2 + |S_{12}|^2 + |S_{21}|^2 + |S_{22}|^2 = 1. \quad (2.91)$$

In numerical simulations, the electric field intensity at the incident port (say, port 1) and transmission port (say, port 2) are used to calculate S-parameters as [119]

$$S_{11} = \frac{\int_{\text{port1}} [(E_c - E_1) \cdot E_1^*] dS}{\int_{\text{port1}} (E_1 \cdot E_1^*) dS}, \quad (2.92)$$

$$S_{21} = \frac{\int_{\text{port2}} (E_c \cdot E_2^*) dS}{\int_{\text{port1}} (E_2 \cdot E_2^*) dS}, \quad (2.93)$$

wherein E_c represents the measured electric field intensity, while E_1 and E_2 denote the electric field intensity of a specific microwave mode. S_{12} and S_{22} can be calculated in the same way. And to an N-port network, the summation of all $|S_{ij}|^2$ is computed to be 1 (i, j refers to the port number).

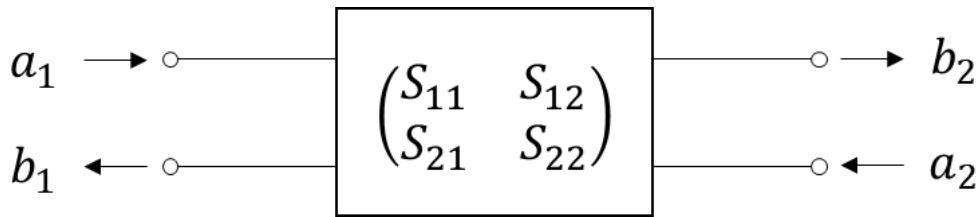


Fig. 2-3 Two-port network.

2.3 Experimental apparatus

2.3.1 Microwave generation

In this study, a vector network analyzer (Agilent Technologies, E8363B) is employed for exciting coaxial TEM mode microwaves and measuring the transmission/reflection characteristics in a frequency domain. The network analyzer is characterized by a working frequency range from 10 MHz to 40 GHz with a dynamic range of 110dB, 32 channels, and 16001 points at maximum. The network analyzer has two ports, enabling us to measure two-port S-parameters. A ‘transform’ function is available to transform the measured frequency-domain signal into a time domain, while a built-in ‘average’ function can automatically measure the signals for a certain number of times and then calculate the average values of multiple measurements. In this study, the average operation is set to 30 times.

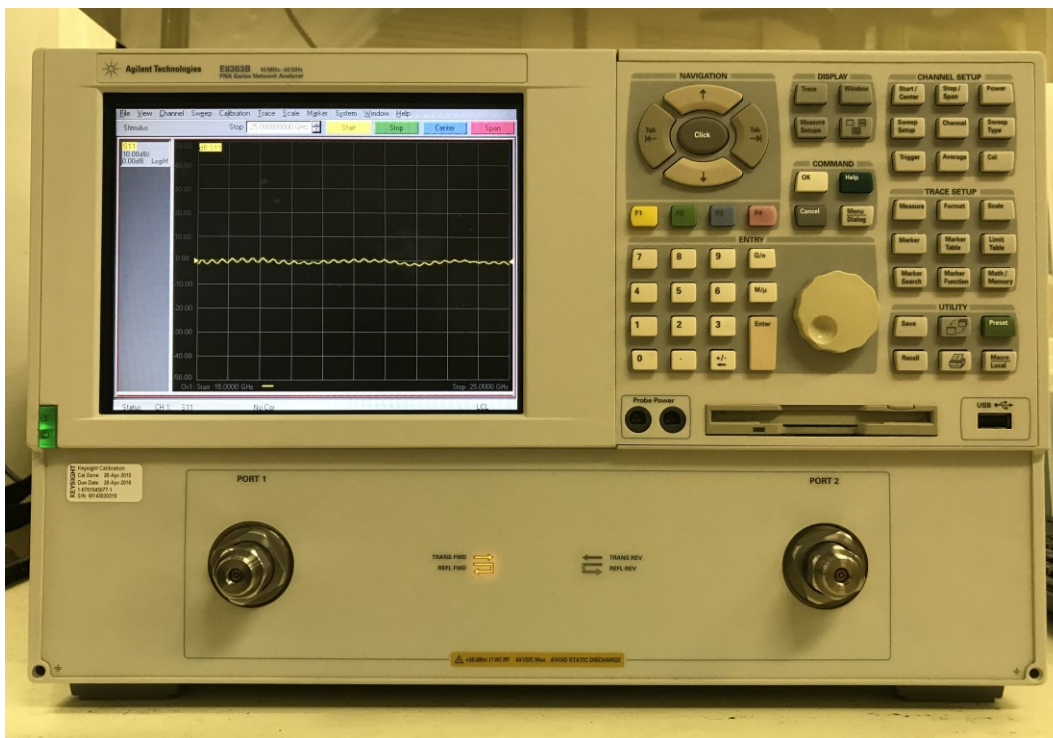


Fig. 2-4 Network analyzer.

2.3.2 Flexible cable

A flexible cable (Junkosha, MWX051, made by) is used to transmit the TEM mode microwaves generated by the vector network analyzer. It should be noted that: prior to the measurement, the vector network analyzer together with the flexible cable needs to be calibrated to compensate for the cable characteristic and channel delay, by using a calibration toolkit (Keysight Technologies, 85056D) and the

SOLT method [121].



Fig. 2-5 Flexible cable.

2.3.3 Semi-rigid cable and connector

A semi-rigid cable (Anritsu Corporation, K118) is also used for microwave transmission, and a K connector (Anritsu Corporation, K101F-R) from the same manufacturer is adopted to connect the flexible to the semi-rigid cable. The K connector and the semi-rigid cable are often used to make mode converters in conjunction with a conductive epoxy (Chemtronics, CW2400 or MG Chemicals, 8331), which glues them together or to other objects.

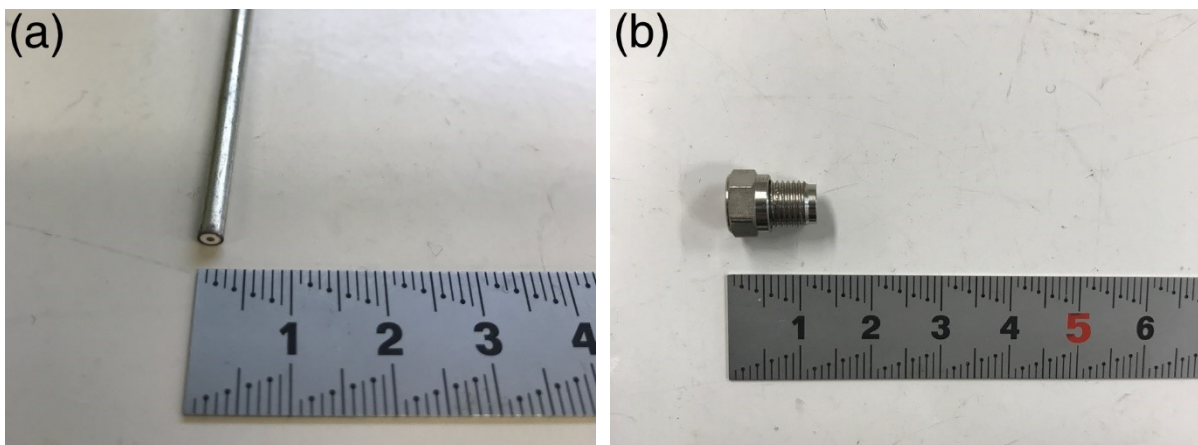


Fig. 2-6 (a) Semi-rigid cable (left) and (b) K connector (right).

2.4 Signal-processing method

2.4.1 Fourier and inverse Fourier transform

In this study, the experimentally measured S-parameters are in the frequency domain, while the analysis is mainly made in the time-domain for detecting and locating the flaw. The Fourier and inverse Fourier transform are used and given by

$$F(\omega) = \int_{-\infty}^{+\infty} f(t)e^{-j\omega t} dt, \quad (2.94)$$

$$f(t) = \frac{1}{2\pi} \int_{-\infty}^{+\infty} F(\omega)e^{-j\omega t} d\omega, \quad (2.95)$$

where $\omega = 2\pi f$ is the angular frequency. The above two equations apply to the transform of continuous signals, while the practical measurement was made at equidistant frequencies over a wide range. Ergo, the discrete Fourier transform and inverse discrete Fourier transform should be utilized as

$$X[k] = \sum_{n=0}^{N-1} x[n]e^{-j(2\pi nk/N)}, \quad (2.96)$$

$$x[n] = \frac{1}{N} \sum_{k=0}^{N-1} X[k]e^{j(2\pi nk/N)}, \quad (2.97)$$

where N is the sequence length (number of points).

Here we set N as the sampling rate in the frequency-domain, and define f_s as the sweeping frequency span, Δf as the frequency-domain resolution, t_R as the time range, Δt as the time-domain resolution, and it is obvious that

$$f_s = N \cdot \Delta f, \quad (2.98)$$

$$t_R = N \cdot \Delta t, \quad (2.99)$$

where the number of points N in the frequency domain is consistent with that in the time domain. According to the characteristic of Fourier and inverse Fourier transform, the time domain resolution is inversely proportional to the frequency span:

$$\Delta t = \frac{1}{f_s} = \frac{1}{N \cdot \Delta f}. \quad (2.100)$$

Equation (2.100) indicates that a higher time-domain resolution Δt can be achieved with a wider sweeping frequency span f_s . Meanwhile, the time range t can be further expressed as

$$t_R = N \cdot \Delta t = \frac{1}{\Delta f}, \quad (2.101)$$

manifesting that time range t_R is inversely proportional to the frequency-domain resolution Δf . Hence, the sampling rate in the frequency domain should be carefully selected to achieve the balance between Δt and t_R , in other words, detection resolution and range.

Besides, a window function is also used to suppress the sidelobe and maximize the energy in the main lobe. The expression of the window function is given by

$$W_{\text{Kaiser}}(n) = 2 \cdot \frac{I_0 \left[\beta \sqrt{1 - \left(\frac{2n}{N-1} - 1 \right)^2} \right]}{I_0(\beta)}, \quad (2.102)$$

where I_0 is the zeroth-order modified Bessel function of the first kind, N is the window length, and β is the shape factor. In this study, the value of β is set to 6 as an empirical value.

2.4.2 Dispersion compensation

As discussed in Section 2.1.3, when wideband waves propagate and the phase velocity for different frequencies are also different, so the signal distortion, i.e., dispersion, inevitably occurs. A signal-processing method [122,123] was thereby developed to compensate for the dispersion of microwaves during propagation. The details of the method are elucidated as follows. The dispersion of microwaves is compensated by shifting the phase from a certain propagation distance L_C to obtain a pulse, as given by the equation below:

$$\varphi(f) = 2L_C \cdot \left[\frac{1}{\lambda_p} - \frac{1}{\lambda} \right] \cdot 2\pi, \quad (2.103)$$

where φ denotes the shifted phase, f is the frequency, λ and λ_p refer to the wavelengths in free space and in a pipe, respectively. The coefficient 2 accounts for the roundtrip of microwave propagation. Taking TM_{01} mode as an instance, the parameter λ_p is given by

$$\lambda_p = \frac{1}{\sqrt{\left(\frac{f}{c}\right)^2 - \left(\frac{p_{01}}{\pi D}\right)^2}}, \quad (2.104)$$

where c is the speed of light in a vacuum, D is the inner pipe diameter, and p_{01} is the first root of the Bessel function of the first kind J_0 . This process was conducted for a series of L_C . The position of the flaw was predicted by calculating the time-of-flight of the reflection without dispersion and obtaining the peak values for the distance range of the pipe length. A flow chart summarizing the signal-processing method is shown in Fig. 2-7.

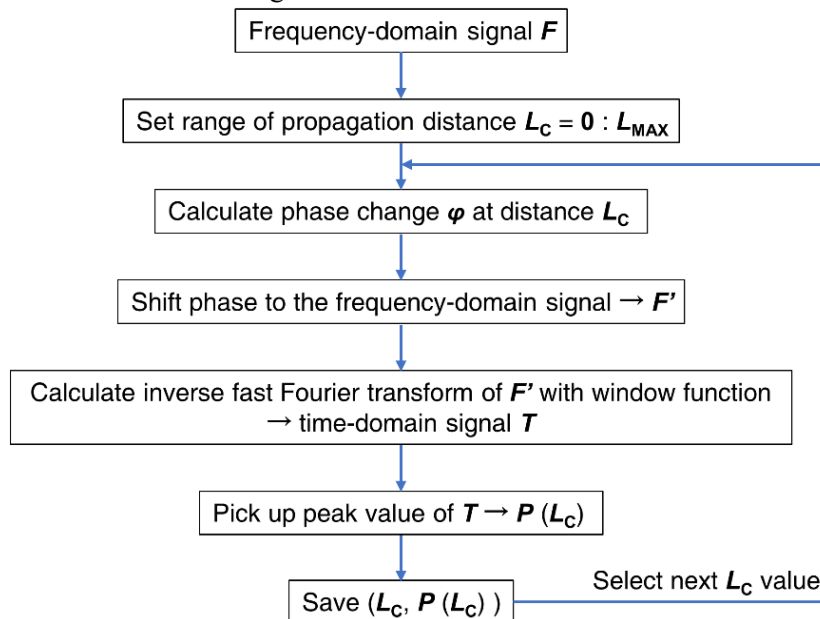


Fig. 2-7 Flow chart of the signal-processing method.

Chapter 3 The effect of a bend on microwave transmission and reflection

In this chapter, how a bend influences the transmission and reflection of microwaves is evaluated. Firstly, an overview of microwave propagation inside a bent pipe is given to offer an intuition; Secondly, the dependence of mode conversion at a bend is clarified via theoretical derivation and numerical simulation; Finally, the effects of multiple bends on reflection signals from pipe wall thinning flaws is evaluated via experiments.

3.1 Overview of microwave propagation in a bent pipe

The propagation of TM_{01} mode microwaves inside a bent pipe is analyzed as an instance, as illustrated in Fig. 3-1 and analyzed as follows. Firstly, the coaxial TEM mode microwaves (generated by a network analyzer, not shown in the figure) are transmitted to a microwave probe. The TEM- TM_{01} mode converter, one of the common microwave probes, is hereby used as an example, while the details of the TEM- TM_{01} mode converter will be given in Section 3.4. Subsequently, the TEM mode microwaves are converted into circular TM_{01} mode and enter the pipe. The TM_{01} mode microwaves undergo mode conversions twice at the bend region: (1) the transmitted TM_{01} mode microwaves are partially converted into several modes when passing through the bend for the first time; (2) the converted modes along with TM_{01} mode are reflected back at the defect (or the pipe fitting, pipe end, etc.), and undergo the second mode conversion on their return trip through the bend. In the second conversion, a portion of other modes (particularly TE_{11} mode in this scenario) can also be converted into the TM_{01} mode. It should be noted that: only TM_{01} mode microwaves can be 'retrieved' by the microwave probe, then converted into TEM mode microwaves, and eventually received by the network analyzer. On the basis of the above analysis, the energy loss of transmission mode (TM_{01}) is inevitable because of the mode conversion at the bend. Therefore, it can be presumed that the reflections in a bent pipe (behind the bend, specifically) would become more dispersed and of smaller amplitudes, compared with those in a straight pipe.

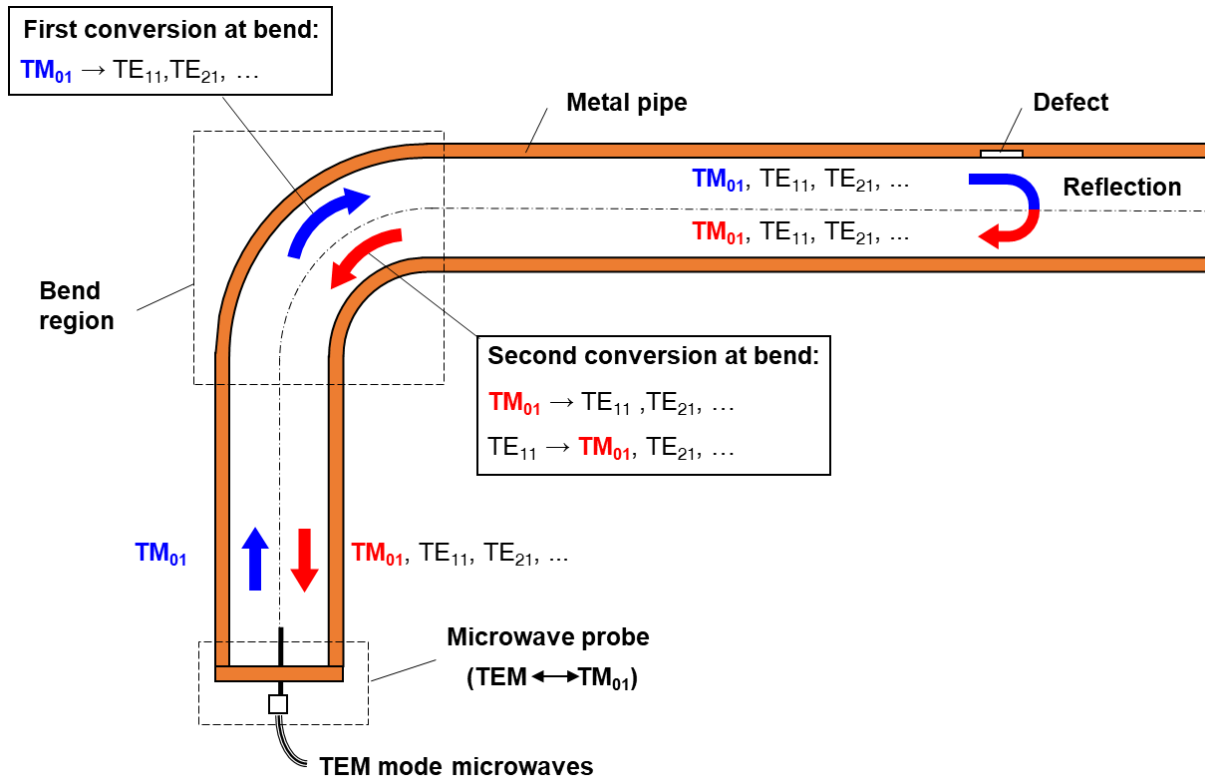


Fig. 3-1 Overview of microwave transmission and conversion inside a bent pipe.

3.2 Theoretical derivation of the mode conversion due to a bend

From the analysis in Section 3.1, we can see the mode conversion of microwaves at a bend is very crucial and should be clarified at first.

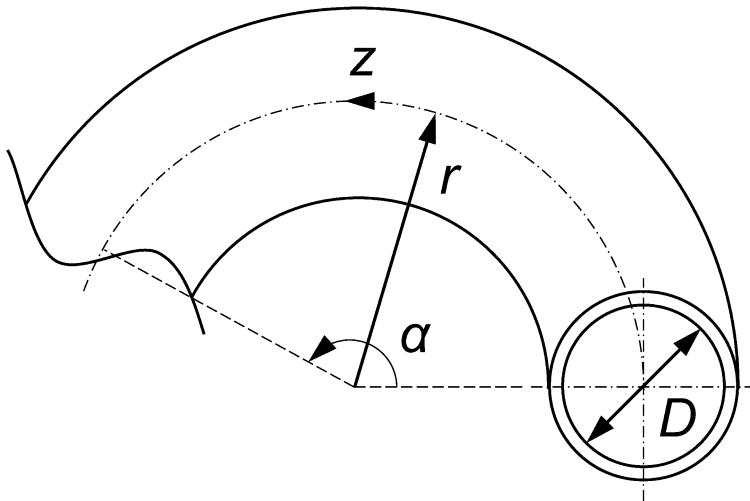


Fig. 3-2 Illustration of a curved pipe.

A geometric illustration of a curved pipe is shown in Fig. 3-2, in which parameters D , r , α , and z represent the pipe's inner diameter, the curvature radius, the bend angle, and the distance measured along the curved axis, respectively. In fact, many theoretical studies on mode conversion/coupling due to a bend have been carried out in several earlier studies [124-127], and the mathematical expression is given as the equation system below:

$$\begin{cases} \frac{dA_{m'n'}^+}{dz} = -j\beta_{m'n'}A_{m'n'}^+ - j\sum_{mn} C_{(m'n')(mn)}^\pm A_{mn}^\pm \\ \frac{dA_{m'n'}^-}{dz} = j\beta_{m'n'}A_{m'n'}^- + j\sum_{mn} C_{(m'n')(mn)}^\pm A_{mn}^\pm \end{cases}, \quad (3.1)$$

wherein A , C , and β are the complex amplitude of the coupled mode, coupling coefficient, and phase constant, respectively. The signs '+' and '-' refer to the forward and backward direction of propagation, respectively. The subscripts m , n , m' and n' denote the mode numbers, bound by the condition $|m - m'| = 1$. The symbol j is the imaginary unit.

According to the formula of the coupling coefficient C among different microwave modes [128], C is dependent on r , D , and the frequency f when the coupled modes are certain. Meanwhile, the phase constant β is dependent on D and f . Therefore, it can be easily seen that the mode conversion of microwaves at a bend is a function of four factors, as $F(r, D, \alpha, f)$. However, in the authors' previous works [129,130], the results suggested that: it was the curvature radius normalized by the pipe's inner diameter r/D , the frequency normalized by the cut-off frequency f/f_c , and the bend angle α that serve as the major factors influencing the mode conversion at a bend, as expressed below:

$$F(r, D, \alpha, f) = F_N\left(\frac{r}{D}, \frac{f}{f_c}, \alpha\right). \quad (3.2)$$

This conclusion simplifies the computation of the mode conversion at a bend with fewer parameters and merges similar cases. A concise mathematical demonstration is given here.

Firstly, since $z = r\alpha$, Eq. (3.1) can be rewritten as:

$$\begin{cases} \frac{dA_{m'n'}^+}{d\alpha} = -jr\beta_{m'n'}A_{m'n'}^+ - j\sum_{mn} rC_{(m'n')(mn)}^\pm A_{mn}^\pm \\ \frac{dA_{m'n'}^-}{d\alpha} = jr\beta_{m'n'}A_{m'n'}^- + j\sum_{mn} rC_{(m'n')(mn)}^\pm A_{mn}^\pm \end{cases}. \quad (3.3)$$

The term $r\beta_{m'n'}$ in Eq. (3.3) can be expressed as:

$$r\beta_{m'n'} = r\sqrt{k^2 - k_{cm'n'}^2} = r\sqrt{k^2 - \frac{X_{m'n'}^2}{(D/2)^2}}, \quad (3.4)$$

where k is the wave number, while $k_{cm'n'}$ refers to the cut-off wavenumber of the $m'n'$ -th mode. The symbol $X_{m'n'}$ is the n' -th root of the Bessel function of the first kind $J_m(X)$ (for TM modes) or the derivative of the Bessel function of the first kind $J'_m(X)$ (for TE modes). Parameters $u_{m'n'}$ and $v_{m'n'}$ are introduced to express $X_{m'n'}$ for TM and TE modes hereafter, respectively, to distinguish the two types of modes.

Define k_{cTM01} as the cut-off wavenumber of TM_{01} mode, given by

$$k_{cTM01} = \frac{u_{01}}{(D/2)}, \quad (3.5)$$

where u_{01} is the first root of $J_0(X)$ and stands for TM_{01} mode. Since the wavenumber k is proportional to the frequency f , Eq. (3.4) is expressed as:

$$r\beta_{m'n'} = k_{cTM01} \cdot r\sqrt{\frac{k^2}{k_{cTM01}^2} - \frac{k_{cm'n'}^2}{k_{cTM01}^2}} = 2u_{01}\sqrt{\frac{k^2}{k_{cTM01}^2} - \frac{X_{m'n'}^2}{u_{01}^2}} \cdot \frac{r}{D} = 2u_{01}\sqrt{\frac{f^2}{f_{cTM01}^2} - \frac{X_{m'n'}^2}{u_{01}^2}} \cdot \frac{r}{D}, \quad (3.6)$$

where f_{cTM01} is the cut-off frequency of TM_{01} mode.

Equation (3.6) suggested that $r\beta_{m'n'}$ is dependent on r/D and $ff_{c_{TM01}}$. Similarly, the term $rC_{(m'n')(mn)}$ can be expressed by $ff_{c_{TM01}}$, and the demonstration will be given subsequently. Also, in the following context of this section, brackets ‘()’ and ‘[]’ at the subscripts of the coupling coefficient C are used to differentiate between TM and TE modes, respectively.

Take the coupling coefficient from TE_{mn} to $TE_{m'n'}$ mode $rC_{[m'n']_{[mn]}}$ as an example:

(i) when $m = 0$,

$$C_{[m'n']_{[mn]}}^{\pm} = \frac{v_{mn}v_{m'n'}^2 \cdot (\beta_{mn} \pm \beta_{m'n'})^2}{\sqrt{2[v_{mn}^2 - (m+1)^2]} \cdot (v_{m'n'}^2 - v_{mn}^2) \cdot \sqrt{\beta_{mn} \cdot \beta_{m'n'}}} \cdot \frac{D}{2r} \cdot (-1)^{n+n'+1}. \quad (3.7)$$

Let

$$c_{EE0} = \frac{v_{mn}v_{m'n'}^2 \cdot (-1)^{n+n'+1}}{\sqrt{2[v_{m'n'}^2 - (m+1)^2]} \cdot (v_{m'n'}^2 - v_{mn}^2)}, \quad (3.8)$$

hence

$$rC_{[m'n']_{[mn]}}^{\pm} = \frac{c_{EE0} \cdot (\beta_{mn} \pm \beta_{m'n'})^2}{\sqrt{\beta_{mn} \cdot \beta_{m'n'}}} \cdot \frac{D}{2} = c_{EE0}u_{01} \cdot \frac{\left(\sqrt{\left(\frac{f}{f_{cTM01}}\right)^2 - \frac{v_{mn}^2}{u_{01}^2}} \pm \sqrt{\left(\frac{f}{f_{cTM01}}\right)^2 - \frac{v_{m'n'}^2}{u_{01}^2}} \right)}{\sqrt{\sqrt{\left(\frac{f}{f_{cTM01}}\right)^2 - \frac{v_{mn}^2}{u_{01}^2}} \cdot \sqrt{\left(\frac{f}{f_{cTM01}}\right)^2 - \frac{v_{m'n'}^2}{u_{01}^2}}}}. \quad (3.9)$$

(ii) when $m > 0$,

$$C_{[m'n']_{[mn]}}^{\pm} = c_{EE1} \cdot \frac{k^2(D/2)}{r\sqrt{\beta_{mn} \cdot \beta_{m'n'}}} \cdot \left[c_{EE2} + c_{EE2} \frac{\beta_{mn} \cdot \beta_{m'n'}}{k^2} - \frac{c_{EE3}}{k^2(D/2)^2} \right], \quad (3.10)$$

where

$$c_{EE1} = \frac{(-1)^{n+n'}}{2\sqrt{(v_{mn}^2 - n^2)[v_{m'n'}^2 - (n+1)^2]} \cdot (v_{m'n'}^2 - v_{mn}^2)}, \quad (3.11)$$

$$c_{EE2} = 2v_{m'n'}^2v_{mn}^2 - m(m+1)(v_{m'n'}^2 + v_{mn}^2), \quad (3.12)$$

and

$$c_{EE3} = v_{m'n'}^2v_{mn}^2[v_{m'n'}^2 + v_{mn}^2 - 2m(m+1)]. \quad (3.13)$$

Thus $rC_{[m'n']_{[mn]}}$ is written as:

$$\begin{aligned} rC_{[m'n']_{[mn]}}^{\pm} &= c_{EE1} \cdot \frac{k^2(D/2)}{\sqrt{\beta_{mn} \cdot \beta_{m'n'}}} \cdot \left[c_{EE2} + c_{EE2} \frac{\beta_{mn} \cdot \beta_{m'n'}}{k^2} - \frac{c_{EE3}}{k^2(D/2)^2} \right] \\ &= c_{EE1}u_{01} \cdot \left[c_{EE2} \frac{\left(\frac{f}{f_{cTM01}}\right)^2}{\sqrt{\sqrt{\left(\frac{f}{f_{cTM01}}\right)^2 - \frac{v_{mn}^2}{u_{01}^2}} \cdot \sqrt{\left(\frac{f}{f_{cTM01}}\right)^2 - \frac{v_{m'n'}^2}{u_{01}^2}}}} + c_{EE2} \sqrt{\sqrt{\left(\frac{f}{f_{cTM01}}\right)^2 - \frac{v_{mn}^2}{u_{01}^2}} \cdot \sqrt{\left(\frac{f}{f_{cTM01}}\right)^2 - \frac{v_{m'n'}^2}{u_{01}^2}}} \right. \\ &\quad \left. - \frac{c_{EE3}}{u_{01}^2 \sqrt{\sqrt{\left(\frac{f}{f_{cTM01}}\right)^2 - \frac{v_{mn}^2}{u_{01}^2}} \cdot \sqrt{\left(\frac{f}{f_{cTM01}}\right)^2 - \frac{v_{m'n'}^2}{u_{01}^2}}}} \right] \end{aligned} \quad (3.14)$$

From Eqs. (3.9) and (3.14), it is evident that $rC_{[m'n']_{[mn]}}$ is a function of $ff_{c_{TM01}}$. Therefore, it can be

concluded that the coefficients $r\beta$ and rC in Eq. (3.3) are determined by r/D and $ff_{c_{TM01}}$, while the solution is determined by α . The mathematical demonstrations for other coupling coefficients ($C_{[m'n'](mn)}$, $C_{(m'n')(mn)}$, and $C_{(m'n')[mn]}$) are given in Section A of Appendix. The above deductions confirm that the mode conversion of microwaves depends on three factors: r/D , $ff_{c_{TM01}}$, and α . Actually, the cut-off frequency f_c used for normalizing f can be arbitrary, which can be proved by a simple derivation and will be validated in Section 3.3 via numerical simulation. Furthermore, it is noteworthy that: although the discussion above is purely analytical, in practice the mode conversion needs to be solved numerically due to ordinary differential parameters.

3.3 Numerical simulation on mode conversion

Three-dimensional finite element simulations were performed in the frequency domain to further verify the conclusion of the theoretical deduction: $F(r, D, \alpha, f) = F_N(r/D, ff_c, \alpha)$. The simulation environment is the same as Section 2.2, and the geometric model of a bent pipe is displayed in Fig. 3-3. The $TM_{01}/TE_{01}/TE_{11}$ mode microwaves were respectively excited from one pipe end (Surface I), while the transmission characteristic was evaluated at the other one (Surface II) for each of them. The energy ratio of each mode was evaluated by normalizing the transmitted energy with the energy of the input mode. A perfectly matched layer (PML) was used to simulate infinite space from which the reflections to Surface II will be eliminated. Second-order tetrahedral and triangular elements were used for discretization. The simulation parameters of the simulation are itemized in Table 3-1. Parameters $f_{c_{TM01}}$ and $f_{c_{TE01}}$ are the cut-off frequencies of TM_{01} and TE_{01} , respectively. The frequency span of each mode for different D values was chosen to make the range of $f_{TM01}/f_{c_{TM01}}$ or $f_{TE01}/f_{c_{TE01}}$ or $f_{TE11}/f_{c_{TM01}}$ approximately identical (note: here f_{TE11} was normalized by $f_{c_{TM01}}$). Furthermore, it should be mentioned that TE_{11} mode here was linearly-polarized (by convention, the polarization refers to the electric field direction in the pipe cross-section), thus TE_{11} mode under horizontal and vertical polarizations was studied here. (note: here ‘horizontal’ is defined to be perpendicular to gravity direction, while ‘vertical’ is defined to be parallel to gravity direction)

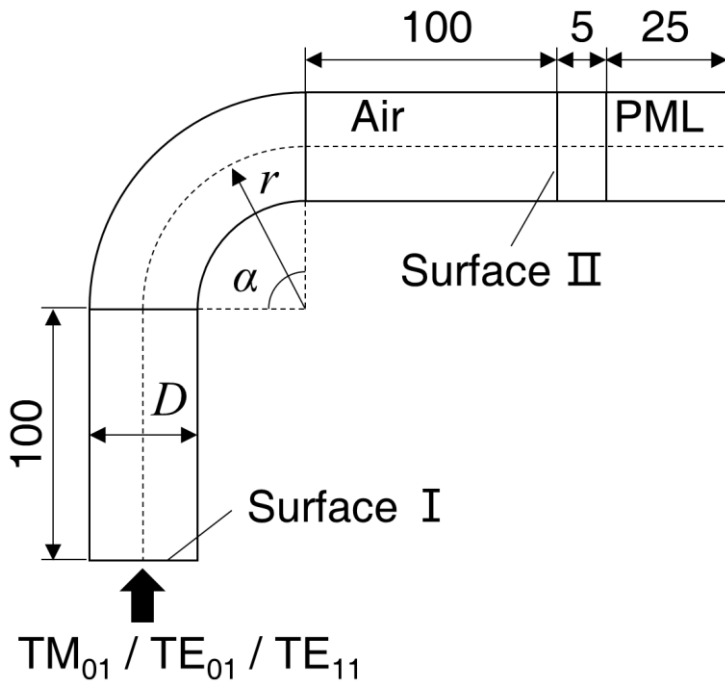


Fig. 3-3 Geometric model of bent pipe for simulation (unit: mm, not to scale).

Table 3-1 Simulation parameters

Parameter (unit)	Value
Pipe's inner diameter, D (mm)	12.7, 39.0, 74.0
Normalized curvature radius, r/D (-)	1, 2, 3, 4, 5
Bend angle, α ($^\circ$)	90, 180
Frequency span of TM_{01} mode, $f_{TM_{01}}$ (GHz)	19.0 – 38.5 (step = 0.5 GHz, $D = 12.7$ mm) 6.5 – 12.5 (step = 0.5 GHz, $D = 39.0$ mm) 3.3 – 6.5 (step = 0.2 GHz, $D = 74.0$ mm)
$f_{TM_{01}}/f_{cTM_{01}}$ (-)	1.05 – 2.12 (approx.)
Frequency span of TE_{01} mode, $f_{TE_{01}}$ (GHz)	30.0 – 38.5 (step = 0.5 GHz, $D = 12.7$ mm) 10.0 – 12.4 (step = 0.4 GHz, $D = 39.0$ mm) 5.2 – 6.6 (step = 0.2 GHz, $D = 74.0$ mm)
$f_{TE_{01}}/f_{cTE_{01}}$ (-)	1.05 – 1.33 (approx.)
Frequency span of TE_{11} mode, $f_{TE_{11}}$ (GHz)	18 – 36 (step = 0.5 GHz, $D = 12.7$ mm) 6 – 12 (step = 0.2 GHz, $D = 39.0$ mm) 3.2 – 6.2 (step = 0.1 GHz, $D = 74.0$ mm)
$f_{TE_{11}}/f_{cTM_{01}}$	1.00 – 2.00 (approx.)

Figures 3-4 and 3-5 present two groups of simulation results for TM_{01} and TE_{01} . Figure 3-4 (a) depicts the simulated fractional energy of TM_{01} , TE_{11} , and TM_{11} modes, when $r/D = 4$, $\alpha = 90^\circ$, and TM_{01} mode was the excitation mode. The transmission characteristics for three different D values are distinctly separated given that their frequency spans are also different. However, if we normalize the results with the cut-off frequencies of TM_{01} mode for $D = 12.7$, 39.0, and 74.0 mm, as shown in Fig. 3-4 (b), the simulation results of the three different D values completely overlap each other and coincide with the theoretically calculated results. Similarly, the simulation result of mode conversion from TE_{01} mode ($r/D = 2$, $\alpha = 180^\circ$) is presented in Fig. 3-5, and a similar consequence was also obtained: the simulation results agree with the theoretically calculated results after normalization using the cut-off frequencies of TE_{01} mode.

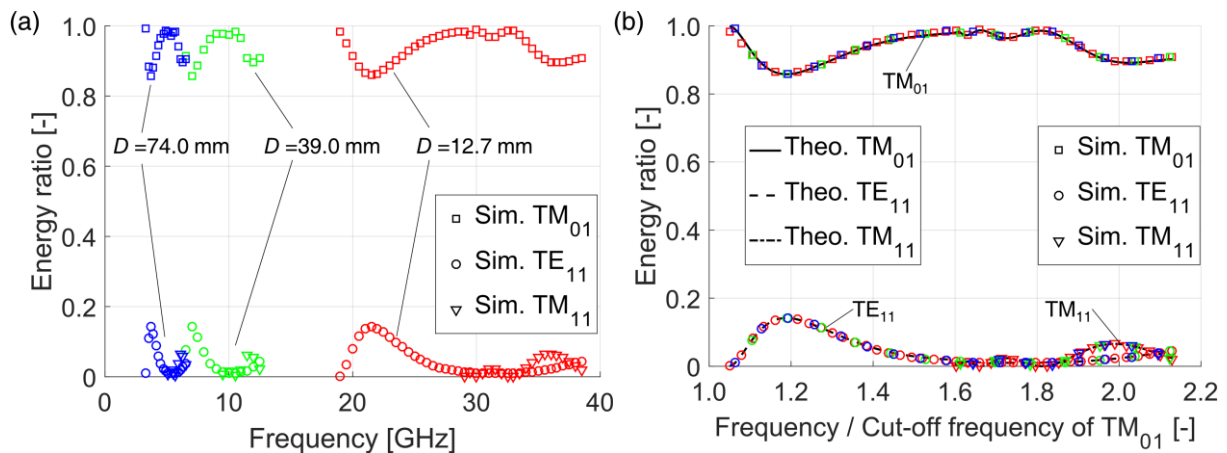


Fig. 3-4 Mode conversion of TM_{01} mode microwaves at a bend ($r/D = 4$, $\alpha = 90^\circ$), (a) simulated fractional energy for $D = 12.7$, 39.0, and 74.0 mm, (b) comparison between the theoretical results and normalized simulation results.

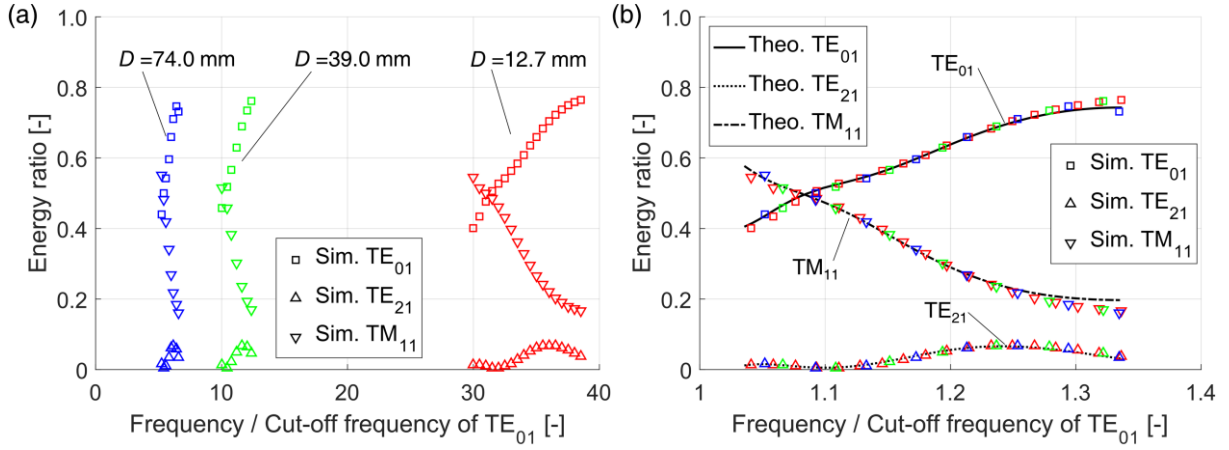


Fig. 3-5 Mode conversion of TE₀₁ mode microwaves at a bend ($r/D = 2$, $\alpha = 180^\circ$), (a) simulated fractional energy for $D = 12.7, 39.0,$ and 74.0 mm, (b) comparison between the theoretical results and normalized simulation results.

In the case of TE₁₁ mode exhibited in Figs. 3-6 and 3-7, we can also see that the energy ratio of each mode for different diameters tends to become consistent after normalization of the frequency. Note that the theoretical model for calculating mode conversion of TE₁₁ mode is only applicable to horizontal polarization, so only simulation results were presented in Fig. 3-7. Comparing the results in Figs. 3-6(b) and 3-7(b), it is also clear that the mode conversion of TE₁₁ mode under horizontal and vertical polarizations are also different from each other. Therefore, when calculating the mode conversion from a non-axisymmetric mode, the polarization should also be taken into consideration. Furthermore, the polarization of TE₁₁ mode is not influenced or twisted by the bend and maintains unchanged, as shown in Figs. 3-8(a) and (b). Although only four sets of data were exhibited in this section, similar results could also be acquired for other r/D & α combinations, which are supplemented in Section B of Appendix. Therefore, the conclusion of the theoretical analysis was also verified numerically.

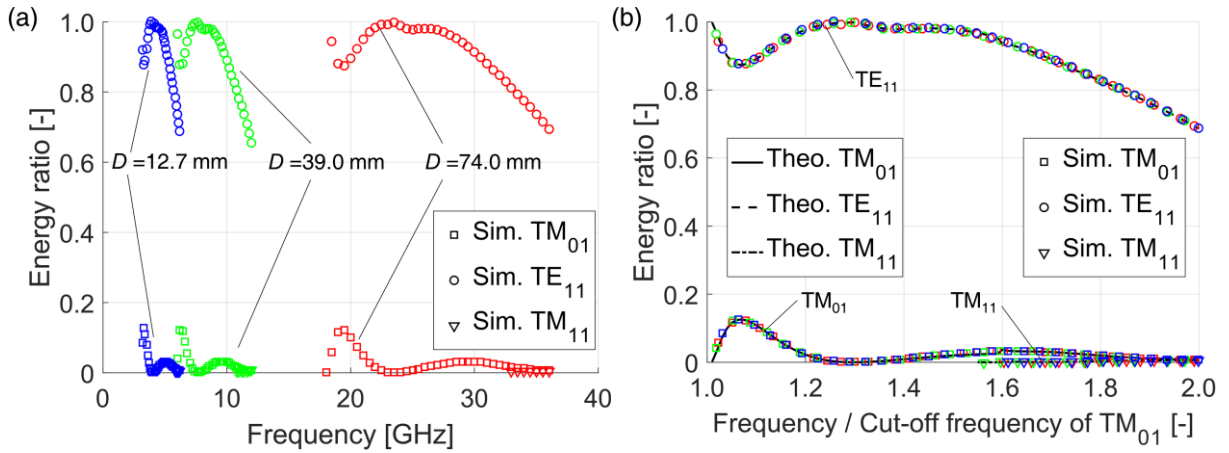


Fig. 3-6 Mode conversion of TE₁₁ mode microwaves under horizontal polarization at a bend ($r/D = 3$, $\alpha = 90^\circ$), (a) simulated fractional energy for $D = 12.7, 39.0,$ and 74.0 mm, (b) comparison between the theoretical results and normalized simulation results.

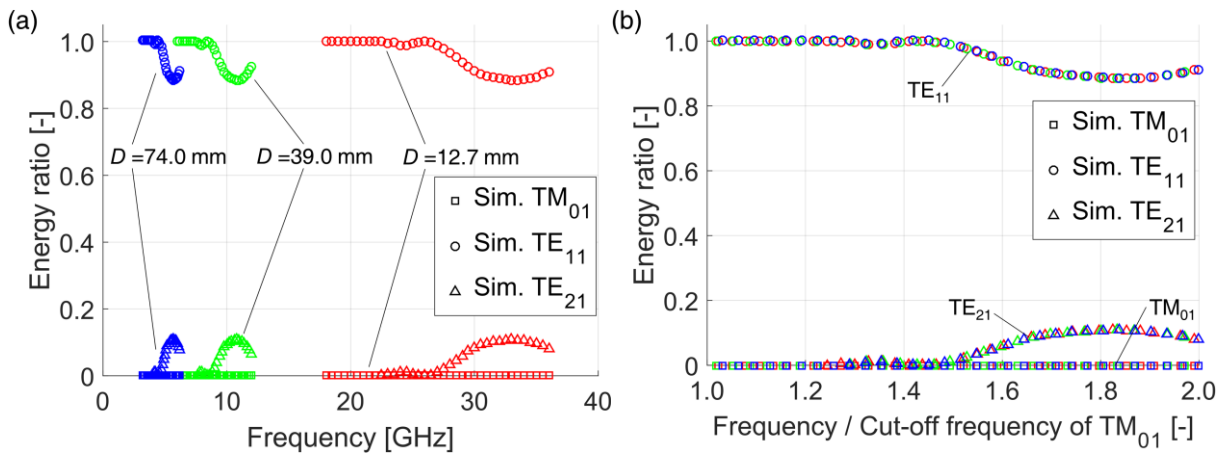
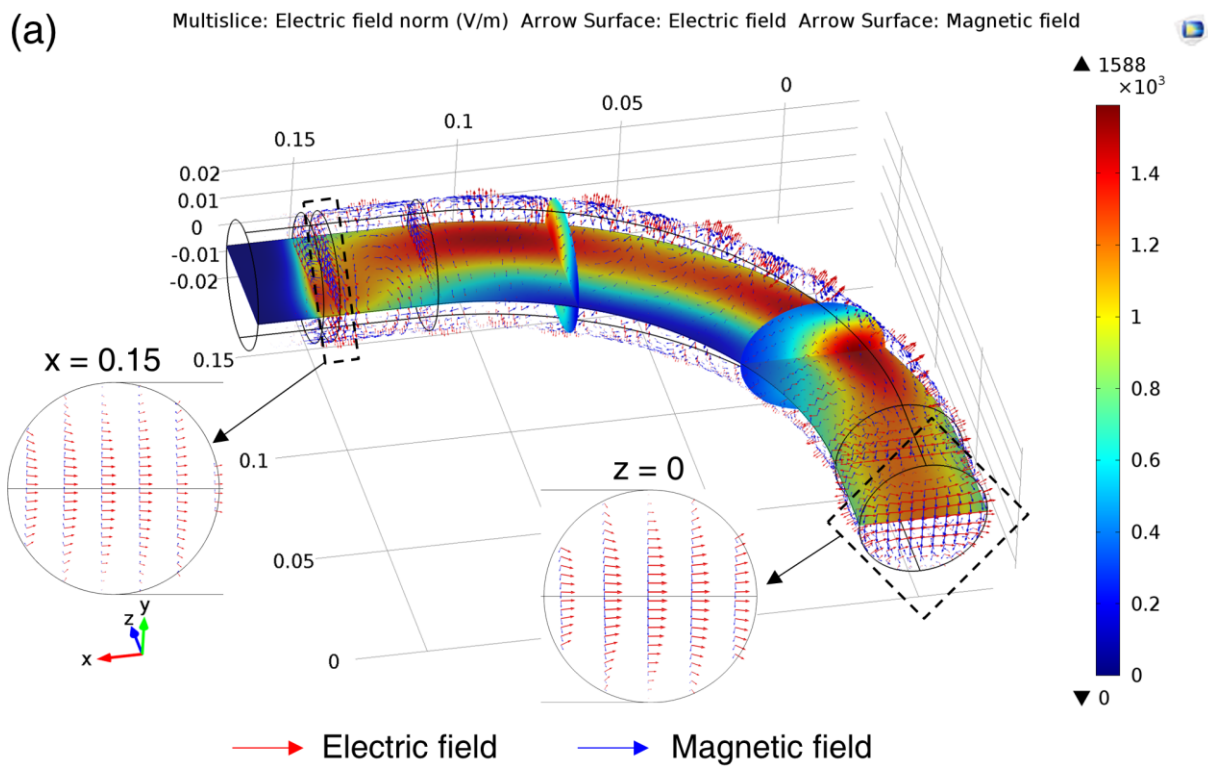


Fig. 3-7 Mode conversion of TE_{11} mode microwaves at a bend under vertical polarization ($r/D = 3$, $\alpha = 90^\circ$), (a) simulated fractional energy for $D = 12.7$, 39.0 , and 74.0 mm, (b) normalized simulation results.



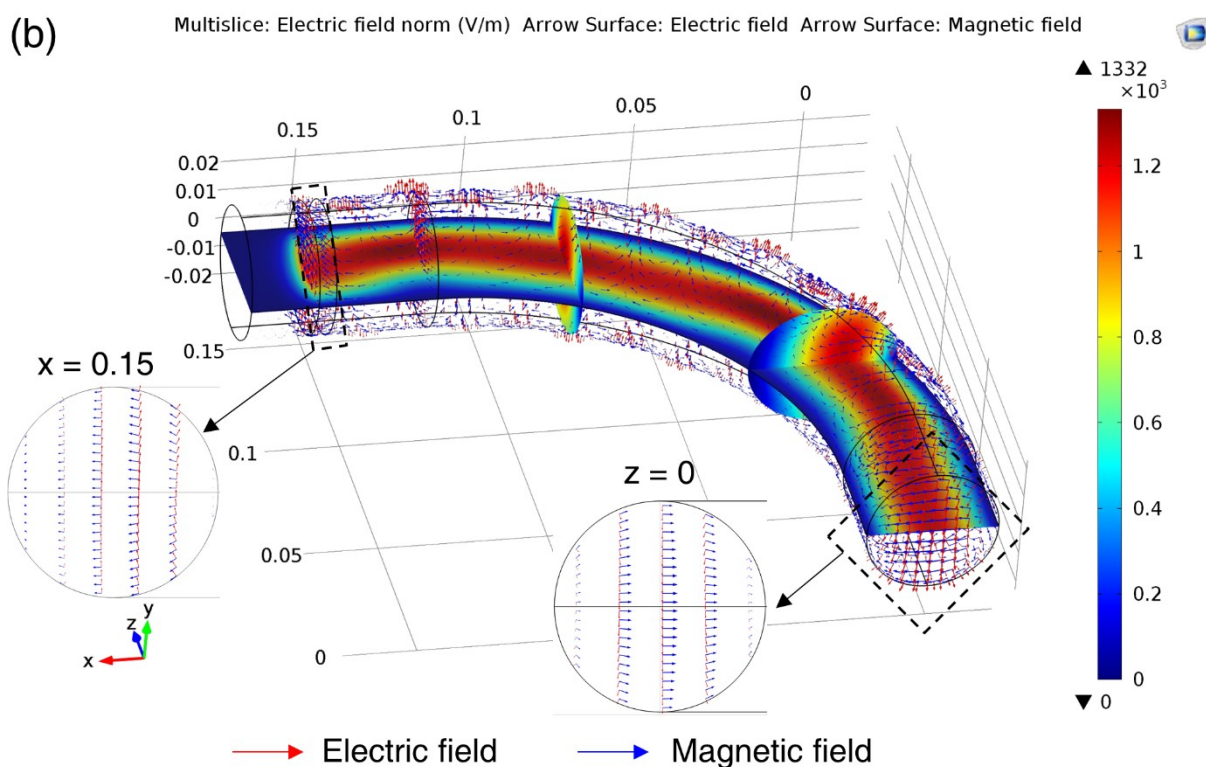


Fig. 3-8 Electric field distribution of linearly-polarized TE₁₁ mode microwaves in a bent pipe ($D = 39$ mm, $r/D = 3$, $\alpha = 90^\circ$, $f = 10$ GHz), under (a) horizontal polarization, (b) vertical polarization.

3.4 Experiment

In Sections 3.2 and 3.3, the effect of a bend on microwave transmission, i.e. mode conversion, has been investigated. In this section, how a bend influences the reflection signals will be studied and quantitatively assessed through experiment.

3.4.1 Experimental system

The effect of a bend on reflection was evaluated by comparing the reflections from pipe wall thinning flaws deployed in a straight pipe and a bent pipe. Figures 3-9 (a) and (b) show the straight pipe and bent pipe under test, respectively. A network analyzer generated TEM mode microwaves, which propagated through a flexible cable and reached the TEM-TM₀₁ mode converter. This mode converter corresponds to the TM₀₁ mode microwave probe in Section 3.1, and it converted the TEM mode microwaves into TM₀₁ mode and emitted it into the pipe. Either the straight or the bent pipe was composed of seven straight pipes, each of which was 1 m in length and made from stainless steel. Table 3-2 summarizes the specifications of the pipes and bends used in this study. Four groups of pipes with different inner diameters D were adopted for testing. One bend was prepared for pipe groups 1 to 3 each (bend 1, 2, 3), while two bends were prepared for pipe group 4 (bend 4A and bend 4B). The model numbers of the five bends and a photograph are presented in Table 3-3 and Fig. 3-10, respectively. All pipes and bends were connected by standard ferrule connections (ISO sanitary ferrule fitting, Osaka Sanitary Co., Ltd.), and a tailored O-ring was used at each connection to eliminate the gap and ensure the alignment of the connection. Figure 3-9 (c) illustrates another connection layout for the bent pipe, in which the bend was positioned at 3 m relative to the TEM-TM₀₁ mode converter, so as to evaluate the effect of a bend on the reflections ahead of it. Only pipe group 2 ($D = 17.5$ mm) was additionally connected in terms of the

layout shown in Fig. 3-9 (c), and the result of this scenario is independently presented in Section 3.4.2.4. The photograph of the experimental setup is shown in Fig. 3-11.

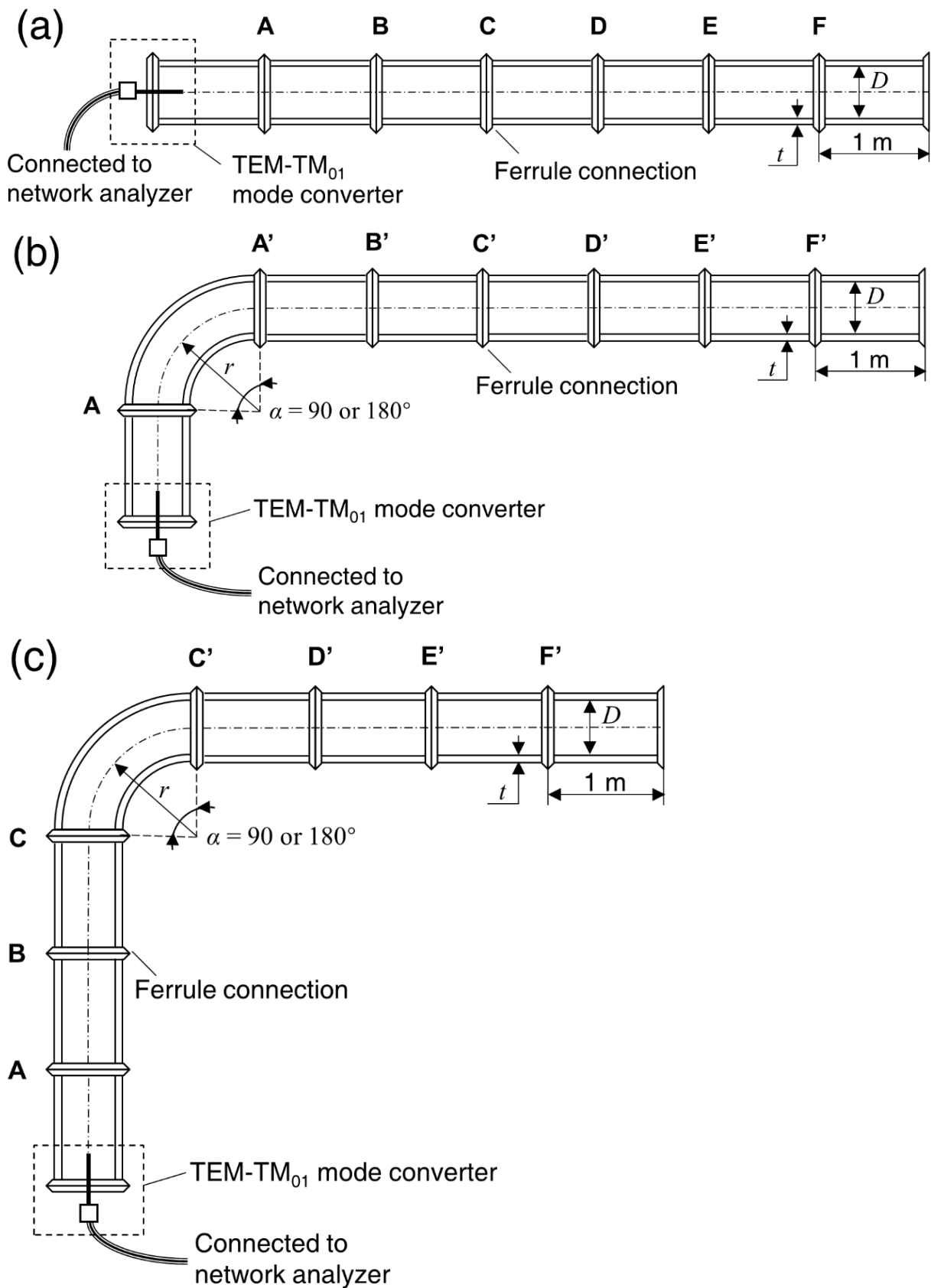
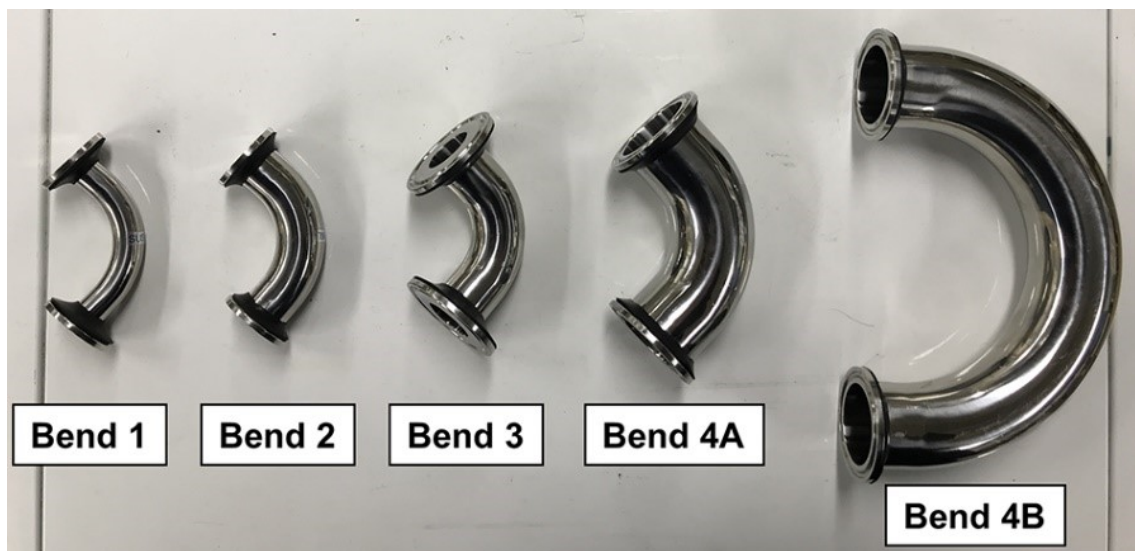


Fig. 3-9 Experimental system, (a) without bend, (b) with bend at 1 m, (c) with bend at 3 m (for pipe group 2).

Table 3-2 Experimental specifications of four pipe groups.

Pipe group	1	2	3	4
Inner pipe diameter, D (mm)	10.5	17.5	23.0	35.7
Normalized curvature radius, r/D (-)	3.62	2.17	1.48	1.37 (bend 4A) 2.13 (bend 4B)
Bend angle, α ($^{\circ}$)	90	90	90	90 (bend 4A) 180 (bend 4B)
Pipe wall thickness, t (mm)	1.65	1.65	1.2	1.2
Material of the pipe	316L SS	316L SS	304 SS	304 SS
Sweeping frequency span, f_{TM01} (GHz)	22.5 – 39.0	13.6 – 22.6	10.3 – 16.3	6.5 – 10.5
Cut-off frequency of TM_{01} mode, f_{cTM01} (GHz)	21.87	13.12	9.98	6.43
f_{TM01} / f_{cTM01} (-)	1.03 – 1.72	1.04 – 1.72	1.03 – 1.63	1.01 – 1.63

**Fig. 3-10** Photograph of the five bends used in the experiment.**Table 3-3** Model numbers of the five bends used in the experiment

Bend	Model number	Manufacturer
1	EL-2C-316L-8A	Osaka Sanitary Co., Ltd.
2	EL-2C-316L-15A	Osaka Sanitary Co., Ltd.
3	SNBE1S	Misumi Group Inc.
4A	SNBE1.5S	Misumi Group Inc.
4B	18BND-2C-304-1.5S	Osaka Sanitary Co., Ltd.

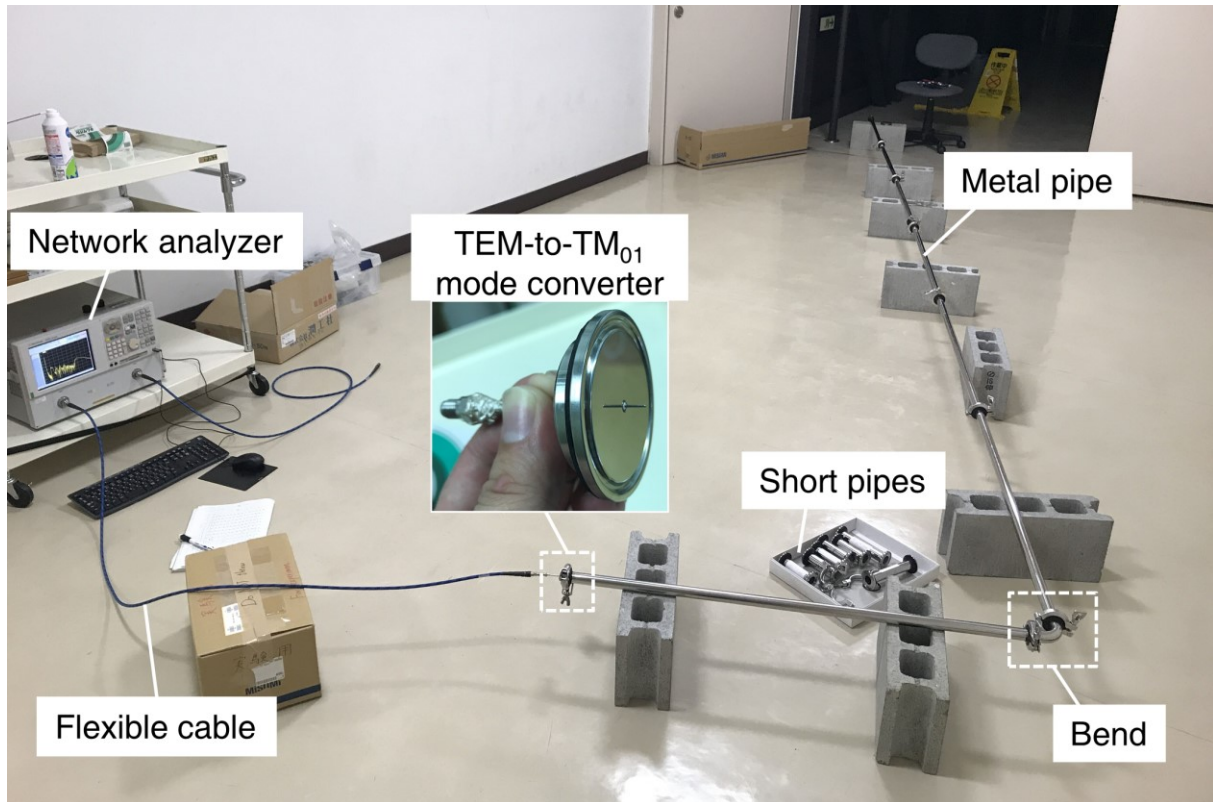


Fig. 3-11 Overview of the experimental setup (pipe group 3, bent pipe).

The structure of the TEM-TM₀₁ mode converter is portrayed in Fig. 3-12, and the mode converter for each pipe group was designed in accordance with the study [131] via numerical simulations. The plate-structure mode converter was chosen in this study. A semi-rigid cable was attached to the center of a metal cap with a standard ferrule connection (the full-circumferential groove in the figure). Two types of metal caps were used for pipe groups 1,2 ($D_1=34$ mm, $D_2=27.5$ mm, CLF-B-316L-15A, Osaka Sanitary Co., Ltd.) and pipe groups 3,4 ($D_1=50.5$ mm, $D_2=43.5$ mm, CLF-B-304-1.5S, Osaka Sanitary Co., Ltd.), respectively. A portion of core wire of the semi-rigid cable was exposed, while the exposed core wire lengths (l_E in Fig. 3-12) of the mode converters for pipe groups 1 to 4 were set to 2, 4, 6, and 9 mm, respectively, in order to maximize the conversion efficiency from TEM to TM₀₁ mode on the basis of the simulation results. The transmission and reflection characteristics of the four mode converters are displayed in Fig. 3-13. The sweeping frequency spans of the four pipe groups listed in Table 3-2 were determined by the energy ratio of the TM₀₁ mode with respect to the frequency. It should be noted that: even though the plate-structure TEM-TM₀₁ mode converter can generate not only TM₀₁ but also TM₀₂ or other higher-order modes [131], the upper limit of the sweeping frequency span of each pipe group was lower than the corresponding cut-off frequency of TM₀₂ mode. Therefore, in this section, we only take the mode conversion of TM₀₁ mode into account.

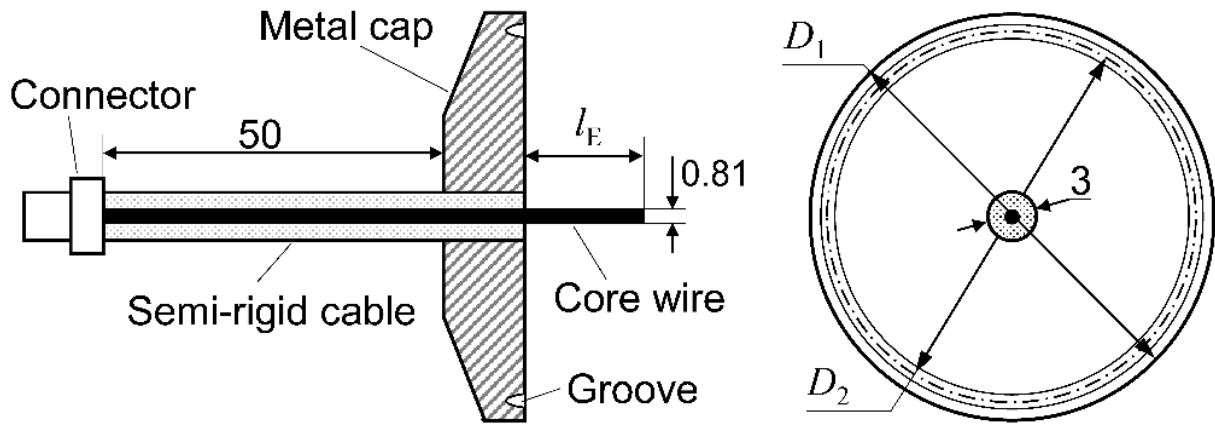


Fig. 3-12 Structure of the TEM-TM₀₁ mode converter (unit: mm, not to scale).

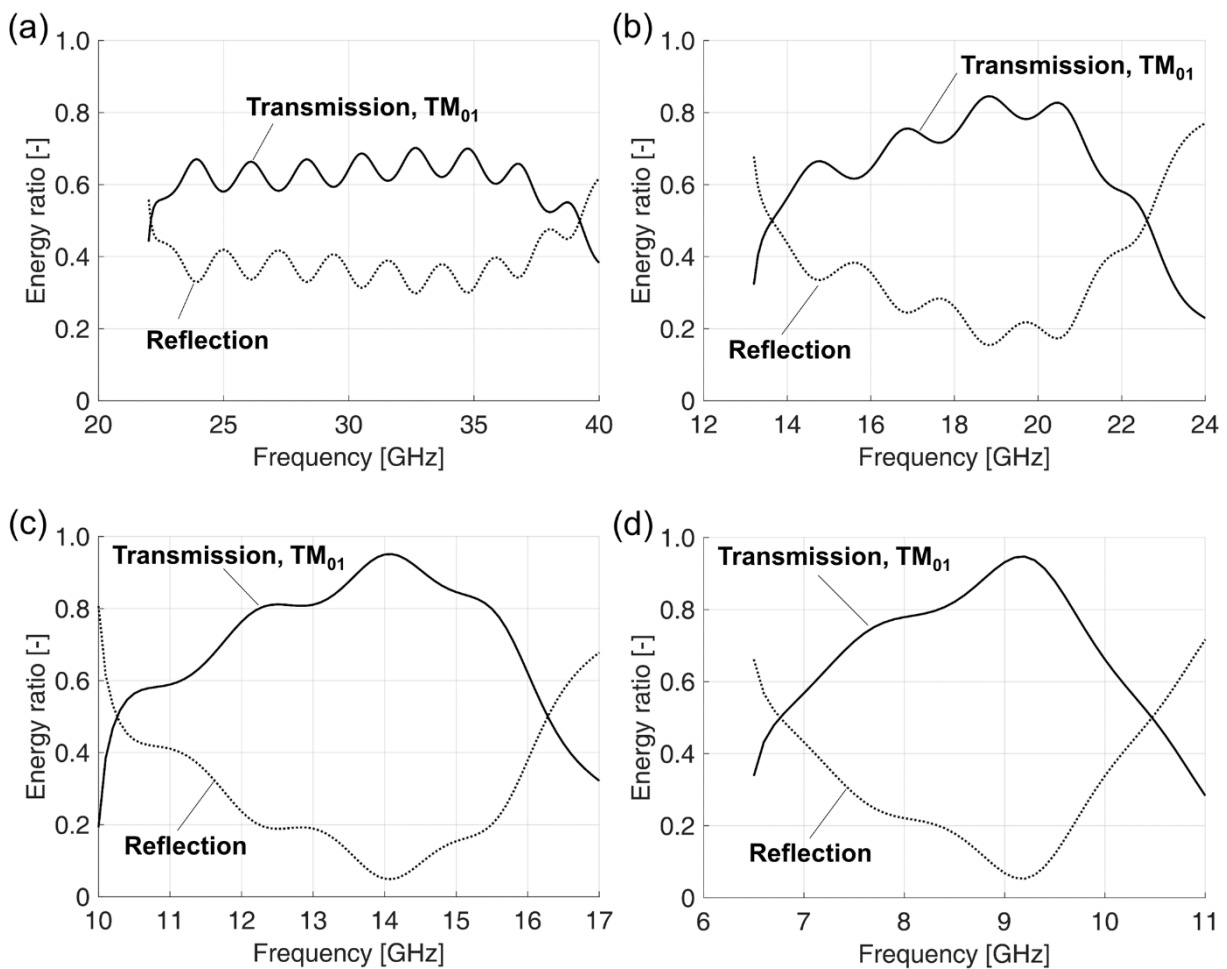


Fig. 3-13 Transmission and reflection characteristics of the TEM-TM₀₁ mode converters for four pipe groups, (a) pipe group 1 ($D=10.5$ mm, $l_E=2$ mm), (b) pipe group 2 ($D=17.5$ mm, $l_E=4$ mm), (c) pipe group 3 ($D=23.0$ mm, $l_E=6$ mm), (d) pipe group 4 ($D=35.7$ mm, $l_E=9$ mm).

To simulate the flaw of full-circumferential pipe wall thinning for each pipe group, a short pipe with a larger inner diameter was inserted at points A to F in Fig. 3-9(a), and points A to F' in Fig. 3-9(b) (or points A to F' in Fig. 3-9(c)). The effect of the bend was evaluated by measuring and comparing the reflection signals at the corresponding points (e.g., A and A'). Table 3-4 itemizes the dimensions of the short pipes, wherein L_F and D_F are the length and the inner diameter of the short pipe (except for short

pipe 3-2, see the explanation in Table 3-4), respectively. In total, eight short pipes simulating pipe wall thinning and five additional reference pipes (1-0, 2-0, 3-0a, 3-0b, and 4-0) were used in the experiments. Figure 3-14 displays the photograph of the short pipes.

Table 3-4 Dimensions of the short pipes used in the experiments.

Short pipe	Inner diameter of the short pipe, D_F (mm)	Length of the short pipe, L_F (mm)
1-0	10.5	100
1-1	11.5	100
2-0	17.5	100
2-1	18.5	100
3-0a	23.0	100
3-0b	23.0	150
3-1	23.5	100
3-2*	24.0	50
3-3	24.0	100
3-4	24.0	150
3-5	24.5	100
4-0	35.7	100
4-1	36.7	100

*: The length of the short pipe 3-2 is 100 mm, while only 50 mm long pipe wall thinning was machined in the middle with an inner diameter of 24 mm, the inner diameter of the rest portion remains to be 23 mm. Thus, L_F and D_F for short pipe 3-2 refer to the length and inner diameter of the portion with pipe wall thinning, respectively.

The reflections were measured in the frequency domain as S-parameters. In total, 3201 evenly-spaced points were sampled over the sweeping frequency span of each pipe group with an average of 30 measurements. Subsequently, the measured reflection signals were converted into a time domain by means of inverse fast Fourier transform and further processed using the signal-processing method introduced in Section 2.4.

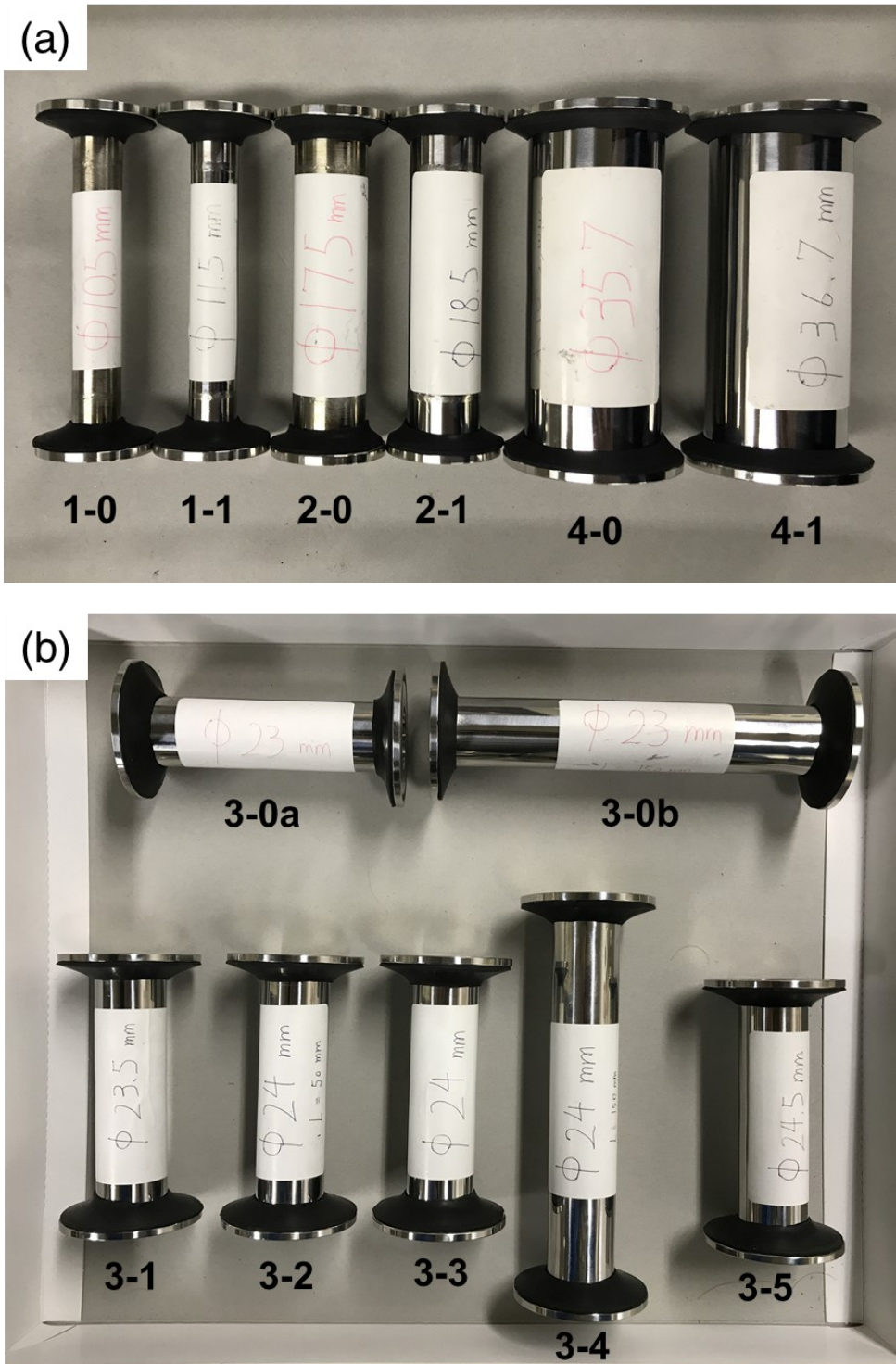


Fig. 3-14 Short pipes used in the experiment for (a) pipe groups 1, 2, and 4, (b) pipe group 3.

3.4.2 Experiment results

3.4.2.1 Analysis of the reflection signals and qualitative evaluation of the effect of a bend

Figure 3-15 exhibits the time domain reflection signals obtained using pipe group 3 ($D = 23.0$ mm) and short pipe 3-3 ($L_F = 100$, $D_F = 24.0$ mm), wherein (a) and (b) are the reflection signals without and with a bend, respectively. In both Figs. 3-15(a) and (b), the huge reflections appearing near 0 ns are due

to the TEM-to-TM₀₁ mode converter, while the reflections at around 70 ns correspond to the pipe end. Reflections caused by the pipe wall thinning situated at different points can be clearly observed from about 10 to 60 ns, while the amplitude of the reflection signal of one point (e.g., B') in the bent pipe is discernibly smaller than that of the corresponding point (e.g., B) in a straight pipe. This is probably because a portion of the TM₀₁ mode microwaves was converted into other modes, which could not be received by the TEM-TM₀₁ mode converter. The energy loss of TM₀₁ mode may have led to the decrease in amplitude of reflections. The reference reflections obtained using the reference short pipe 3-0 ($L_F=100$, $D_F=23.0$ mm) were omitted in the figure because the amplitudes of the reflection signals were negligibly small, compared with those obtained using short pipe 3-3 simulating pipe wall thinning.

The signals shown in Fig. 3-15 were re-processed using the method described in Section 2.4 and presented in Fig. 3-16. The explicit reflection peaks in both Figs. 3-16(a) and (b) indicate that the short pipe with pipe wall thinning was detected and located at each point. Similarly, the amplitudes of reflection signals in the bent pipe were also smaller than those of corresponding points in the straight pipe. Moreover, in Fig.3-16 (b), there are some small and dispersive reflection peaks appearing ahead of the main reflection peaks, and they are highlighted with black down-arrows. According to the analysis in Section 3.1, these reflections may have resulted from the portion of TM₀₁ mode microwaves converted from the TE₁₁ mode in the second mode conversion at the bend. Because the TE₁₁ mode has a higher group velocity and propagates faster than the TM₀₁ mode, these reflections appear prior to those of the 'unconverted' TM₀₁ mode. In addition, since the signal-processing only compensated for the dispersion of the 'unconverted' TM₀₁ mode correctly, the reflections of the TM₀₁ mode converted from the TE₁₁ mode are smaller and dispersed. Based on the above discussion, it is clear that the main effect of a bend is the decrease in amplitude of the reflection signals due to the energy loss of TM₀₁ mode caused by the mode conversion at the bend. The processed reflection signals for pipe groups 1, 2, and 4 are additionally shown in Figs. 3-17 to 3-19.

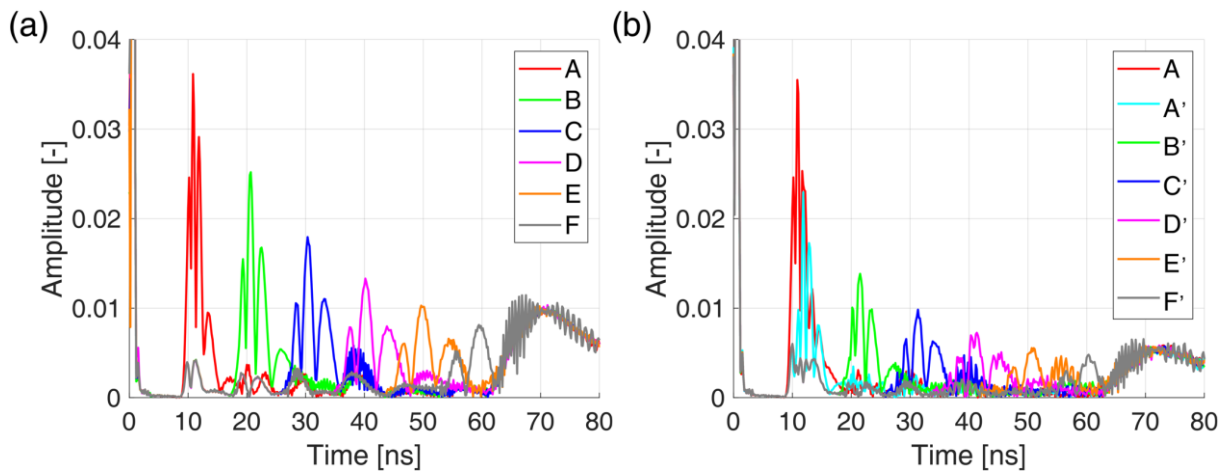


Fig. 3-15 Time domain reflection signals from short pipe 3-3 deployed at multiple positions in pipe group 3, (a) without bend (straight pipe), (b) with bend 3 (bent pipe).

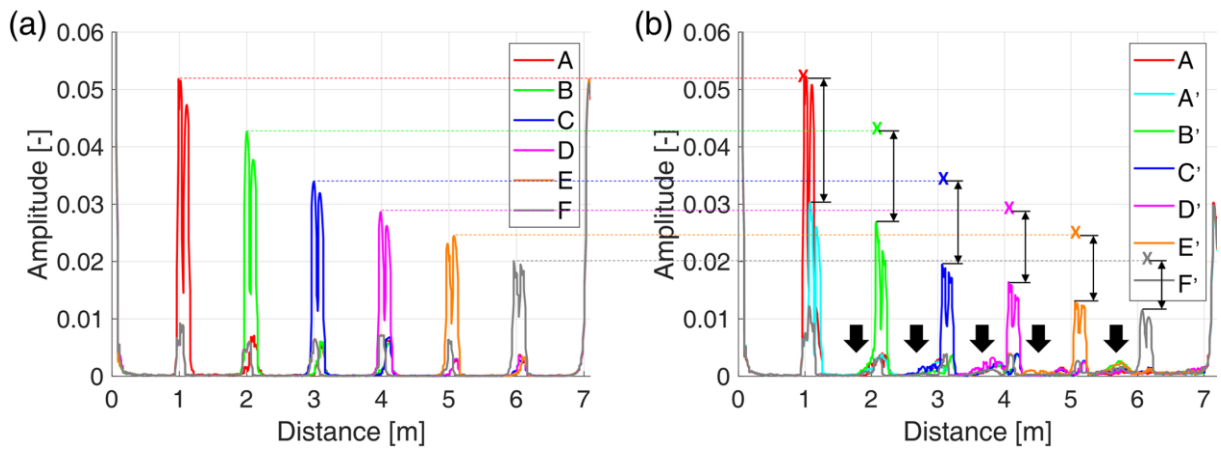


Fig. 3-16 Processed reflection signals from short pipe 3-3 deployed at multiple positions in pipe group 3, (a) without bend (straight pipe), (b) with bend 3 (bent pipe).

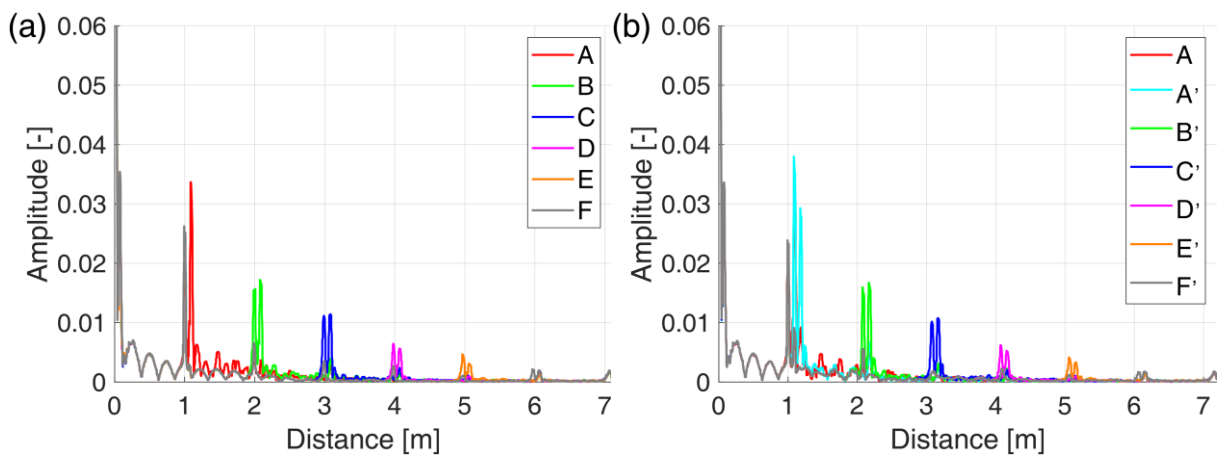


Fig. 3-17 Processed reflection signals from short pipe 1-1 deployed at multiple positions in pipe group 1, (a) without bend (straight pipe), (b) with bend 1 (bent pipe).

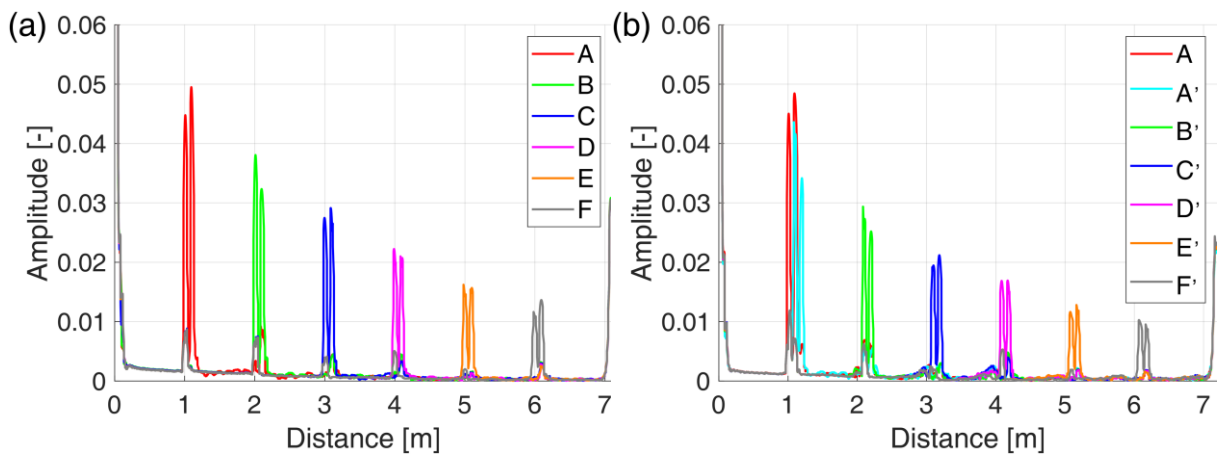


Fig. 3-18 Processed reflection signals from short pipe 2-1 deployed at multiple positions in pipe group 2, (a) without bend (straight pipe), (b) with bend 2 (bent pipe).

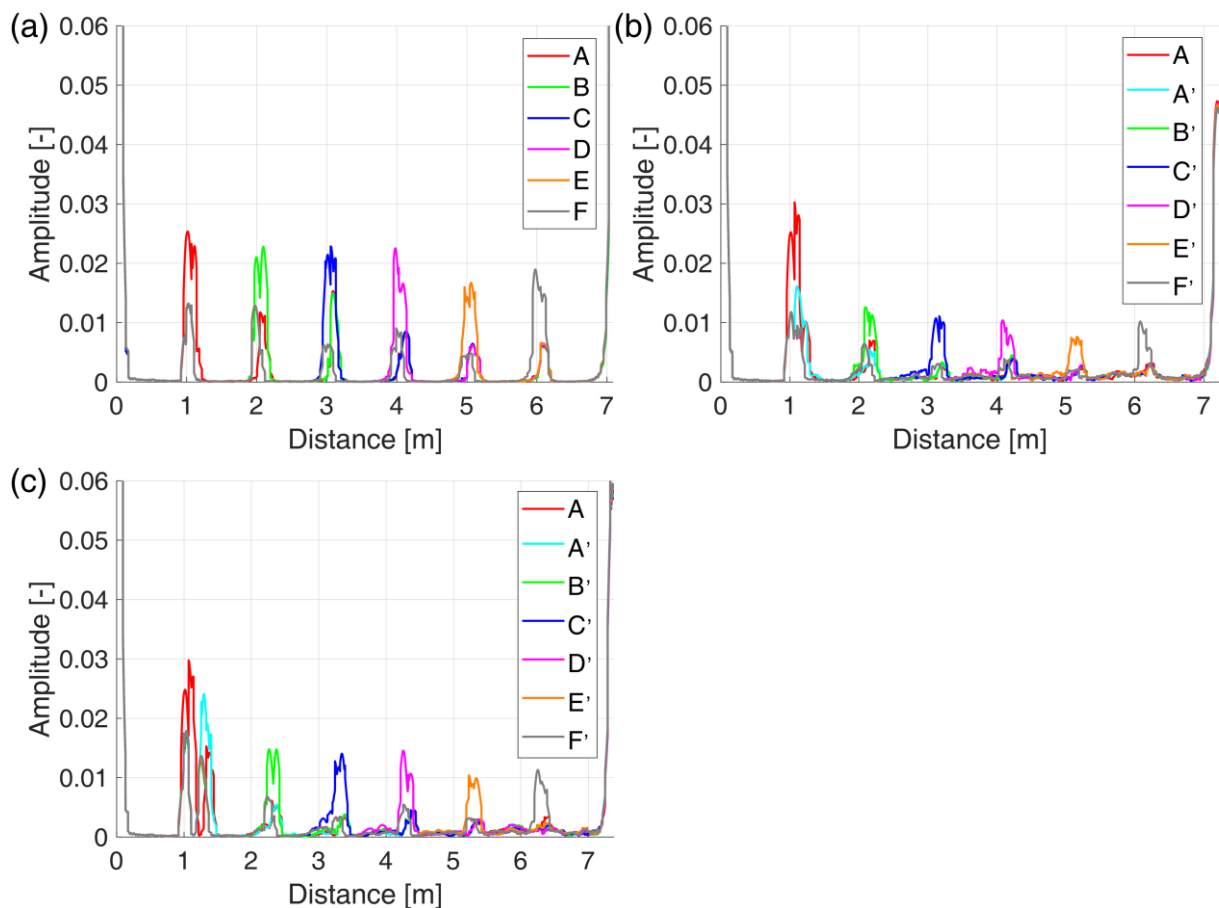


Fig. 3-19 Processed reflection signals from short pipe 4-1 deployed at multiple positions in pipe group 1, (a) without bend (straight pipe), (b) with bend 4A (bent pipe), (c) with bend 4B (bent pipe).

3.4.2.2 Quantitative evaluation of the effect of the bend

In Section 3.4.2.1, the effect of a bend was discussed and evaluated qualitatively, i.e., the decrease in amplitude of the reflection signals. In this section, quantitative evaluations for all four pipe groups are conducted to clarify the practical effect of a bend.

In an earlier study [110], the attenuation of microwave signals with respect to the propagation distance was studied theoretically and experimentally. The results showed that the amplitude of microwave signal attenuates exponentially as the propagation distance increases. Referring to the approach utilized in that study and taking the results in Fig.3-16 as an example, the reflection signals were further processed in terms of the following steps: (1) the peak value of the reflection at each point was normalized with the peak value at point A in either the ‘without bend’ or ‘with bend’ scenario; (2) the regression lines for both scenarios were calculated with the normalized peak values (A to F for without bend, and A’ to F’ for with bend) using the least square method (LSM) from 1 m to 7 m. It should be noted that normalized peak value at point A’ was excluded when calculating the LSM fitting, because the reflection at this point could be easily influenced by the pipe fitting connection and seriously deviated from the main trend.

Using the method narrated in the preceding paragraph, the regression lines for the four pipe groups were calculated and are displayed in Fig. 3-20, in which the short pipes 1-1, 2-1, 3-3 and 4-1 were used to simulate the pipe wall thinning for pipe groups 1 to 4, respectively. As shown in every sub-figure, the regression lines without and with bend are basically parallel to each other, which reveals that the effect of a bend is a consecutive and basically constant decrease in amplitude of reflection signal. Since the vertical axes are in log scale, the expression ‘amplitude-decrease coefficient’ is more appropriate for

describing the effect of a bend.

To discuss the effect of a bend quantitatively, this study assumes that the relationship between the amplitude of reflection signal without bend X and that with bend X' is described as

$$X' = X \cdot 10^{-\Delta}, \quad (3.15)$$

where Δ denotes the amplitude-decrease coefficient. Suppose that the regression lines of the straight pipe and bent pipe are formulated as below:

$$\begin{cases} y^S = k^S x + b^S \\ y^B = k^B x + b^B \end{cases}, \quad (3.16)$$

in which k^S , k^B , b^S , and b^B are the slopes and intercepts evaluated from the LSM fitting, while y^S and y^B are the normalized amplitudes of reflection signals (in log scale). 'S' and 'B' at the superscripts stand for 'straight pipe' and 'bent pipe', respectively. Variable x is the distance, ranging from 1 to 7 m. Since there is a discrepancy between the k^S and k^B , Δ is evaluated as the average 'distance' between the two regression lines from 1 to 7 m:

$$\Delta = \frac{\int_1^7 (y^S - y^B) dx}{7-1} = (y^S - y^B)|_{x=4}. \quad (3.17)$$

Table 3-5 summarizes the evaluated k_i^S , k_i^B and Δ_i for each pipe group, where the subscript i (=1,2,3,4A and 4B) corresponds to the five bends in the four pipe groups. It can be seen that the values of Δ_i vary from pipe group to pipe group, which indicates that bends of different r/D or α exert distinct effects: as the range of f_{TM01}/f_{cTM01} for the four pipe groups are nearly consistent, to 90° bends 1, 2, 3 and 4A, r/D is a critical factor which significantly influences Δ_i ; while to bend 2 and bend 4B whose α are 90° and 180°, respectively, Δ_2 and Δ_4 are also quite contrasting even though their r/D values are very close. Moreover, when the extent of mode conversion at the bend is drastic, namely the energy loss of TM_{01} mode is relatively large, the value of Δ_i tends to become large, and the decrease in reflection signal is also large. If the mode conversion is not drastic, then Δ_i will remain small accordingly, while the decrease in signal is small as well. The theoretical and simulation results of the mode conversions at the five bends are presented in Fig. 3-21. We can also infer the extent of the mode conversion at a bend from the energy ratio of each mode. For instance, the mode conversions at bends 1 and 2 are not very drastic, because the energy ratio of the TM_{01} mode is still dominant among all coupled modes. On the other hand, the mode conversions at bends 3, 4A, and 4B are relatively drastic because the energy ratios of the converted TE_{11} and TE_{21} mode are quite large and cannot be ignored. On the other hand, the values of k_i^S and k_i^B are similar within one pipe group (like bend 4A and 4B in pipe group 4), but vary among different pipe groups. This is because the attenuation of reflection signal versus distance is largely influenced by the frequency f , whose range also varies among pipe groups.

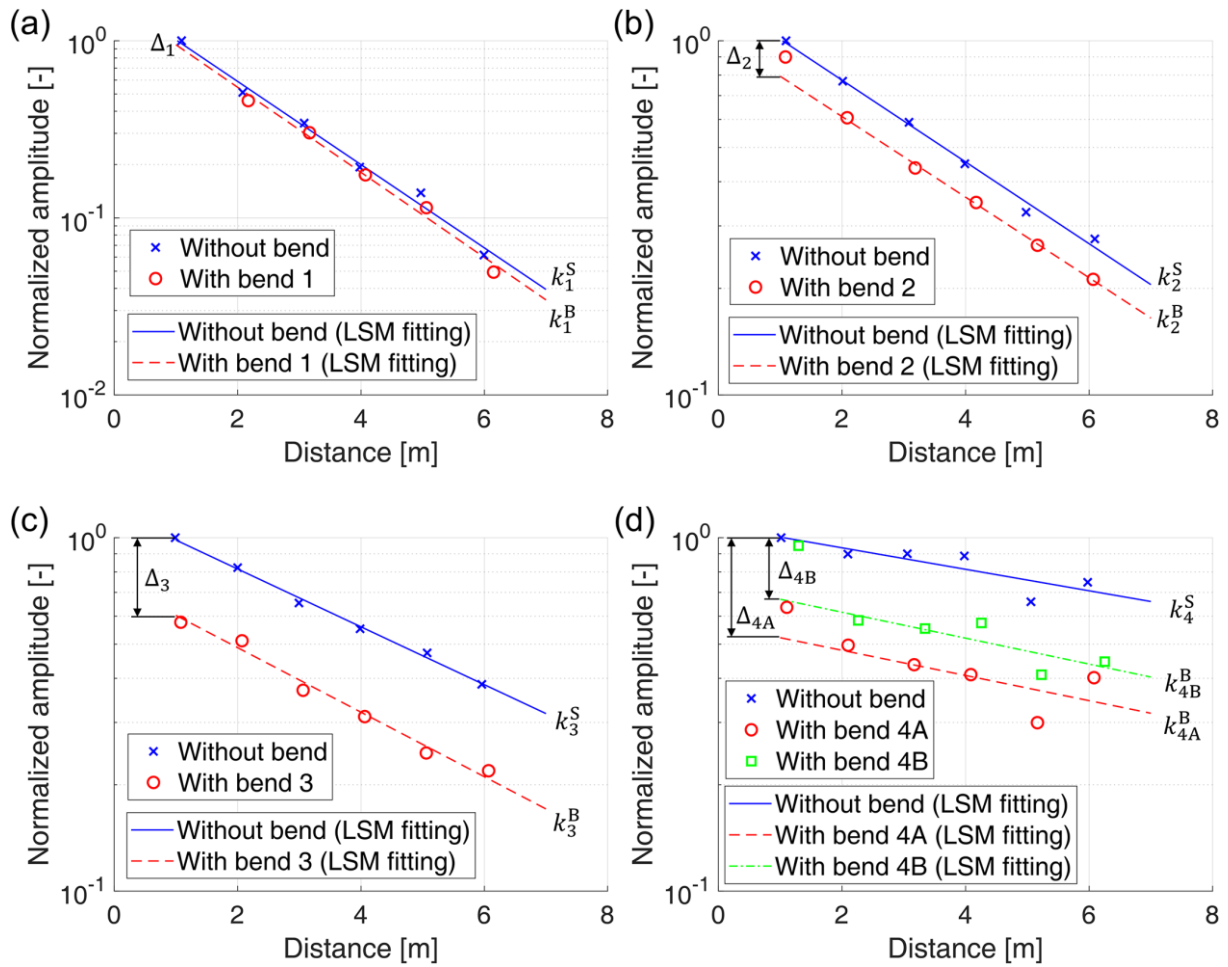


Fig. 3-20 Calculated regression lines of four pipe groups, (a) pipe group 1 with short pipe 1-1, (b) pipe group 2 with short pipe 2-1, (c) pipe group 3 with short pipe 3-3, (d) pipe group 4 with short pipe 4-1.

Table 3-5 Evaluations of k_i^S , k_i^B and Δ_i for four pipe groups.

Pipe group	1	2	3	4	
				4A	4B
D (mm)	10.5	17.5	23.0	35.7	
r/D (-)	3.62	2.17	1.48	1.37	2.13
α (deg.)	90	90	90	90	180
Δ_i (-)	0.0436	0.0995	0.2415	0.3005	0.1949
$10^{-\Delta_i}$ (-)	0.9045	0.7952	0.5735	0.5006	0.6384
k_i^S (-)	-0.2349	-0.1155	-0.0818	-0.0304	
k_i^B (-)	-0.2401	-0.1138	-0.0913	-0.0356	-0.0367

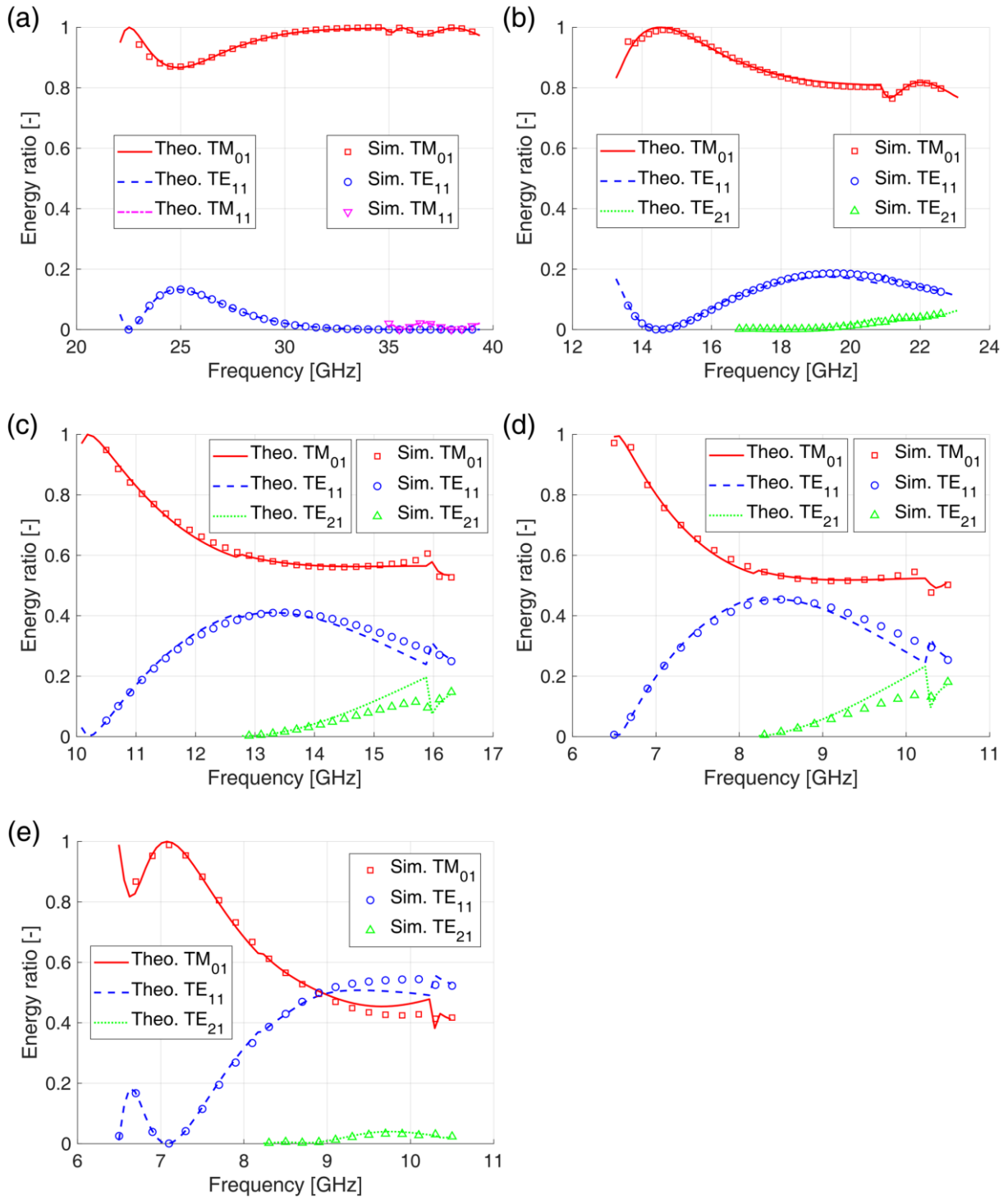


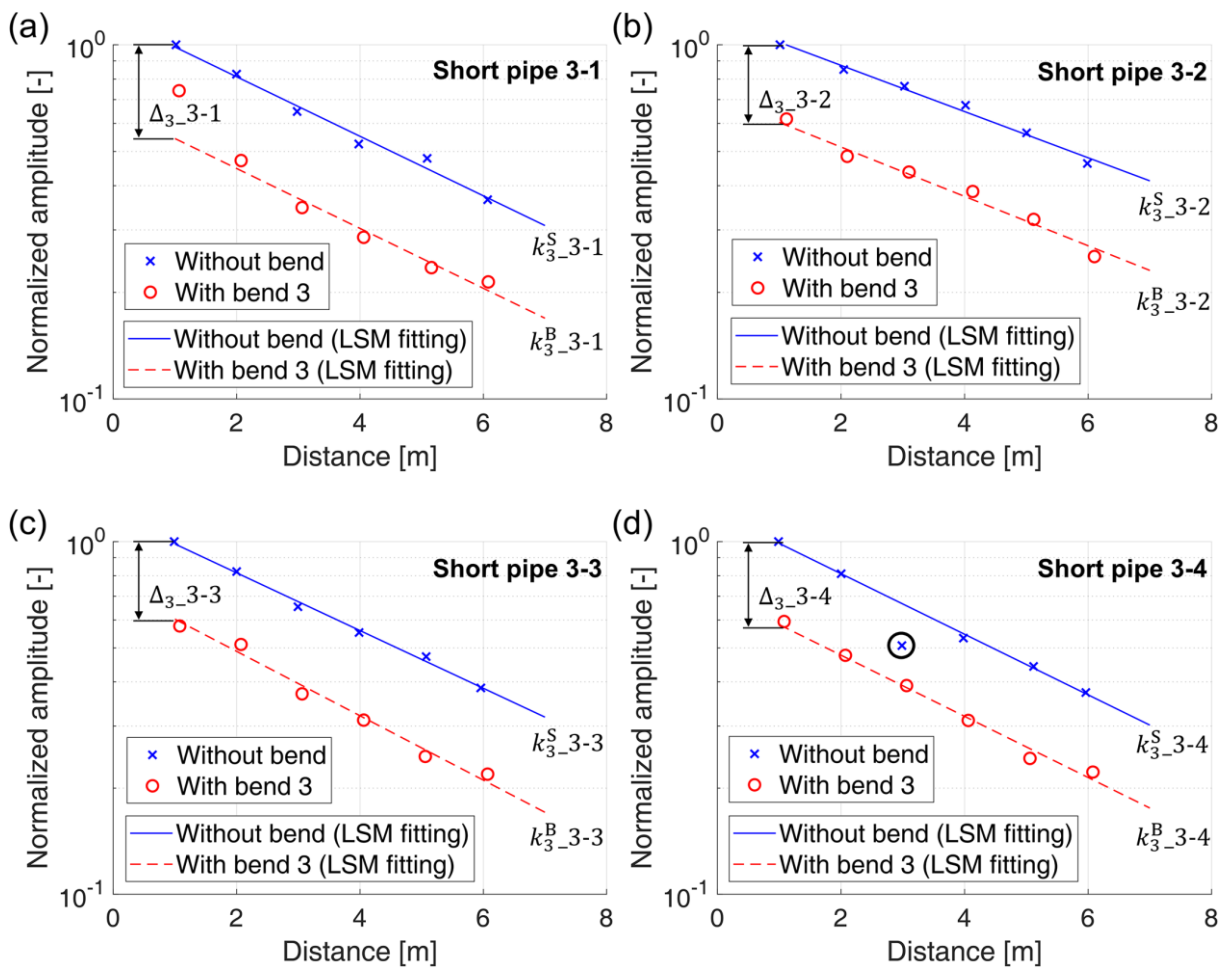
Fig. 3-21 Theoretical and simulated results of the mode conversions at the five bends applied in the experiments, (a) bend 1 ($D = 10.5$ mm, $r/D = 3.62$, $\alpha = 90^\circ$), (b) bend 2 ($D = 17.5$ mm, $r/D = 2.17$, $\alpha = 90^\circ$), (c) bend 3 ($D = 23.0$ mm, $r/D = 1.48$, $\alpha = 90^\circ$), (d) bend 4A ($D = 35.7$ mm, $r/D = 1.37$, $\alpha = 90^\circ$), (e) bend 4B ($D = 35.7$ mm, $r/D = 2.13$, $\alpha = 180^\circ$).

3.4.2.3 Dependence of a bend's effect on the flaw size

In this section, the dependence/independence of Δ on the flaw size is studied and evaluated. Pipe group 3 ($D = 23.0$ mm) was chosen, hence the bend's dimension was fixed. The layout of the pipes as well as the deployment of the short pipes was the same as in Fig. 3-9 (a) and (b). In total, six short pipes

(3-1, 3-2, 3-3, 3-4, 3-5, and 4-0) with different D_F or L_F values were tested in the experiment. Note that adopting the short pipe 4-0 here is meant for introducing an extreme case of pipe wall thinning to study the impact of the flaw's size. The measured reflection signals were also processed in terms of the method described in Section 3.4.2.2 and then presented in Fig. 3-22. Furthermore, k_3^S , k_3^B and Δ_3 of each short pipe were evaluated and are listed in Table 3-6 for comparison. Be aware that in Fig. 3-22(d), one data point (pipe wall thinning at point C in the straight pipe, 3 m, circled with a black circle) was excluded when calculating the LSM fitting and regression lines, because it seriously deviated from the trend and can be deemed as a gross error.

From figure 3-22 and table 3-6, it is easy to see that the two regression lines in every sub-figure are almost parallel to each other, while the evaluated Δ_3 are nearly consistent for each short pipe, suggesting that the effect of a bend is consistent despite the flaw size D_F and L_F . In contrast, the values of k_3^S and k_3^B of the short pipe 3-2 are distinguished from those of the other short pipes, showing that the attenuation rate of the reflection signals can be influenced by the extent of pipe wall thinning.



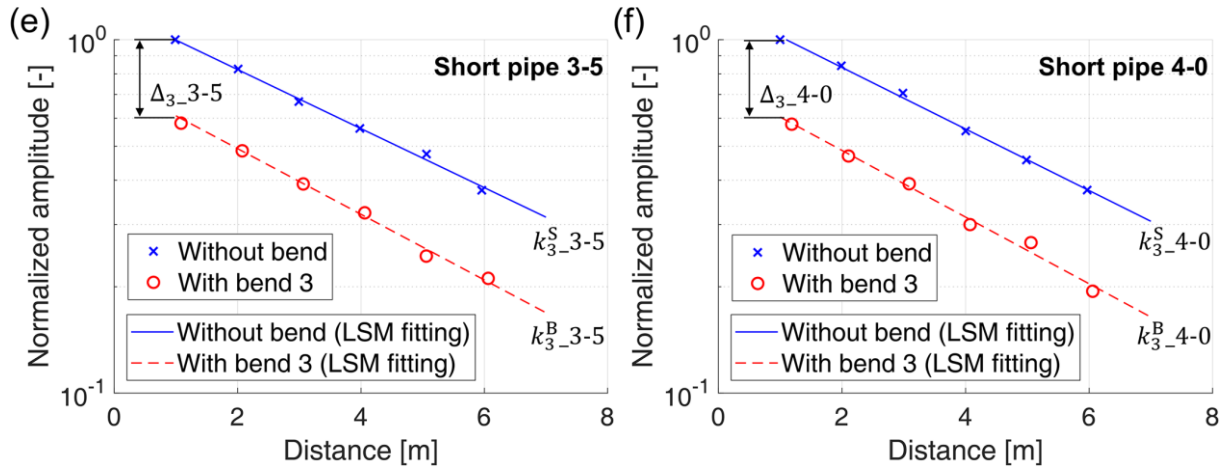


Fig. 3-22 Regression lines of pipe group 3 obtained using six short pipes, (a) short pipe 3-1, (b) short pipe 3-2, (c) short pipe 3-3, (d) short pipe 3-4, (e) short pipe 3-5, (f) short pipe 4-0.

Table 3-6 Evaluations of Δ_3 , k_3^S and k_3^B for six different short pipes

Short pipe	3-1	3-2	3-3	3-4	3-5	4-0
D_F (mm)	23.5	24.0	24.0	24.0	24.5	35.7
L_F (mm)	100	50	100	150	100	100
$\Delta_{3_S.P.}$ (-)	0.2601	0.2395	0.2415	0.2328	0.2424	0.2492
$10^{-\Delta_{3_S.P.}}$ (-)	0.5494	0.5761	0.5735	0.5851	0.5723	0.5634
$k_{3_S.P.}^S$ (-)	-0.0845	-0.0652	-0.0818	-0.0859	-0.0835	-0.0870
$k_{3_S.P.}^B$ (-)	-0.0840	-0.0697	-0.0912	-0.0867	-0.0929	-0.0943

3.2.2.4 Influence of a bend on the reflections ahead of it

Figure 3-23 shows the experimental results when the bend 2 was positioned at 3 m relative to the TEM-TM₀₁ mode converter, as previously illustrated in Fig. 3-9(c). The processed reflection signal of the short pipe 2-1 is shown in Fig. 3-23(a), while the normalized peak values of reflection signals at points A to F' (bend at 3 m) and the results in Fig. 3-20(b) (bend at 1 m) are plotted together in Fig. 3-23(b). Both Figs. 3-23(a) and (b) reveal that the bend started to 'take effect' on the reflection signals from point C', while the reflections at points A, B, and C, located ahead of the bend, were not noticeably influenced. Therefore, it can be concluded that a bend imposes its effect mainly on the reflections behind it, while those ahead of it are not affected significantly. Besides, its effect does not change along with the position where the bend is situated.

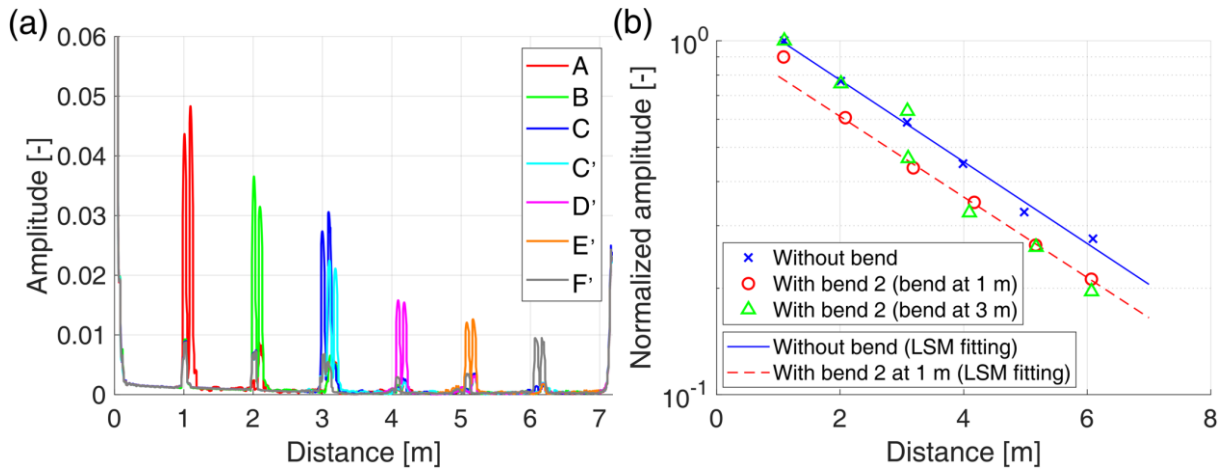


Fig. 3-23 Bend 2 deployed at 3 m relative to the TEM-TM₀₁ mode converter and its effect, (a) processed reflection signals, (b) comparison between the normalized peak values (bend at 3 m) and results of Fig. 3-20(b) (bend at 1 m).

3.4.2.5 Effect of bends with the same or close r/D and α

In Section 3.4.2.2, we confirmed that bends with r/D or α possessed different Δ , namely the effect of a bend on reflection. However, if there are two bends with the same or similar r/D and α but different inner diameter D , will they lead to an identical or akin Δ , when the range of f/f_c is also set to be consistent? To clarify the point, an additional bend 4C (not listed in Table 3-2) was fabricated by cutting the bend 4B from the middle. The photo as well as the dimensions of the bend 4C is given in Fig. 3-24. The r/D and α for bend 4C are 2.13 and 90°, respectively, which are very close to those of the bend 2 ($D = 17.5$ mm, $r/D = 2.17$, and $\alpha = 90^\circ$). The experiment for bend 4C was conducted in terms of Section 3.4.1 and the measured signals were processed according to the method in 3.2.4.2. Moreover, the experimental data for the two bends were also trimmed to have the same range of f/f_c (1.04 – 1.63). Figure 3-25 exhibits the regression lines of bend 2 and bend 4C after data trimming. As we see, the evaluated Δ of them are also close even though they have different D . The small discrepancy of evaluated Δ can be possibly attributed to the difference in the characteristics of microwave probes or mode converters (Fig. 3-13), data length, etc. From the above results, we can infer that there should be some consistency in Δ between two bends with different D but close r/D and α , if the range of f/f_c is also accordant.



Fig. 3-24 Bend 4C and its dimensional parameters.

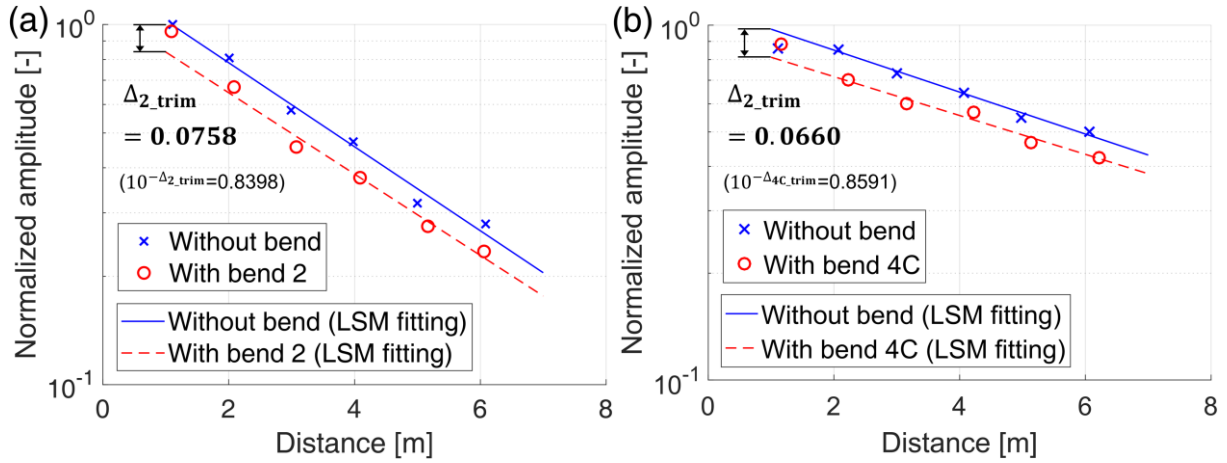


Fig. 3-25 Comparison between the effects of (a) bend 2 and (b) bend 4C, after trimming to data to the same range of f/f_c (1.04 – 1.63). (**Note:** for straight pipe, the data point at 1 m was excluded when calculating LSM regression because of its too large deviation)

3.5 Summary

In this section, we investigated the effect of a bend on microwave transmission and reflection. The factors affecting the mode conversion of microwaves due to a bend were studied theoretically and via numerical simulation, while the effect of a bend on reflection was studied and quantitatively evaluated through experiments. Both theoretical and simulation results indicate that the mode conversion at a bend is dependent on three factors: the curvature radius normalized by the inner pipe diameter r/D , the frequency normalized by cut-off frequency f/f_c , and the bend angle α . Besides, to non-axisymmetric modes like TE_{11} , its polarization also influences the mode conversion and should be taken into account. However, the polarization itself is not affected by mode conversion at a bend and maintained unchanged. The experimental results show that the existence of a bend reduces the amplitudes of reflection signals, and its practical effect on reflection is actually an amplitude-decrease coefficient (Δ), describing the quantitative relationship between the amplitudes of reflection signals in a straight pipe and in a bent pipe. Meanwhile, a bend does not influence the attenuation rate of reflection signal with respect to the distance. Furthermore, the effect of a bend is not significantly influenced by the size of pipe wall thinning, and a bend mainly influences the reflections behind it but has little impact on the reflections ahead of it. Finally, we confirmed that bends with different D but close r/D and α possess similar evaluated Δ , namely the similar effect on reflection, if the ranges of f/f_c is consistent. These conclusions enable us to quantitatively analyze the behavior of microwaves inside a bent pipe, and estimate how a bend influences the signal amplitude or detection range.

Chapter 4 Crack detection in open-ended bent pipes using a TE₁₁ mode microwave probe

In this chapter, a crack-detection method using a TE₁₁ mode microwave probe is proposed for the inspection of bent pipes with open-end. Moreover, the applicability of this approach to multiple diameters, long-range detection, and bent pipe (including bend-region) is also investigated.

4.1 Theoretical basis of using TE₁₁ mode for crack detection

When microwaves propagate inside a metal waveguide or pipe, the surface current is induced on the inner surface of the pipe, and the surface current density J_s is calculated as:

$$J_s = n \times H, \tag{4.1}$$

where n denotes the outward normal to the inner surface of the pipe, while H is the magnetic field intensity.

Sasaki [115] discussed the relationship between J_s and the detection sensitivity towards crack: if the orientation of the crack is parallel to J_s , little reflection arises and the crack is undetectable; if the crack perturbs J_s (e.g., perpendicular to J_s), large reflection is generated and the crack is detectable. For instance, to TM₀₁ and TE₀₁ modes, their electromagnetic field and surface current density distributions are displayed in Figs. 4-1 and 4-2, respectively. As shown in Fig. 4-1(b), the surface current density of TM₀₁ is axial, thus TM₀₁ mode is sensitive to circumferential cracks [107] but insensitive to axial cracks; by contrast, the TE₀₁ mode's surface current density is circumferential as displayed in Fig. 4-2(b), so it is susceptible to axial cracks [108] but insusceptible to circumferential cracks.

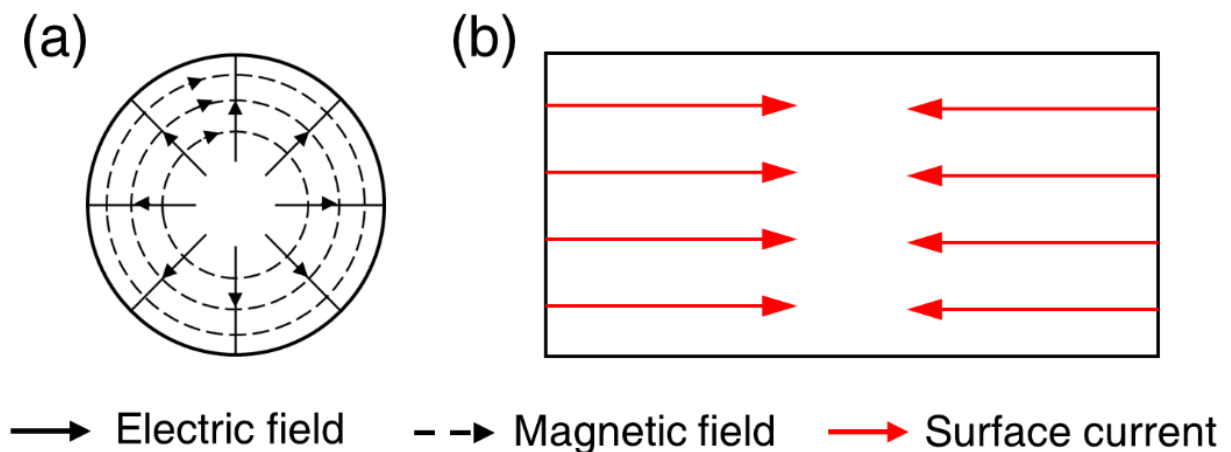


Fig. 4.1 Circular TM₀₁ mode, (a) electromagnetic field distribution at cross-section, (b) side view of surface current distribution.

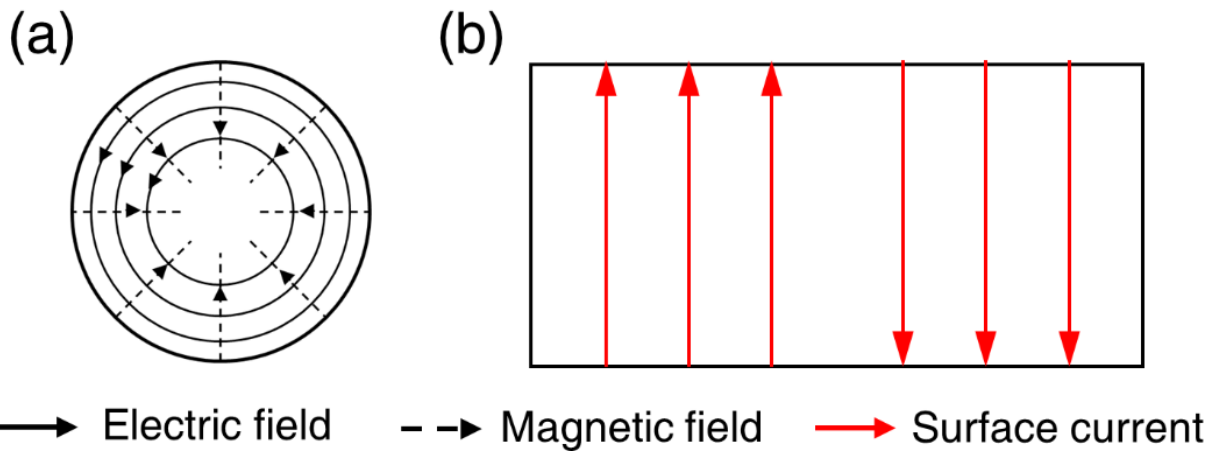


Fig. 4.2 Circular TE_{01} mode, (a) electromagnetic field distribution at cross-section, (b) side view of surface current distribution.

In the case of the linearly-polarized TE_{11} mode, its electromagnetic field distribution is not asymmetric like TM_{01} or TE_{01} , and its surface current also contains both axial and circumferential components, as shown in Fig. 4-3. By contention, the ‘polarization’ of electromagnetic waves refers to the direction of the electric field, so the polarization in Fig. 4-3(b) is defined as horizontal polarization. Therefore, when the polarization of TE_{11} mode is horizontal, axial cracks at points A and C as well as circumferential cracks at points B and D in Fig. 4-3(b) are expected to be detectable. On the other hand, if the TE_{11} mode is vertically polarized as given in Fig. 4-4(a), the distribution of electromagnetic field and surface current density also rotate by 90 degrees relative to Fig. 4-3(b), hence axial cracks at points B and D as well as circumferential cracks at points A and C in Fig. 4-4(b) are expected to be detected. Based on the discussions above, since the sensitive areas of horizontal or vertical polarization exactly overlap the detection dead zone of each other, a joint analysis of reflection signals under two polarizations would make both axial and circumferential cracks detectable despite their circumferential positions in a pipe.

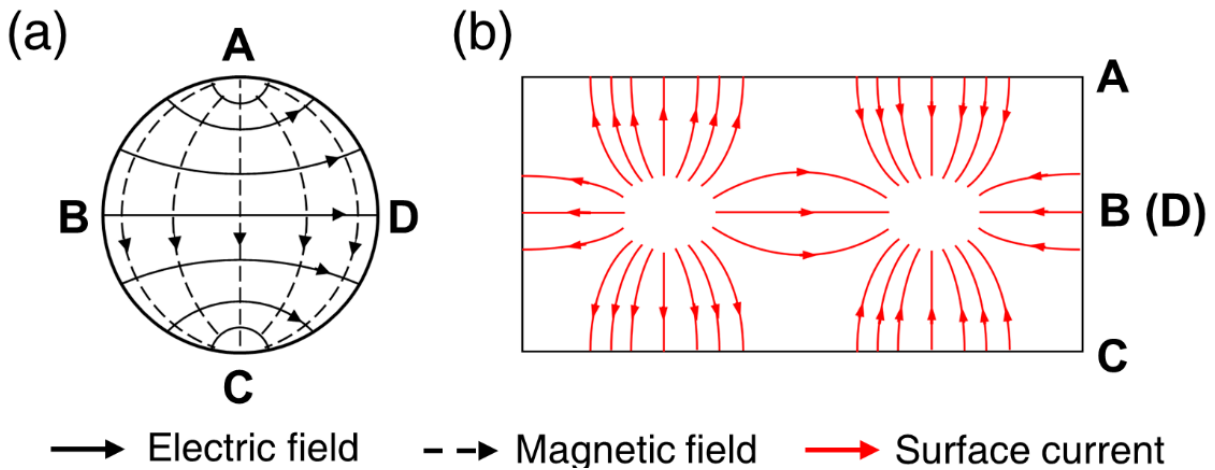


Fig. 4.3 Linearly-polarized TE_{11} mode under horizontal polarization, (a) electromagnetic field distribution at cross-section, (b) side view of surface current distribution.

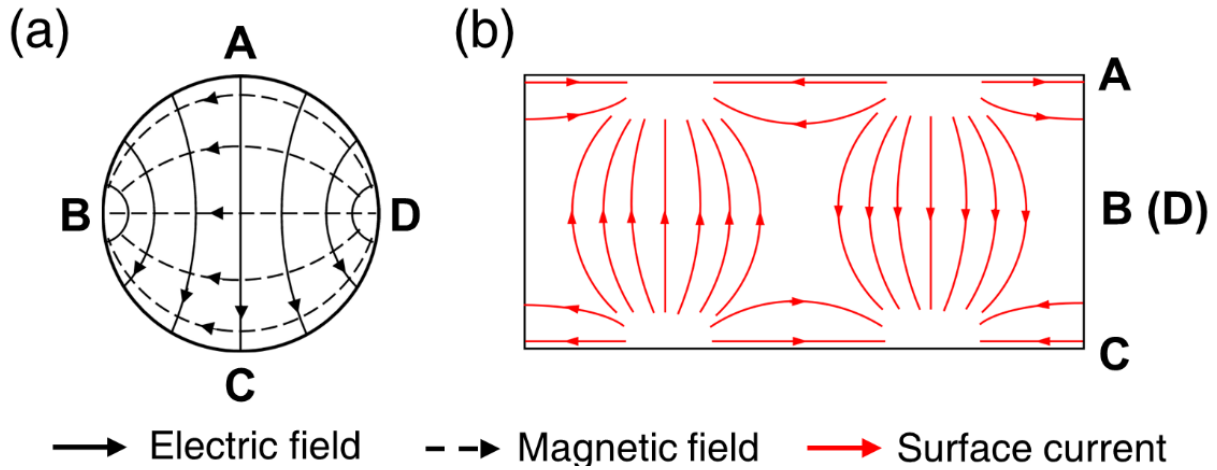


Fig. 4.4 Linearly-polarized TE_{11} mode under vertical polarization, (a) electromagnetic field distribution at cross-section, (b) side view of surface current distribution.

4.2 Design of TE_{11} mode microwave probe

The structure of the TE_{11} mode microwave probe in this study is illustrated in Fig. 4-5. It is composed of a TEM- TM_{01} mode converter [131] and a TM_{01} - TE_{11} mode converter, comprising two inversely connected bends. Actually, the dual-bend TM_{01} - TE_{11} mode converter or a similar type was proposed and developed in several earlier studies [132-135] for high power microwave systems. However, most of them were dedicated to working at a certain center frequency with a relatively narrow operating frequency range. In the case of microwave NDT, the inner pipe diameter D is the main factor, while a wider working bandwidth is preferable for a higher time-domain resolution as elucidated in Chapter 2. Moreover, these studies mainly concentrated on the conversion from TM_{01} to TE_{11} mode but paid little attention to the excitation of the TM_{01} mode. In this study, the TE_{11} mode microwave probe was systematically designed following three steps: (1) Design the TEM- TM_{01} mode converter for a designated inner pipe diameter D by means of numerical simulation, and obtain the operational frequency range of TM_{01} mode; (2) Over the obtained frequency range, calculate the fractional energy of each mode on the condition that TM_{01} mode microwaves propagate through the dual-bend TM_{01} - TE_{11} mode converter, based on the theory of mode conversion due to a bend; (3) In terms of the theoretically calculated results, optimize the dimensions (curvature radius r , bend angle α) of the dual-bend TM_{01} - TE_{11} mode converter.

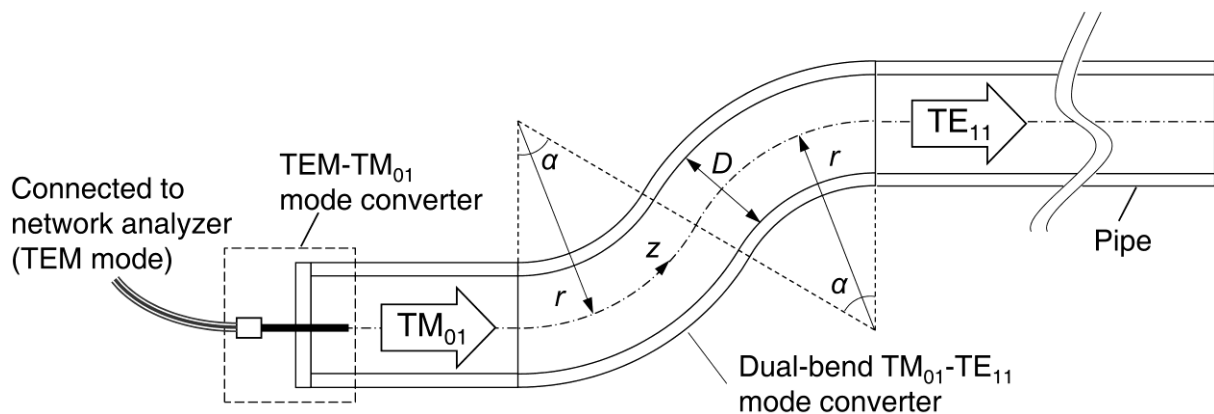


Fig. 4-5 Structure of TE_{11} mode microwave probe.

4.2.1 Design of TEM-TM₀₁ mode converter

The TEM-TM₀₁ mode converter was designed based on a former study of ours [131], and its geometric structure is shown in Fig. 4-6 (a). A semi-rigid cable was attached to the center of a plate cap (Osaka Sanitary Co., Ltd, CLF-B-304-1.5S) with a standard ferrule connection (the full circumferential groove with a diameter of 43.5mm on the plate). A portion of the core wire was exposed for an optimum length in order to achieve a higher conversion efficiency from TEM to TM₀₁ mode. In this study, the pipe's inner diameter D was set to 23 mm, while the optimized exposure length of the core wire was 6 mm, which was determined by the results of the numerical simulations. Figure 4-6(b) presents the reflection and transmission characteristics of the TEM-TM₀₁ mode converter. The operational frequency range of TM₀₁ mode was from 10.3 to 16.3 GHz, over which the energy ratio of the converted TM₀₁ mode was above 50%. The conversion from TM₀₁ to TE₁₁ mode over this frequency range will be evaluated in Section 4.2.2.

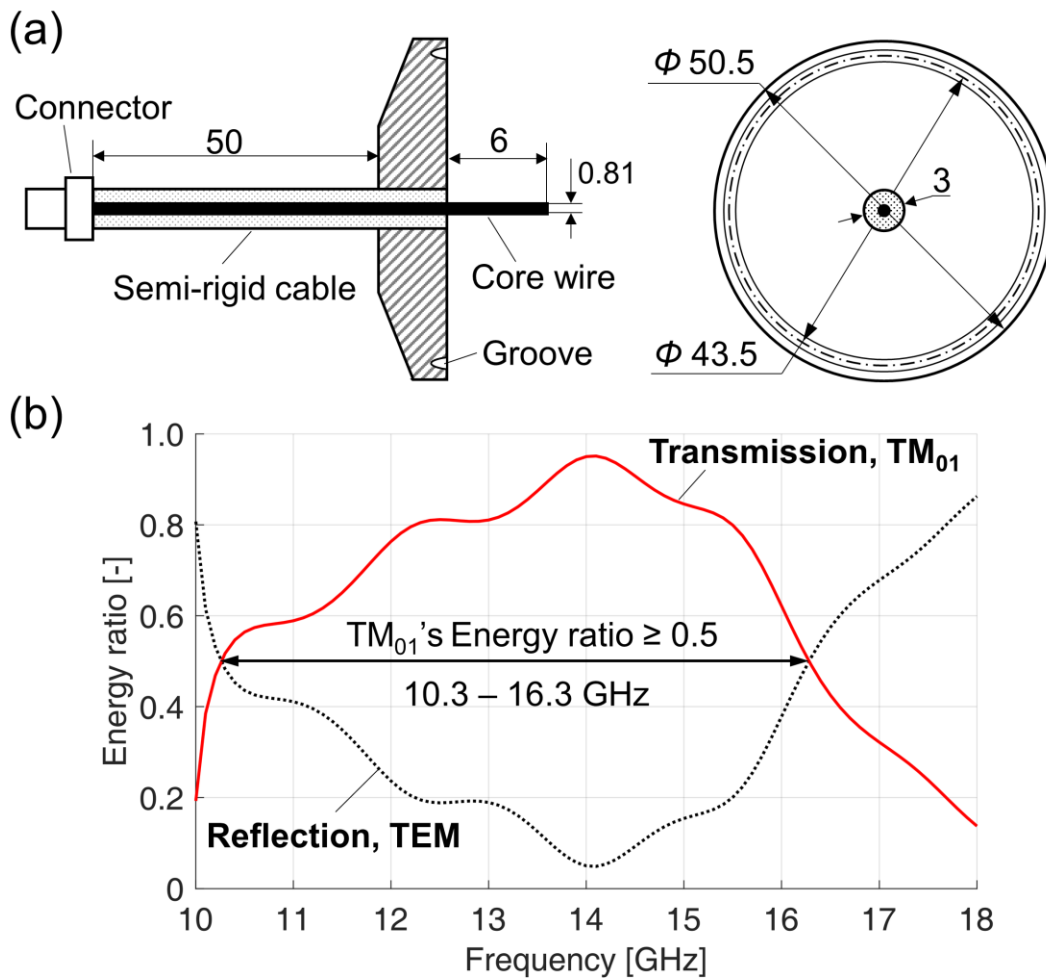


Fig. 4-6 TEM₀₁-TM₀₁ mode converter for $D = 23$ mm, (a) structure (not to scale), (b) reflection and transmission characteristics.

4.2.2 Design of TM₀₁-TE₁₁ mode converter

4.2.2.1 Theoretical calculation of the mode conversion in two inversely-connected bends

The conversion from the TM₀₁ to TE₁₁ mode is computed based on the principle of mode conversion due to a bend, which has been introduced in Chapter 3. Over the operational frequency range of the TM₀₁ mode determined in 4.2.1 (10.3 – 16.3 GHz), a total of four propagating modes were involved in

the calculation of the mode conversion. They are TE₁₁, TM₀₁, TE₂₁ and TM₁₁ mode, and their cut-off frequencies are 7.64, 9.98, 12.68 and 15.91 GHz, respectively, when $D = 23$ mm. It should be noted that the TE₀₁ mode was excluded from the mode coupling even though its cut-off frequency is within the input frequency range. That is because the preliminary simulation results revealed that the TE₀₁ mode could not be generated in the mode coupling when TM₀₁ mode was the only excitation mode. The mode coupling among the above mentioned four modes to the forward direction was calculated as:

$$\frac{d}{d\alpha} \begin{pmatrix} A_1 \\ A_2 \\ A_3 \\ A_4 \end{pmatrix} = -j \begin{pmatrix} r\beta_1 & rC_{12} & rC_{13} & rC_{14} \\ rC_{21} & r\beta_2 & rC_{23} & rC_{24} \\ rC_{31} & rC_{32} & r\beta_3 & rC_{34} \\ rC_{41} & rC_{42} & rC_{43} & r\beta_4 \end{pmatrix} \begin{pmatrix} A_1 \\ A_2 \\ A_3 \\ A_4 \end{pmatrix}, \quad (4.2)$$

where subscripts 1 – 4 refer to modes TE₁₁, TM₀₁, TE₂₁, and TM₁₁, C_{ij} ($i, j=1-4$) denotes the coupling coefficient among four modes, and $C_{ij} = C_{ji}$. When the two coupled modes do not fulfill the condition $|m - m'| = 1$, their coupling coefficient C_{ij} is 0. The symbols r , α denote the curvature radius and bend angle, respectively, while β is the phase constant. The initial value was set to $A_0 = [0, 1, 0, 0]^T$. The solution of Eq. (4.2) is the result of mode conversion of a single bend. To calculate the mode conversion in two inversely connected bends, we should proceed as follows. Firstly, calculate Eq. (4.2) and obtain the output of first bend; secondly, replace the r and α in Eq. (4.2) with $-r$ and $-\alpha$; finally, calculate Eq. (4.2) again utilizing the result of the first step as the initial value. Note that the calculated result $A = [A_1, A_2, A_3, A_4]^T$ is a vector of complex amplitudes, while the fractional energy of each mode is the square of absolute value of A .

On the basis of the results in Chapter 3, the mode conversion at a bend depends on three major factors: r/D , α and the normalized frequency ff_c (wherein f_c is the cut-off frequency of an arbitrary mode.) It simplifies the calculation of mode conversion by reducing the number of parameters, and merges similar cases. This conclusion will be adopted in the next section to optimize the dimensions of the TM₀₁-TE₁₁ mode converter.

4.2.2.2 Dimensional optimization of the dual-bend TM₀₁-TE₁₁ mode converter

As discussed in Section 2.4, the working bandwidth of the mode converter ought to be as wide as possible so as to obtain a higher time-domain resolution. As the operational range of TM₀₁ mode has been determined, if using the cut-off frequency of TM₀₁ mode f_{cTM01} for normalization, the normalized operational frequency range of TM₀₁ mode ff_{cTM01} was calculated as 1.03 – 1.63. Therefore, an optimum combination of r/D and α should be selected to maximize working bandwidth over the given range of ff_{cTM01} . This study defines the working bandwidth as the frequency range within which the energy ratio of TE₁₁ mode is greater than or equal to 90%. In order to simplify the calculation, the curvature radii r and bend angles α of two bends of the mode converter were set to identical. Then, r/D and α were scanned in terms of the values listed in Table 4-1 to calculate the normalized working bandwidth of the converted TE₁₁ mode.

Figure 4-7 (a) presents the computational results of normalized working bandwidth for the r/D & α combinations in Table 4-1. As shown in the figure, the maximum normalized working bandwidth was 0.35, acquired when $r/D = 2.6$ & $\alpha = 51^\circ$ or $r/D = 2.7$ & $\alpha = 49^\circ$. Figure 4-7 (b) shows the theoretically calculated results of one scenario ($r/D = 2.6$ & $\alpha = 51^\circ$). The energy ratio of TE₁₁ mode was greater than or equal to 90% when ff_{cTM01} ranged from 1.24–1.59. The calculated result of another scenario ($r/D = 2.7$ & $\alpha = 49^\circ$) was similar to the result displayed in Fig. 4-7(b), enabling us to discuss only one of them.

Table 4-1. Parameters and values of theoretical calculation.

Parameter	Value (step)
r/D [-]	1 – 8 (0.1)
α [deg.]	0 – 180 (1)
f/f_{cTM01} [-]	1.03 – 1.63 (0.01)

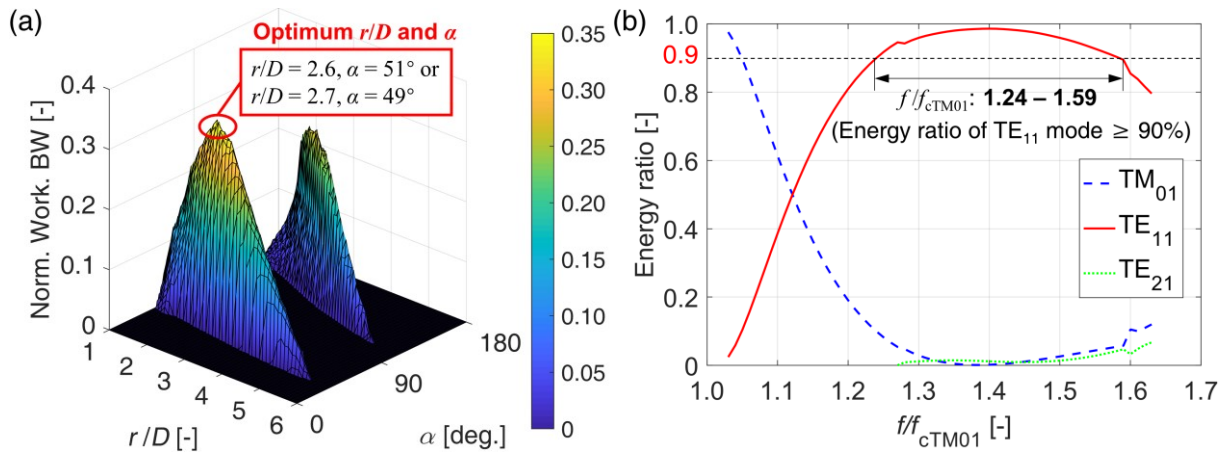


Fig. 4-7 Theoretical calculation of the mode conversion at the TM_{01} - TE_{11} mode converter, (a) normalized working bandwidths of different combinations of r/D and α , (b) fractional energy of each mode versus f/f_{cTM01} when $r/D=2.6, \alpha=51^\circ$.

Three-dimensional numerical simulation was conducted to verify the optimization result of theoretical calculation. The geometrical model is illustrated in Fig. 4-8. The inner diameter of the pipe was 23 mm, while the curvature radius r and bend angle α were set to 60 mm ($r/D \approx 2.6087$) and 51° , respectively. The TM_{01} mode microwaves were excited at Surface I of the model, while the transmission characteristics of converted modes were evaluated at Surface II. A perfectly matched layer (PML) was placed at the other end to eliminate the reflection to Surface II. Second-order tetrahedral were used for discretization. The sweeping frequency span was from 12.0 to 16.0 GHz, with a step of 0.1 GHz.

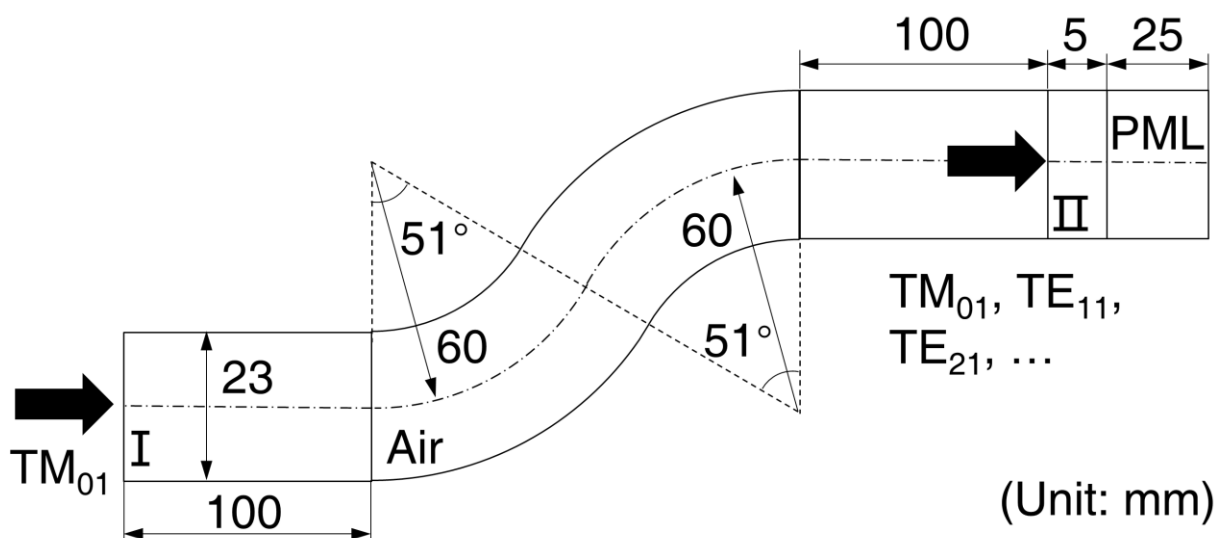


Fig. 4-8 Geometric model of numerical simulation (not to scale).

Figure 4-9 shows the simulation results. The electromagnetic field distribution inside the TM_{01} - TE_{11} mode converter is displayed in Fig. 4-9(a), at the frequency of 14.0 GHz. As illustrated in the figure, when propagating through the inversely-connected dual-bend, the axisymmetric TM_{01} mode is converted into the linearly-polarized TE_{11} mode as expected. Figure 4-9(b) exhibits the comparison between theoretical calculation and numerical simulation. The theoretically calculated energy ratio of each mode was consistent with the simulation result. The working bandwidth of the dual-bend TE_{11} mode microwave probe was 3.5 GHz, approximately ranging from 12.4 to 15.9 GHz.

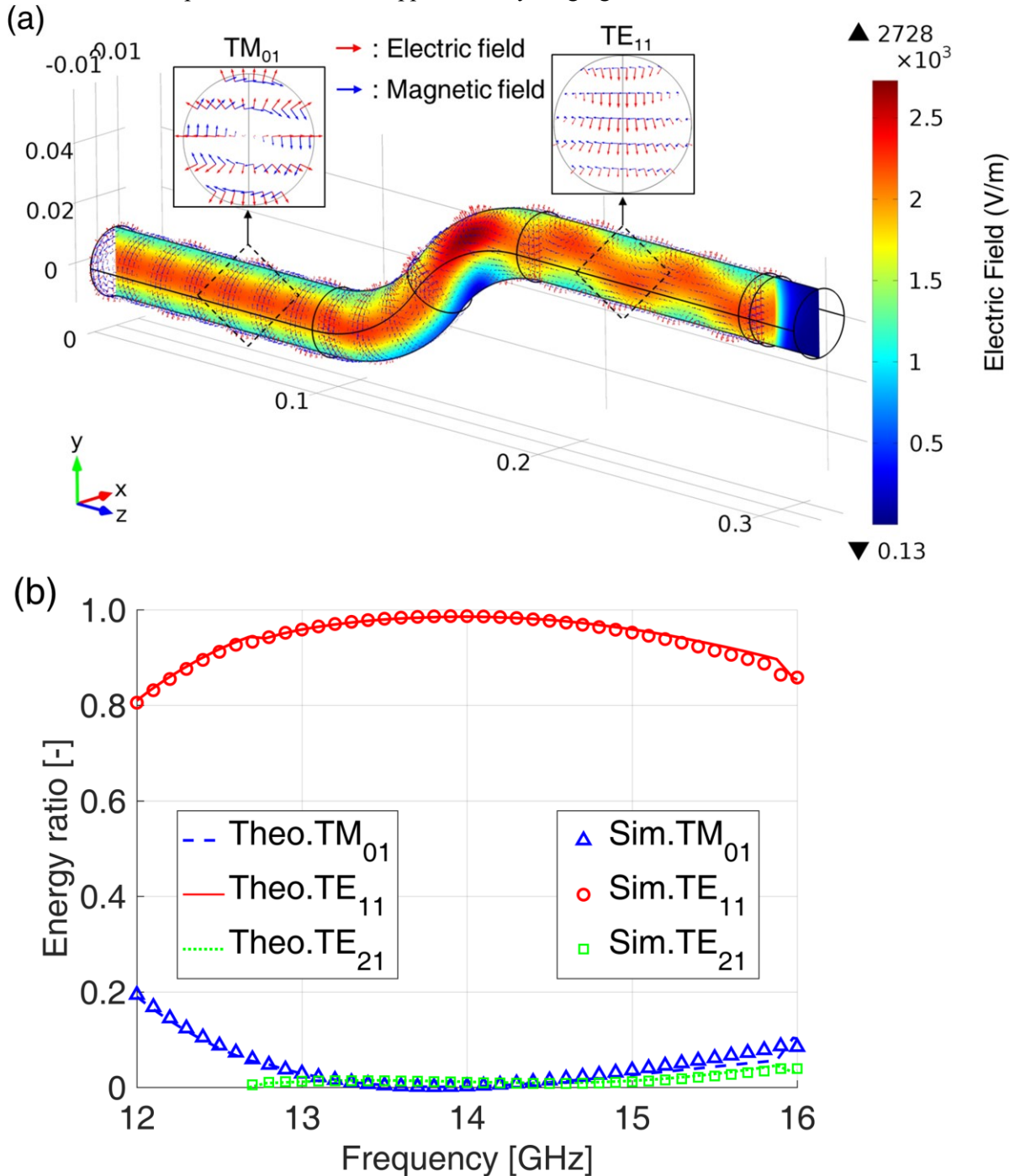


Fig. 4-9 Simulation results ($r = 60$ mm, $D = 23$ mm, $\alpha = 51^\circ$). (a) Electromagnetic field distribution when $f = 14$ GHz, (b) comparison between the result of theoretical calculation and that of numerical simulation.

4.3 Experimental verification

Experiment was performed to verify the effectiveness of the TE_{11} mode microwave probe designed in Section 4.2, by detecting artificial slits simulating axial/circumferential cracks at different longitudinal and circumferential positions in a pipe.

4.3.1 Experimental setup

Figure 4-10(a) depicts the overview of the experimental system of this study. A network analyzer was utilized to emit coaxial TEM mode microwaves. The excited TEM mode microwaves were subsequently propagated through a flexible cable and transmitted to the TE_{11} mode microwave probe or a TEM-to- TM_{01} mode converter, in terms of the layout illustrated in Figs. 4-10(b), (c), and (d). Note that the TE_{11} mode microwave probe was deployed orthogonally in Figs 4-10(b) and (c), to realize horizontal or vertical polarization of TE_{11} mode.

A seven-meter long metal pipe was used for testing, and the material was type 304 stainless-steel. Given that it is difficult to prepare a long seamless pipe, seven short pipes with a length of 1 m were arranged and connected with ferrule connections. The inner diameter and wall thickness of the pipes were 23 mm and 1.2 mm, respectively. A tailored O-ring and two rubber mats were installed at every ferrule connection to eliminate misalignment in the pipe connections and reduce the reflection from the connections. The photograph of the experimental setup is shown in Fig. 4-11.

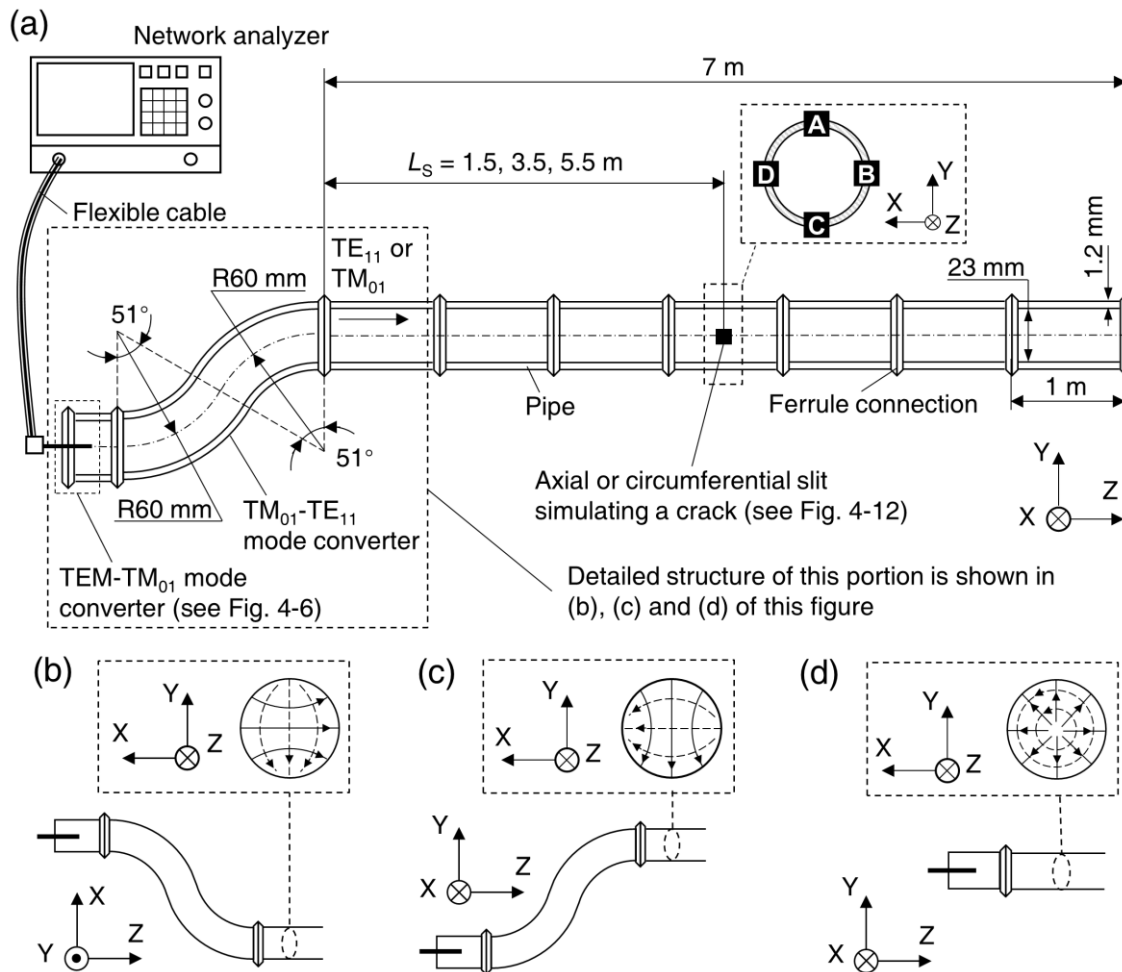


Fig. 4-10 Experimental system (not to scale), (a) experimental apparatus, (b) generating horizontally-polarized TE_{11} mode, (c) generating vertically polarized TE_{11} mode, (d) generating TM_{01} mode. (**Note:**

In (b), (c), and (d), the solid vector-line and broken vector-line in the circular cross-section inside the wireframe denote electric field and magnetic field, respectively.)

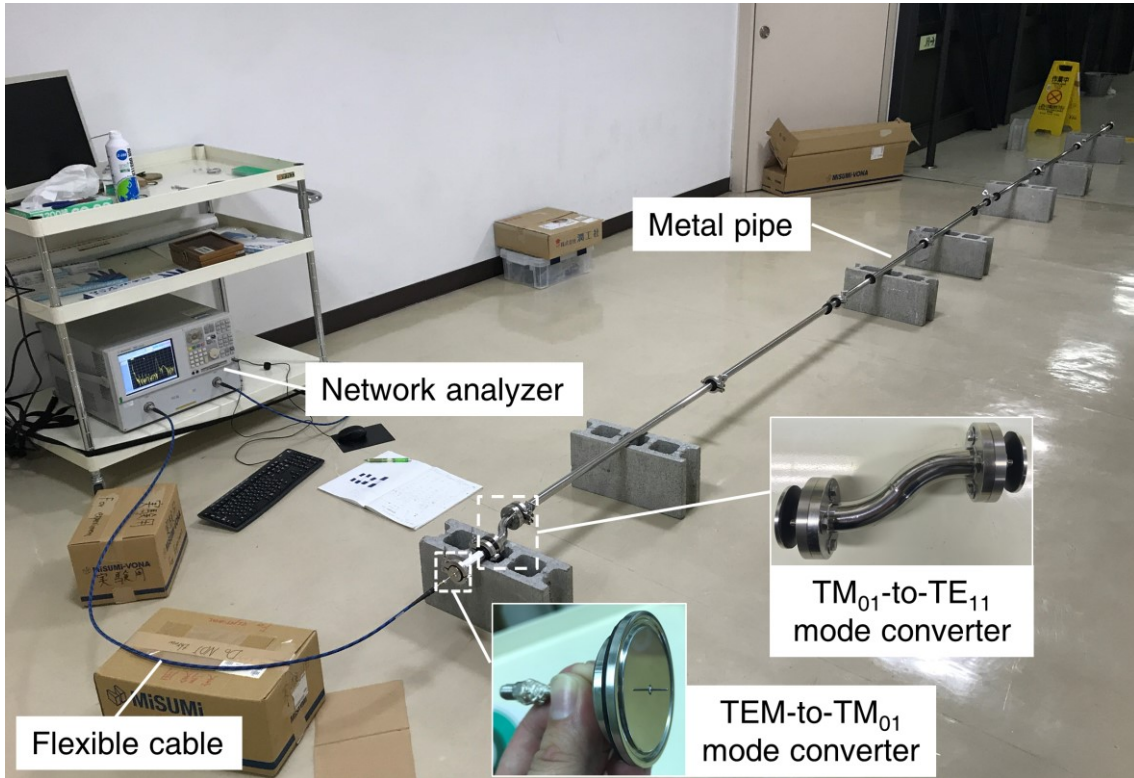


Fig. 4-11 Photograph of the experimental setup.

To simulate cracks in a pipe, an axial slit and a circumferential slit were fabricated in the middle of two pipes by a machine saw. The slits were longitudinally deployed at $L_s = 1.5, 3.5,$ and 5.5 m, and circumferentially situated at four points, A, B, C, and D as shown in the dash line box in Fig.4-10 (a). The photos of the axial and circumferential slits are shown in Fig. 4-12. Table 4-2 summarizes the details of the deployments of the two slits.

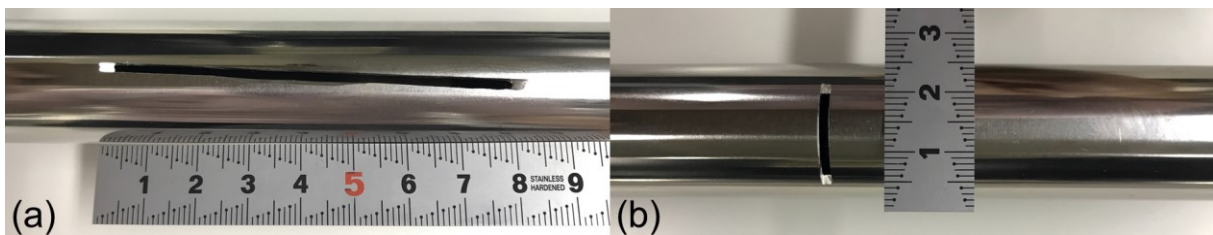


Fig. 4-12 Photographs of the artificial slits simulating cracks, (a) axial slit, (b) circumferential slit.

Table 4-2 Longitudinal and circumferential positions of axial and circumferential slits in the pipe

L_s (m)	Cir. Pos.			
	A	B	C	D
1.5	axial	circumferential	circumferential	axial
3.5	axial and circumferential			
5.5	circumferential	axial	axial	circumferential

The reflection coefficients were measured in the frequency domain as S-parameters, over the working frequency span of the TE₁₁ mode microwave probe, i.e., 12.4 – 15.9 GHz. A total of 3201 equidistant frequency points were sampled over this frequency span. Every measurement was conducted 30 times and the average result was recorded. The measured frequency domain signals were converted into the time domain with inverse fast Fourier transform and further processed using the signal-processing method narrated in Section 2.4.

4.3.2 Results and discussions

Figures 4-13 and 4-14 exhibit the time-domain reflection signals from the axial and circumferential slits situated at $L_s = 3.5$ m, while the propagating modes are TE₁₁ mode under horizontal polarization and vertical polarization, respectively. In each figure, the large reflection peak near 0 ns is from the TEM-to-TM₀₁ mode converter, while the reflection appearing at around 59 ns corresponds to the pipe end (7 m). There is another discernible reflection peak appearing at about 3.5 ns, corresponding to the outlet of the TM₀₁-TE₁₁ mode converter, namely the inlet of the pipe. Reflection signals from the slits are highlighted with down-arrows. As shown in Fig. 4-13, reflections due to the axial slit at points A, C and circumferential slit at points B, D are clearly observed at 31 ns or so, which accords with the analysis of sensitive areas in Fig. 4-3. Likewise, in Fig. 4-14, axial slit at points B and D and circumferential slit at points A and C are also explicitly detected, corresponding to the analysis in Fig. 4-4. There are several local reflection peaks from about 10 ns to 55 ns, which were caused by the ferrule connections. On the basis of the above discussions, it can be concluded that: orthogonally deploying the TE₁₁ mode microwave probe and jointly analyzing the reflection signals under two polarizations enable us to detect both axial and circumferential slits located at arbitrary circumferential positions in a pipe.

Figure 4-15 shows the time-domain reflection signals when the TM₀₁ mode was used for testing, while the axial and circumferential slits were also situated at $L_s = 3.5$ m. Similarly, the reflection peaks at around 0 ns and 67 ns correspond to the TEM-to-TM₀₁ mode converter and the pipe end. The local reflection peaks from about 10 to 60 ns were also caused by the ferrule connections, and they are a little bit larger than the reflections caused by ferrule connections in Figs. 4-13 and 4-14. That is because the surface current density of TM₀₁ mode is longitudinal, which makes it susceptible to the circumferential anomalies inside the pipe. The discernible reflections resulting from the slits are also marked with down-arrows. From (a)–(d) and (e)–(h) in Fig. 4-15, we can see the TM₀₁ mode shows an all-around sensitivity to circumferential slits, but zero detectability against axial slits.

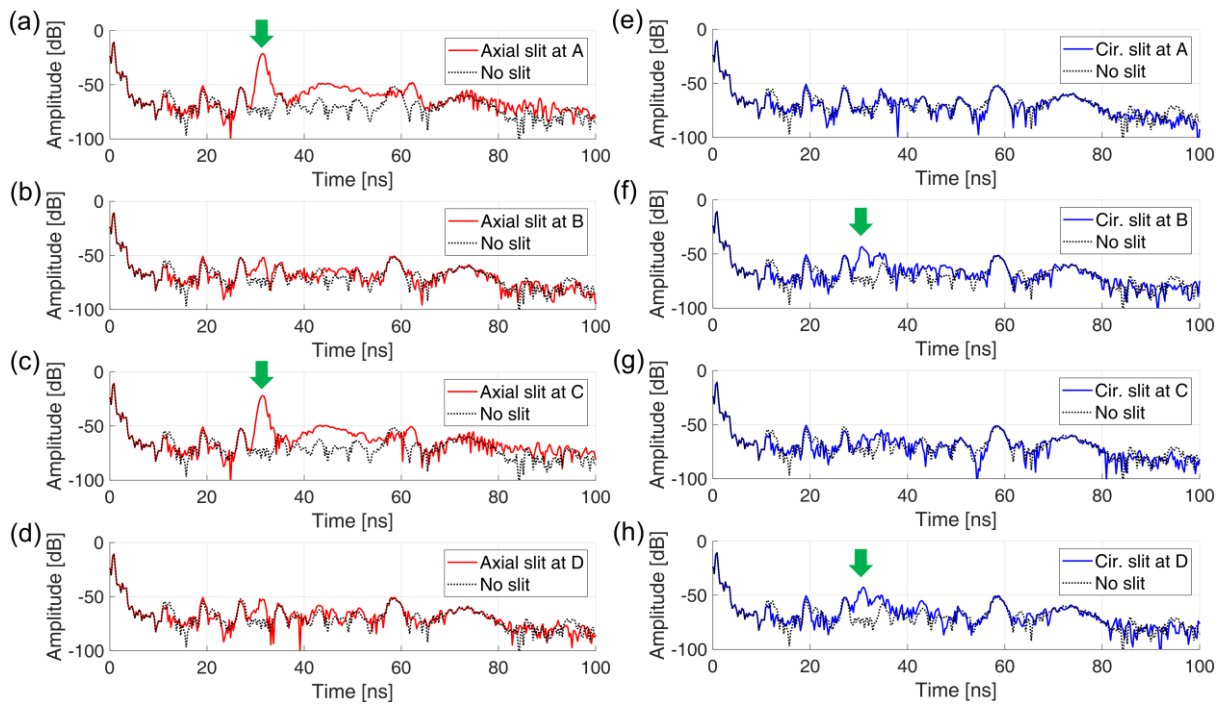


Fig. 4-13 Reflection signals due to slits at $L_S=3.5$ m, using TE_{11} mode microwaves under horizontal polarization, (a) – (d) axial slit at points A, B, C, and D, (e) – (h) circumferential slit at points A, B, C, and D.

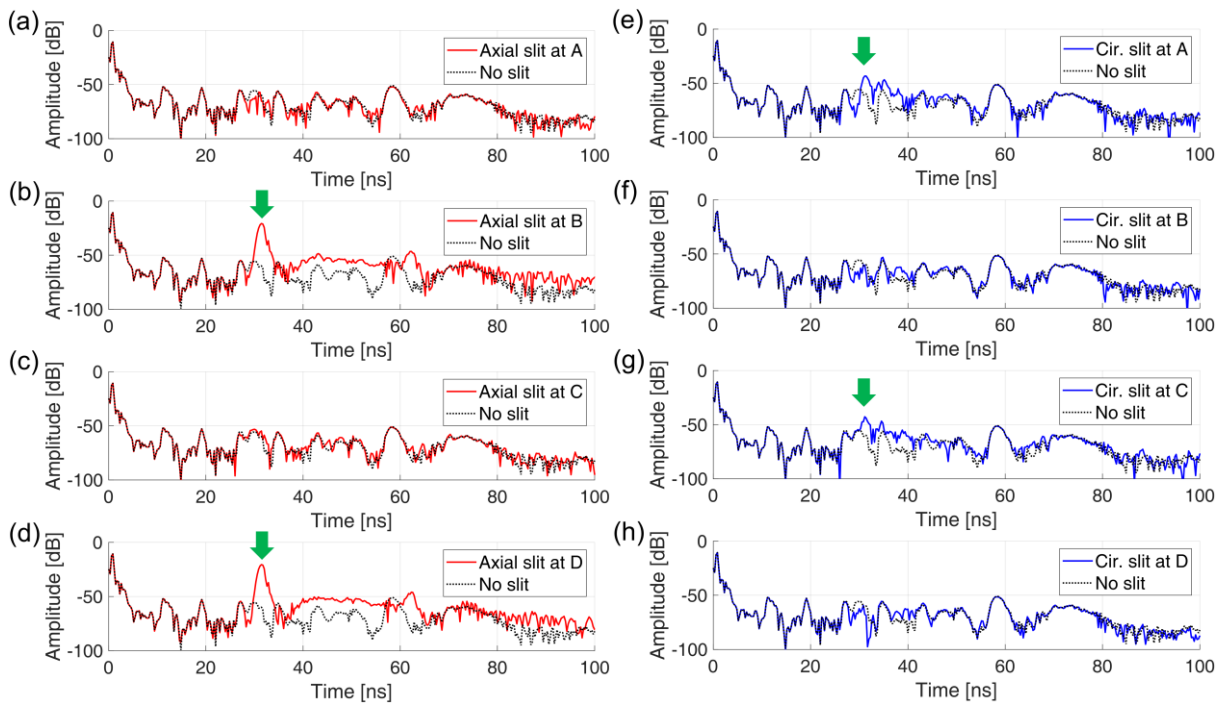


Fig. 4-14 Reflection signals due to slits at $L_S=3.5$ m, using TE_{11} mode microwaves under vertical polarization, (a) – (d) axial slit at points A, B, C, and D, (e) – (h) circumferential slit at points A, B, C, and D.

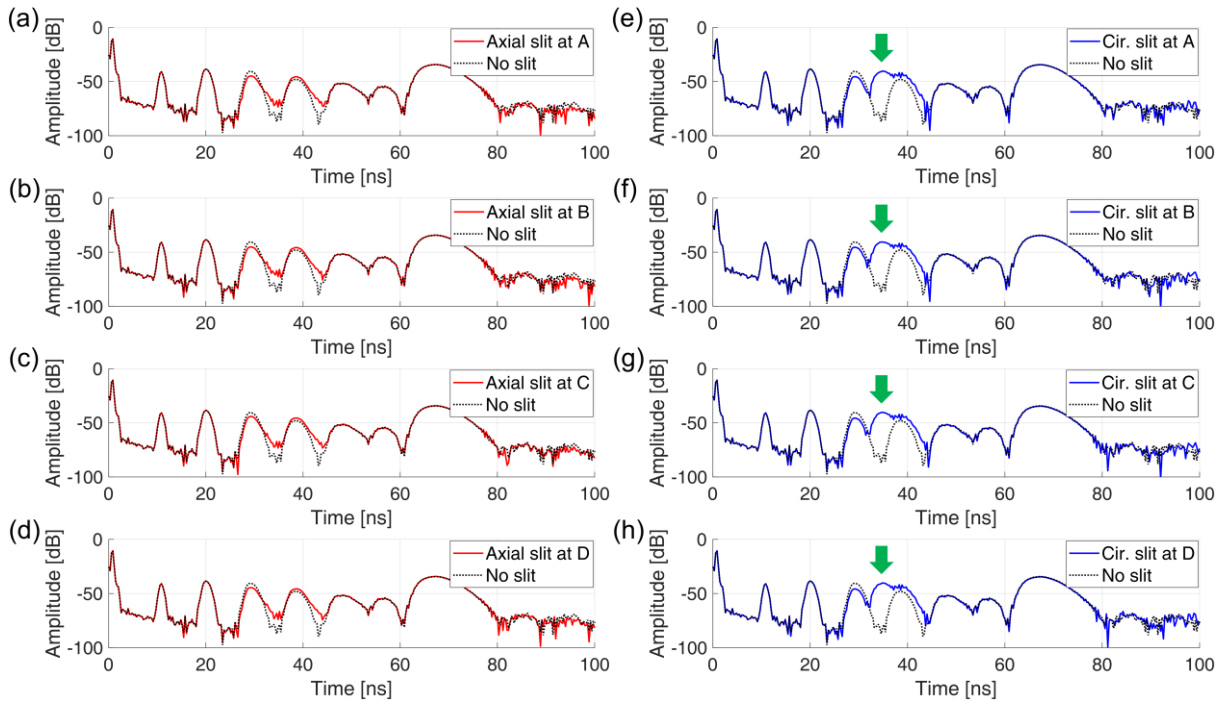


Fig. 4-15 Reflection signals due to slits at $L_S=3.5$ m, using TM_{01} mode microwaves, (a) – (d) axial slit at points A, B, C, and D, (e) – (h) circumferential slit at points A, B, C, and D.

The processed reflection signals from the slits listed in Table 4-2 are presented in Figs. 4-16 and 4-17, respectively. The results indicate that either axial or circumferential slit situated at $L_S = 1.5$ m, 3.5 m, 5.5 m and four different circumferential positions can be effectively detected and located, employing the TE_{11} mode microwaves under two orthogonal polarizations. Small localized peaks appearing at 1 m, 2 m ..., 6 m correspond to the ferrule connections. Therefore, the viability of using linearly-polarized TE_{11} mode microwaves to detect cracks with arbitrary orientations in a pipe has been demonstrated, and the efficacy of the TE_{11} mode microwave probe has also been verified.

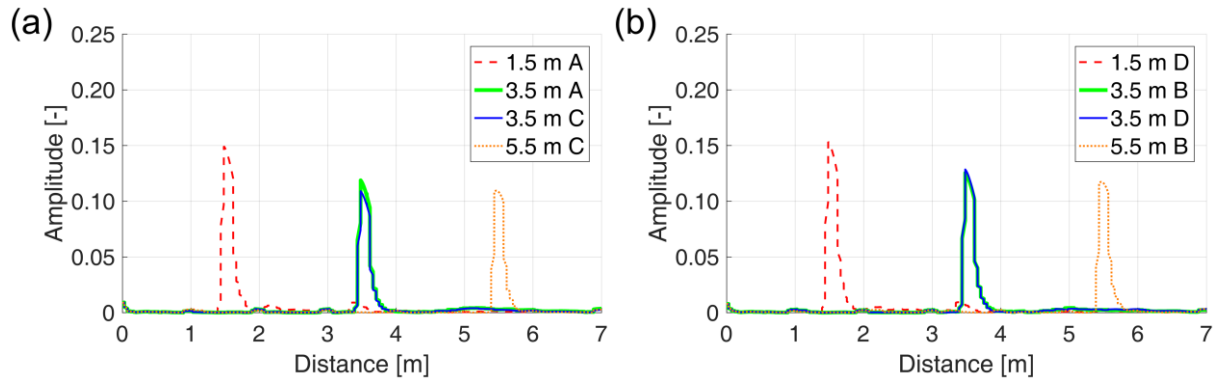


Fig. 4-16 Processed reflection signals from axial slit located at $L_S = 1.5, 3.5, 5.5$ m and different circumferential positions, using TE_{11} mode microwaves under (a) horizontal polarization, (b) vertical polarization.

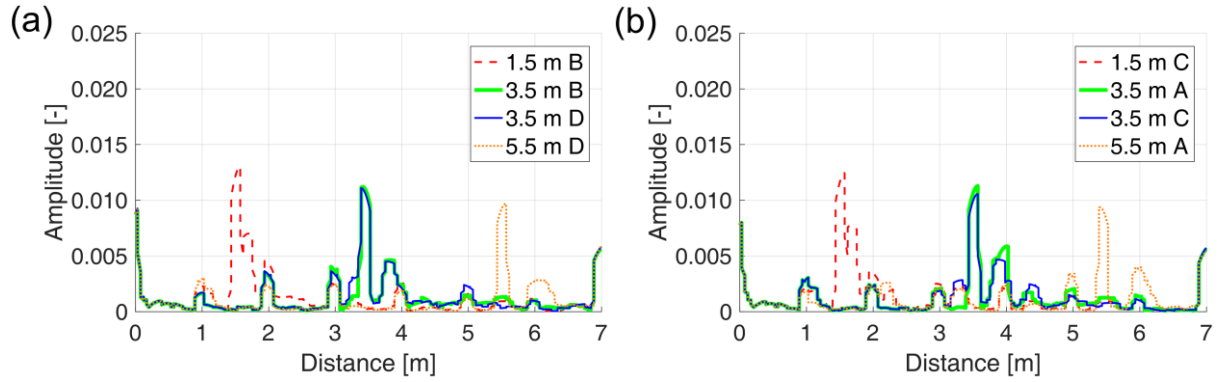


Fig. 4-17 Processed reflection signals from circumferential slit located at $L_S = 1.5, 3.5, 5.5$ m and different circumferential positions, using TE_{11} mode microwaves under (a) horizontal polarization, (b) vertical polarization.

4.4 Application to bent pipe

In Section 4.3, the proposed crack-detection method using linearly-polarized TE_{11} mode microwaves has been proved to be effective for straight pipe inspection. However, whether it works for bent pipe should be confirmed as the mode conversion occurs at the bend. In this section, the TE_{11} mode microwave probe in the previous section was utilized again to detect cracks in a bent pipe, and the experimental setup is shown in Fig. 4-18. In fact, the experimental system and parameters were almost identical to that in Section 4.3, while the change was that a bend ($D = 23$ mm, $r = 34$ mm, $\alpha = 90^\circ$) was inserted at 1 m distant from the probe. According to the simulation results of the mode conversion of TE_{11} mode in Section 3.3, the polarization remains unchanged when linearly-polarized TE_{11} mode microwaves pass through a bend. Hence, the deployment of the TE_{11} mode microwave probe and the slits were arranged as follows: (1) firstly, the probe was horizontally deployed to generate TE_{11} mode under horizontal polarization, while the axial and circumferential slits were longitudinally deployed at $L_S = 0.5$ m, 1.5 m $+l_{\text{Bend}}$, 2.5 m $+l_{\text{Bend}}$, 3.5 m $+l_{\text{Bend}}$, ..., 6.5 m $+l_{\text{Bend}}$ (l_{Bend} denotes the length of the bend and is 95.4 mm). Note that the two slits were situated at corresponding sensitive area, e.g., axial slit at point A and circumferential slit at point B; (2) then, the probe was vertically deployed to generate TE_{11} mode under vertical polarization, and the two slits were only deployed at $L_S = 3.5$ m $+l_{\text{Bend}}$, but circumferentially deployed at both sensitive and insensitive areas (like both points A and B, refer to the analysis in the preceding sections). Besides, reference test was also made for straight pipe (like Fig. 4-10), where the slits were also positioned at $L_S = 0.5, 1.5, 2.5, 3.5, \dots, 6.5$ m and corresponding sensitive areas in the circumferential direction, and the polarization was horizontal.

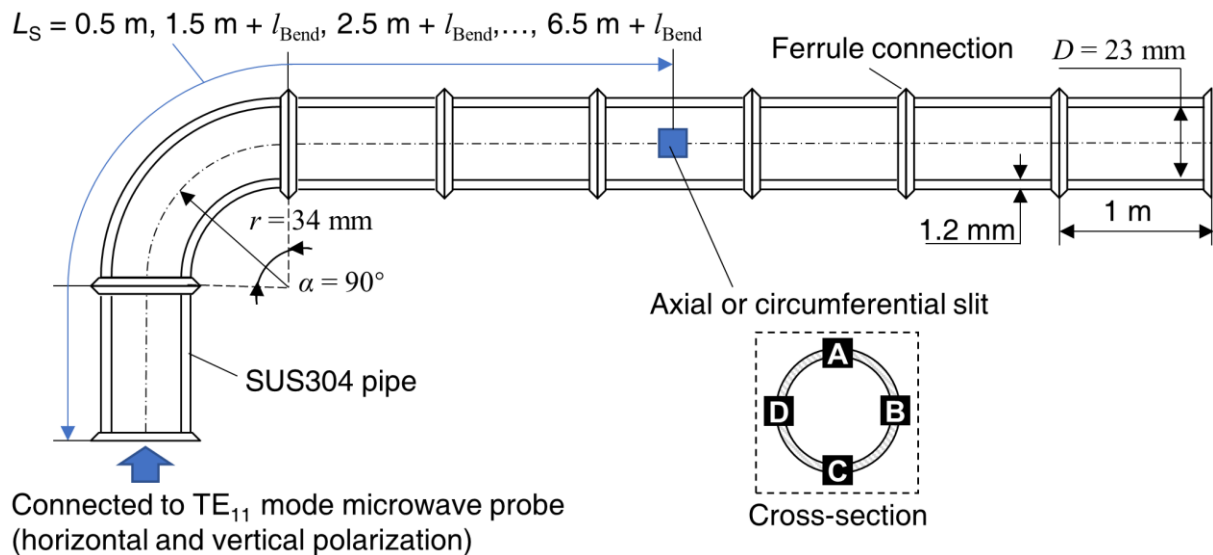


Fig. 4-18 Experimental setup for bent pipe testing using the TE₁₁ mode microwave probe. (Note: the illustration of L_S is not accurate in this figure, as L_S was measured along the axial line of the pipe.)

Figures 4-19 and 4-20 exhibit the processed reflection signals in the straight pipe and bent pipe, while the polarization of TE₁₁ mode was horizontal. In Fig. 4-20(a), discernible reflection peaks suggest that axial slits in the bent pipe were detectable using TE₁₁ mode microwaves. Moreover, comparing Figs. 4-19(a) and 4-20(a), the obvious decrease in reflection amplitude from 0.5 m to 1.5 m + l_{Bend} indicates that the bend did ‘take effect’. On the other hand, the reflections from the circumferential slit were rather complicated in the bent pipe. As shown in Fig. 4-20(b), the noticeable reflection peaks were possibly due to the TM₀₁ mode converted from TE₁₁ mode at the bend, as the peak locations do not accord with where the actual slit was situated. In contrast, the reflections due to the TE₁₁ mode were drowned in the relatively large reflections of TM₀₁ mode. Nevertheless, since the TE₁₁ mode microwave probe itself incorporates a TM₀₁ mode microwave probe (i.e., TEM-TM₀₁ mode converter), we can thus make use of it to detect circumferential flaws inside bent pipes. Fig. 4-21 shows the reflection signals from the circumferential slit in the straight and bent pipes adopting TM₀₁ mode. The results indicate that the circumferential slit was detectable given the existence of the bend, while the effect of the bend can also be confirmed by comparing Figs. 4-21(a) and (b). The reflections at around 1, 2, 3..., 6 m in both two sub-figures were due to the ferrule joints between two pipes or pipe and bend. Therefore, when a bend imposes a relatively large effect on TE₁₁ mode under horizontal polarization, utilizing the ‘self-integrating’ TM₀₁ mode microwave probe would be an effective and alternative way for detecting circumferential cracks.

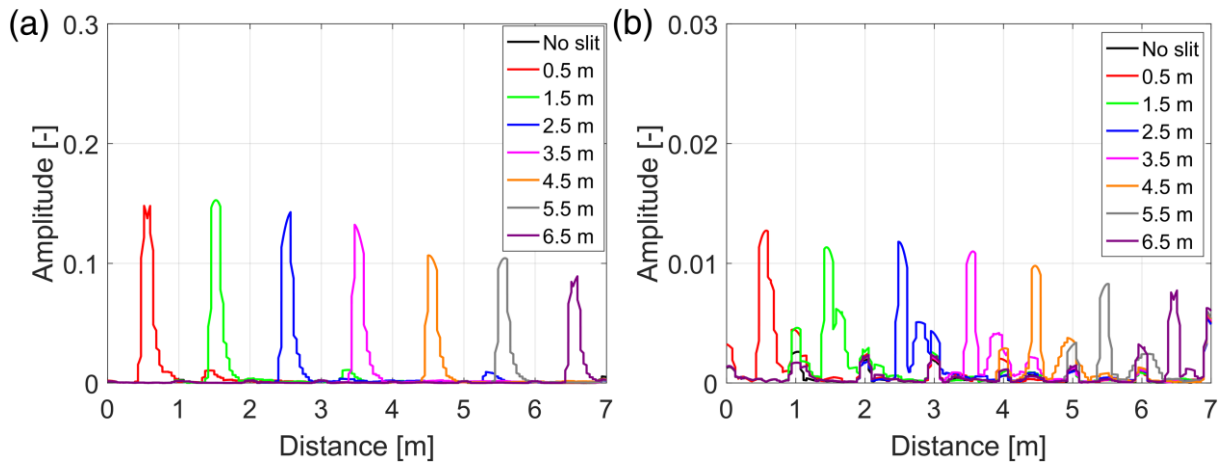


Fig. 4-19 Processed reflection signals from axial/circumferential slit in the straight pipe using TE_{11} mode under horizontal polarization, (a) axial slit, (b) circumferential slit.

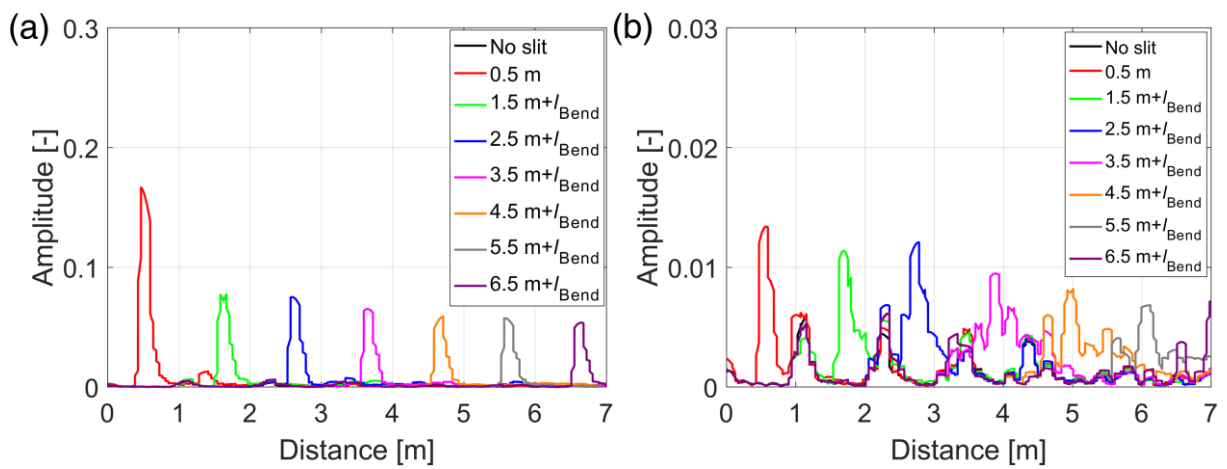


Fig. 4-20 Processed reflection signals from axial/circumferential slit in the bent pipe using TE_{11} mode under horizontal polarization, (a) axial slit, (b) circumferential slit.

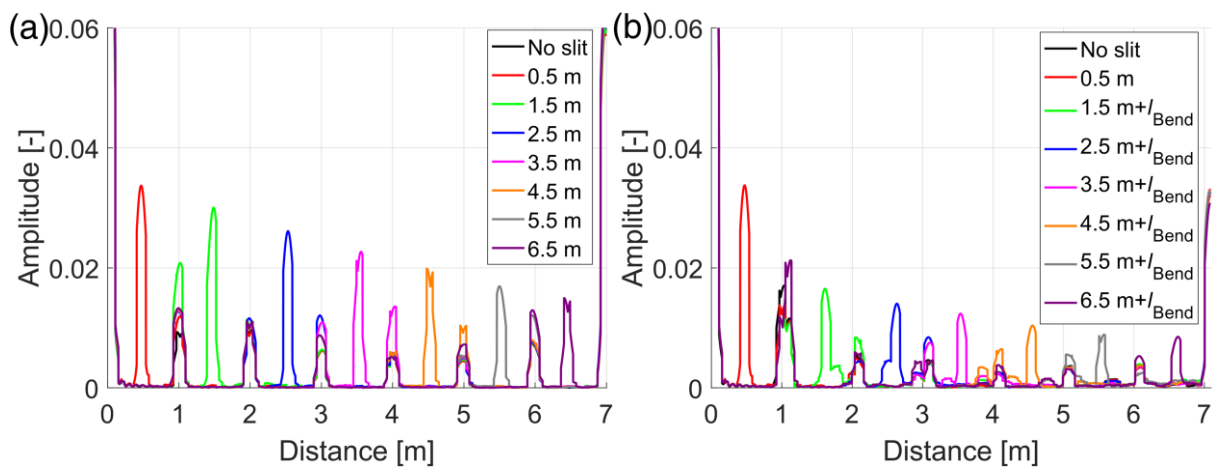


Fig. 4-21. Processed reflection signals from circumferential slit using TM_{01} mode in a (a) straight pipe, (b) bent pipe. (The frequency span of TM_{01} mode was the same as the working frequency span of TE_{11} mode microwave probe, namely 12.4 – 15.9 GHz)

The reflection signals of vertical polarization are exhibited in Fig. 4-22. As shown in the figure, both axial and circumferential slits deployed in sensitive areas were detected, while those deployed at

insensitive areas were undetectable. This result also verified the analysis in Section 3.3, i.e., the polarization itself is not affected by the bend. Furthermore, we can see that the amplitudes of reflections from axial and circumferential slits at the sensitive areas are basically identical to those in Fig 4-19, where the results of straight pipe are presented. The reason has been discussed in Chapter 3, the polarization of TE₁₁ mode affects its mode conversion at the bend, thus the results under vertical polarization are also expected to be a bit different from those under horizontal polarization shown in Fig. 4-20. The simulation results of the mode conversion of TE₁₁ mode under horizontal and vertical polarizations at the bend are displayed in Fig. 4-23. Clearly and obviously, more TE₁₁ mode ‘passed through’ the bend under vertical polarization and the mode conversions of two polarizations are quite different from each other, which leads to the disparity in reflection amplitude.

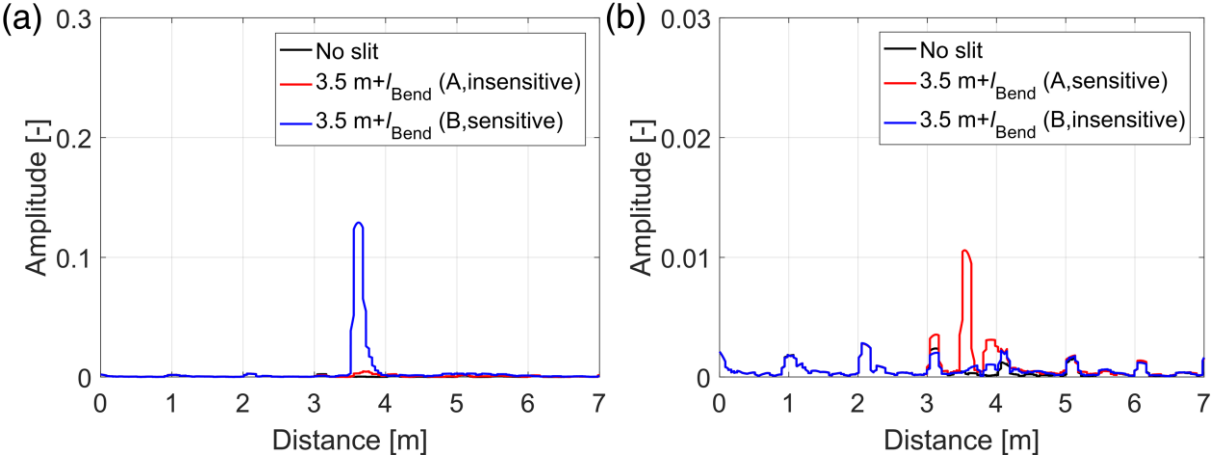


Fig. 4-22 Processed reflection signals from axial/circumferential slit in the bent pipe using TE₁₁ mode under vertical polarization, (a) axial slit, (b) circumferential slit.

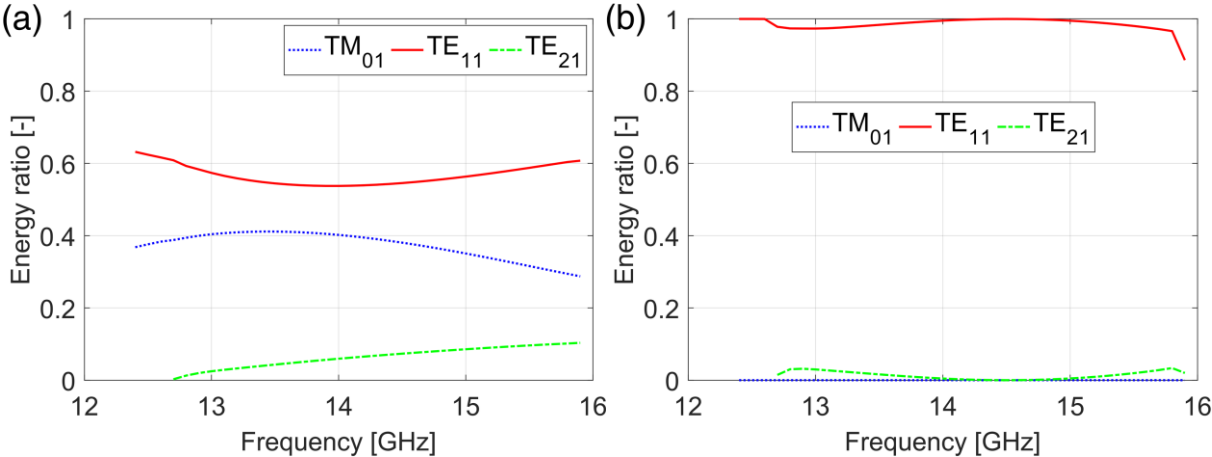


Fig. 4-23 Simulation results of mode conversion of TE₁₁ mode at the bend, (a) horizontal polarization, (b) vertical polarization.

On the basis of the discussions above, although the presence of a bend influences the intensity of the reflections from cracks and the detection sensitivities for TE₁₁ mode under two orthogonal polarizations are also different, the axial cracks are still anticipated to be detectable. Meanwhile, the thorough detectability against cracks can still be achieved by additionally adopting the ‘self-integrating’ TM₀₁ mode as an auxiliary approach to detect circumferential cracks, if the effect of the bend on reflection is relatively large.

4.5 Applicability to multiple pipe diameter and long pipes

In the previous sections, only one pipe diameter $D = 23$ mm was studied, while this crack-detection approach is designed for arbitrary inner pipe diameter. Besides, the length of the pipe under test was merely 7 meters. Therefore, in this section, three more TE_{11} mode microwave probes with different D are designed in terms of the method in Section 4.2 and fabricated for validation. Furthermore, the experimental verification was conducted by detecting axial slit and circumferential slit (simulating cracks) deployed at multiple longitudinal positions in pipes with lengths ranging from 21 to 25.5 m.

Figure 4-24 illustrates the structure of the TE_{11} mode microwave probe used in this section. The difference between the probe in Section 4.2 and this one is the joint: the ferrule connection is replaced by flange for easy connection and disconnection. The inner pipe diameter $D = 11, 19,$ and 39 mm, and the curvature radii r and bend angles α of two bends were also set to be identical to simplify the computation of mode conversions at the dual-bend TM_{01} - TE_{11} mode converter. Table 4-3 summarizes the optimized dimensional parameters for three TE_{11} mode converters (i.e. $l_E, r, r/D,$ and α), and their working frequency spans f_w were obtained accordingly, over which the energy ratio of TE_{11} mode was greater than or equal to 90%.

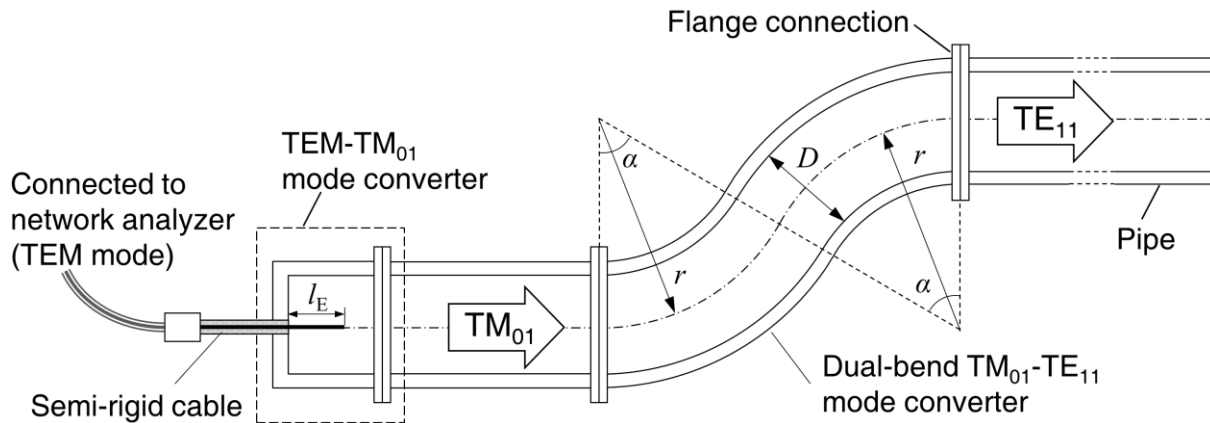


Fig. 4-24 Structure of the TE_{11} mode microwave probe with flange connections.

Figure 4-25 shows the comparisons between the theoretical and numerical results of the optimized frequency-domain characteristics for the three TE_{11} mode microwave probes. Good consistency is observed for each of them, and the working bandwidths of the three mode converters were 7.0, 4.0, and 1.9 GHz. It can be seen that the working bandwidth of the TE_{11} mode converter decreases when D becomes larger, which is not preferable because the time-domain resolution is inversely proportional to the frequency bandwidth as discussed in Chapter 2. The solution to this problem will be given in the latter part of this section.

Table 4-3 Parameters of the three mode converters

D (mm)	r (mm)	r/D (-)	α (deg.)	l_E (mm)	f_w (GHz)
11	30	2.73	48	3	26.0–33.0
19	50	2.63	50	5	15.0–19.0
39	100	2.56	51	9	7.3–9.2

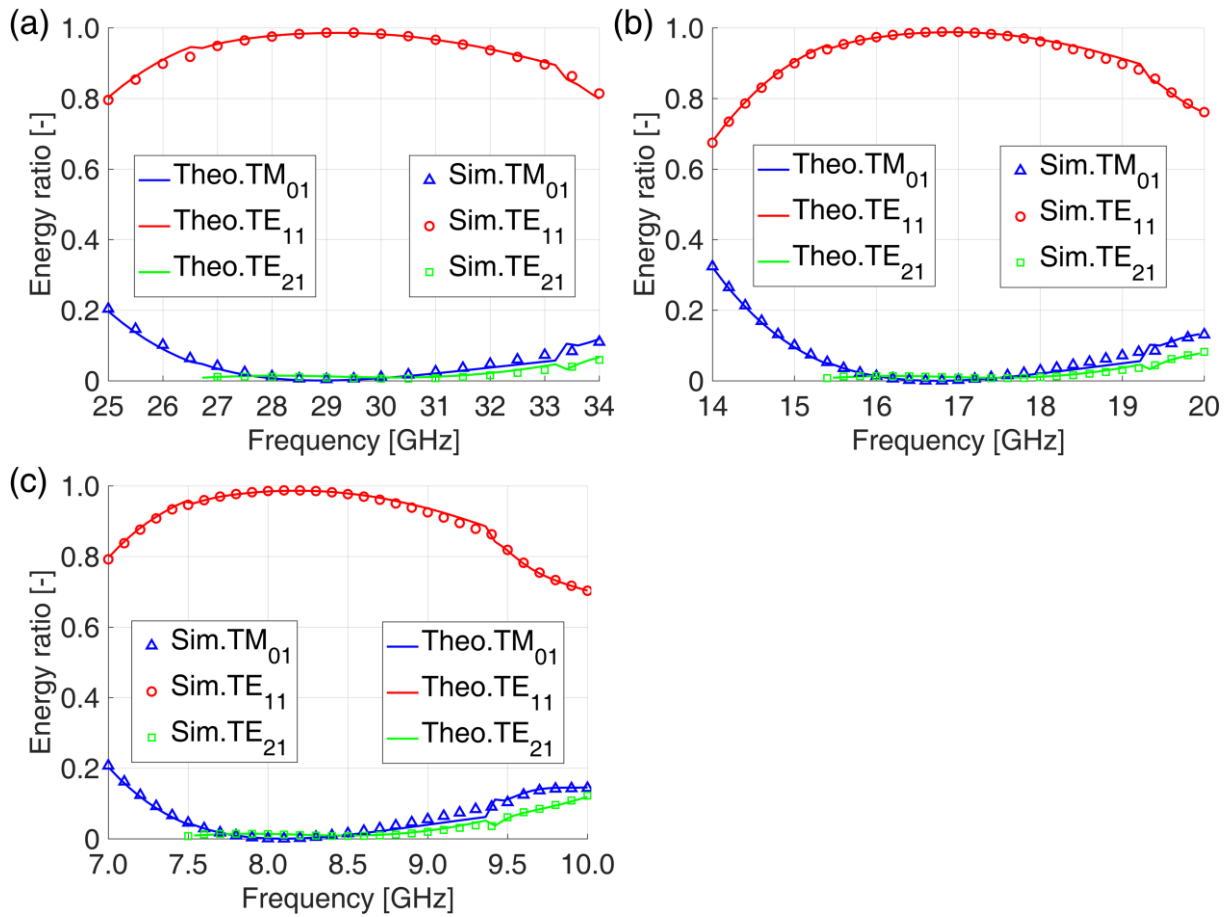


Fig. 4-25 Frequency-domain characteristics of the three TE_{11} mode microwave probes, (a) $D = 11$ mm, (b) $D = 19$ mm, (c) $D = 39$ mm.

The experimental verification was carried out as follows. Figure 4-26(a) illustrates the experimental apparatus. The system is akin to that in Fig. 4-10, while the pipe length was up to 21 – 25 m, by connecting several brass pipes (1.0, 1.5, or 2.0 m in length each) with flange joints. The three TE_{11} mode converters were fabricated based on the results in Table 4-3 and portrayed in Fig. 4-26(b). An axial or a circumferential slit was machined in the middle of a short pipe (200 mm in length, $D = 11, 19,$ and 39 mm) to simulate a crack, and the dimensions of the slits are specified by l_A and θ_C depicted in Fig. 4-26(c). To each inner pipe diameter D , another short pipe of the same length but with no fabricated slit was used for reference. The short pipes were longitudinally situated at different positions (L_S) along the pipes under test, and the slits were positioned at the corresponding sensitive areas in the circumferential direction. Table 4-4 summarizes the experimental parameters. It should be noted that: due to the precision limitations of the mechanical fabrication of bends, the inner diameter of the TM_{01} - TE_{11} mode converter for $D = 19$ mm was actually 18.7 mm, and the 0.3 mm change in diameter led to a 0.4 GHz frequency span shift, compared with the frequency span f_w given in Table 4-3. The reflections were measured as S-parameters (S11) in the frequency domain at 3201 equidistant points. The frequency-domain signals were further processed using the method in Chapter 2 to predicate the location of the slit.

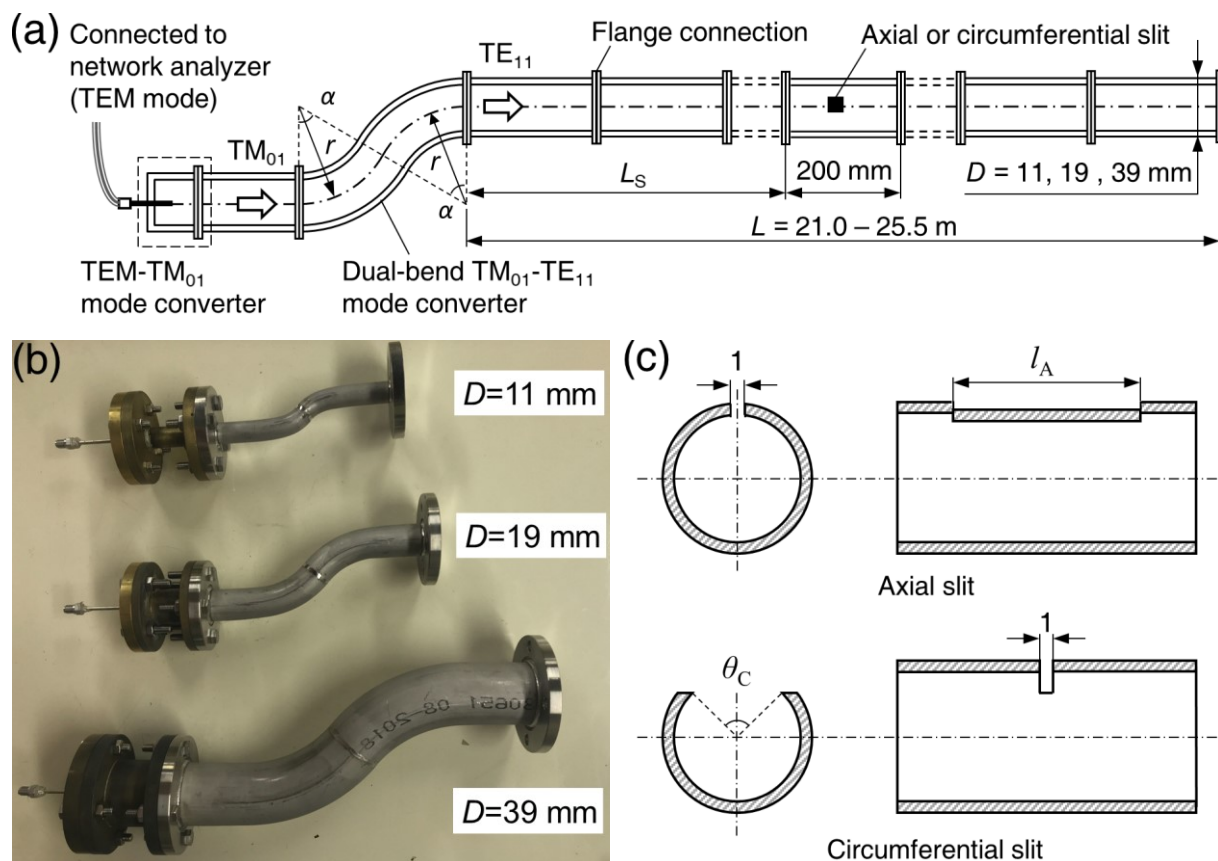


Fig. 4-26 Experimental setup, (a) overview of the experimental system (not to scale), (b) three TE_{11} mode microwave probes, (c) dimensions of the axial and circumferential slits ($D = 11, 19,$ and 39 mm, not to scale).

Table 4-4 Experimental parameters

Parameter (unit)	Inner pipe diameter, D (mm)		
	11	19	39
Frequency span, f (GHz)	26.0 – 33.0	15.4 – 19.4	7.3 – 9.2
Pipe length, L (m)	21.0	22.5	25.5
Short pipe position, L_s (m)	5, 10, 15, 20	4, 8, 12, 16, 20	4, 8, 12, 16, 21, 24
Axial slit length, l_A (mm)	20	10, 20	20
Circumferential slit angular width, θ_C ($^\circ$)	90	45, 90	90

The experimental results are presented in Figs. 4-27 to 4-29. In the case of $D = 39$ mm, as shown in Figs. 4-27(a) and (b), the clear reflection peaks appearing at $L_s = 4, 8, \dots, 24$ m indicate that both the axial and circumferential slits were detected at each location in the pipe. Small reflection peaks with amplitudes smaller than 0.002 were mainly due to the flange connections, while the reflection at 25.5 m corresponds to the pipe end. It should be emphasized that the reflections exhibit clear pulses even though the working bandwidth was not so wide. It reveals that this method is prospectively applicable to the inspections of pipes with larger diameters after further optimizing the frequency-domain characteristic of the TE_{11} mode microwave probe. Likewise, when $D = 19$ mm as shown in Fig. 4-28, explicit reflection

signals can be observed where the axial and circumferential slits were deployed, and detection sensitivity was still very good even though the size of the slits was reduced by 50% as given in Figs. 4-28(c) and (d). When D is 11 mm, the sharp and steep reflection peaks shown in Fig. 4-29(a) suggest that the axial slit can be detected with high sensitivity. However, the result of the circumferential slit shown in Fig. 4-29(b) is more complicated: the reflection from the circumferential slit became smaller, meanwhile, some unknown reflections (highlighted with the dashed-line box) occurred at positions where neither slit nor flange connections existed. However, after comparing the reflection signal of the circumferential slit with that obtained using the reference pipe (no slit) shown in Fig. 4-29(c), it can be seen that the reflections from the circumferential slit (highlighted with solid-line box) at $L_S = 5, 10,$ and 15 m are still discernible for detection, while the unknown reflections may result from some hidden corrosion inside a two-meter long pipe. Moreover, it should be noted that: when the pipe diameter becomes smaller, the working bandwidth increases accordingly, while the reflection signal tends to attenuate more quickly because the sweeping frequency also increases.

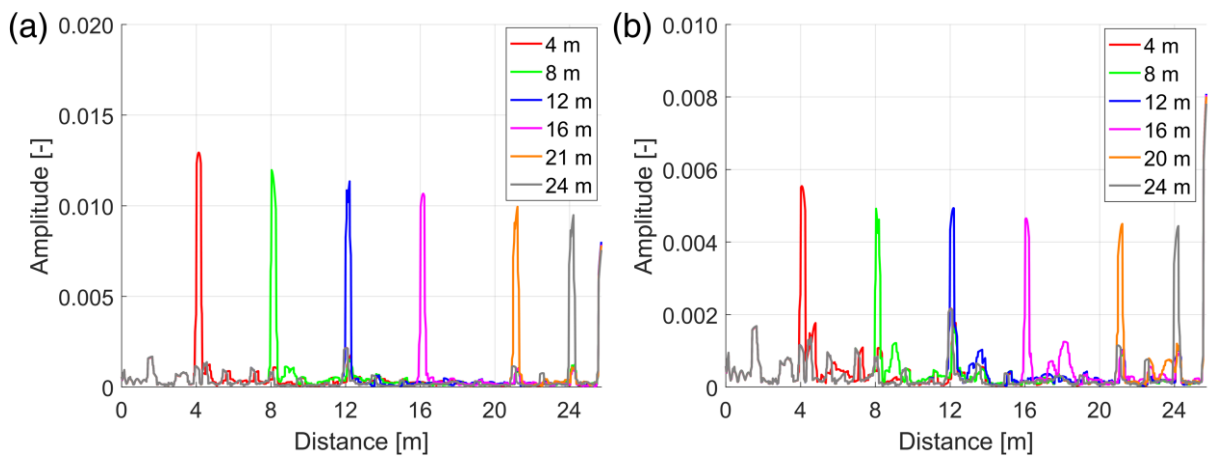
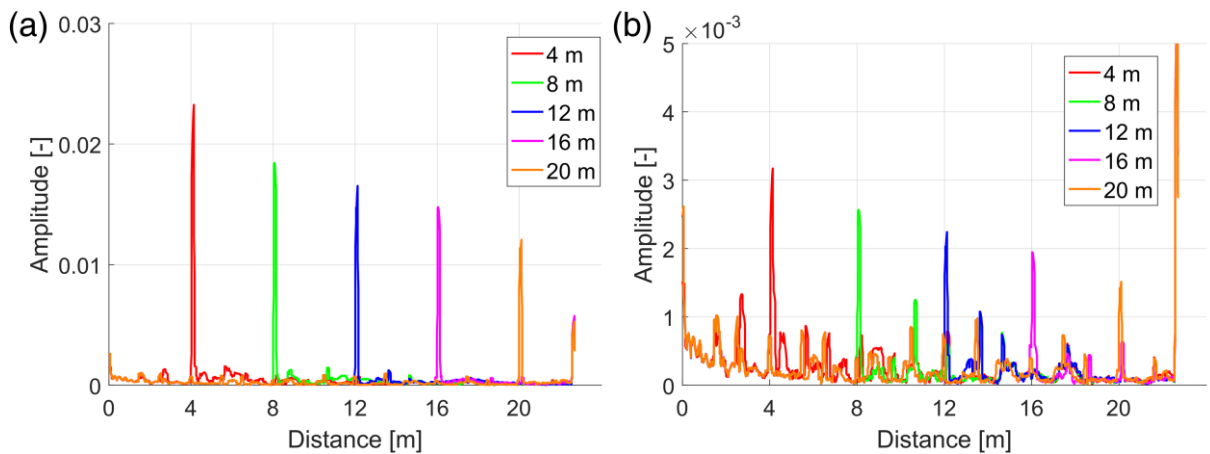


Fig. 4-27 Processed reflection signals ($D=39$ mm) from two slits situated at $L_S= 4, 8, 12, 16, 21$ and 24 m, (a) axial slit with $l_A = 20$ mm, (b) circumferential slit with $\theta_C = 90^\circ$.



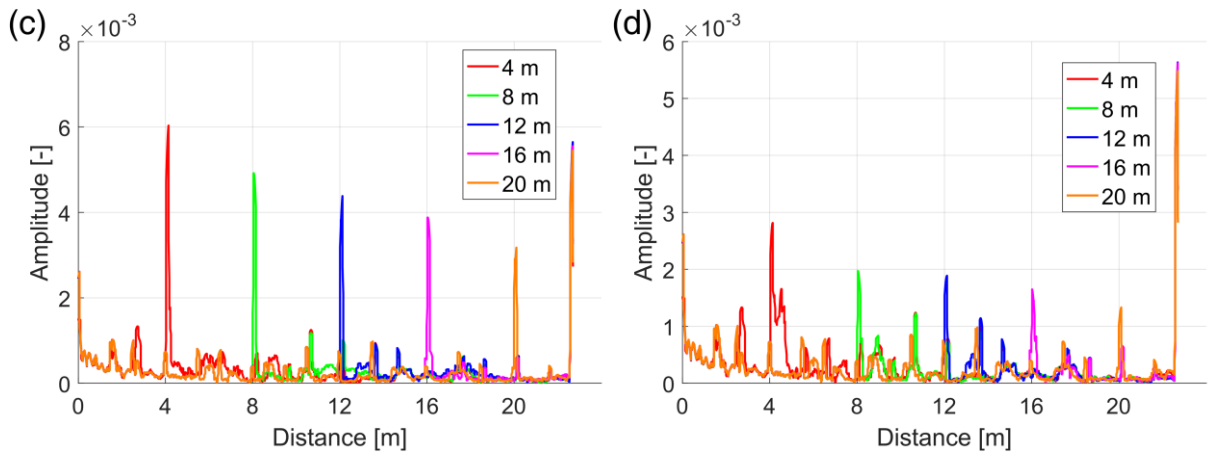


Fig. 4-28 Processed reflection signals ($D=19$ mm) from two slits situated at $L_S=4, 8, 12, 16$ and 20 m, (a) axial slit with $l_A = 20$ mm, (b) circumferential slit with $\theta_C = 90^\circ$, (c) axial slit with $l_A = 10$ mm, (d) circumferential slit with $\theta_C = 45^\circ$.

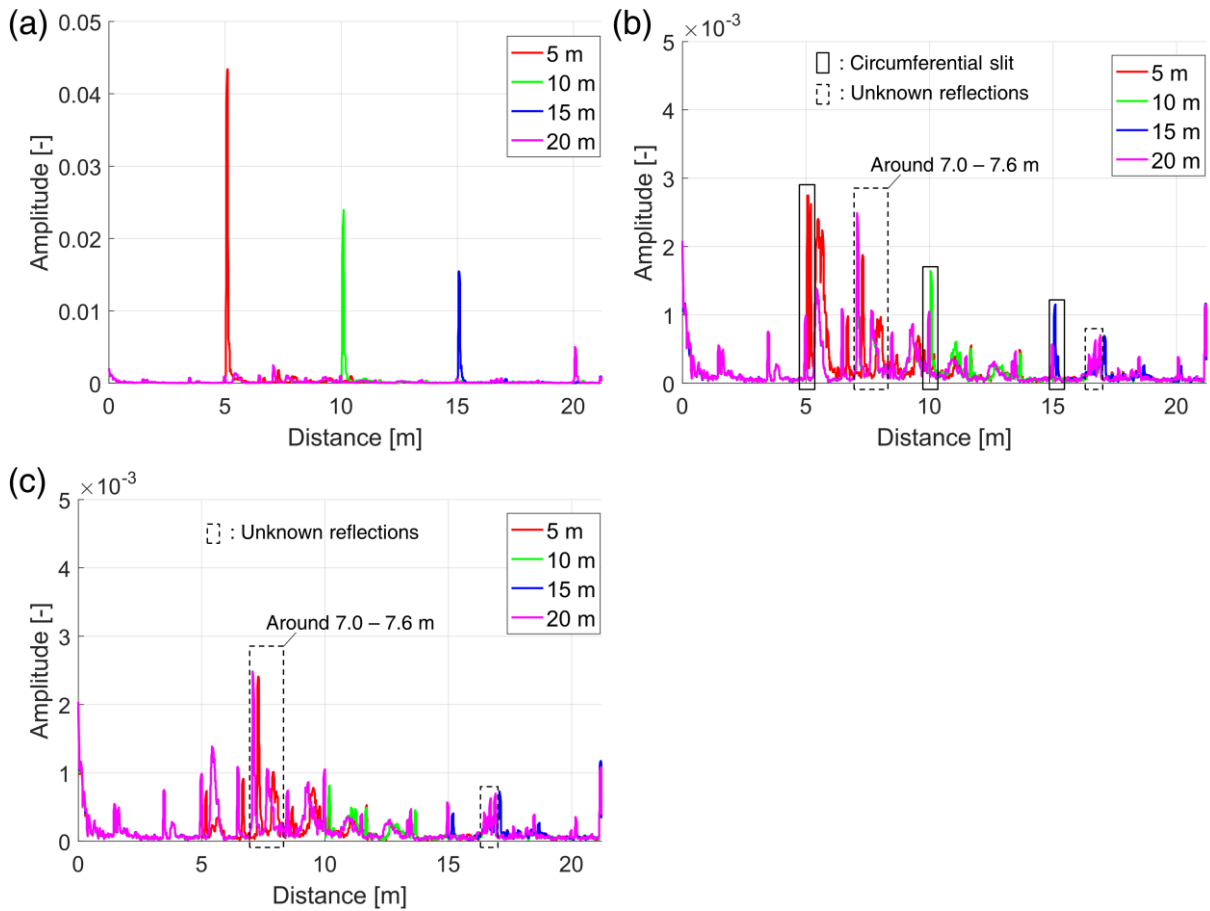


Fig. 4-29 Processed reflection signals ($D = 11$ mm) from two slits situated at $L_S=5, 10, 15$ and 20 m, (a) axial slit with $l_A = 20$ mm, (b) circumferential slit with $\theta_C = 90^\circ$, (c) reference signal.

In addition, to achieve a wider working bandwidth and be applicable to the pipe with a larger inner diameter, the TE_{11} mode microwave probe needs further modifications in structure. An improved TE_{11} mode microwave probe design is shown in Fig. 4-30(a). It is composed of an improved TEM- TM_{01} mode converter proposed in [131] and a ‘non-symmetric’ dual-bend TM_{01} - TE_{11} mode converter whose $r_1 \neq r_2$ and $\alpha_1 \neq \alpha_2$. The improved TEM- TM_{01} mode converter possesses an elliptical incident part, which

can generate TM_{01} mode of very wide span. Please refer to [131] for more information about the detailed design process. Meanwhile, the non-symmetric structured TM_{01} - TE_{11} mode converter is also able to achieve a high conversion efficiency and thus leads to a wider working bandwidth of TE_{11} mode. For instance, the frequency-domain characteristic of the improved TE_{11} mode microwave for $D = 39$ mm is shown in Fig. 4-30(b), and the working frequency span is extended to 8.5 – 15.4 GHz. Here the working bandwidth is 5.9 GHz, which is more than three times of the previous one (1.9 GHz). Furthermore, another improved probe was also designed for $D = 57.5$ mm, and its working bandwidth is 4.6 GHz as shown in Fig. 4-30(c). The above results reveal that the improved TE_{11} mode microwave probe can significantly enhance the frequency-domain characteristic and realize an ultra-wide working bandwidth. Hence, it also shows a great prospect for application to large pipe diameter. The experimental validation should also be performed in future works. Furthermore, when designing a mode converter or microwave probe, we usually expect its working bandwidth to be as wide as possible, or the working bandwidth is the primary metric for probe design. Also in future studies, more factors should be taken into account when designing microwave probes, such as reflection characteristic of the flaws, attenuation of the certain mode, etc.

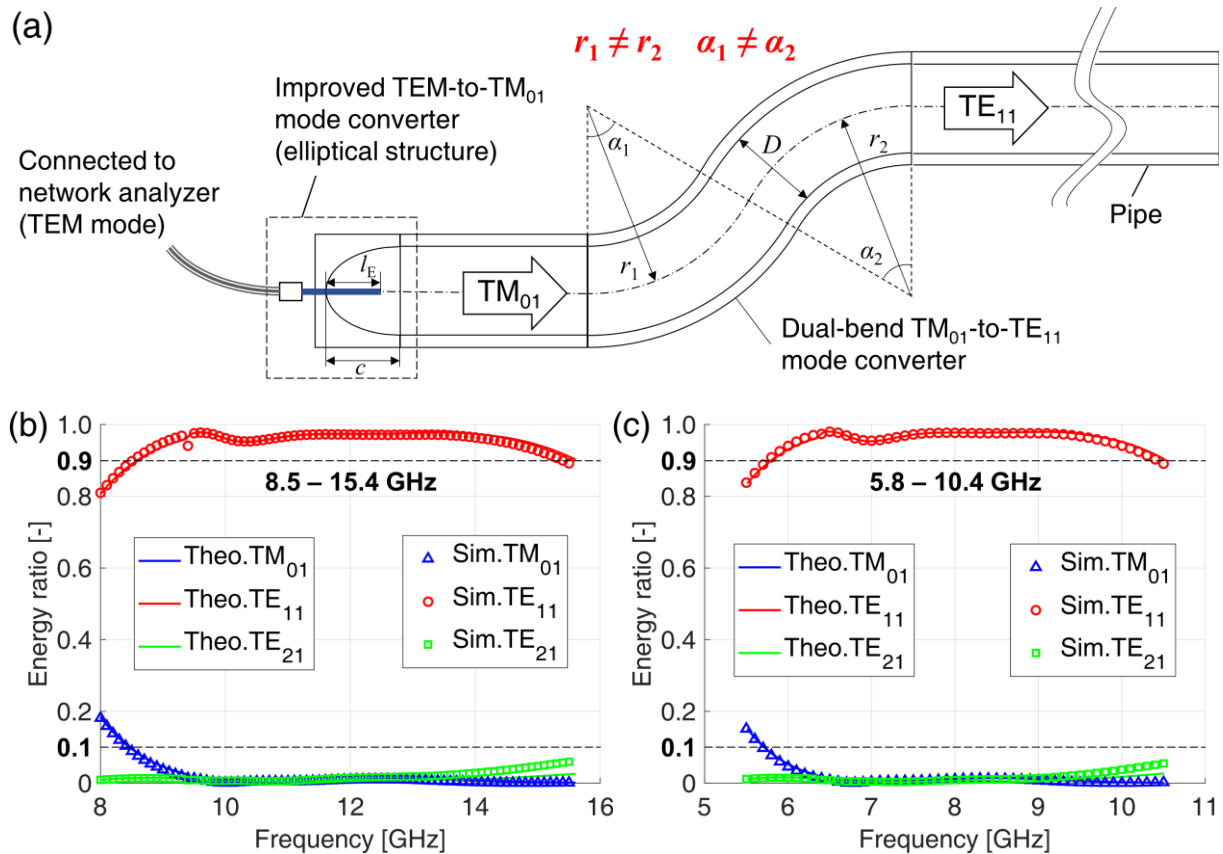


Fig. 4-30 (a) Structure of the improved TE_{11} mode microwave probe; (b) the frequency-domain characteristic of the improved probe with $D = 39$ mm ($c = 30$ mm, $l_E = 7$ mm, $r_1 = 230$ mm, $r_2 = 60$ mm, $\alpha_1 = 26^\circ$, and $\alpha_2 = 60^\circ$); (c) the frequency-domain characteristic of the improved probe with $D = 57.5$ mm ($c = 44.5$ mm, $l_E = 11$ mm, $r_1 = 320$ mm, $r_2 = 150$ mm, $\alpha_1 = 27^\circ$, and $\alpha_2 = 60^\circ$).

4.6 Bend-region crack detection

In Section 4.4, we confirmed that it is feasible to apply the proposed crack-detection method to bent pipe. However, the artificial slit was positioned only at the straight part of the pipe instead of the bend

region, which should also be concerned. Because in the bending process, the pipe wall at extrados of the bend will become thinner and thus more sensitive to corrosion and stress. Therefore, it is of necessity to test the detectability of this method to bend-region crack. In fact, ultrasonic guided waves have been adopted for bend-region inspections [136,137] and revealed some significances, whereas the signal-to-noise ratio of the experimental reflection signals is not adequately high for detection. This section presents an experimental investigation into bend-region crack detection utilizing TE_{11} mode microwaves.

Figure 4-31 illustrates the experimental apparatus. The network analyzer (not shown in the figure) excites TEM mode microwaves, and the TE_{11} mode microwave probe generates linearly-polarized TE_{11} mode and emits it into the bent pipe for testing. The bent pipe system consisted of two 1 m pipes, two 0.5 m pipes, and a bend under test. They were connected with a ferrule or flange pipe fitting. The material of the bend and pipes was stainless steel (SUS304). An axial or circumferential slit was machined at the extrados of the bend to simulate the bend-region crack, because the wall thickness of the extrados was thinner than other part of the bend, and the flow-accelerated corrosion [138,139] or liquid droplet impingement [140-141] also tends to occur at the extrados. The size and angular position of the slit were denoted by the angles θ_A/θ_C and δ , respectively, as shown in the dash line box in the figure. In total, three bends with two inner diameters ($D = 23.0$ and 35.7 mm) were tested in the experiment. The dimensions of the bends (curvature radius r and bend angle α), along with the size and angular positions of the machined slits, are itemized in Table 4-5. Meanwhile, the flawless bends were also tested in the experiment for reference, and their photograph is displayed in Fig. 4-32.

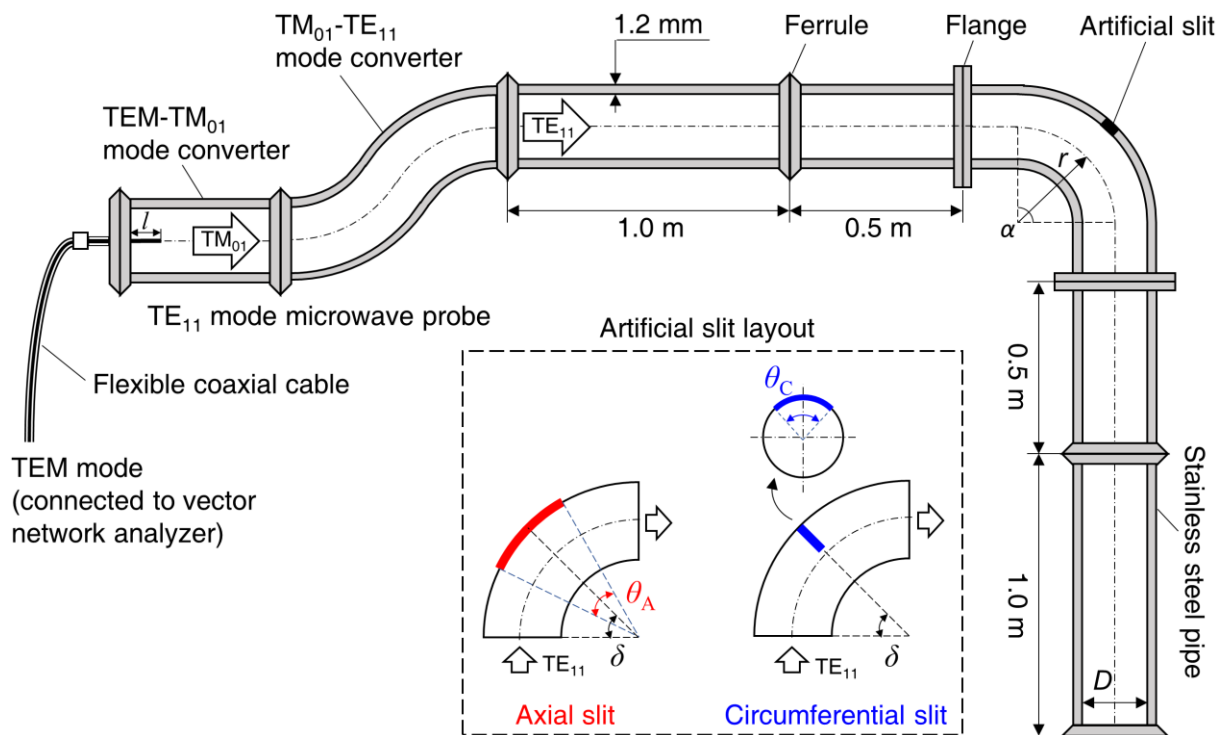


Fig. 4-31 Experimental apparatus (not to scale).

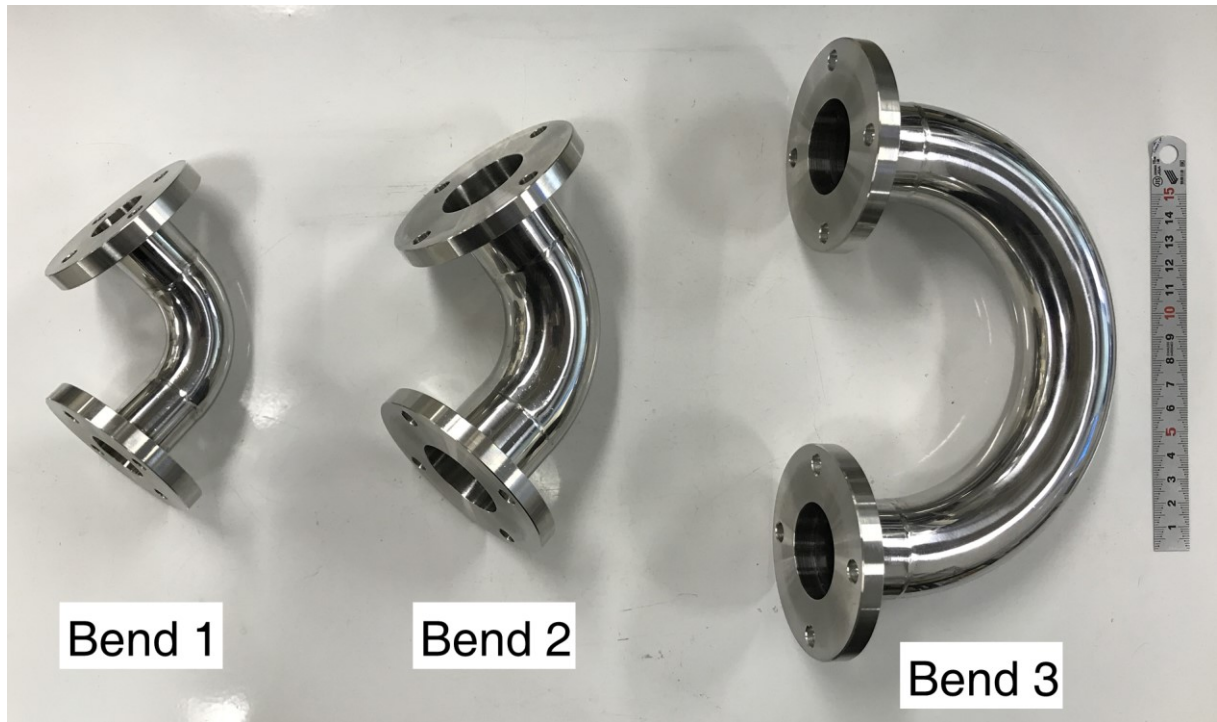


Fig. 4-32 Three types of bends (without slit) tested in the experiment.

Table 4-5 Experimental parameters.

Parameter (unit)	Bend 1	Bend 2	Bend 3
D (mm)	23.0	35.7	35.7
r (mm)	34.0	49.0	76.2
r/D (-)	1.478	1.373	2.134
α ($^\circ$)	90	90	180
θ_A ($^\circ$)	10, 20, 30	30	30
θ_C ($^\circ$)	30, 60, 90	90	90
δ ($^\circ$)	20, 45, 70	20, 45, 70	45, 90, 135
l (mm)	6	9	9
f_W (GHz)	12.4–15.9	8.5–10.6	8.5–10.6
f_{CTM01} (GHz)	9.98	6.43	6.43
f_W/f_{CTM01} (-)	1.24–1.59	1.32–1.65	1.32–1.65

Two TE_{11} mode microwave probes were designed for testing. The designing process of TE_{11} mode microwave probe has been depicted in Section 4. 2, and the photograph as well as the dimensions of the two TE_{11} mode microwave probes is shown in Fig. 4-33. The specifications of the two probes such as working frequency spans f_W , are also listed in Table 4-5. The parameter f_W/f_{CTM01} refers to the working frequency span normalized by the cut-off frequency of TM_{01} mode f_{CTM01} . Moreover, the TE_{11} mode microwave probe was orthogonally deployed to achieve the horizontal and vertical polarizations of the TE_{11} mode microwaves, and thereby to realize thorough detection sensitivity against both axial and

circumferential cracks.

The reflection coefficients were measured in the frequency domain as S-parameters, over the working frequency span of each TE₁₁ mode microwave probe. A total of 3201 frequency points with equal intervals were sampled over the working frequency span of each microwave probe. Every measurement was conducted 30 times and the average result was recorded. The measured frequency-domain signals were processed using the signal-processing method in Chapter 2.

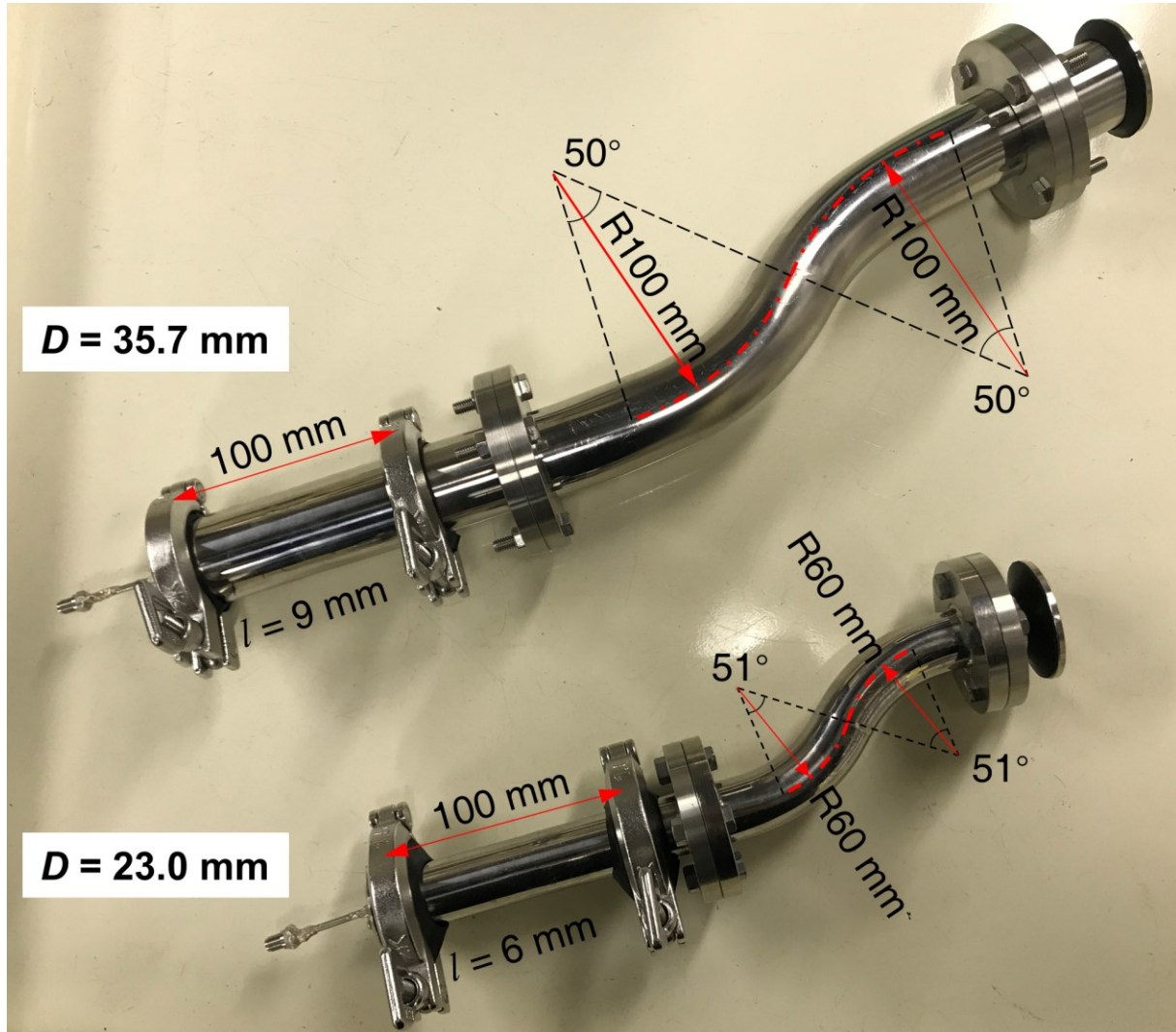


Fig. 4-33 Two TE₁₁ mode microwave probes and their dimensions. (Note: The inner diameter of the TM₀₁-TE₁₁ mode converter for $D = 35.7$ mm was 35.0 mm, due to the precision limitations of mechanical fabrication. Other dimensional parameters, such as the curvature radius and bend angle were also optimized accordingly.)

The processed reflection signals of the three tested bends are exhibited in Figs. 4-34 to 4-36, respectively. It should be noted that the reflection signals of the axial slits shown in each figure were obtained under vertical polarization of TE₁₁ mode microwaves, while those of the circumferential slits were obtained under horizontal polarization, as stated in the preceding context. Correspondingly, the reflection signals under ‘insensitive’ polarizations show very small reflections from slits, and thereby are omitted here.

Firstly, in Figs.4-34(a) and (b), the small reflections at 0 m and ~3 m correspond to the inlet of the pipe and the pipe end, respectively. Meanwhile, the small reflection at 1 m and ~2.2 m resulted from the

ferrule pipe fittings. At around 1.5 m, where the bend was deployed, the large and noticeable reflection peaks indicate that both the axial and circumferential slits are detectable. Moreover, it is evident that the reflections from the slits at different angular positions of the bend δ also show different peak locations (predicted distances) and peak amplitudes. This is because the mode conversion at the bend, which affects the amplitude and the phase of the TE_{11} mode microwaves, is dependent on δ . Interestingly, comparing Figs. 4-34(c) and (d), the reflection from a larger axial slit has a larger peak amplitude as expected, whereas the reflection from a larger circumferential slit ($\theta_C = 90^\circ$) is lower than that from a smaller circumferential slit ($\theta_C = 60^\circ$). In the case of bend 2, as shown in Fig. 4-35, the shape of the reflections from the axial slits appears to be a bit similar to that in Fig. 4-34(a), whereas the shape of the reflections from the circumferential slits is not similar to that in Fig. 4-34(b). One probable explanation is that the normalized working frequency spans f_w/f_{CTM01} for bend 1 and bend 2 are not that consistent and the dimensions of the slits are also different. In Fig. 4-36 for bend 3, the reflection peaks for $\delta = 45^\circ, 90^\circ$, and 135° can be clearly distinguished, as the bend itself is long. Meanwhile, the reflection signals are dissimilar from those in Fig. 4-35 because the r/D of the two bends or δ are different. Furthermore, it turns out that the axial slit situated in the middle of the bend usually leads to the largest reflection, while the reflection signals of the circumferential slits are rather complicated. Nevertheless, it is explicit that the peak location of reflection is dependent on the angular position δ , while the peak amplitude of reflection is affected by the mode conversion at the bend. Moreover, if the slits were machined at the intrados, the detection sensitivity should not be affected as the polarization of TE_{11} mode remains unchanged when it propagates through a bend.

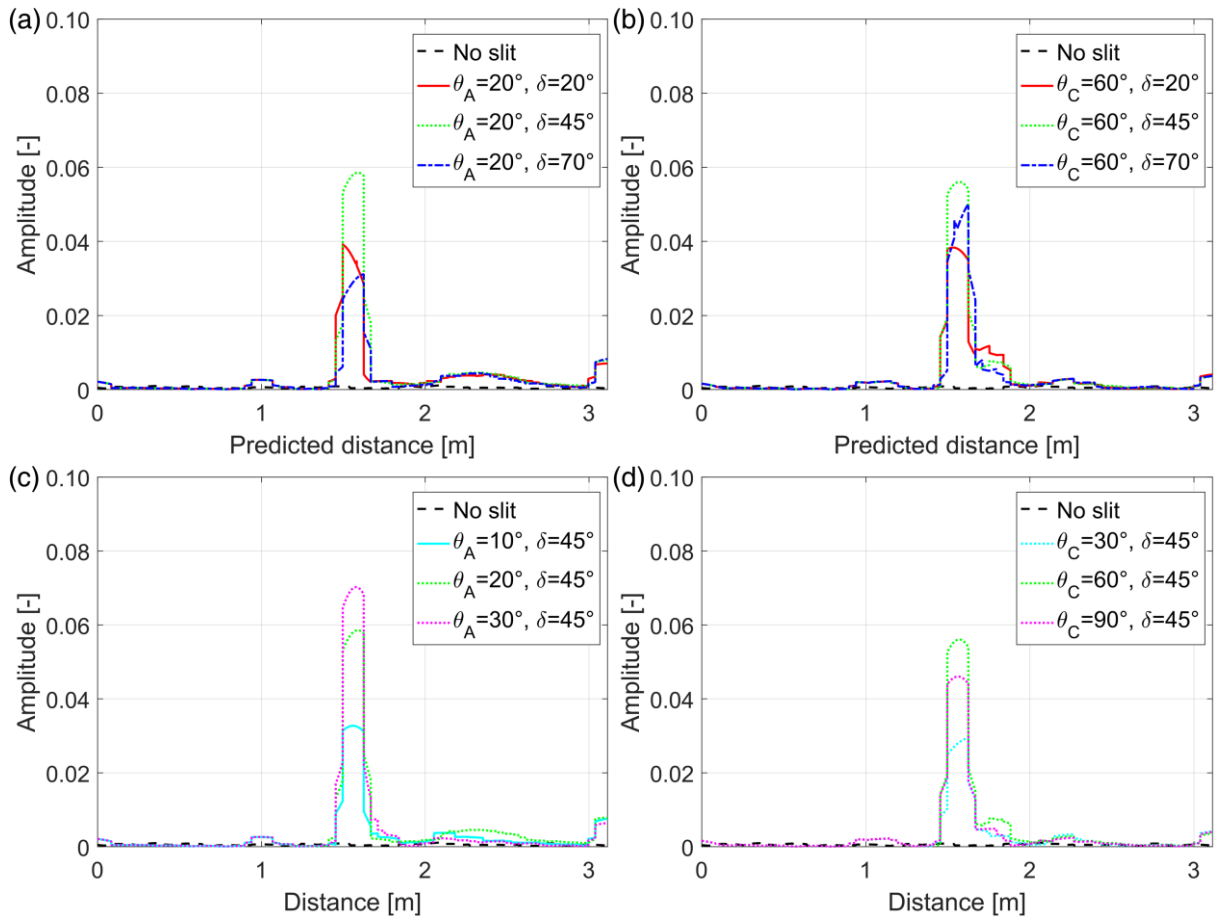


Fig. 4-34 Processed reflection signals of bend 1 ($D = 23.0$ mm, $r/D = 1.478$, $\alpha = 90^\circ$, $f_w/f_{CTM01} = 1.24$ – 1.59), (a) axial slit with $\theta_A = 20^\circ$, (b) circumferential slit with $\theta_C = 60^\circ$, (c) axial slit at $\delta = 45^\circ$, (d) circumferential slit at $\delta = 45^\circ$.

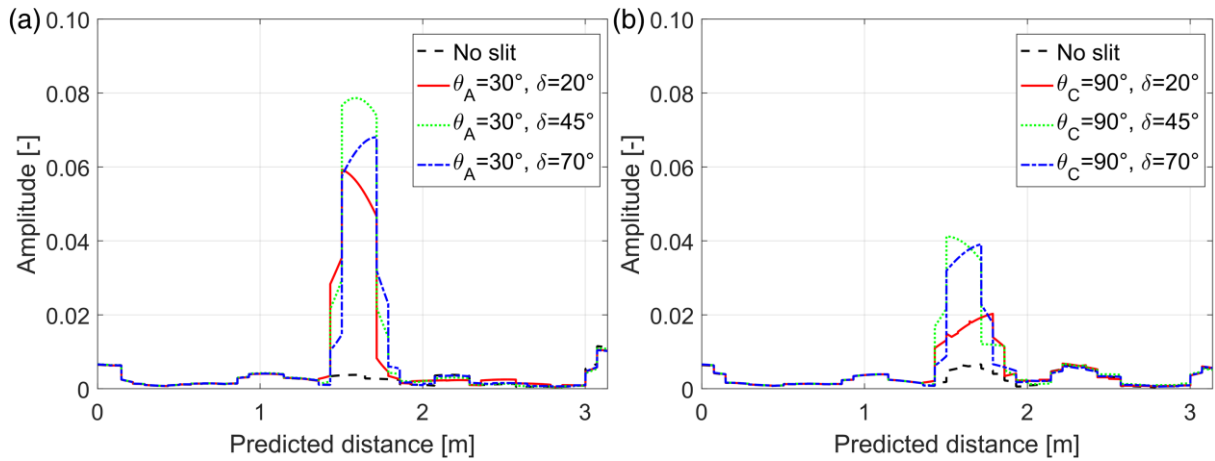


Fig. 4-35 Processed reflection signals of bend 2 ($D = 35.7$ mm, $r/D = 1.373$, $\alpha = 90^\circ$, $f_w/f_{CTM01} = 1.32-1.65$), (a) axial, (b) circumferential slit.

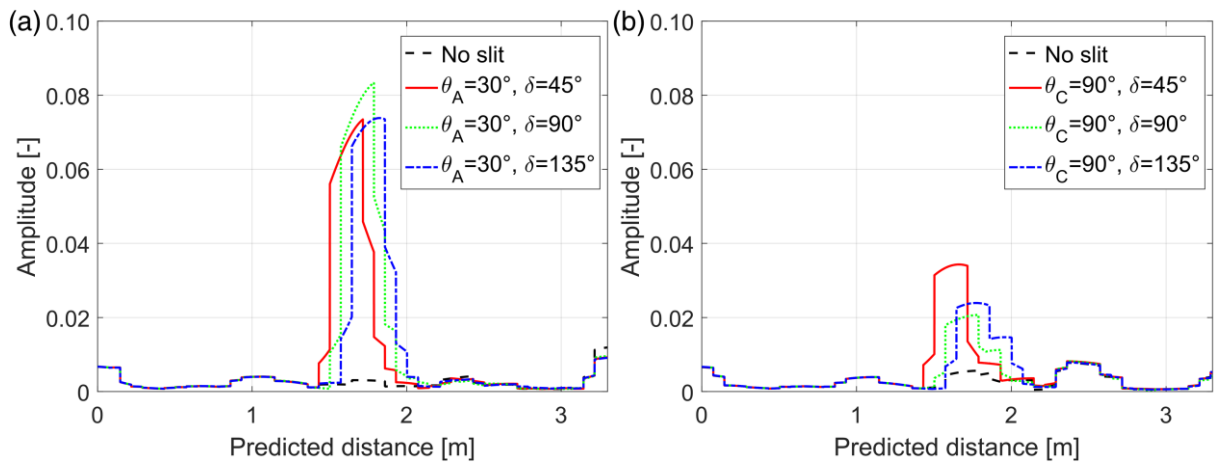


Fig. 4-36 Processed reflection signals of bend 3 ($D = 35.7$ mm, $r/D = 2.134$, $\alpha = 180^\circ$, $f_w/f_{CTM01} = 1.32-1.65$), (a) axial, (b) circumferential slit.

Based on the results above, we have preliminarily confirmed the efficacy of using TE_{11} mode microwaves in detecting bend-region cracks. The reflection from either axial or circumferential slit is discernible for detection, and the peak location of reflection signal basically reveals the slit's angular position δ . Nevertheless, the relevance between the peak amplitude of reflection and mode conversion at the bend should be further investigated and clarified in the future.

4.7 Supplementary discussions on TE_{11} mode

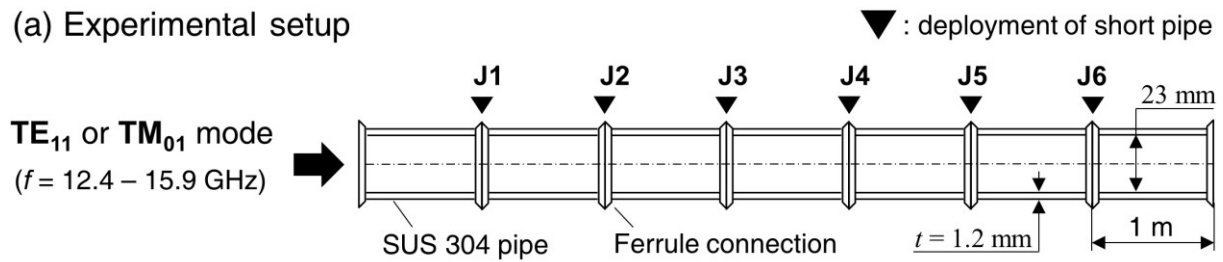
4.7.1 Detection of pipe wall thinning using TE_{11} mode

The main contents of this chapter are about crack detection using a TE_{11} mode microwave probe, while we also tested the detectability of TE_{11} mode towards pipe wall thinning through experiment. The experiment system is shown below as Fig. 4-37, in which the experimental parameters are basically identical to those of Fig. 4-10 in Section 4.3 but the slit was replaced by pipe wall thinning. The TE_{11} mode microwave probe used here was also the same as the one in Section 4.3. A short pipe with a part of full-circumferential wall thinning in its longitudinal direction was used to emulate the pipe wall

thinning flaw, and its dimensions are illustrated in Fig. 4-37(c). The short pipe was situated at each ferrule joint of the pipe, as J1, J2, ..., J6, which is 1 m, 2 m, ..., 6 m distant from the TE₁₁ mode microwave probe. Meanwhile, a flawless short pipe was also used in the test as reference. The TE₁₁ mode microwave probe was deployed horizontally and vertically for orthogonal polarizations. In addition, the ‘self-integrating’ TM₀₁ mode with the same frequency range was also used for comparison.

The experimental results are shown in Fig. 4-38 to 4-40. From the comparison between Figs. 4-38 (a) and (b), we can see the pipe wall thinning was detectable by the horizontally-polarized TE₁₁ mode while the signal-noise ratio was low. The reflection signals of vertical polarization in Fig. 4-39 show similar consequences to Fig. 4-38. However, in Fig. 4-40 where the results of TM₀₁ mode are presented, large and clearer reflection peak at each joint can be observed and a high signal-to-noise ratio is achieved. These results reveal that TM₀₁ mode is more effective than TE₁₁ mode in detecting pipe wall thinning. Combining the results in Section 4.4, it can be concluded that utilizing TE₁₁ mode in conjunction with the self-integrating TM₀₁ mode can detect both pipe wall thinning as well as cracks, and thereby achieve thorough detection capability.

(a) Experimental setup



(b) TE₁₁ mode microwave probe ($D = 23$ mm)



(c) Short pipe

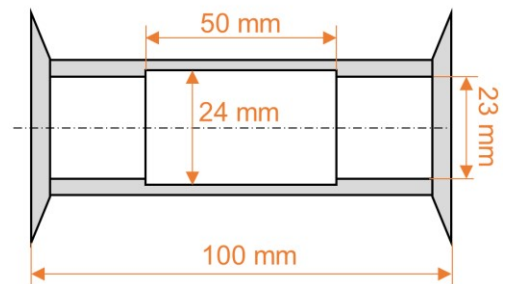


Fig. 4-37 Experimental apparatus (not to scale).

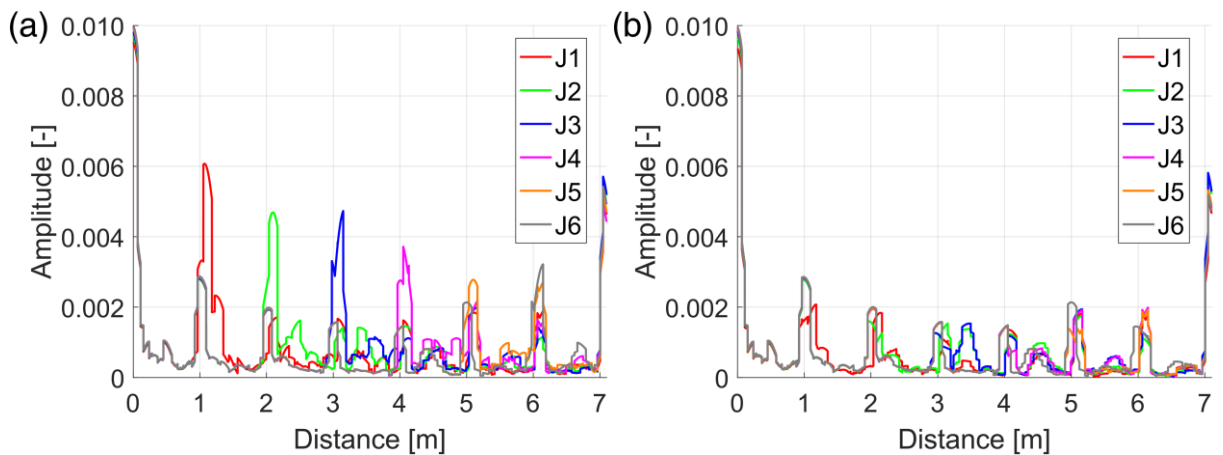


Fig. 4-38 Processed reflection signals of TE₁₁ mode under horizontal polarization, (a) with pipe wall thinning, (b) without pipe wall thinning.

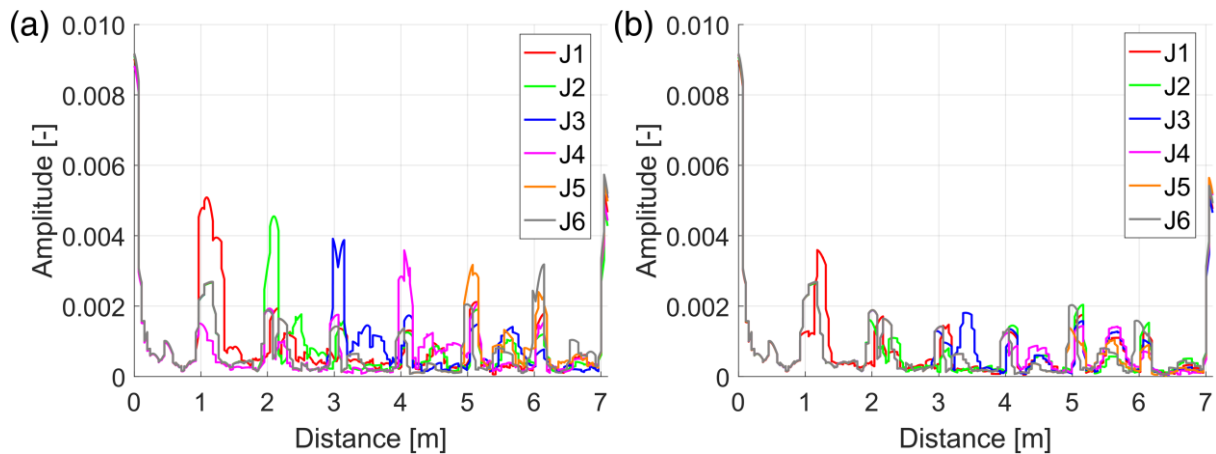


Fig. 4-39 Processed reflection signals of TE₁₁ mode under vertical polarization, (a) with pipe wall thinning, (b) without pipe wall thinning.

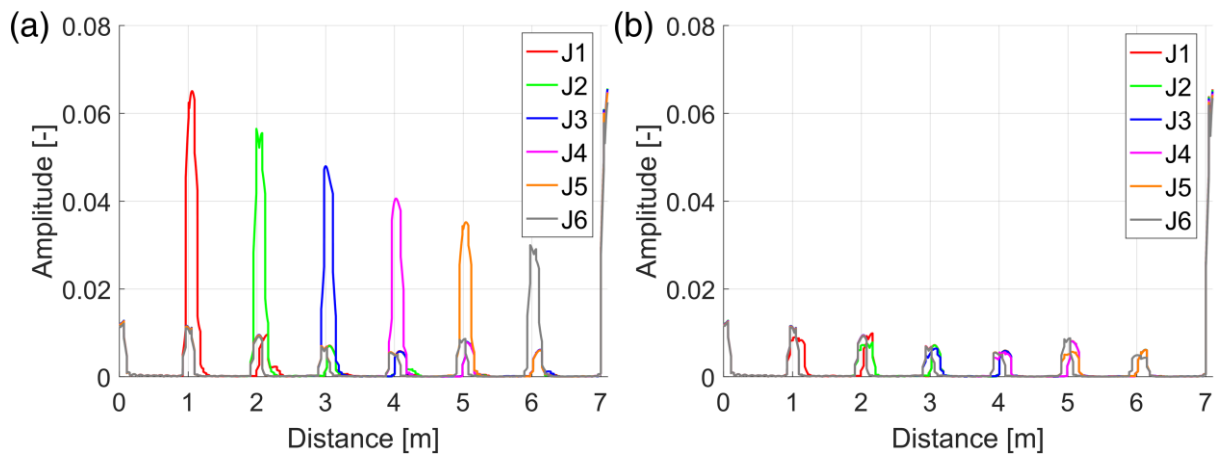


Fig. 4-40 Processed reflection signals of TM₀₁ mode, (a) with pipe wall thinning, (b) without pipe wall thinning.

4.7.2 Detection of non-penetrant slit

In the previous sections, through-wall or penetrant slits were used to emulate cracks. However, these artificial slits are usually too large in size or visibly observable, so a more practical flaw close to the real crack should be introduced.

To address this concern, we prepared two non-penetrant axial slits with different longitudinal lengths for testing. The testing system and the dimensions of the slits are portrayed in Fig. 4-41. The TE₁₁ mode microwave probe with an inner diameter of 19 mm in Section 4.5 was employed for detection. The polarization was set to be horizontal. A short pipe with an axial non-penetrant slit fabricated on its inner surface was deployed in a 4 m brass pipe, 3 m relative to the probe. The lengths of the two slits were 10 and 30 mm, while their width and depth were 1 mm. In addition, a short pipe without any slit was used for comparison.

The time-domain reflection signals are shown in Fig. 4-42. The reflection from the 30 mm non-penetrant slit is clearly observable, while that from the 10 mm slit is a little bit vague on account for some undetermined reflections. Meanwhile, the relevance between detection sensitivity and polarization was also confirmed as the slit positioned at insensitive area was undetectable. Compared with the amplitude of reflection from through-wall slit in Section 4.5, the reflection from the non-penetrant slit

is smaller in amplitude, but still noticeable. Although this is a very preliminary test using non-penetrant slit, the detectability of TE₁₁ mode against cracks and other conclusions in previous sections remain to be unchanged and valid. Meanwhile, more endeavors should be made to further study crack-detection using TE₁₁ mode, e.g., by introducing non-through circumferential slits or real cracks.

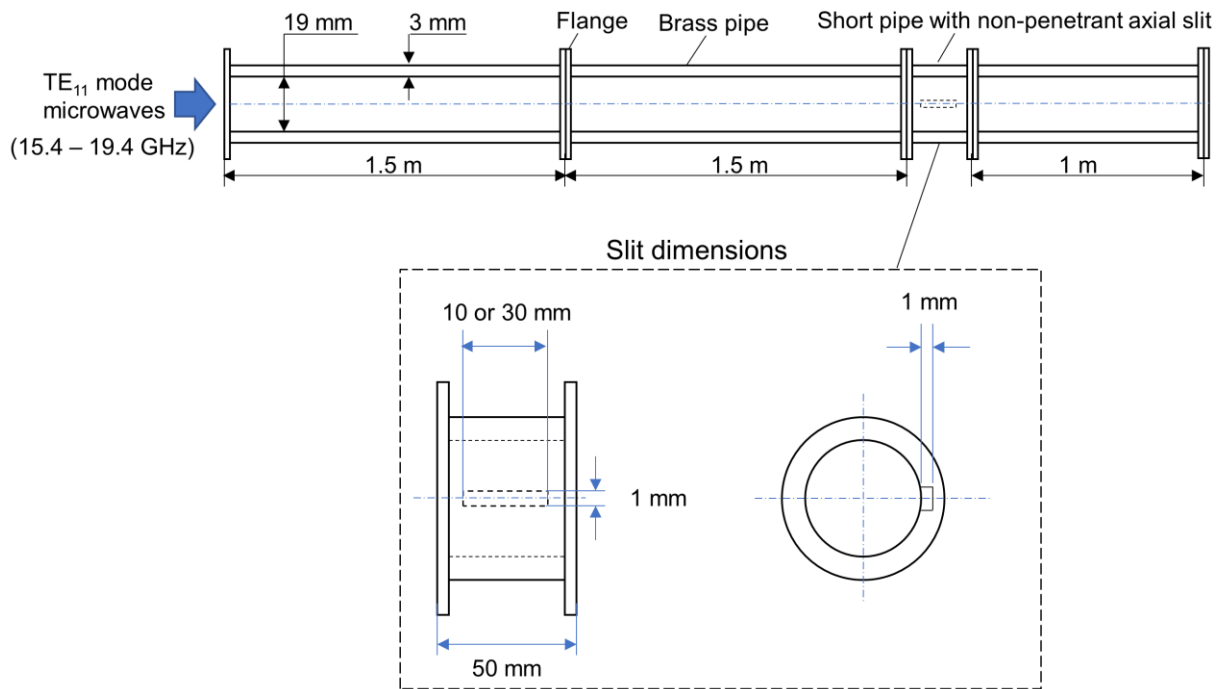


Fig. 4-41 Testing system and dimensions of the non-penetrant axial slit.

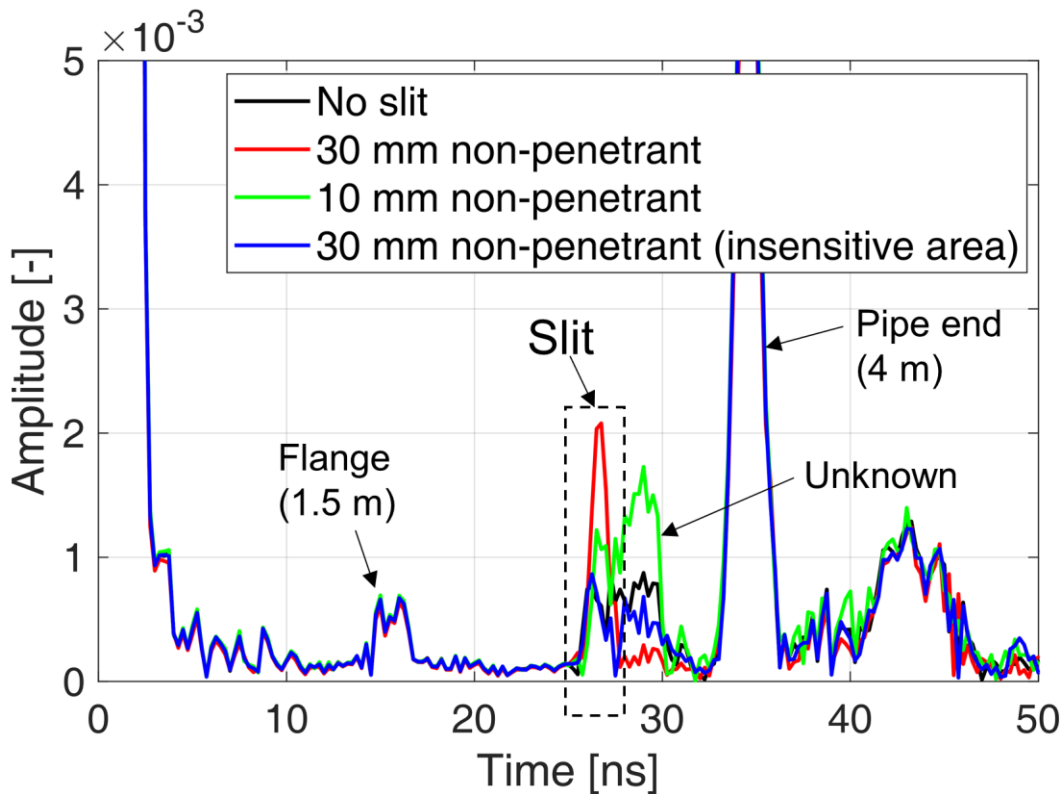


Fig. 4-42 Reflection signal of non-penetrant axial slits.

4.8 Summary

In this chapter, a crack-detection method using a TE_{11} mode microwave probe has been developed, and it can be applied for inspection of bent pipes with open-end. Firstly, the detection sensitivity against cracks with different orientations was discussed based on the theory of surface current density on the inner surface of the pipe, and the linearly-polarized TE_{11} mode exhibits the potential of being sensitive to both axial and circumferential cracks in a pipe. A systematical method is proposed to design the TE_{11} mode microwave probe for a designated inner pipe diameter, and the experimental verification also suggests that either axial or circumferential slit simulating crack can be detected by jointly analyzing the reflection signals under two orthogonal polarizations (horizontal and vertical). This method was also confirmed to be effective for inspecting bent pipes, while the dependence of mode conversion at the bend on the polarization of TE_{11} mode should also be taken into account. Furthermore, the application to long-range pipe inspection and multiple inner pipe diameters further proved the versatility of this method, and an improved TE_{11} mode microwave probe was also proposed to achieve a wide working bandwidth and applicability to large diameter pipes. Next, the effectiveness in detecting bend-region cracks was also preliminary verified. The angular position of the bend-region crack could be determined from the peak locations of reflection signals, while more efforts should be made for investigating the correlation between mode conversion at the bend and peak amplitude of reflections. Finally, the detection of pipe wall thinning and non-penetrant slit using TE_{11} mode were studied through experiment.

Chapter 5 Side-incident probe design for directional inspection of closed piping systems

In this Chapter, a dual-port, side-incident microwave probe is designed for directional inspection of closed piping systems. Two types of probes (LJ and JL) are proposed to transmit TM_{01} and TM_{02} mode microwaves into the pipe under test to opposite directions. Numerical simulation is conducted to determine the dimensional parameters affecting the transmission characteristic of the probe, while the probe's dimensions are also optimized based on the simulation results. Besides, the simulation results also confirm the adaptability of the proposed probe to other inner pipe diameters. Experiment is carried out to test and verify the effectiveness of the designed probe in directional pipe inspection.

5.1 Side-incident method

The side-incident method is proposed given that the pipe end may not always be open for probe insertion, especially in some complicated closed piping systems. Besides, if there are some valves, orifices, or other pipe components that disturb the transmission of microwaves, using the side-incident enables a more flexible way for probe deployment. One former study proposed a single-port, side-incident microwave probe [111] to resolve this problem. The structure of the probe is shown in Fig. 5-1(a). The TEM mode microwaves are emitted to the pipe from the pipe's sidewall through a bent semi-rigid coaxial cable inserted into the pipe. TM mode microwaves are mainly generated inside the pipe. The direction of the microwave propagation inside the pipe can be altered by specifically selecting the frequency range as shown in Figs. 5-1(b) and (c). When the frequency ranges from 18.5 GHz to 25.5 GHz, the TM_{01} mode microwaves mainly propagate inside the pipe to the right direction; when the frequency ranges from 30 GHz to 37 GHz, the TM_{02} mode microwaves mainly propagate inside the pipe to the left direction. Experiment was also conducted to verify the directional characteristic of the probe, and the result agreed with the simulations. However, only a limited number of numerical simulations were performed in the previous study, so the probe was not adequately optimized to obtain better mode purity and transmission directivity, as the dimensional parameters influencing the transmission characteristic of the probe were not completely clarified. For instance, as highlighted by the black arrow in Fig. 5-1(b), a portion of the TM_{01} mode microwaves (mainly transmitted to the right) is also transmitted to the left side, which could lead to a misjudgment or interference in analyzing the reflection signals. Moreover, only the probe with an inner diameter of 19 mm was studied and developed in that study, while the practicability of applying this side-incident method to other diameters was not discussed.

To address the above issues, we proposed a dual-port, side-incident microwave probe that can realize the directional dual-way pipe inspection. The rest of this chapter is organized as follows. In Section 5.2, numerical simulations are conducted for both single-port and dual-port, side-incident probes. First, the dimensional parameters influencing the transmission characteristics of the single-port probe is investigated. Then two types of dual-port, side-incident probes are proposed and optimized to acquire good mode purity and transmission directivity. Moreover, the adaptability of this method to other inner

pipe diameters are also studied. In Section 5.3, experimental verification is carried out to confirm the effectiveness of the proposed dual-port probe by specifically detecting flaws at different positions in pipes, and the applicability of this side-incident method to other inner pipe diameters is examined. The conclusions and discussions are presented in Section 5.4.

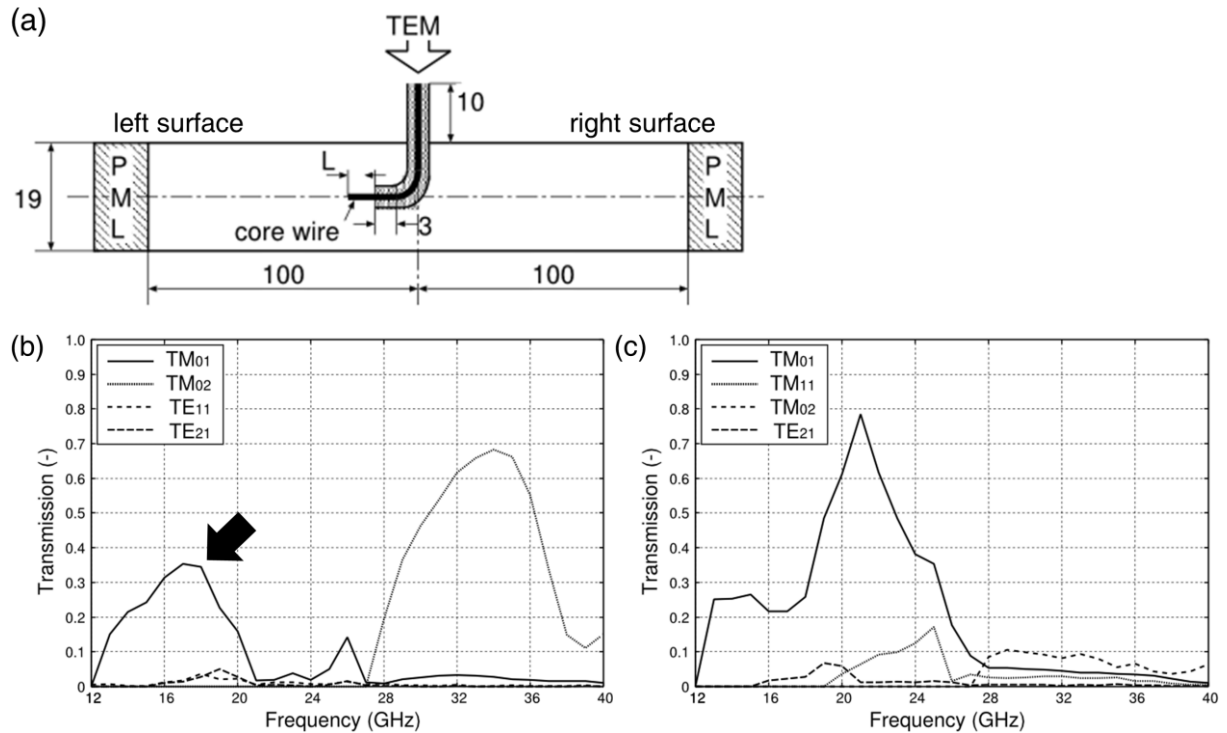


Fig. 5-1 Single-port, side-incident microwave probe, (a) structure (not to scale), (b) microwave modes transmitted to the left surface, and (c) microwave modes transmitted to the right surface. [111]

5.2 Numerical simulation

In this section, three-dimensional numerical simulations are carried out for both the previous single-port probe and the newly proposed dual-port probe. The simulation environment has been introduced in Chapter 2. The single-port probe is simulated to investigate the dimensional parameters affecting the transmission characteristic of the probe and thus to obtain an optimized result for the single-way microwave transmission. The simulation for the dual-port probe is conducted based on the results of the single-port probe simulation to evaluate the mode purity and transmission directivity of the proposed dual-port model in two directions. Furthermore, the feasibility of applying the side-incident method to other pipe diameters is also discussed.

5.2.1 Single-port, side-incident probe

The geometrical model of the single-port, side-incident shown in Fig. 5-2 is basically the same as the model in Fig. 5-1(a), which comprises a cylindrical air entity as the interior of the pipe and a side-inserted semi-rigid coaxial cable. The diameter of the cable core wire was 0.8 mm, while the inner and outer diameters of the outer layer of the cable were 2.2 mm and 2.9 mm [143], respectively. A dielectric insulator was filled between the core wire and the outer layer of the cable, and its relative permittivity was 1.687. The inner diameter of the pipe was set to 19 mm, and the perfectly matched layer (PML) was positioned at each end of the pipe to simulate the infinite space. The boundary conditions of the pipe

wall and the surface of the cable were defined as the perfect electric conductor. The TEM mode microwaves were excited at the port outside the pipe, and the converted microwaves were transmitted to two directions in the pipe. Two virtual surfaces were situated at the left side and the right side of the model, 100 mm relative to the inserted cable. The two surfaces were defined as the left surface and right surface, highlighted with the blue and red color in the figure, respectively. The domain-backed slit condition was applied to these two surfaces, and the transmission characteristic of each mode (S-parameter 21) was evaluated on both left and right surfaces. More specifically, the energy ratio of each mode was evaluated by normalizing the transmitted energy with the inputted energy of TEM mode. The labels (1) and (2) in the figure denote the ports 1 and 2 for evaluating S-parameter 21, respectively. Some dimensional parameters of the probe were chosen and altered in the simulation to investigate their effects on the transmission characteristic of the probe, including the curvature radius of the bent cable r_C , the exposed length of the cable core wire l_E , the straight portion cable length l_S , and the outer cable length l_V . Table 5-1 summarizes the values of the investigated parameters in the numerical simulation. The sweeping frequency span f ranged from 12 GHz to 43 GHz, with a step of 0.5 GHz.

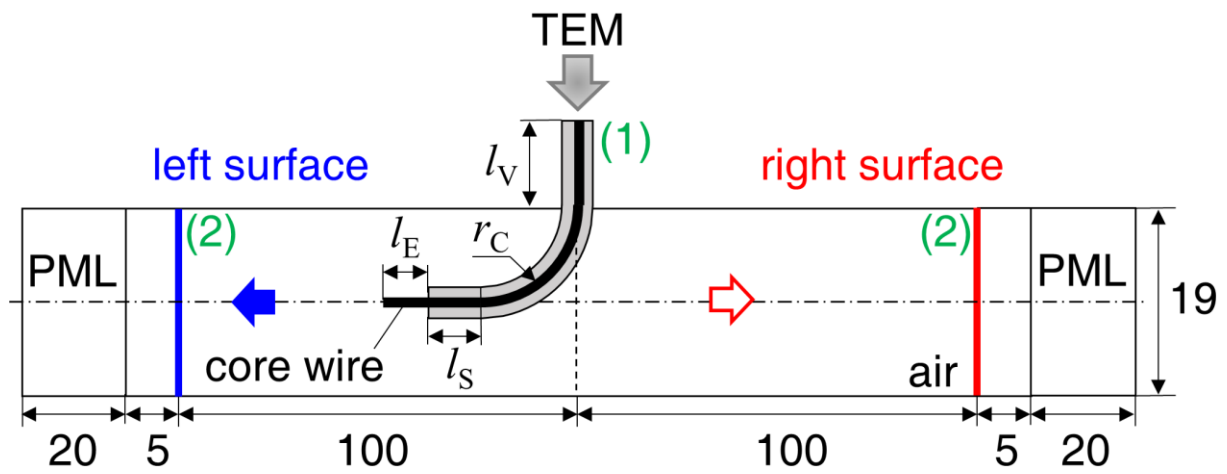


Fig. 5-2 Geometrical model of the single-port, side-incident probe for simulation (unit: mm, not to scale).

Table 5-1 Simulation parameters of the single-port, side-incident probe

Parameter	r_C	l_E	l_S	l_V^*
Value (mm)	4, 5, 6, 7, 8	3, 4, 5	1, 2, 3, 4, 5, 6, 7, 8	10, 20, 30

(*: The parameter l_V was tested just for several groups of r_C , l_E , and l_S . The result of each group indicates that l_V has nearly no influence on the transmission characteristic of the probe)

A series of simulations were conducted in terms of the parameters listed in Table 5-1. After analyzing the simulation results of the different parameter combinations, we found that the dimensional parameters r_C , l_E , and l_S jointly affected the transmission characteristic of the probe and that l_V nearly had no influence. Figures 5-3, 5-4, 5-5, and 5-6 present four sets of simulation results, displaying the effects of the dimensional parameters r_C , l_E , l_S , and l_V on the transmission characteristic of the probe. The reference values for r_C , l_E , l_S , and l_V were set to 6, 4, 5, and 10 mm, respectively, for the comparison with the results of other dimensional parameter combinations. For simplicity, only the energy ratios of the TM_{01} and TM_{02} modes are exhibited in each figure. From Fig. 5-4, we can clearly see that l_E affects the transmission characteristic of the probe significantly, as the energy ratios of the TM_{01} and TM_{02} modes

transmitted to either left or right direction varied drastically for different l_E . On the other hand, the effects of l_S and r_C are not as significant as l_E , while the difference in the energy ratio of each mode could still be discernibly observed for different l_S or r_C , as given in Figs 5-3 and 5-5. Based on these results and discussions, the correlation between the transmission characteristic of the probe and the dimensional parameters r_C , l_S , and l_E was proved. Furthermore, as shown in Fig. 5-6, the results of each sub-figure show excellent consistency, demonstrating the lack of a relationship between l_V and the transmission characteristic of the probe.

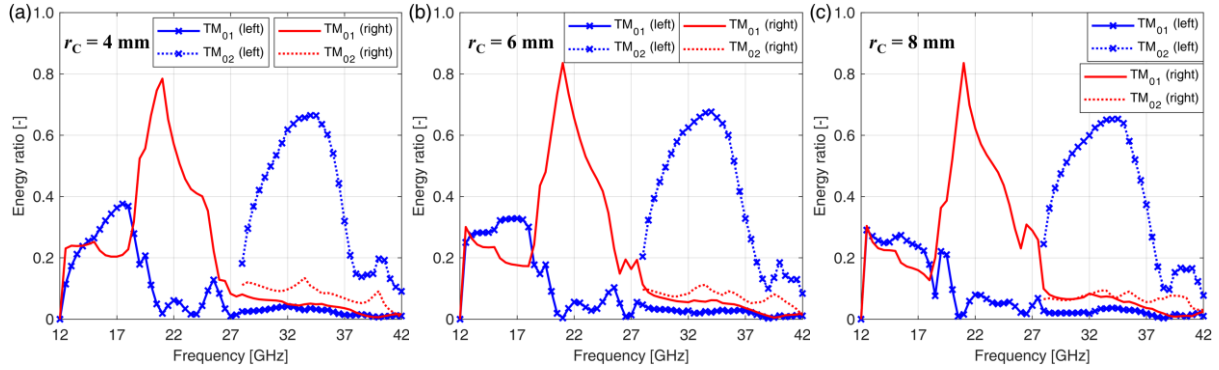


Fig. 5-3 Simulation results of the single-port probe when $l_S = 5$ mm, $l_E = 4$ mm, $l_V = 10$ mm, and (a) $r_C = 4$ mm, (b) $r_C = 6$ mm, and (c) $r_C = 8$ mm.

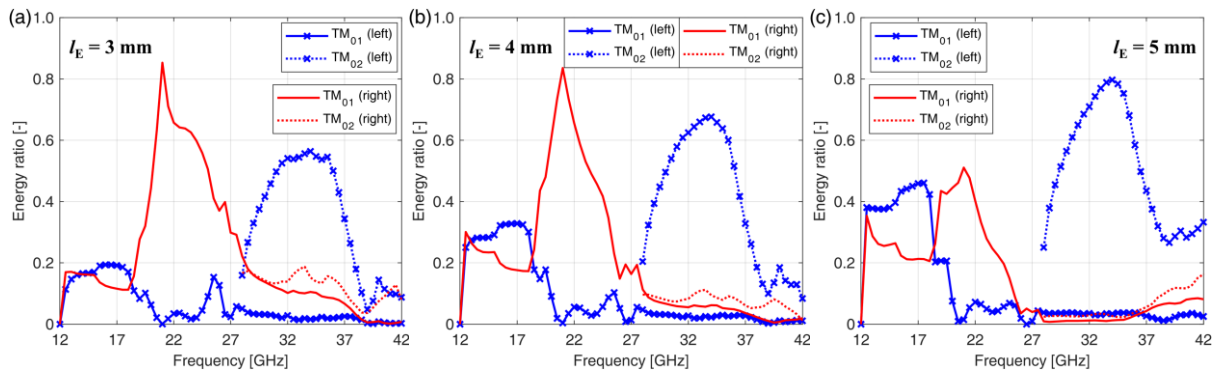


Fig. 5-4 Simulation results of the single-port probe when $r_C = 6$ mm, $l_S = 5$ mm, $l_V = 10$ mm, and (a) $l_E = 3$ mm, (b) $l_E = 4$ mm, and (c) $l_E = 5$ mm.

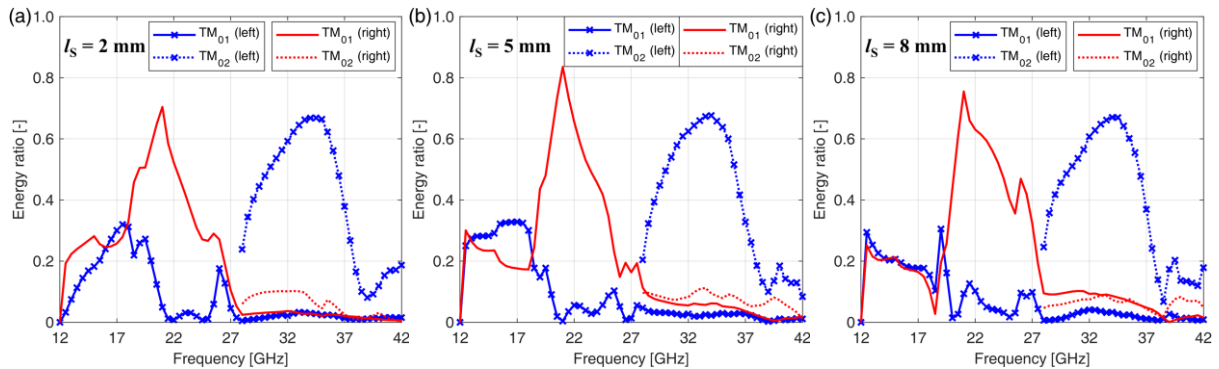


Fig. 5-5 Simulation results of the single-port probe when $r_C = 6$ mm, $l_E = 4$ mm, $l_V = 10$ mm, and (a) $l_S = 2$ mm, (b) $l_S = 5$ mm, and (c) $l_S = 8$ mm.

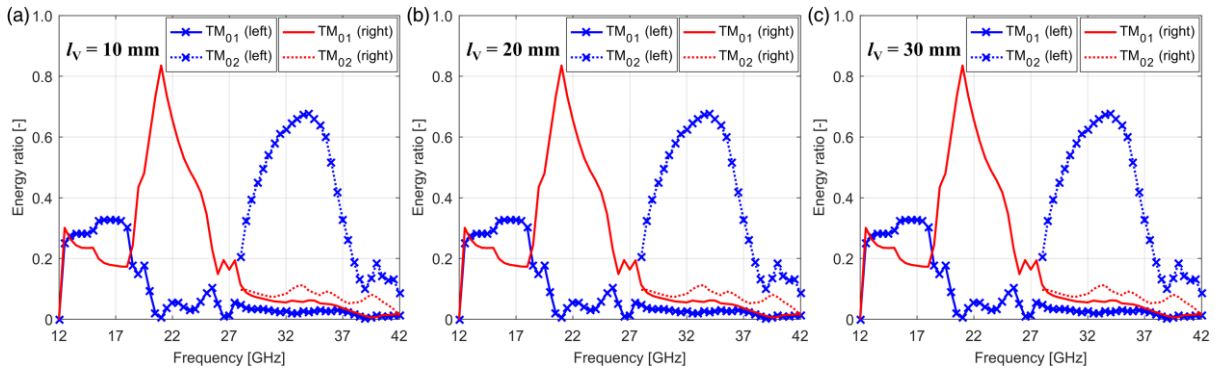


Fig. 5-6 Simulation results of the single-port probe when $r_C = 6$ mm, $l_E = 4$ mm, $l_S = 5$ mm, and (a) $l_V = 10$ mm, (b) $l_V = 20$ mm, and (c) $l_V = 30$ mm.

The simulation results also suggested that a very good single-way transmission characteristic could be achieved for the TM_{01} or TM_{02} mode microwaves when r_C , l_S , and l_E were selected to certain value combinations. As shown in Fig. 5-7(a), when $r_C = 7$ mm, $l_E = 3$ mm, and $l_S = 8$ mm and the frequency ranged from 20.5 GHz to 27.0 GHz, the TM_{01} mode is dominant and mainly transmitted to the right side. The energy ratio of the TM_{01} mode is larger than 0.5, and the energy ratios of other converted modes are less than 0.1. Also as shown in Fig. 5-7(b), when $r_C = 5$ mm, $l_E = 5$ mm, and $l_S = 1$ mm and the frequency ranged from 29.5 GHz to 36.5 GHz, the TM_{02} mode is preponderant and basically transmitted to the left side. The energy ratio of the TM_{02} mode is greater than 0.5, and the energy ratios of other modes are below 0.05. Compared with the probe in the previous study (Fig. 5-1), which can realize the dual-way microwave propagation with a single port by specifically selecting the span of sweeping frequency, the optimized single-port probe in this section can only implement a single-way transmission but possesses higher mode purity and better transmission directivity. To achieve the dual-way pipe inspection, two ports (cables) should be integrated into the current probe for transmitting microwaves to two opposite directions.

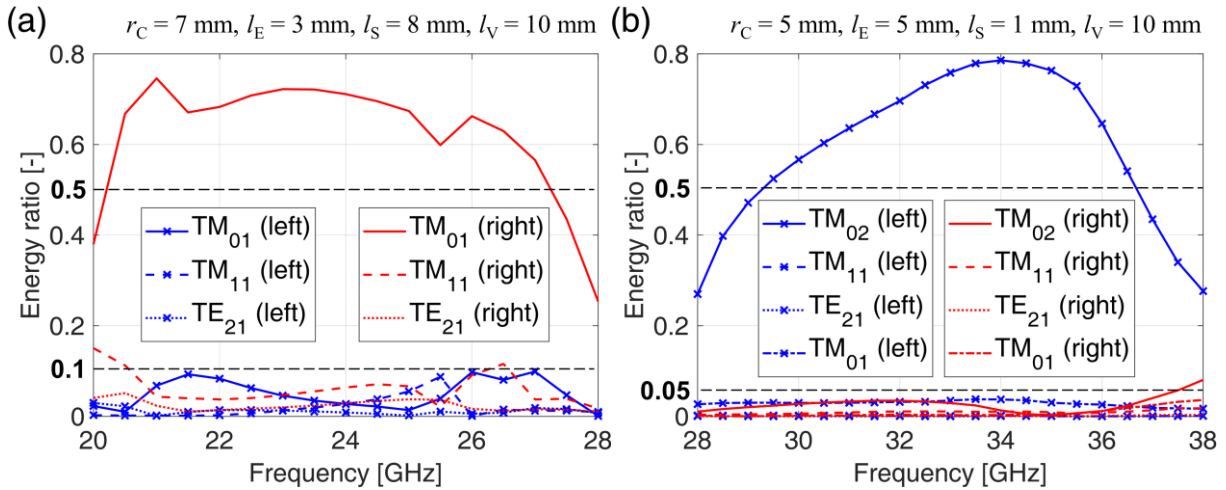


Fig. 5-7 Transmission characteristics of the optimized probes for transmitting (a) TM_{01} , (b) TM_{02} mode microwaves.

5.2.2 Dual-port, side-incident probe

On the basis of the results in 5.2.1, we proposed two types of dual-port, side-incident probes: the LJ type and the JL type. The geometric models of the LJ and JL-type probes are illustrated in Figs. 5-8(a) and (b), respectively. Each type of probe has two ports (L and R) for the microwave transmission to the

left and right sides, respectively. The dimensions (r_c , l_E , and l_S) of each inserted cable were identical to the optimized results in 5.2.1, and the value of l_V was set to 10 mm. The sweeping frequency step was changed to 0.2 GHz. The S-parameter 21 was evaluated on both left and right surfaces, while the labels (1) and (2) in Fig. 5-8 refer to the ports 1 and 2, respectively. The LJ-type probe consisted of two bent cables that were deployed face-to-face as shown in Fig. 5-8(a), and the TM_{01} mode was the dominant mode. The simulation result of the LJ-type, side-incident probe is presented in Fig. 5-9, which shows the transmission characteristics when $r_c = 7$ mm, $l_E = 3$ mm, $l_S = 8$ mm, and the TEM mode microwaves were excited at the two ports, respectively. Over the frequency span of 20.6–25.6 GHz, the energy ratio of the TM_{01} mode to either left or right direction is larger than 0.5 and those of other modes are mostly smaller than 0.1. Clearly, ports L and R are identical as the transmission characteristics of the two ports are consistent, as shown in Figs. 5-9(a) and (b), respectively.

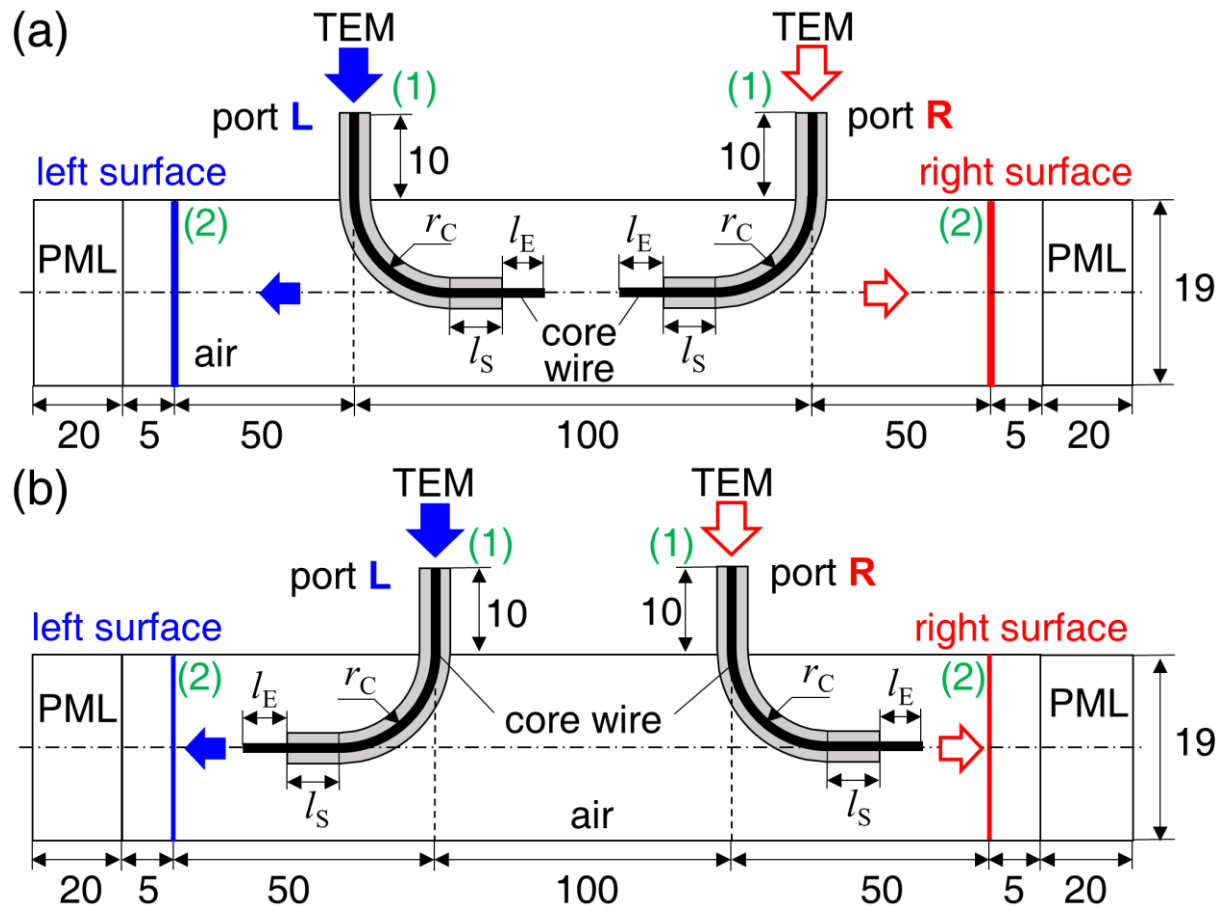


Fig. 5-8 Structures of the dual-port, side-incident probes: (a) LJ type and (b) JL type. (unit: mm, not to scale)

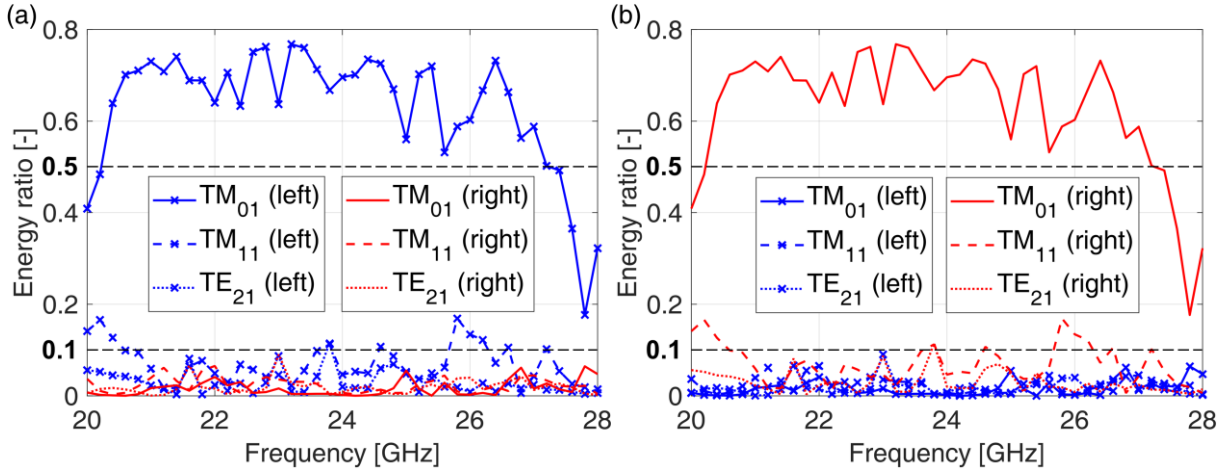


Fig. 5-9 Transmission characteristics of the LJ-type, side-incident probe when $r_C = 7$ mm, $l_E = 3$ mm, and $l_S = 8$ mm, (a) port L (b) port R was used.

Similarly, when the inserted cables were deployed back-to-back as shown in Fig. 5-8(b), the TM_{02} mode microwaves were mainly generated, and this type of probe was the JL type. As shown in Fig. 5-10, when $r_C = 5$ mm, $l_E = 5$ mm, and $l_S = 1$ mm and the frequency ranges from 29.0 GHz to 36.8 GHz, the fractional energy of the TM_{02} mode is above 0.5 and those of others are basically below 0.05. The JL-type probe seems to have a better mode purity than the LJ-type probe. However, its relatively higher operating frequency also leads to a quicker signal decay, meanwhile bending the cable into smaller curvature radii is difficult. Therefore, the LJ-type probe was mainly studied and experimentally examined in Section 5.3. In comparison with the results acquired using the single-port probe shown in Fig. 5-7, those of the dual-port probes were slightly fluctuant probably because of interference from the unused port. As shown in Figs. 5-11(a) and (b), the 3D simulation models of the LJ-type probe and the single-port probe are presented, wherein $D = 19$ mm, $r_C = 7$ mm, $l_E = 3$ mm, $l_S = 8$ mm, and the frequency was 23 GHz. In Fig. 5-11(a), the TEM mode microwaves were excited at port L (located at $z = 0.05$ m), while port R (located at $z = 0.15$ m) was not used. Comparing the two sub-figures, the wave distribution between ports L and R ($z = \sim 0.08 - 0.14$ m) in Fig. 5-11(a) indicates that the existence of the unused port R did affect the microwave transmission of the probe.

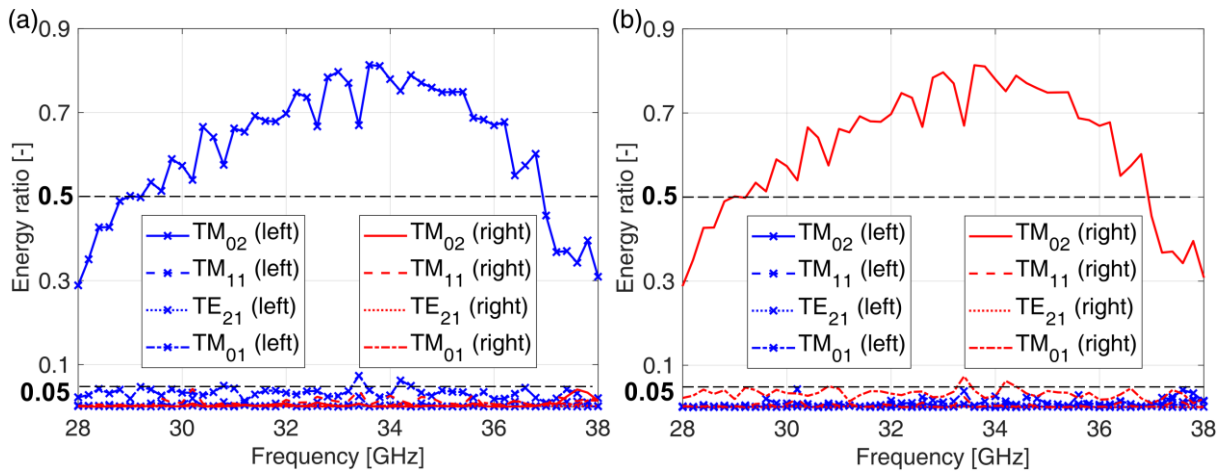


Fig. 5-10 Transmission characteristics of the JL-type, side-incident probe when $r_C = 5$ mm, $l_E = 5$ mm, and $l_S = 1$ mm, (a) port L, (b) port R was used.

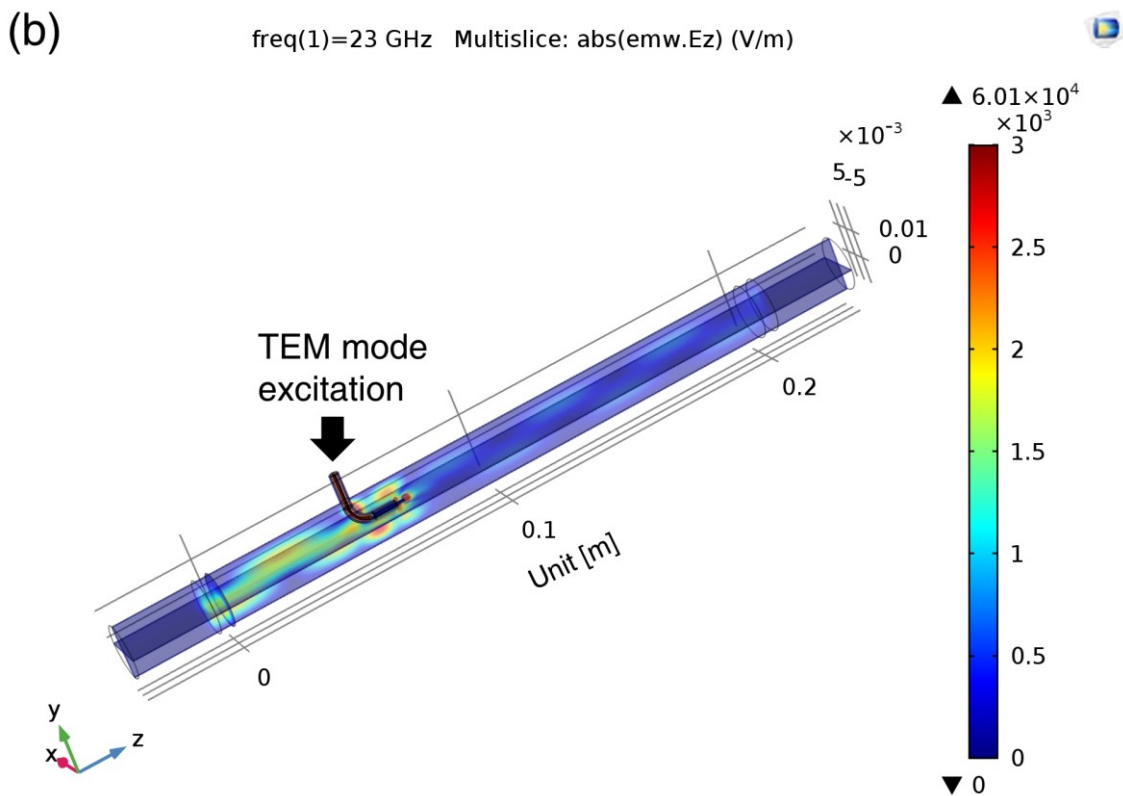
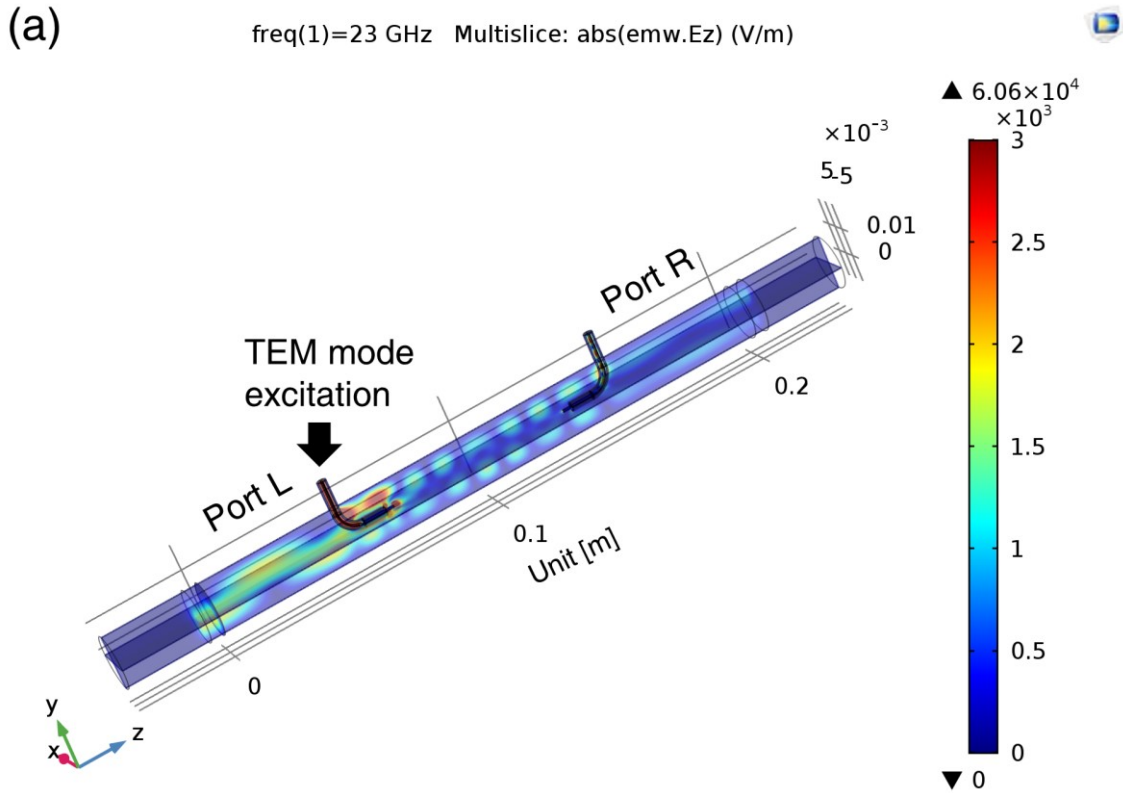


Fig. 5-11 3D simulation models. (a) LJ type probe ($D = 19$ mm, $r_C = 7$ mm, $l_E = 3$ mm, $l_S = 8$ mm, the distance between two ports were 100 mm) and the intensity of electric field E_Z when the frequency was 23 GHz. The TEM mode microwaves were excited at port L ($z = 0.05$ m); (b) Single-port probe ($D = 19$ mm, $r_C = 7$ mm, $l_E = 3$ mm, $l_S = 8$ mm) and the intensity of electric field E_Z when the frequency was 23 GHz. The TEM mode was excited $z = 0.05$ m.

Besides, we confirmed the distance between the two ports also affected the transmission characteristic of the probe. More specifically, a too large or a too small interval could lead to the degradation of mode purity and transmission directivity as shown in Fig. 5-12. The result shows that: the distance (interval) between the two ports did affect the transmission characteristic of the probe, while a longer interval seemingly did not mitigate the interference of the unused port or led to a better transmission characteristic. In this study, the distance between the two ports was set to 100 mm or 150 mm. More effort should be made in the future to further optimize the transmission characteristic of the proposed probe.

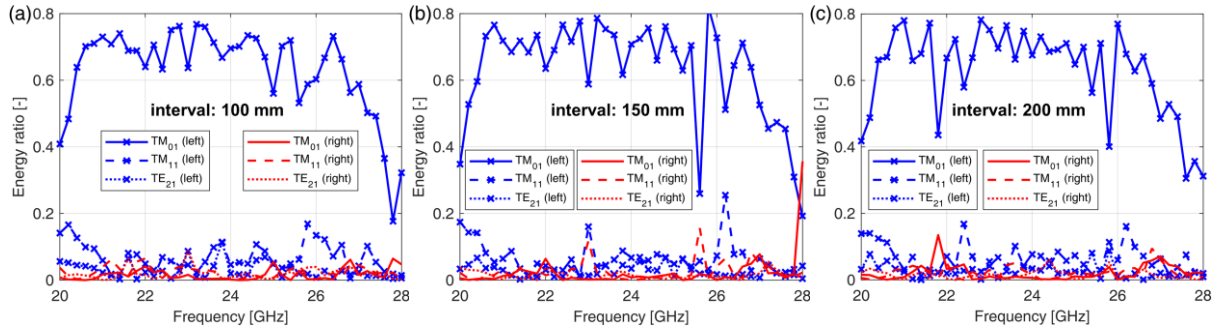


Fig. 5-12 Simulation results of the LJ type, dual-port probe when $r_C = 7$ mm, $l_E = 3$ mm, $l_S = 8$ mm, $l_V = 10$ mm, and the distance (interval) between the two ports was (a) 100 mm, (b) 150 mm, and (c) 200 mm.

5.2.3 Applicability to other inner pipe diameters

The simulation results in 5.2.2 are valid only on the condition that the inner pipe diameter D is 19 mm. If D is changed to another value, the values of r_C , l_E , and l_S will also need to be changed accordingly, which takes extra works for the probe design and optimization.

Hopefully, we have discovered a proportional relationship between the optimized values of r_C , l_E , l_S , and the diameter D , which could significantly reduce the time and work for probe design. For instance, when D is 19 mm, the optimal values of r_C , l_E , and l_S for the LJ-type probe are 7, 3, and 8 mm, respectively. If D is changed to 39 mm, which is about two times of 19 mm, we can simply multiply the optimal values of r_C , l_E , and l_S for $D = 19$ mm by a factor 2 as the fiducial values (i.e., 14, 6, and 16 mm), and then make small adjustments to the fiducial values to obtain better transmission characteristic.

Figure 5-13 shows the simulation result of the optimized LJ-type probe with $D = 39$ mm based on the proportional relationship between D and the dimensional parameters. Here, the values of r_C , l_E , and l_S are 14, 7, and 16 mm, respectively. The simulation results show that, when the frequency span is 8.8–11.6 GHz, the energy ratio of the TM_{01} mode is larger than 0.5, whilst those of the other modes are smaller than 0.1 for both ports L and R. Similarly, if D is changed to 57.5 mm, meanwhile $r_C = 21$ mm, $l_E = 11$ mm, $l_S = 24$ mm, and over the frequency span of 5.7 – 7.3 GHz, the energy ratio of TM_{01} mode is above 0.5, while those of other modes are basically below 0.1, as shown in Fig. 5-14. Another group of simulation results for $D = 30$ mm is presented in Fig. 5-15, showing a similar consequence. These results reveal the potential that the optimized values could be applicable and adaptable to another inner pipe diameter by multiplying the current optimal values by a factor determined by the diameters and making small adjustments to the adapted values.

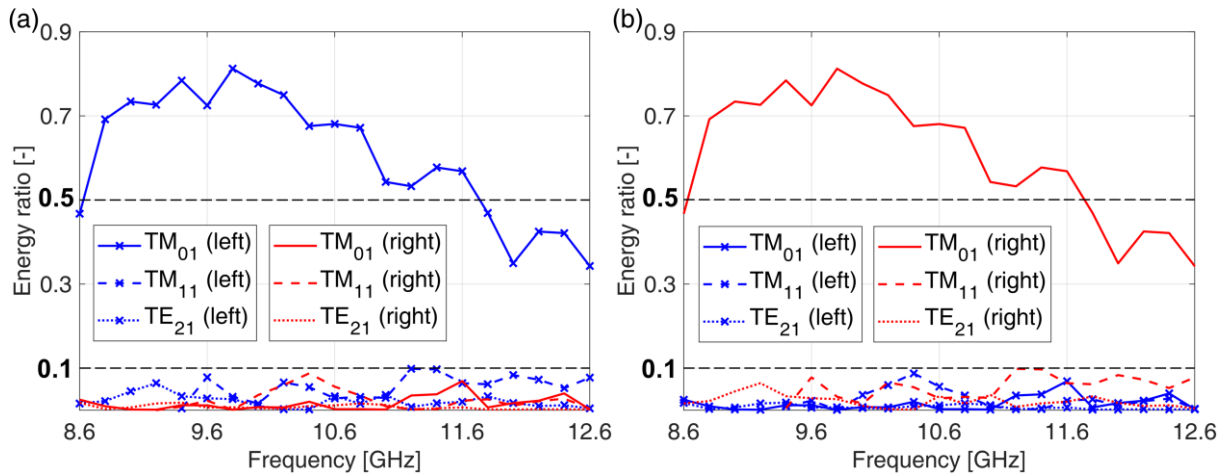


Fig. 5-13 Transmission characteristics of the LJ-type, side-incident probe when D is changed to 39 mm, and $r_C = 14$ mm, $l_E = 7$ mm, $l_S = 16$ mm, (a) port L, (b) port R was used. (Distance between the two ports was 100 mm)

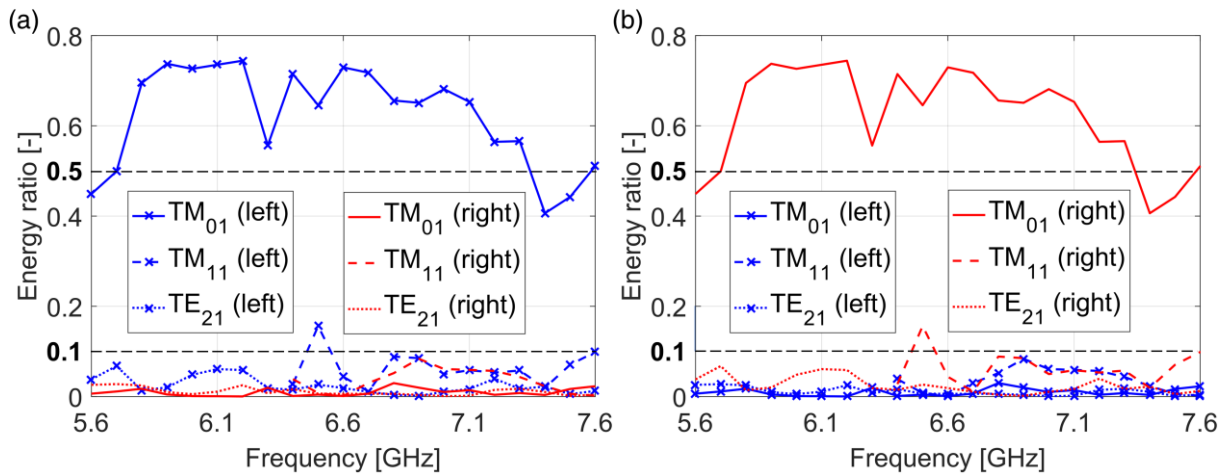


Fig. 5-14 Transmission characteristics of the LJ-type, side-incident probe when D is changed to 57.5 mm, and $r_C = 21$ mm, $l_E = 11$ mm, $l_S = 24$ mm, (a) port L, (b) port R was used. (Distance between the two ports was 150 mm)

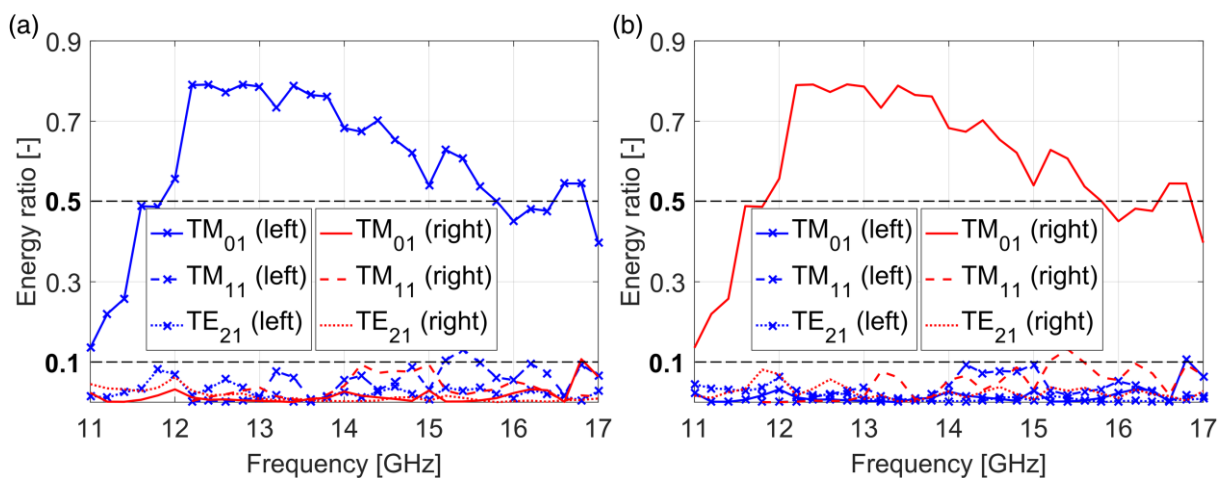


Fig. 5-15 Transmission characteristics of the LJ-type, side-incident probe when D is changed to 30 mm,

and $r_C = 11$ mm, $l_E = 5$ mm, $l_S = 12$ mm, (a) port L, (b) port R was used. (Distance between the two ports was 100 mm)

5.3 Experimental verification

Two LJ-type, dual-port side-incident probes with an inner diameter of 19 mm or 39 mm were fabricated in terms of the simulation results in Section 5.2. An experimental study was carried out to verify the detection directivity of the LJ-type, side-incident probes by detecting the pipe wall thinning positioned at different positions in pipes.

5.3.1 Experimental setup

Figure 5-16 illustrates an overview of the experimental setup. A network analyzer (not shown in the figure) was utilized for generating coaxial TEM mode microwaves. The output of the network analyzer was connected to one port (port L or R) of the dual-port, side-incident probe by a flexible coaxial cable. The generated TEM mode microwaves were propagated through the flexible cable and subsequently entered the brass pipe ($D = 19$ or 39 mm) through the dual-port, side-incident probe, which was deployed at the middle of the pipes under test. Note that the ports L and R worked individually: when the left pipe was inspected, port L should be connected and port R should be disconnected, and vice versa. The left or right pipe was composed of several 1 m or 1.5 m straight brass pipes connected with flange fittings, and the total length of each pipe was 4 m or 4.5 m. Also please note that the length of the left pipe and that of the right pipe were different, so that the reflection from any pipe end could be distinguished and determined. Concretely, when port L was connected to inspect the left pipe, the length of the left pipe was 4 m and that of the right pipe was 4.5 m; when port R was connected to inspect the right pipe, the right pipe was 4 m in length and the left pipe was 4.5 m. In brief, the pipe (left or right) that was 4 m in length always corresponded to the port (L or R) in use, and a large reflection peak was expected to be observed at 4 m whereas little reflection should be seen at 4.5 m. To simulate pipe wall thinning as a flaw, short pipes with a larger inner diameter D_{SP} than the pipe's inner diameter D were used in the experiment and situated at different positions in the pipes (points A, B, A', and B') to test the detection directivity of the probe. The inner diameter D_{SP} and length L_{SP} of the short pipes are presented in Table 5-2, in which the short pipes Nos. 1 and 4, with an inner diameter of 19.0 mm and 39.0 mm, respectively, were used as reference. The detailed configuration of the short pipe is illustrated in Fig 5-17. The original pipe wall thickness for either $D = 19$ mm or $D = 39$ mm pipe was 3 mm. Figure 5-18 displays the photographs of the experimental setup and the short pipes.

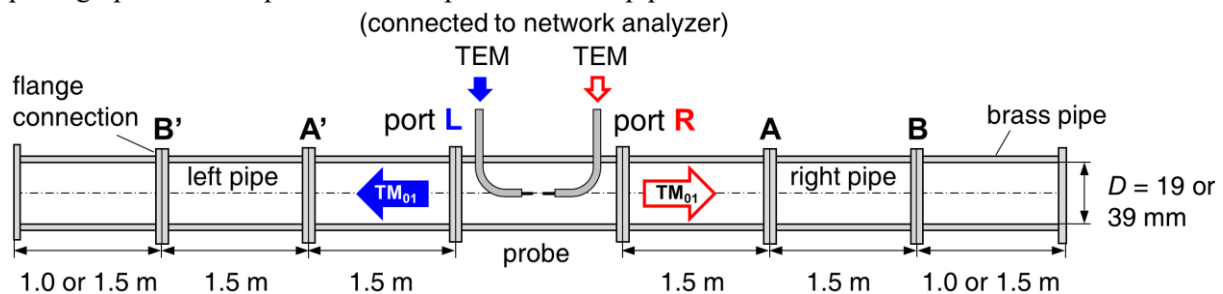


Fig. 5-16 Illustration of the experimental setup (not to scale).

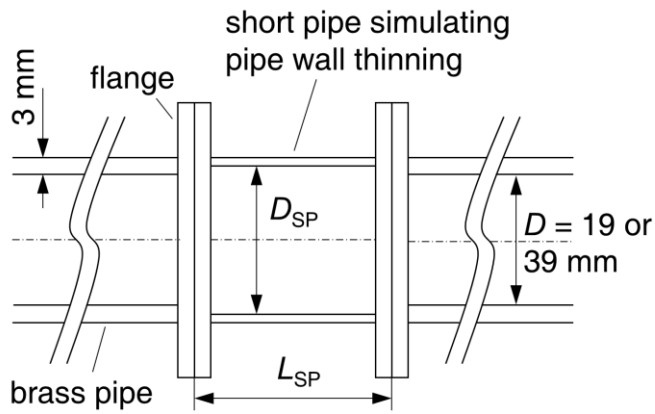
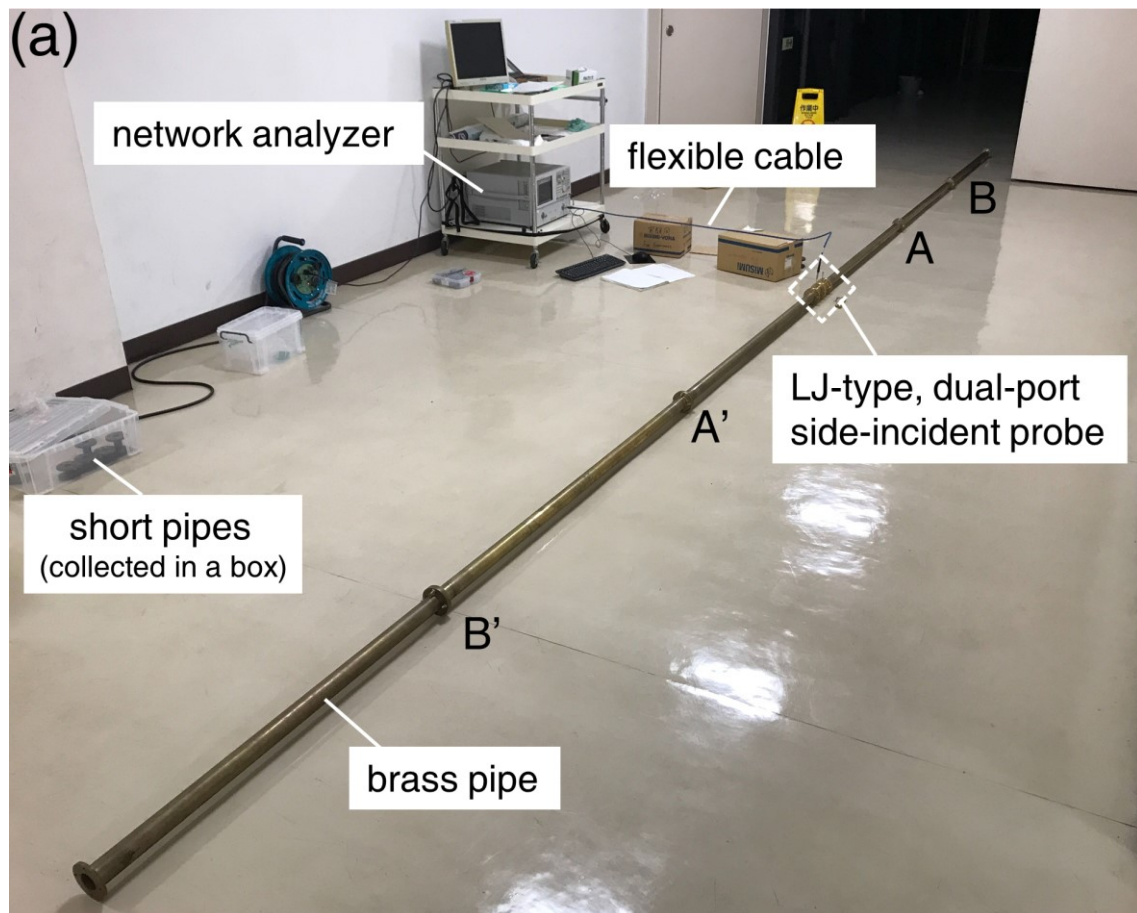


Fig. 5-17 Illustration of the short pipe simulating pipe wall thinning (not to scale).

Table 5-2 Dimensions of the short pipes used in the experiment.

No.	D_{SP} (mm)	L_{SP} (mm)
1	19.0	38
2	19.4	38
3	19.8	38
4	39.0	50
5	40.0	50
6	41.0	50



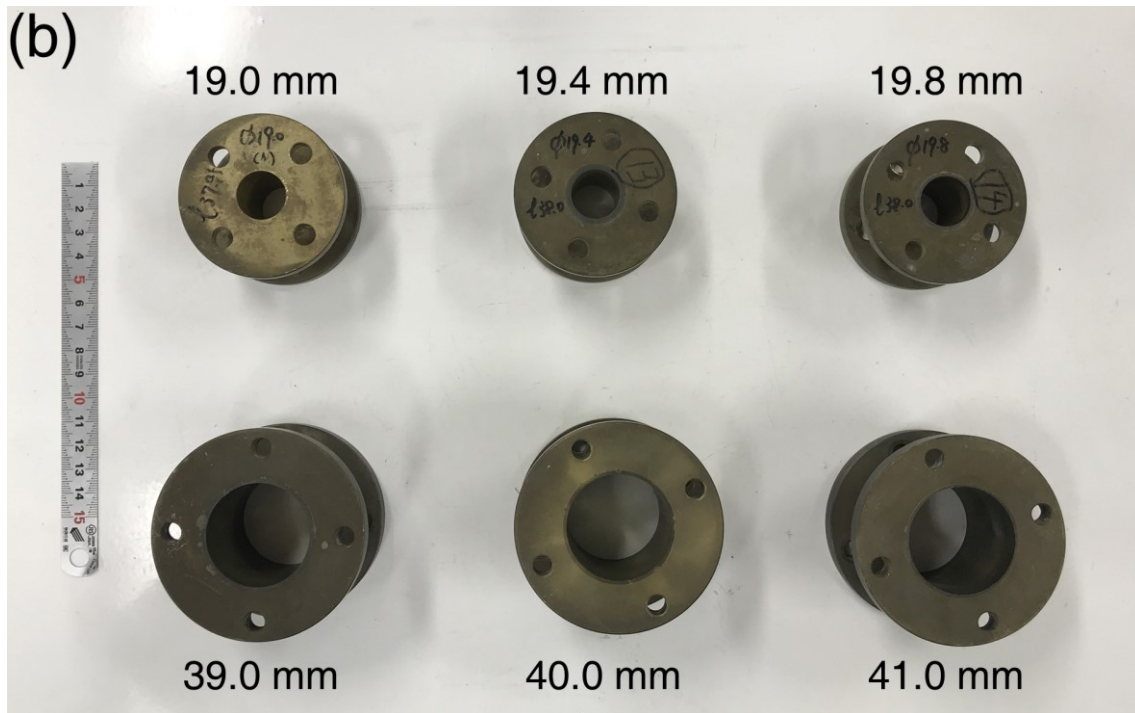


Fig. 5-18 Photograph of the (a) experimental setup, (b) short pipes.

Figure 5-19 shows the 19 mm and 39 mm LJ-type, side-incident probes. The probes were fabricated by inserting semi-rigid cables into a brass pipe, on which two through-wall grooves were fabricated for cable insertion. The cables were manually bent into certain curvature radii using the self-designed benders made of resin and by 3D printing, and they were fixed to the pipe using an adhesive conductive epoxy. The photographs of cable benders and a bent cable are displayed in Fig. 5-20. A connector was attached to the end of each cable for connection. Regarding the 19 mm side-incident probe shown in Fig. 5-19(a), the dimensional parameters of the fabricated probe were $r_C = 8$ mm, $l_E = 3$ mm, and $l_S = 7$ mm, which were slightly different from the simulation results in Section 5.2.2. The change of probe dimensions was mainly due to the difficulty in bending the cable into a smaller curvature radius. The interval between the two ports was 84 mm, and the total length of the probe was 180 mm. However, the simulation result for the fabricated probe was comparable with the optimal result in 5.2.2 and possessed a similar transmission characteristic to that shown in Fig. 5-9. The 39 mm LJ-type side-incident probe consisted of two single-port, side-incident probes assembled face-to-face as shown in Fig. 5-19(b). This fabrication process made it easier to control the position of the cable inside the pipe and the alignment of the two face-to-face situated cables. The working frequency spans for the 19 mm and 39 mm side-incident probes were 20.6–25.4 GHz and 8.8–11.6 GHz, respectively. The measurement was implemented in the frequency domain as a spectrum of the reflection coefficients (scattering parameters, S_{11}). A total of 3,201 uniformly spaced points were sampled over the working frequency span of each side-incident probe. The measured frequency-domain reflection signals were processed using the signal-processing method presented in Chapter 2.

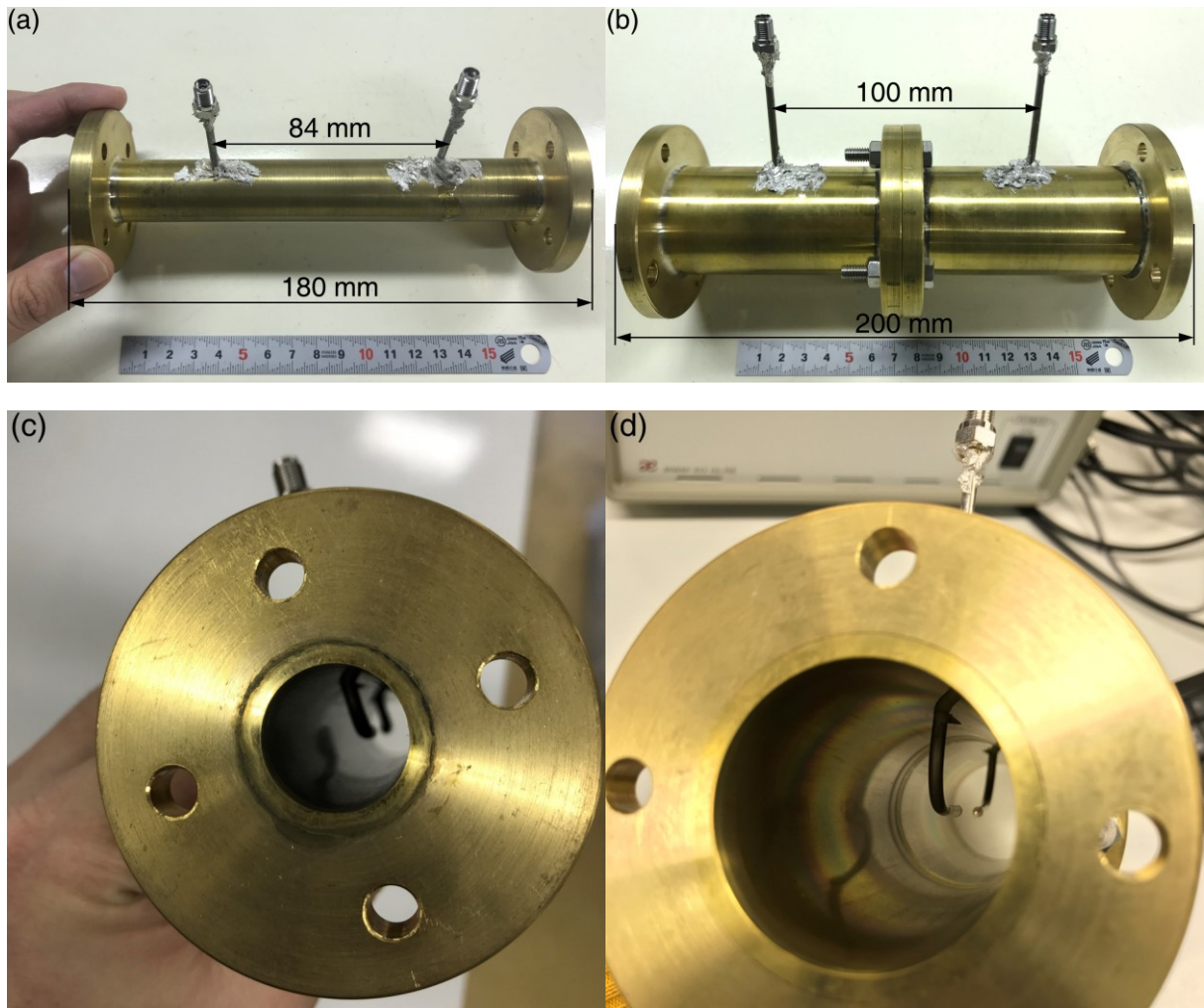


Fig. 5-19 Dimensions and internal structures of the two LJ-type, side-incident microwave probes; (a), (c): 19 mm and (b), (d): 39 mm.

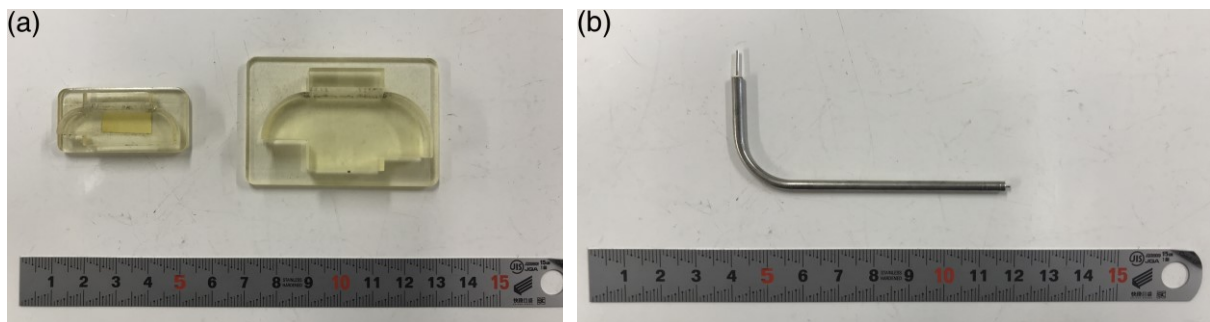


Fig. 5-20 (a) cable benders for $r_c = 8$ and 14 mm; (b) a bent cable with $r_c = 14$ mm.

5.3.2 Results and discussion

Figures 5-21 and 5-22 present the processed reflection signals of 19 mm pipe and probe when ports L and R were used, respectively. When port L was adopted and the left pipe was under inspection (Fig. 5-21), the two types of pipe wall thinning ($D_{SP} = 19.4$ and 19.8 mm) were detected at points A' and B' in the left pipe, whereas no obvious reflection signal was observed from the pipe wall thinning deployed at points A and B in the right pipe. The large reflection appearing at 4 m corresponded to the left pipe end, while no noticeable reflection appeared at 4.5 m from the right pipe end. Conversely, when port R

was connected and the right pipe was inspected (Fig. 5-22), the reflections from the pipe wall thinning situated at points A and B were discernible, whereas the pipe wall thinning at points A' and B' was undetectable. The large reflection at 4 m was from the right pipe end, whereas no distinct reflection peak was observed at 4.5 m from the left pipe end. Some small and dispersed reflections are observed between 1.5 m and 3 m in Figs. 5-21 and 5-22, and they could have resulted from the spurious modes generated by the probe, such as the TE_{21} and TM_{11} modes. Moreover, the amplitudes of the reflection peaks in Fig. 5-21 (port L) are smaller than those in Fig. 5-22 (port R). The difference in reflection amplitude between the two ports could be attributed to the fabrication error when bending the cables. As the curvature radius r_c was merely 8 mm and the bending process was performed manually, some deformations in the cross-section of the cables were inevitable. Nevertheless, comparing the amplitudes of the reflections from the pipe wall thinning with those from the pipe end and noises in Figs. 5-21(a) and 5-22(b), the results of the two ports show a similar signal-to-noise ratio and nearly consistent detection sensitivities. Therefore, a directional pipe inspection was realized by utilizing the proposed LJ-type, dual-port side-incident probe for $D = 19$ mm.

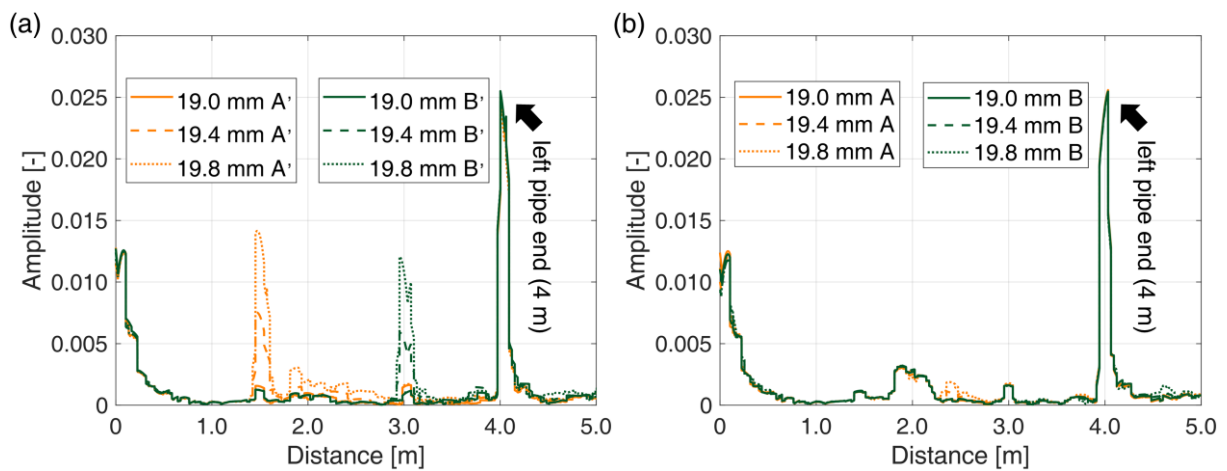


Fig. 5-21 Reflection signals from the pipe wall thinning deployed at (a) points A' and B' and (b) points A and B when $D = 19$ mm and port L of the probe was used. The left pipe was 4 m in length and the right pipe was 4.5 m.

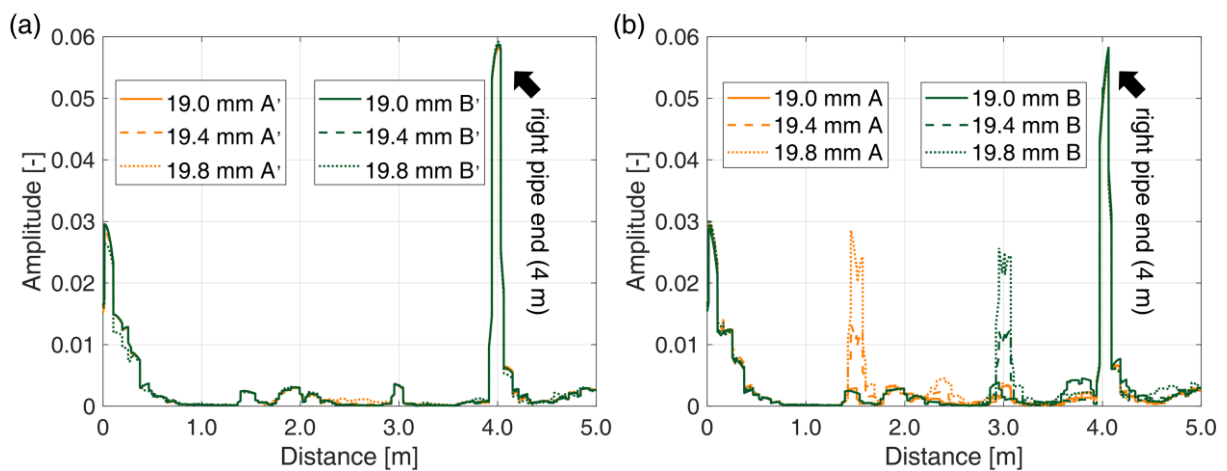


Fig. 5-22 Reflection signals from the pipe wall thinning deployed at (a) points A' and B' and (b) points A and B when $D = 19$ mm and port R of the probe was used. The right pipe was 4 m in length and the left pipe was 4.5 m.

The experimental results for the 39 mm pipe and probe are shown in Figs. 5-23 and 5-24. Similar to the results of the 19 mm scenario, the 39 mm side-incident probe, which was designed based on the proportional relationship between the pipe diameter D and the dimensional parameters (r_c , l_E , and l_S), also showed a good detection directivity. The reflection signals of the two ports show similar amplitudes, indicating that the two ports were almost identical. In summary, the experimental results presented in this section suggest that the proposed dual-port, side-incident probes can achieve directional pipe inspection with excellent directivity. Meanwhile, the applicability of this method to different inner pipe diameters has been confirmed.

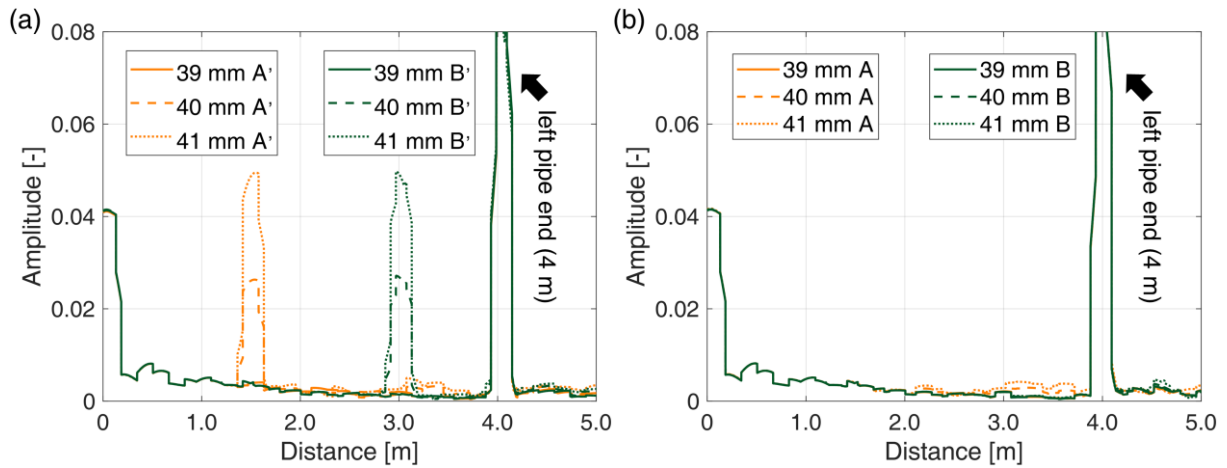


Fig. 5-23 Reflection signals from the pipe wall thinning deployed at (a) points A' and B' and (b) points A and B when $D = 39$ mm and port L of the probe was used. The left pipe was 4 m in length and the right pipe was 4.5 m.

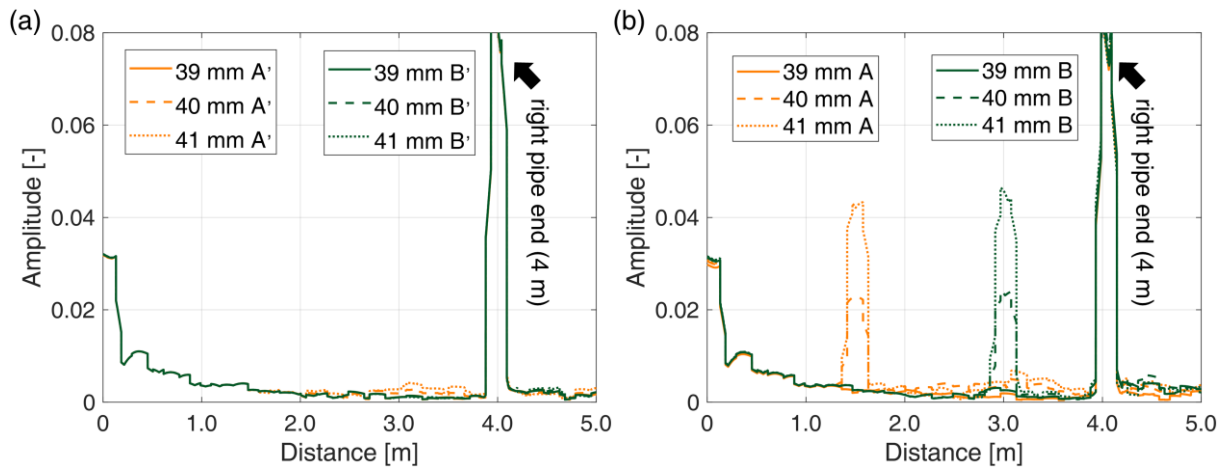


Fig. 5-24 Reflection signals from the pipe wall thinning deployed at (a) points A' and B' and (b) points A and B when $D = 39$ mm and port R of the probe was used. The right pipe was 4 m in length and the left pipe was 4.5 m.

5.4 Summary

In this chapter, we reported a dual-port, side-incident microwave probe for directional inspection of closed piping systems. Two types of probes (LJ and JL) were proposed based on the numerical

simulations, and two LJ-type probes with different inner pipe diameters (19 and 39 mm) were fabricated and examined through an experiment. The simulation results confirm that an optimal selection of the three dimensional parameters (r_C , l_E , and l_S) of the probe could significantly improve the mode purity and transmission directivity of the probe. Besides, the optimized probe dimensions for one inner pipe diameter could also be applied to another diameter by proportionally changing r_C , l_E , and l_S of the current probe with small adjustments. The results of the experimental verification show that the pipe wall thinning deployed on either side of each probe could be detected and located using the corresponding port of the probe. Adopting the side-incident method for use with other inner pipe diameters was verified to be feasible.

Chapter 6 Conclusion

6.1 Summary of this study

In this study, we have made significant improvement in microwave NDT technology for inspection of piping systems with bends, so that to facilitate the usage of this method for practical pipe inspection. To achieve this objective, the following three aspects of works were carried out:

- (1) Investigation into the effect of a bend on microwave's transmission and reflection;
- (2) Development of a crack-detection approach using a TE₁₁ mode microwave probe for inspection of bent pipes with open-end;
- (3) Design of a dual-port, side-incident microwave probe for directional inspection of closed piping systems with bends.

The major works and findings are summarized below.

(1) Investigation into the effect of a bend on microwave's transmission and reflection

The mode conversion of microwaves due to a bend and its dependence were studied theoretically and through numerical simulation. The theoretical and numerical analysis on TM₀₁, TE₀₁, and TE₁₁ modes reflect that the mode conversion at a bend hinges on three factors, they are the normalized curvature radius r/D , the normalized frequency ff_c and the bend angle α . In addition, to linearly-polarized and non-axisymmetric TE₁₁ mode, the polarization is also a critical factor that should be taken into consideration when analyzing mode conversion. Concretely, the simulation results reveal that TE₁₁ mode under horizontal and vertical polarization have different transmission characteristics in a bent pipe, while the polarization is not affected by the bend.

The effect of a bend on microwave's reflection was evaluated quantitatively via experiment, by comparing the reflection signals from pipe wall thinning deployed in straight pipes and bent pipes. The results show that the presence of a bend leads to the decrease in reflection amplitude because the fractional energy of the input TM₀₁ mode decreases (converted to other modes at bend), while an amplitude-decrease coefficient (Δ) was defined to quantitatively assess the effect of a bend. Besides, the experimental results also suggest that: the effect of a bend is correlated with the extent of mode conversion at the bend; the amplitude-decrease coefficient Δ is not noticeably affected by the flaw size; the bend only takes effects on the reflection behind it, while that ahead of it is not affected significantly; bends with different diameters but similar r/D and α possess a similar effect on reflection Δ , if the range of ff_c is certain.

(2) Development of a crack-detection approach using a TE₁₁ mode microwave probe for inspection of bent pipes with open-end

The feasibility of using linearly-polarized TE₁₁ mode microwaves for crack detection was discussed based on the analysis of surface current density. Since TE₁₁ mode has both axial and circumferential components of surface current induced on inner pipe wall, it is expected to be sensitive to both circumferential and axial cracks inside the pipe. Then a systematical method was proposed for designing

a TE_{11} mode microwave probe, which comprises a TEM- TM_{01} mode converter and dual-bend TM_{01} - TE_{11} mode converter, for a certain inner pipe diameter. The dimensions of the probe were optimized to acquire a wide working bandwidth of TE_{11} mode. The experimental verification was conducted by detecting both axial and circumferential slits in a stainless steel pipe, and the results reflect that either axial or circumferential slit was successfully detected at arbitrary longitudinal and circumferential positions in the pipe, by jointly analyzing the reflection signals of TE_{11} mode under two orthogonal polarizations (horizontal and vertical).

After confirming the efficacy of the developed probe, it was subsequently applied for detecting cracks in a bent pipe. Since the polarization of TE_{11} mode has impact on mode conversion at a bend, there exists a distinction in detection sensitivity between two polarizations (especially to circumferential crack). However, if the existence of a bend significantly influences detection sensitivity to circumferential crack, the ‘integrated’ TEM- TM_{01} mode converter can also be utilized as an auxiliary measure for detecting circumferential cracks. On the basis of the preceding discussions, this crack detection method using the TE_{11} mode microwave probe can be applied for inspecting bent pipes with open-end.

The applicability of this method to long-range detection and other inner pipe diameters was also validated through experiment. Three more TE_{11} mode microwave probes with different inner diameters (11, 19, and 39 mm) were designed and fabricated for experimental verification. The results demonstrate the applicability to variant inner pipe diameters, and a detection range of up to 15–24 m has been realized. Moreover, an improved TE_{11} mode microwave probe design was proposed to achieve wider working bandwidth of TE_{11} mode so that this method can be used for large-diameter pipes with high range resolution.

The viability for bend-region crack detection was also preliminarily examined via experiment. Axial and circumferential slits were machined at different angular positions of three bends under test. Discernible reflections from these slits were observed, while their angular positions were characterized by the peak locations of the reflection signals. More endeavors ought to be made to study the correlation between mode conversion at bend and reflection intensity, so as to quantitatively evaluate the slit size.

Finally, the detectability of TE_{11} mode against pipe wall thinning and non-penetrant slit was additionally tested. The results show that the linearly-polarized TE_{11} mode has relatively low sensitivity against pipe wall thinning, compared with TM_{01} mode. Ergo, jointly using TM_{01} and TE_{11} can realize the thorough detection of pipe wall thinning and crack. On the other hand, the non-penetrant axial slit was detected by using the TE_{11} mode microwave probe, but the reflection amplitude is smaller than the penetrant slit. More works should be carried out in the future to detect non-penetrant circumferential slit or real in-pipe cracks.

(3) Design of a dual-port, side-incident microwave probe for directional inspection of closed piping systems with bends.

In view of the unaddressed problems in the previous study on side-incident method, quantities of numerical simulations were firstly performed to determine the dimensional parameters that influence the transmission characteristic of the single-port, side-incident probe. Afterwards, the single-port, side-incident probe was optimized to achieve good mode purity and transmission directivity for TM_{01} or TM_{02} mode in one direction. Then two types of dual-port, side-incident microwave probe (LJ and JL) were designed by combining two ‘unidirectional’ single-port probes, and the adaptability to other pipe diameters were also proved to be feasible according to the proportional relationship between the inner pipe diameter and optimal dimensional parameters. Two LJ type dual-port probes with an inner diameter of 19 or 39 mm were fabricated for experimental verification, by detecting pipe wall thinning flaws on

either side of each probe. The results show that the proposed probe manifests excellent detection directivity: using the corresponding port of the probe can effectively detect the pipe wall thinning in a certain direction, while the pipe wall thinning situated on the other side of the probe does not intervene. Hence the directional pipe inspection can be achieved by adopting the dual-port, side-incident microwave probe.

This study enables us to analyze the bent pipe like the straight pipe, and provides a solution to bent pipe inspection using microwave NDT. Firstly, to the maintenance of bent pipes with open-end in steam generators or heat exchangers, the dimensions of the bends (like inner diameter D , curvature radius r , bend angle α , etc.) are certain, hence the effects of them can be evaluated or estimated. Furthermore, using TE_{11} mode microwaves under two orthogonal polarizations (in conjunction with the ‘self-integrating’ TM_{01} mode if needed) can achieve the thorough detectability against cracks at both straight portion and bend-region of the pipe. Hence, a fast and efficient maintenance method is expected to be realizable for open-ended bent pipes, such as steam generator tubes in pressurized water reactors. On the other hand, to the closed piping systems, the dual-port, side-incident microwave probe can be pre-deployed at some certain positions of the piping system for the periodical inspection or structural health monitoring of some vital or vulnerable structures (e.g., bends). One great progress in this study was finding out a way to readily design and adopt the side-incident probe for other diameters, and thus facilitate the usage of this method for inspections of some complicated closed piping systems.

6.2 Future tasks

To further push forward the practical use of microwave NDT for bent pipe inspection or practical pipe inspection, some works should be carried out in the future:

(1) Evaluation of the amplitude-decrease coefficient Δ of a bend on reflection from its dimensions (r/D and α) as well as the range of ff_c . Establishing a database or a numerical model would also be useful. It can help us estimate amplitude decay or the shrink of detection range due to a bend.

(2) Detection of real cracks using TE_{11} mode. In this study, penetrant slits were mainly used to emulate the crack, while only two tests on non-penetrant axial slits were conducted. However, the real cracks would be much more complicated as it is like a crevice and ‘zero’ in width. Tests using real crack or field-experiment should be carried out in the future.

(3) Identification and quantitative assessment of the flaw. The previous and current studies mainly concentrate on detection and locating of the flaw, while the flaw recognition as well as size evaluation was not studied particularly. Not to mention the presence of a bend or bends will make the reflections more complicated. Some machine learning methods can be used as a tool.

(4) The experimental verification on the improved TE_{11} mode microwave probe should be conducted. Besides, since it possesses wider working bandwidth, tests on its range resolution, in other words, detectability towards multiple contiguous cracks, would be a good trial.

(5) Structure of the side-incident probe should be further strengthened and improved to withstand the fluid flow, pressure, and even corrosion, so that it can be integrated inside the piping system for structural health monitoring.

Acknowledgment

This thesis is prepared in the Department of Quantum Science and Energy Engineering, Graduate School of Engineering, Tohoku University, where I pursue my doctoral study during 2017–2020. I feel so fortunate that I was offered this great opportunity to study and do research in Tohoku University and especially in our department. I am also grateful to China Scholarship Council (CSC), which supports me with stipend for my three-year study. Without any of them, I would not even have a chance to commence my study and draft this thesis.

First of all, I would like to show my cordial thanks to Prof. Hidetoshi Hashizume. As my respectful supervisor, Prof. Hashizume has given me lots of useful guidance, advice, and assistance in not only research but also my life and career. He concerns not only about the research but also my life in Japan. He is an authentic master, meanwhile a warm-hearted superior. Then I would like to appreciate Assoc. Prof. Noritaka Yusa, whom I knew and contacted since I was in China. Prof. Yusa gave me direct guidance on my research work, and I have learned tons of knowledge, skills, and principles of doing researches from him, which I can benefit from for all time. I cannot thank him more, for his generosity, patience, and devotion. I also would like to thank Assoc. Prof. Satoshi Ito and Lect. Weiying Cheng for their help and insightful suggestions to my research and paper writing. I also want to thank Asst. Prof. Hiroki Shishido for his help in my study and daily life, as well as the three-year accompanying at our face-to-face seats. And thank Asst. Prof. Aparicio Finol Luis Ernesto for his advice on my presentations and thesis. In addition, I want to give my deep thanks to Prof. Helena Maria Geirinhas Ramos and Prof. Artur Lopes Ribeiro, affiliated with Técnico Lisboa, Portugal, who helped me a lot in research, presentation, and paper writing.

I'd like to thank the technician Mr. Takao Nagaya, affiliated with Graduate School Engineering, Tohoku University, for his grant assistance in mechanical fabrication. More than half of my experimental specimens were made by him, and owing to his expertise, I can push my progress forward more fluently. And I want to thank Mrs. Yumi Omoto for her warm and kind help to the student affairs of mine.

To students, I would like to thank Mr. Takuya Katagiri who is very smart and works on microwave NDT as well. I received quite a few suggestions and help from him. We discuss, cooperate, stick together in research as partners, and communicate a lot and make good acquaintance. It is a very nice experience to work with him. I also would like to thank Dr. Weixi Chen, who has greatly helped me with my study and especially in daily life. I guess I may not be able to 'survive' without him as my oral Japanese is still far from proficient. And I also want to thank Dr. Jiu hao Ge, Mr. Haicheng Song, and Mr. Takuma Tomizawa from Niibori-Yusa Laboratory for their assistance in my research. Many thanks to the students who assisted me with my experiment: Mr. Pengcheng Pan, Mr. Yijun Guo, Mr. Xiuyuan Zheng, Mr. Yujie Ma, and Ms. Siqi Meng. Also, thanks to Mr. Yuta Imanaka, who was my tutor helped a lot when I first came here, and to Mr. Kenta Muraoka, who helped me with mechanical fabrications using lathe. And I hope to visit you two in Shizuoka and Osaka in the future. Also thanks Mr. Kohei Yuki for helping me with some laboratory affairs such as printing. And I want to thank the professors and students from School of Aerospace Engineering, Xi'an Jiaotong University, for their help and hospitality during my visit there.

Finally, I want to thank my parents and grandparents who have devoted everything to me and support

me unconditionally and persistently. And my special thanks to Ms. Yujie Chen, affiliated with School of Aerospace Engineering, Xi'an Jiaotong University, for the delightful moments and patience from her.

Three years are a long time, you can meet many people and experience many things; but you may also need to face separations and witness people you know to come and leave. And when there is a hard time, every minute is like one year that tortures your will and spirit in the lonely and chill night. Three years are also very short. I still remembered how I got lost on my first day in Japan, how poorly I performed in my first progress report, how nervous I was in my first conference presentation, etc. All these memories appearing in my mind are so clear just like they happened yesterday. Time passes in the blink of eye. I feel very lucky of me that I chose to study in Tohoku University and in this laboratory, and I would make the same decision if I went back to three years ago. Once more, thank all friends in either China or Japan, for your support and concern so far.

Guanren Chen

July 20th, 2020 in Sendai.

Appendix

A. Mathematical demonstrations for other three coupling coefficients:

A.1 TM_{mn} to $TE_{m'n'}$ mode, $C_{[m'n'](mn)}$

The coupling coefficient from TM_{mn} to $TE_{m'n'}$ is described as below:

$$C_{[m'n'](mn)}^{\pm} = \frac{e \cdot (-1)^{n+n'+1} \cdot (m+1) \cdot \left(\frac{\beta_{mn}}{k} \pm \frac{\beta_{m'n'}}{k} \right)}{\sqrt{v_{m'n'}^2 - (m+1)^2} \cdot (v_{m'n'}^2 - u_{mn}^2) \cdot \sqrt{\frac{\beta_{mn}}{k} \cdot \frac{\beta_{m'n'}}{k}}} \cdot \frac{Dk}{2r}, \quad (\text{A.1})$$

where

$$e = \begin{cases} 1/\sqrt{2} & (m=0) \\ 1/2 & (m \geq 1) \end{cases}. \quad (\text{A.2})$$

Thus $rC_{[m'n'](mn)}$ can be rewritten as follows:

$$rC_{[m'n'](mn)}^{\pm} = c_{EM} u_{01} \cdot \frac{\sqrt{\left(\frac{f}{f_{cTM01}}\right)^2 - \frac{u_{mn}^2}{u_{01}^2}} \pm \sqrt{\left(\frac{f}{f_{cTM01}}\right)^2 - \frac{v_{m'n'}^2}{u_{01}^2}}}{\sqrt{\sqrt{\left(\frac{f}{f_{cTM01}}\right)^2 - \frac{u_{mn}^2}{u_{01}^2}} \cdot \sqrt{\left(\frac{f}{f_{cTM01}}\right)^2 - \frac{v_{m'n'}^2}{u_{01}^2}}}} \cdot \frac{f}{f_{cTM01}}, \quad (\text{A.3})$$

where

$$c_{EM} = \frac{e \cdot (-1)^{n+n'+1} \cdot (m+1)}{\sqrt{v_{m'n'}^2 - (m+1)^2} \cdot (v_{m'n'}^2 - u_{mn}^2)}. \quad (\text{A.4})$$

It reveals that $rC_{[m'n'](mn)}$ is a function of ff_{cTM01} .

A.2 TM_{mn} to $TM_{m'n'}$ mode, $C_{(m'n')(mn)}$

The coupling coefficient from TM_{mn} to $TE_{m'n'}$ is expressed as follows:

(i) when $m=0$:

$$C_{(m'n')(mn)}^{\pm} = \frac{(\beta_{mn} \pm \beta_{m'n'}) \cdot [2u_{mn}^2 \beta_{m'n'} \pm (D/2)^2 (\beta_{mn} - \beta_{m'n'}) (k^2 \pm \beta_{mn} \beta_{m'n'})]}{\sqrt{2(u_{m'n'}^2 - u_{mn}^2)} \cdot \sqrt{\beta_{mn} \beta_{m'n'}}} \cdot \frac{(-1)^{(n+n')} \cdot (D/2)}{r}, \quad (\text{A.5})$$

hence $rC_{(m'n')(mn)}$ is given by:

$$rC_{(m'n')(mn)}^{\pm} = c_{MM0} u_{01}^3 \cdot \frac{\left[\sqrt{\left(\frac{f}{f_{cTM01}}\right)^2 - \frac{u_{mn}^2}{u_{01}^2}} \pm \sqrt{\left(\frac{f}{f_{cTM01}}\right)^2 - \frac{u_{m'n'}^2}{u_{01}^2}} \right]}{\sqrt{\left(\frac{f}{f_{cTM01}}\right)^2 - \frac{u_{mn}^2}{u_{01}^2}} \cdot \sqrt{\left(\frac{f}{f_{cTM01}}\right)^2 - \frac{u_{m'n'}^2}{u_{01}^2}}} \cdot \left\{ 2 \left(\frac{u_{mn}}{u_{01}} \right)^2 \sqrt{\left(\frac{f}{f_{cTM01}}\right)^2 - \frac{u_{m'n'}^2}{u_{01}^2}} \pm \right. \\ \left. \left[\sqrt{\left(\frac{f}{f_{cTM01}}\right)^2 - \frac{u_{mn}^2}{u_{01}^2}} - \sqrt{\left(\frac{f}{f_{cTM01}}\right)^2 - \frac{u_{m'n'}^2}{u_{01}^2}} \right] \left[\frac{f^2}{f_{cTM01}^2} \pm \sqrt{\left(\frac{f}{f_{cTM01}}\right)^2 - \frac{u_{mn}^2}{u_{01}^2}} \cdot \sqrt{\left(\frac{f}{f_{cTM01}}\right)^2 - \frac{u_{m'n'}^2}{u_{01}^2}} \right] \right\}, \quad (A.6)$$

where

$$c_{MM0} = \frac{(-1)^{n+n'}}{\sqrt{2(u_{m'n'}^2 - u_{mn}^2)}}. \quad (A.7)$$

(ii) when $m > 0$:

$$C_{(m'n')(mn)}^{\pm} = \frac{(\beta_{mn} \pm \beta_{m'n'}) \cdot (u_{mn}^2 \beta_{m'n'} \pm u_{m'n'}^2 \beta_{mn})}{2 \cdot (u_{m'n'}^2 - u_{mn}^2)^2 \cdot \sqrt{\beta_{mn} \cdot \beta_{m'n'}}} \cdot \frac{D}{2r} \cdot (-1)^{n+n'}, \quad (A.8)$$

we thus have:

$$rC_{(m'n')(mn)}^{\pm} = c_{MM1} u_{01} \frac{\left[\sqrt{\left(\frac{f}{f_{cTM01}}\right)^2 - \frac{u_{mn}^2}{u_{01}^2}} \pm \sqrt{\left(\frac{f}{f_{cTM01}}\right)^2 - \frac{u_{m'n'}^2}{u_{01}^2}} \right] \cdot \left[u_{mn}^2 \sqrt{\left(\frac{f}{f_{cTM01}}\right)^2 - \frac{u_{m'n'}^2}{u_{01}^2}} \pm u_{m'n'}^2 \sqrt{\left(\frac{f}{f_{cTM01}}\right)^2 - \frac{u_{mn}^2}{u_{01}^2}} \right]}{\sqrt{\left(\frac{f}{f_{cTM01}}\right)^2 - \frac{u_{mn}^2}{u_{01}^2}} \cdot \sqrt{\left(\frac{f}{f_{cTM01}}\right)^2 - \frac{u_{m'n'}^2}{u_{01}^2}}}, \quad (A.9)$$

where

$$c_{MM1} = \frac{(-1)^{n+n'}}{2(u_{m'n'}^2 - u_{mn}^2)^2}. \quad (A.10)$$

From Eqs. (A.6) and (A.9), it is obvious that $rC_{(m'n')(mn)}$ is dependent only on ff_{cTM01} .

A.3 TE_{mn} to TM_{m'n'} mode, $C_{(m'n')[mn]}$

(i) when $m = 0$:

$$C_{(m'n')[mn]}^{\pm} = \begin{cases} 0 & (n = n') \\ \frac{(1 \pm 1)}{2\sqrt{2} \cdot u_{m'n'}} \cdot \frac{kD}{2r} & (n \neq n') \end{cases}, \quad (A.11)$$

so

$$rC_{(m'n')[mn]}^{\pm} = \begin{cases} 0 & (n = n') \\ \frac{(1 \pm 1)u_{01}}{2\sqrt{2} \cdot u_{m'n'}} \cdot \frac{f}{f_{cTM01}} & (n \neq n') \end{cases}. \quad (A.12)$$

(ii) when $m > 0$:

the coupling coefficient is

$$C_{(m'n')[mn]}^{\pm} = \frac{-m(\beta_{mn} \pm \beta_{m'n'})}{2\sqrt{v_{mn}^2 - m^2} (u_{m'n'}^2 - v_{mn}^2) \cdot \sqrt{\beta_{mn} \cdot \beta_{m'n'}}} \cdot \frac{(-1)^{m+m'+1} \cdot kD}{2r}. \quad (A.13)$$

Then $rC_{(m'n')[mn]}$ is formulated as:

$$rC_{(m'n')[mn]}^{\pm} = c_{ME0} u_{01} \cdot \frac{\sqrt{\left(\frac{f}{f_{cTM01}}\right)^2 - \frac{u_{mn}^2}{u_{01}^2}} \pm \sqrt{\left(\frac{f}{f_{cTM01}}\right)^2 - \frac{u_{m'n'}^2}{u_{01}^2}}}{\sqrt{\left(\frac{f}{f_{cTM01}}\right)^2 - \frac{u_{mn}^2}{u_{01}^2}} \cdot \sqrt{\left(\frac{f}{f_{cTM01}}\right)^2 - \frac{u_{m'n'}^2}{u_{01}^2}}} \cdot \frac{f}{f_{cTM01}}, \quad (\text{A.14})$$

where

$$c_{ME0} = \frac{-m \cdot (-1)^{m+m'+1}}{2\sqrt{v_{mn}^2 - m^2(u_{m'n'}^2 - v_{mn}^2)}}. \quad (\text{A.15})$$

From Eq. (A.12) and (A.14), it is evident that the $rC_{(m'n')[mn]}$ hinges on ff_{cTM01} .

Based on the above derivations for all coupling coefficients, the dependence of the term rC on ff_{cTM01} has been thoroughly demonstrated.

B. Theoretical and numerical calculation of mode conversion of TM_{01} , TE_{01} , and TE_{11} mode (under horizontal and vertical polarizations) due to a bend

The remained theoretical and numerical results of mode conversion are presented in this section. From the results of TM_{01} , TE_{01} , and TE_{11} mode under horizontal polarization, it seems that the theoretical and simulation results are not perfectly consistent when the value of r/D becomes small. Besides, at some cut-off frequency points, some discontinuities in theoretical results also occur. This is probably because the theoretical model of mode conversion, which is in fact a differential equation system, was solved numerically in this study, meaning that the calculation is not 100% errorless. But on the other hand, all the simulation results for the three inner pipe diameters D exhibit great consistency, proving the dependence of mode conversion on the three factors: r/D , α , and ff_{c} .

B.1. Mode conversion of TM_{01} mode for different r/D and α values

Nine groups of mode conversion of TM_{01} mode at a bend are shown in Figs. B-1 to B-9.

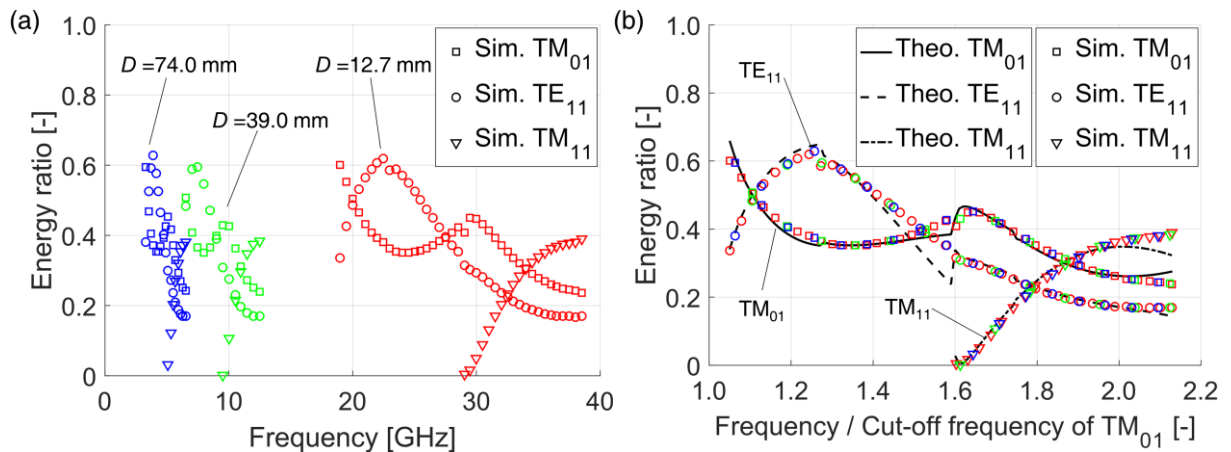


Fig. B-1 Mode conversion of TM_{01} mode microwaves at a bend ($r/D = 1$, $\alpha = 90^\circ$), (a) simulated fractional energy for $D = 12.7$, 39.0 , and 74.0 mm, (b) comparison between the theoretical results and normalized simulation results.

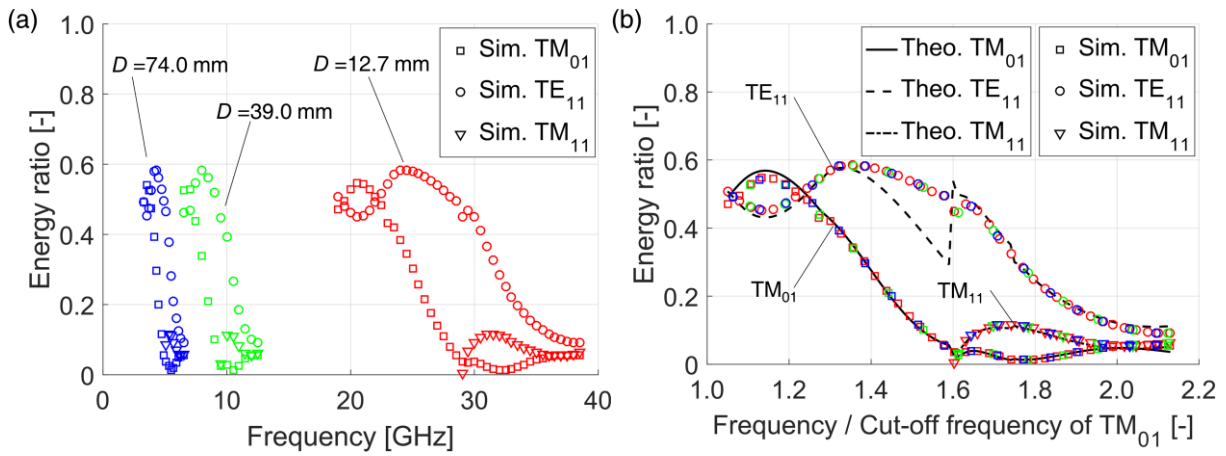


Fig. B-2 Mode conversion of TM_{01} mode microwaves at a bend ($r/D = 1$, $\alpha = 180^\circ$), (a) simulated fractional energy for $D = 12.7$, 39.0 , and 74.0 mm, (b) comparison between the theoretical results and normalized simulation results.

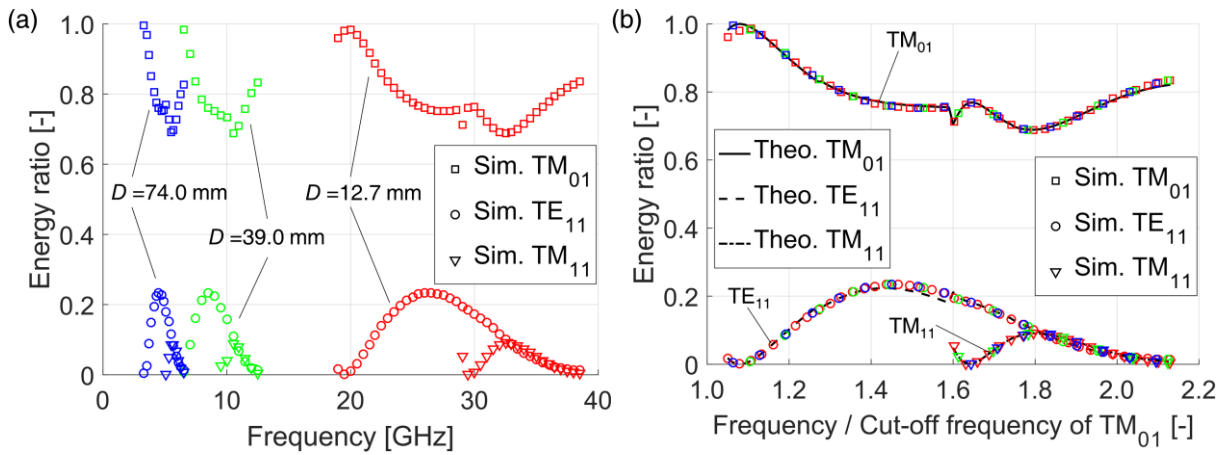


Fig. B-3 Mode conversion of TM_{01} mode microwaves at a bend ($r/D = 2$, $\alpha = 90^\circ$), (a) simulated fractional energy for $D = 12.7$, 39.0 , and 74.0 mm, (b) comparison between the theoretical results and normalized simulation results.

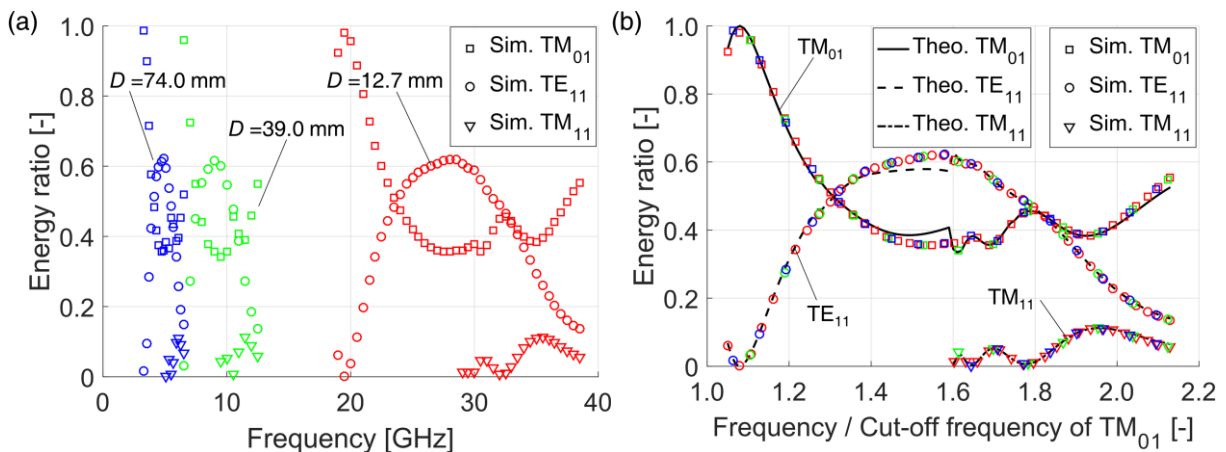


Fig. B-4 Mode conversion of TM_{01} mode microwaves at a bend ($r/D = 2$, $\alpha = 180^\circ$), (a) simulated fractional energy for $D = 12.7$, 39.0 , and 74.0 mm, (b) comparison between the theoretical results and normalized simulation results.

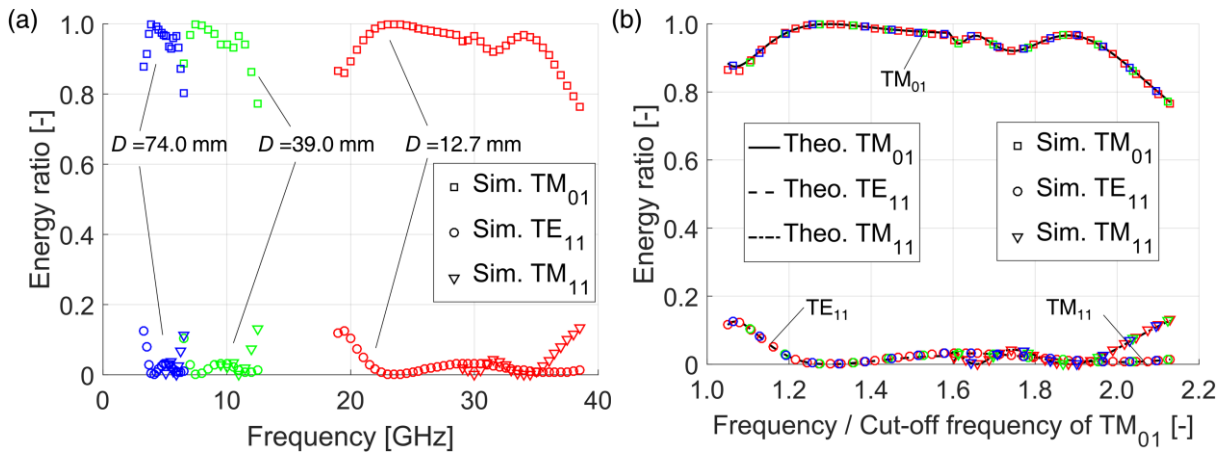


Fig. B-5 Mode conversion of TM_{01} mode microwaves at a bend ($r/D = 3$, $\alpha = 90^\circ$), (a) simulated fractional energy for $D = 12.7$, 39.0, and 74.0 mm, (b) comparison between the theoretical results and normalized simulation results.

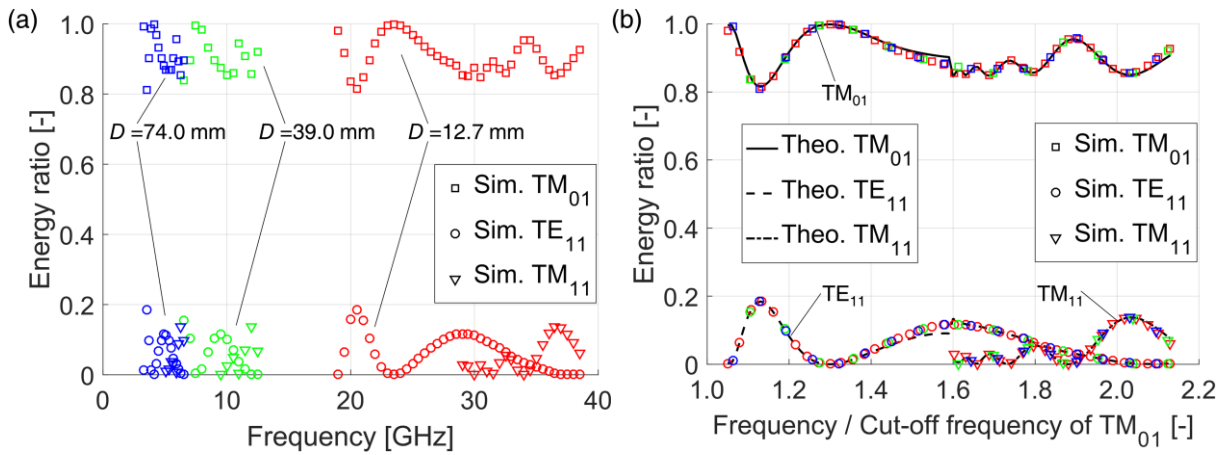


Fig. B-6 Mode conversion of TM_{01} mode microwaves at a bend ($r/D = 3$, $\alpha = 180^\circ$), (a) simulated fractional energy for $D = 12.7$, 39.0, and 74.0 mm, (b) comparison between the theoretical results and normalized simulation results.

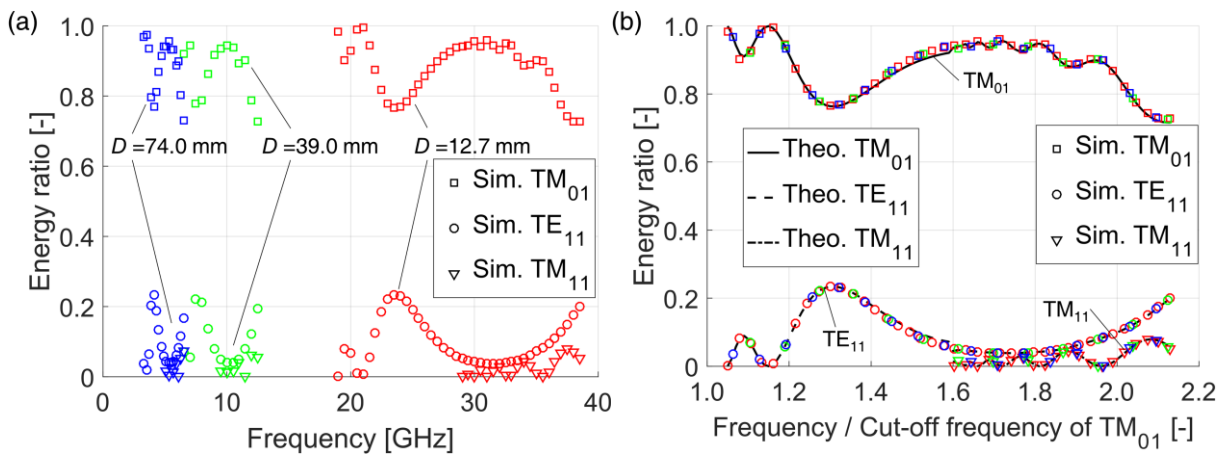


Fig. B-7 Mode conversion of TM_{01} mode microwaves at a bend ($r/D = 4$, $\alpha = 180^\circ$), (a) simulated fractional energy for $D = 12.7$, 39.0, and 74.0 mm, (b) comparison between the theoretical results and normalized simulation results.

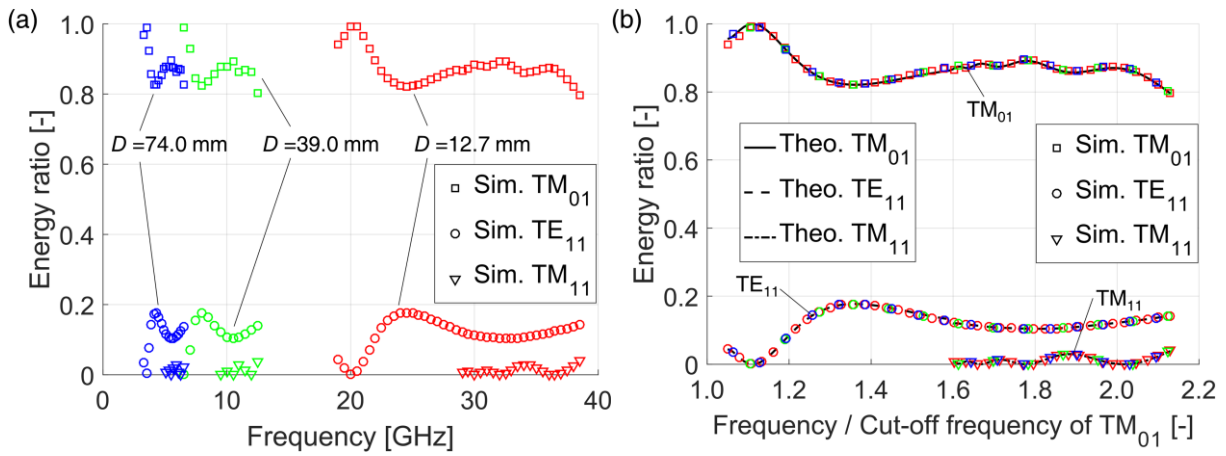


Fig. B-8 Mode conversion of TM_{01} mode microwaves at a bend ($r/D = 5$, $\alpha = 90^\circ$), (a) simulated fractional energy for $D = 12.7$, 39.0, and 74.0 mm, (b) comparison between the theoretical results and normalized simulation results.

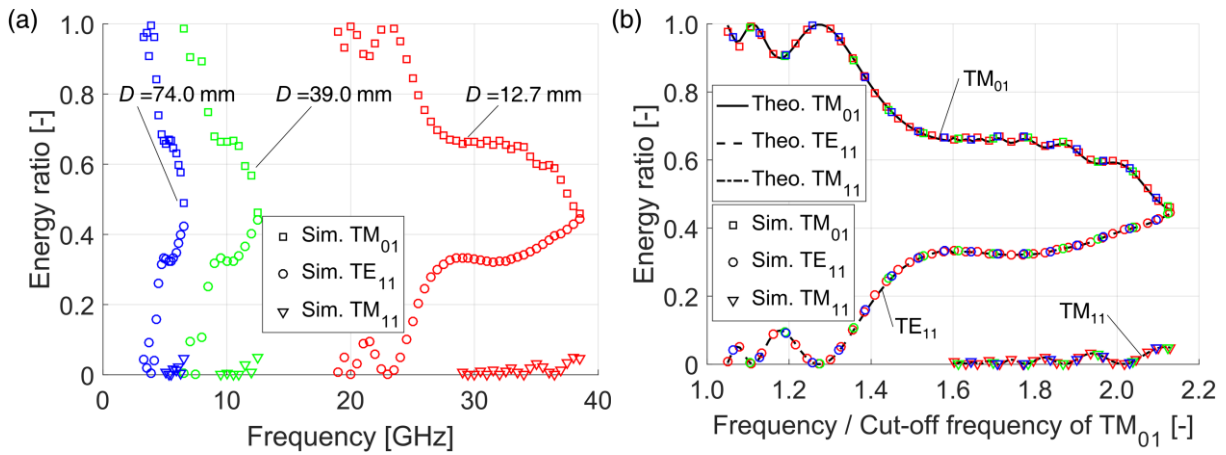


Fig. B-9 Mode conversion of TM_{01} mode microwaves at a bend ($r/D = 5$, $\alpha = 180^\circ$), (a) simulated fractional energy for $D = 12.7$, 39.0, and 74.0 mm, (b) comparison between the theoretical results and normalized simulation results.

B.2. Mode conversion of TE_{01} mode for different r/D and α values

Nine groups of mode conversion of TE_{01} mode at a bend are shown in Figs. B-10 to B-18. To TE_{01} mode, the bend angle seems to be a more influential factor of mode conversion when r/D is certain.

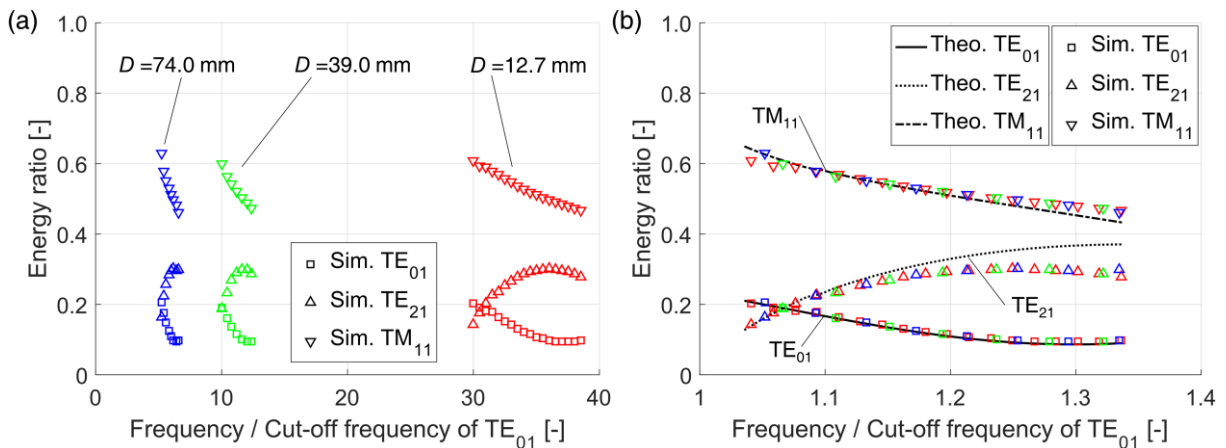


Fig. B-10 Mode conversion of TE_{01} mode microwaves at a bend ($r/D = 1$, $\alpha = 90^\circ$), (a) simulated

fractional energy for $D = 12.7, 39.0,$ and 74.0 mm, (b) comparison between the theoretical results and normalized simulation results.

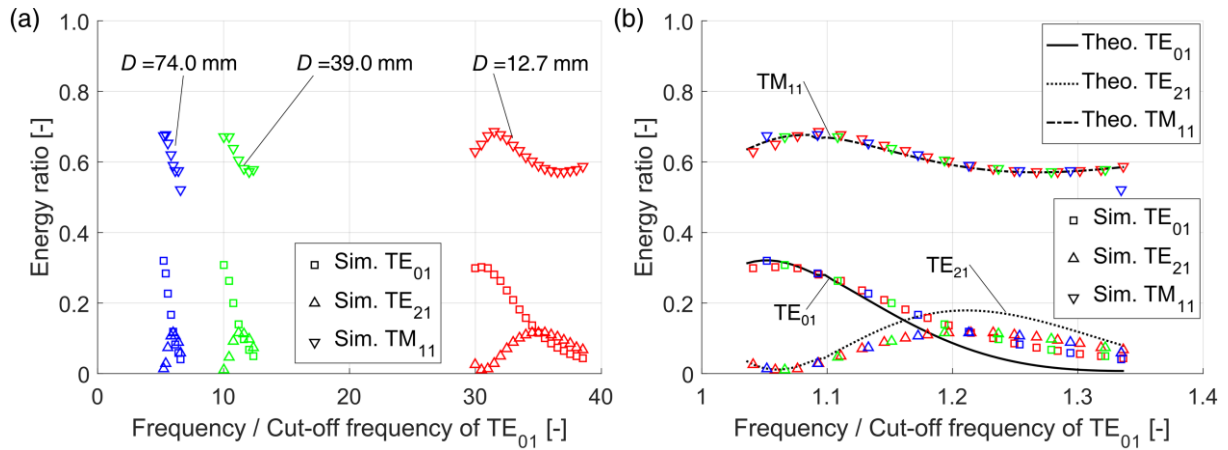


Fig. B-11 Mode conversion of TE_{01} mode microwaves at a bend ($r/D = 1, \alpha = 180^\circ$), (a) simulated fractional energy for $D = 12.7, 39.0,$ and 74.0 mm, (b) comparison between the theoretical results and normalized simulation results.

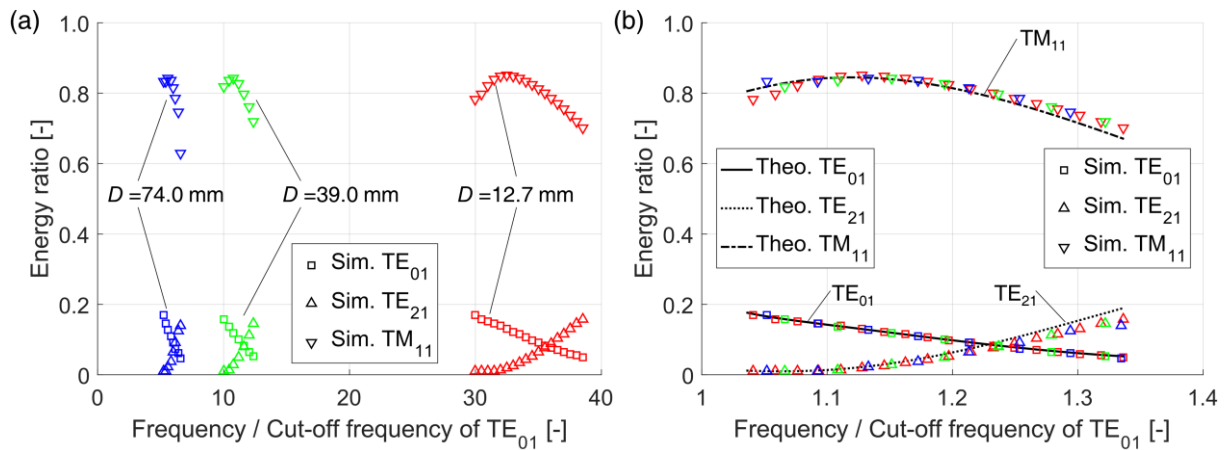


Fig. B-12 Mode conversion of TE_{01} mode microwaves at a bend ($r/D = 2, \alpha = 90^\circ$), (a) simulated fractional energy for $D = 12.7, 39.0,$ and 74.0 mm, (b) comparison between the theoretical results and normalized simulation results.

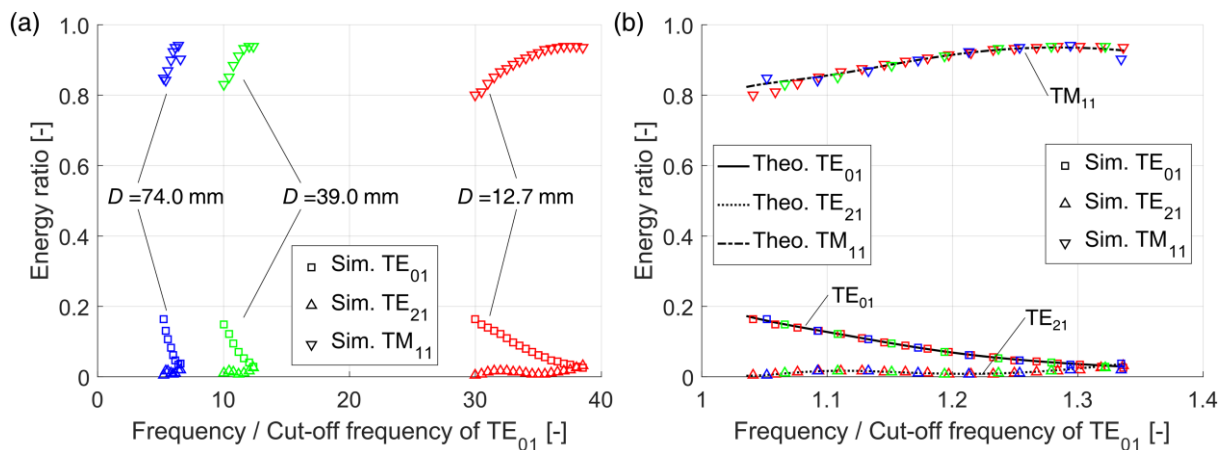


Fig. B-13 Mode conversion of TE_{01} mode microwaves at a bend ($r/D = 3, \alpha = 90^\circ$), (a) simulated

fractional energy for $D = 12.7, 39.0,$ and 74.0 mm, (b) comparison between the theoretical results and normalized simulation results.

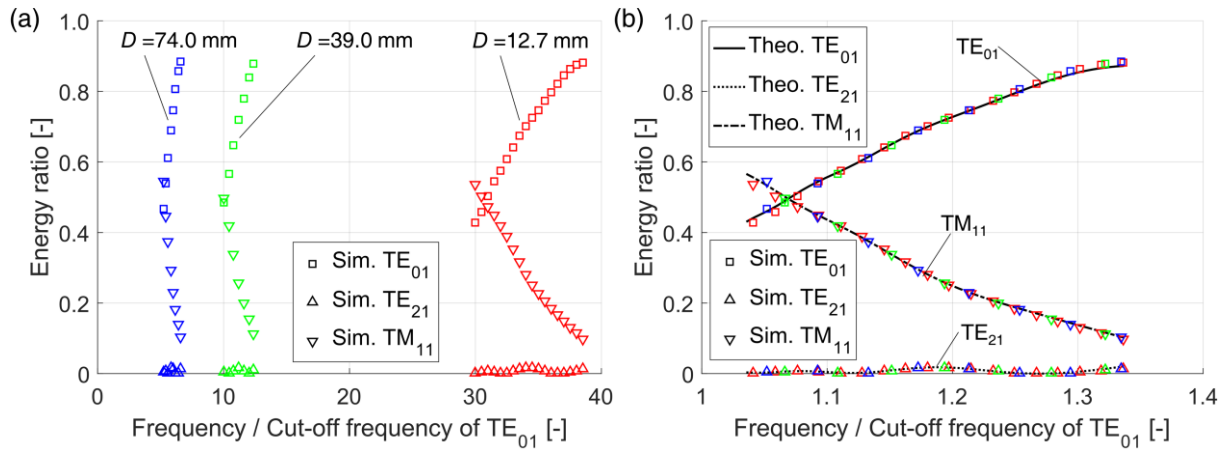


Fig. B-14 Mode conversion of TE_{01} mode microwaves at a bend ($r/D = 3, \alpha = 180^\circ$), (a) simulated fractional energy for $D = 12.7, 39.0,$ and 74.0 mm, (b) comparison between the theoretical results and normalized simulation results.

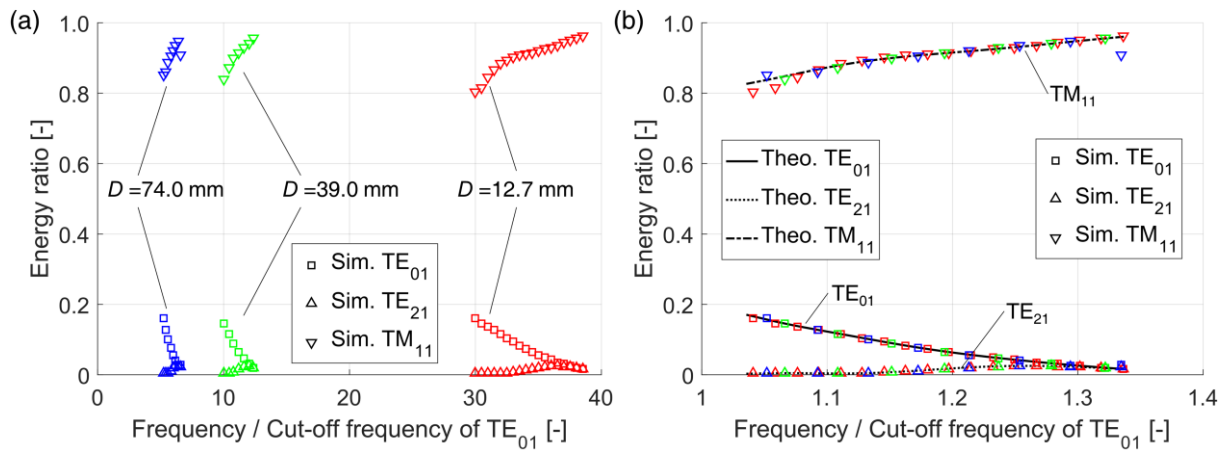


Fig. B-15 Mode conversion of TE_{01} mode microwaves at a bend ($r/D = 4, \alpha = 90^\circ$), (a) simulated fractional energy for $D = 12.7, 39.0,$ and 74.0 mm, (b) comparison between the theoretical results and normalized simulation results.

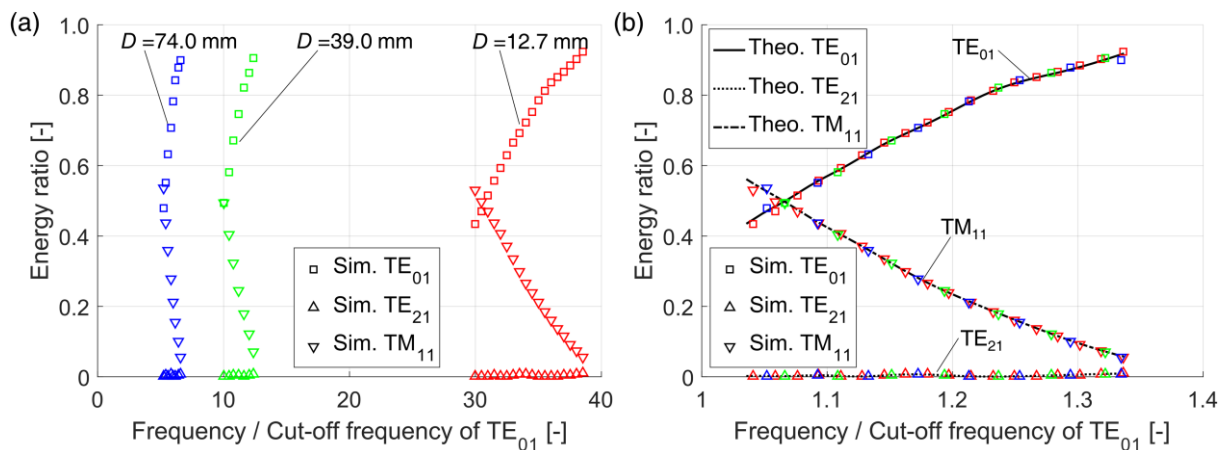


Fig. B-16 Mode conversion of TE_{01} mode microwaves at a bend ($r/D = 4, \alpha = 180^\circ$), (a) simulated

fractional energy for $D = 12.7, 39.0,$ and 74.0 mm, (b) comparison between the theoretical results and normalized simulation results.

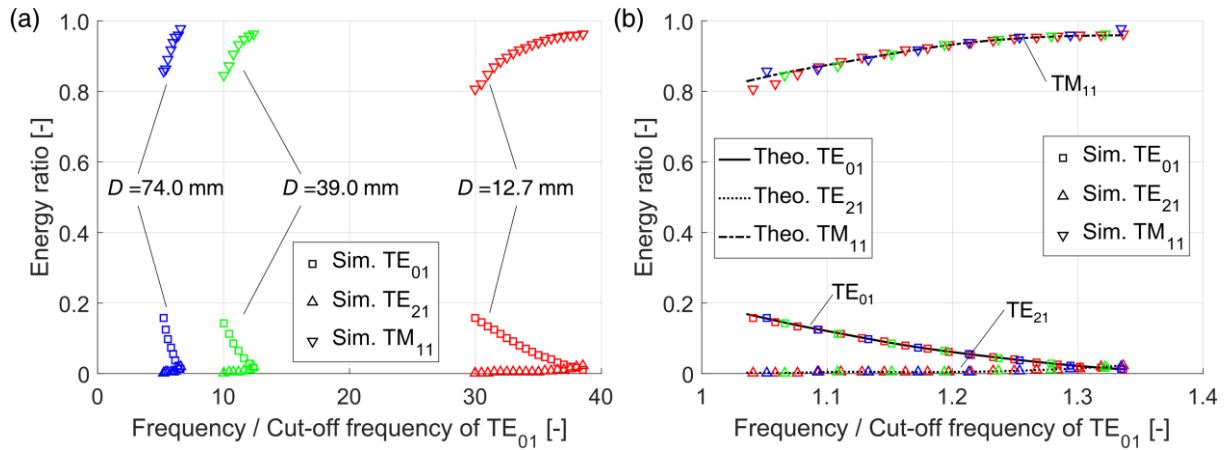


Fig. B-17 Mode conversion of TE_{01} mode microwaves at a bend ($r/D = 5, \alpha = 90^\circ$), (a) simulated fractional energy for $D = 12.7, 39.0,$ and 74.0 mm, (b) comparison between the theoretical results and normalized simulation results.

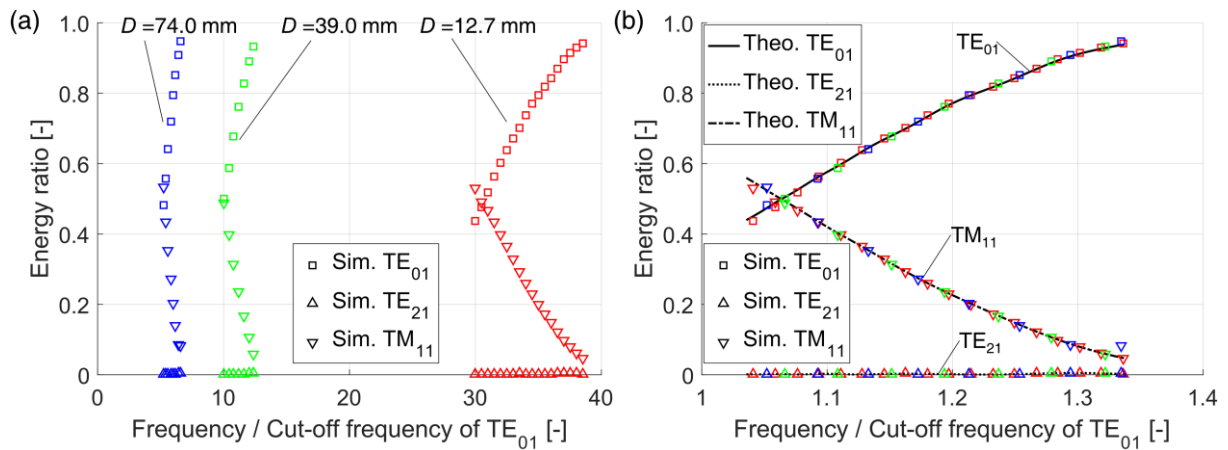


Fig. B-18 Mode conversion of TE_{01} mode microwaves at a bend ($r/D = 5, \alpha = 180^\circ$), (a) simulated fractional energy for $D = 12.7, 39.0,$ and 74.0 mm, (b) comparison between the theoretical results and normalized simulation results.

B.3. Mode conversion of TE_{11} mode under horizontal polarization for different r/D and α values

Nine groups of mode conversion of TE_{11} mode under horizontal polarization at a bend are shown in Figs. B-19 to B-27.

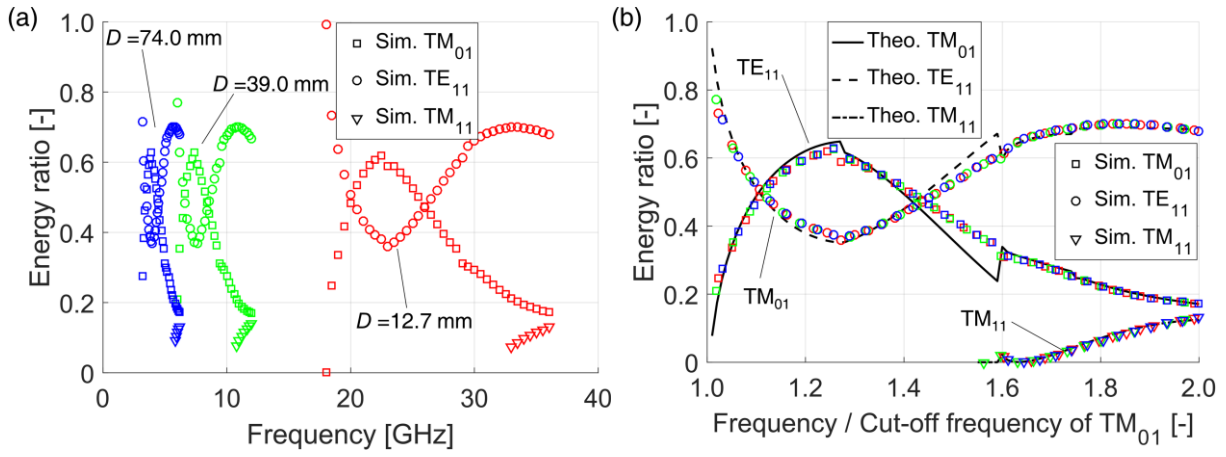


Fig. B-19 Mode conversion of TE_{11} mode microwaves under horizontal polarization at a bend ($r/D = 1$, $\alpha = 90^\circ$), (a) simulated fractional energy for $D = 12.7, 39.0,$ and 74.0 mm, (b) comparison between the theoretical results and normalized simulation results.

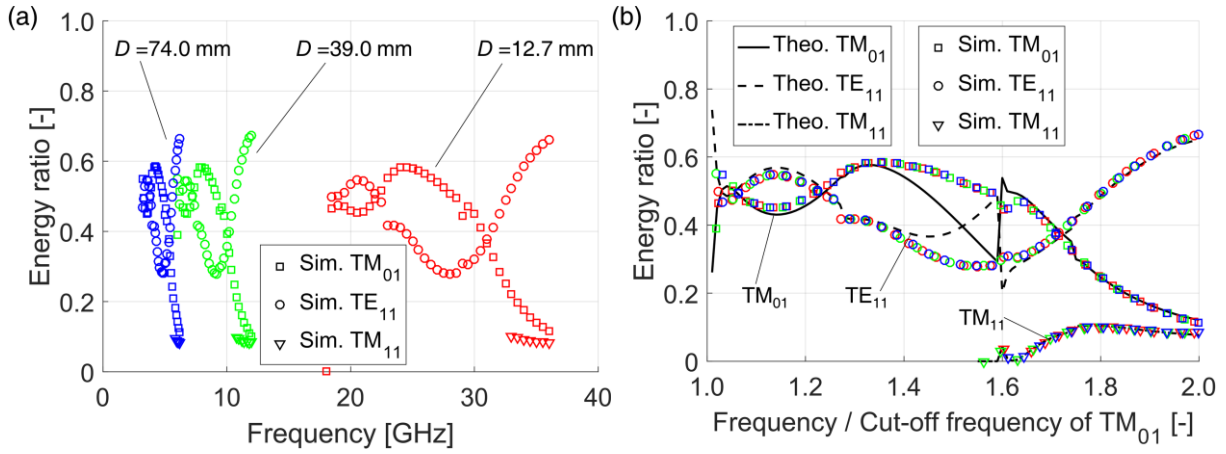


Fig. B-20 Mode conversion of TE_{11} mode microwaves under horizontal polarization at a bend ($r/D = 1$, $\alpha = 180^\circ$), (a) simulated fractional energy for $D = 12.7, 39.0,$ and 74.0 mm, (b) comparison between the theoretical results and normalized simulation results.

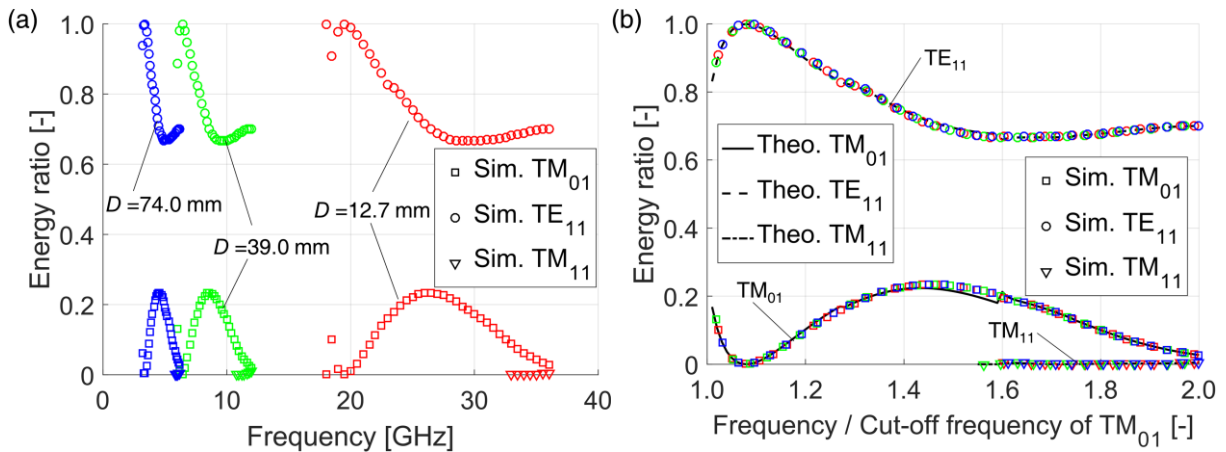


Fig. B-21 Mode conversion of TE_{11} mode microwaves under horizontal polarization at a bend ($r/D = 2$, $\alpha = 90^\circ$), (a) simulated fractional energy for $D = 12.7, 39.0,$ and 74.0 mm, (b) comparison between the theoretical results and normalized simulation results.

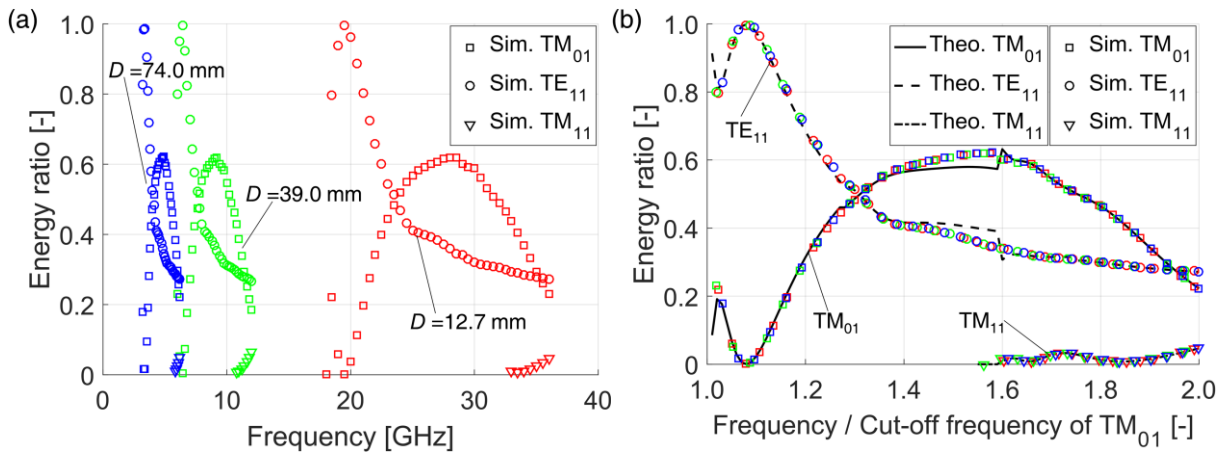


Fig. B-22 Mode conversion of TE_{11} mode microwaves under horizontal polarization at a bend ($r/D = 2$, $\alpha = 180^\circ$), (a) simulated fractional energy for $D = 12.7, 39.0,$ and 74.0 mm, (b) comparison between the theoretical results and normalized simulation results.

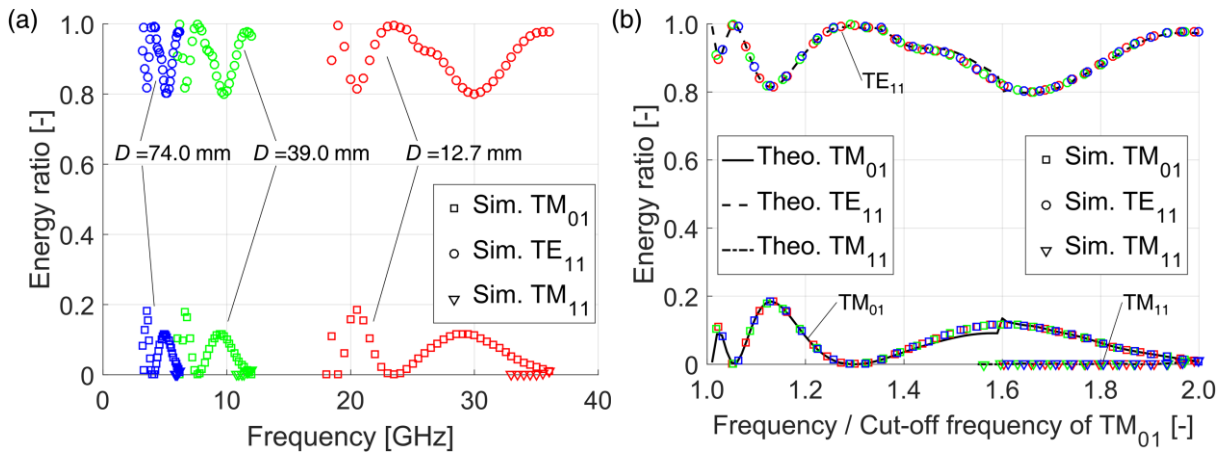


Fig. B-23 Mode conversion of TE_{11} mode microwaves under horizontal polarization at a bend ($r/D = 3$, $\alpha = 180^\circ$), (a) simulated fractional energy for $D = 12.7, 39.0,$ and 74.0 mm, (b) comparison between the theoretical results and normalized simulation results.

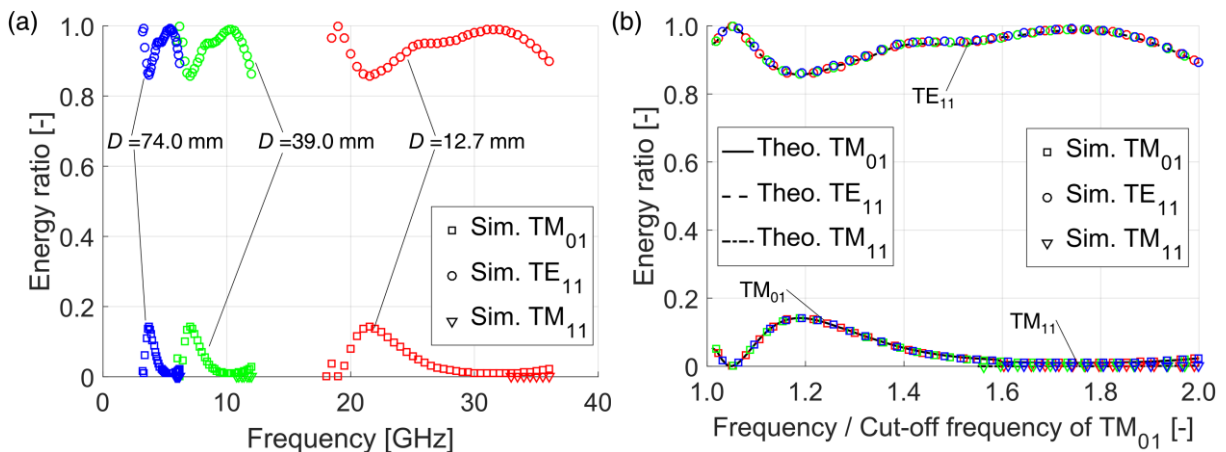


Fig. B-24 Mode conversion of TE_{11} mode microwaves under horizontal polarization at a bend ($r/D = 4$, $\alpha = 90^\circ$), (a) simulated fractional energy for $D = 12.7, 39.0,$ and 74.0 mm, (b) comparison between the theoretical results and normalized simulation results.

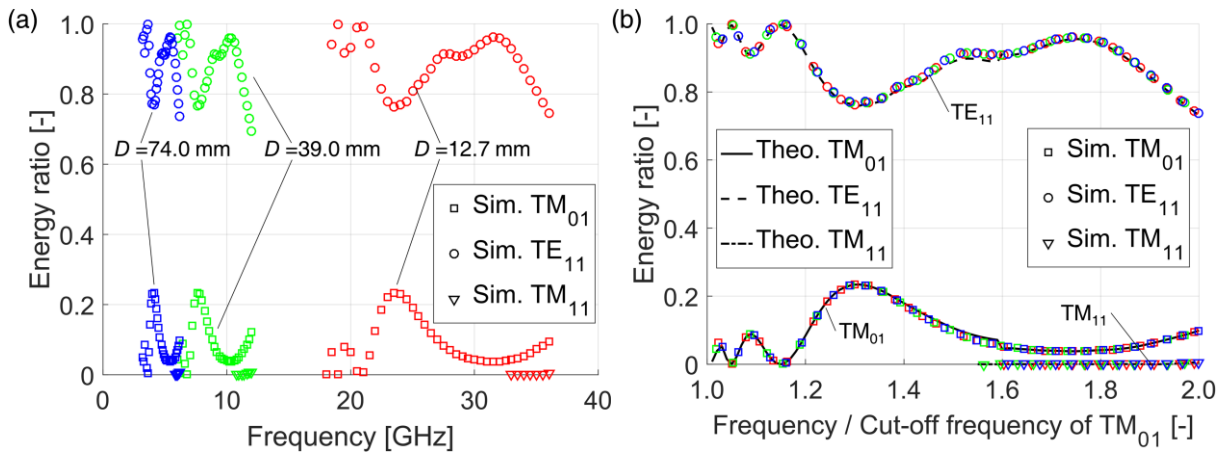


Fig. B-25 Mode conversion of TE_{11} mode microwaves under horizontal polarization at a bend ($r/D = 4$, $\alpha = 180^\circ$), (a) simulated fractional energy for $D = 12.7, 39.0$, and 74.0 mm, (b) comparison between the theoretical results and normalized simulation results.

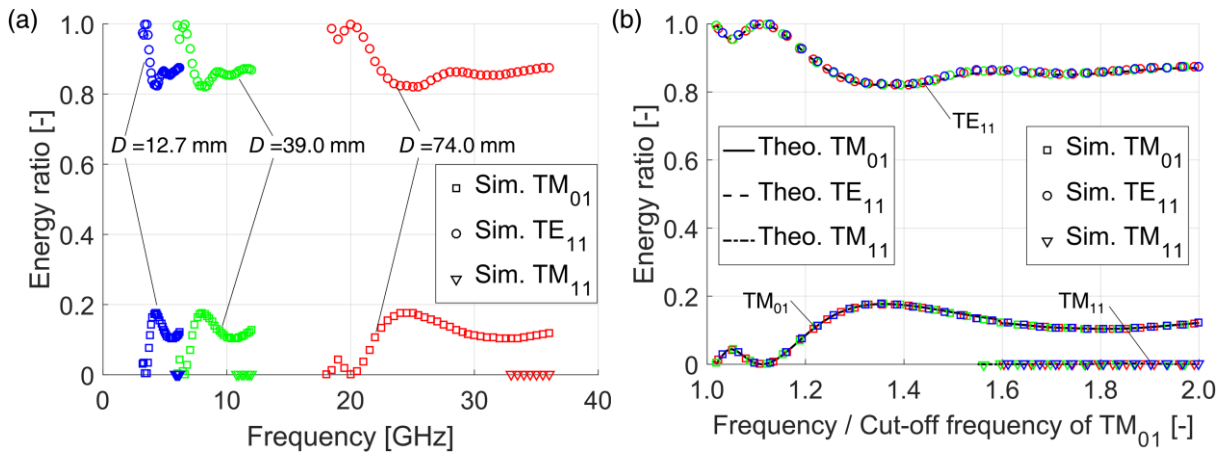


Fig. B-26 Mode conversion of TE_{11} mode microwaves under horizontal polarization at a bend ($r/D = 5$, $\alpha = 90^\circ$), (a) simulated fractional energy for $D = 12.7, 39.0$, and 74.0 mm, (b) comparison between the theoretical results and normalized simulation results.

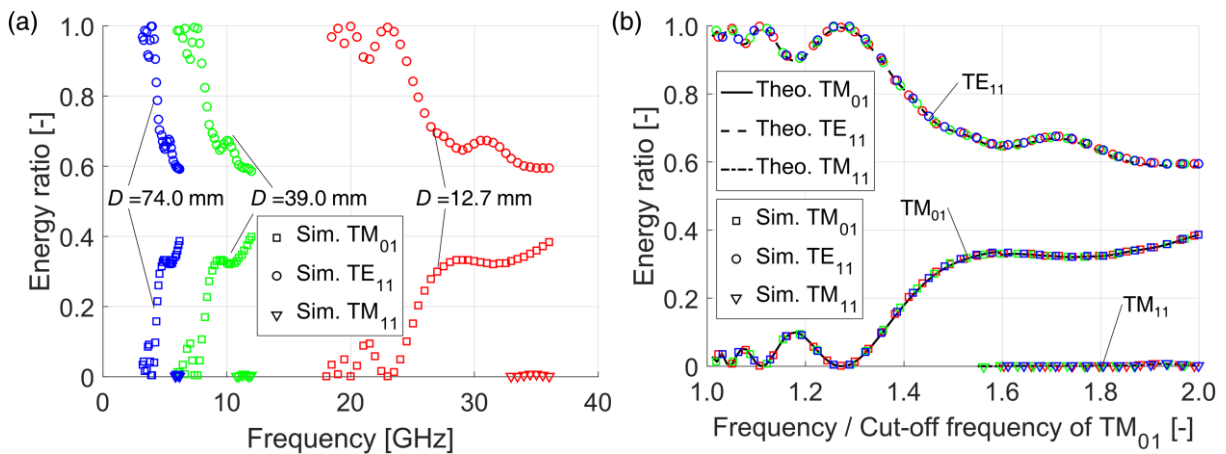


Fig. B-27 Mode conversion of TE_{11} mode microwaves under horizontal polarization at a bend ($r/D = 5$, $\alpha = 180^\circ$), (a) simulated fractional energy for $D = 12.7, 39.0$, and 74.0 mm, (b) comparison between the theoretical results and normalized simulation results.

B.4. Mode conversion of TE₁₁ mode under vertical polarization for different r/D and α values

Nine groups of mode conversion of TE₀₁ mode under vertical polarization at a bend are shown in Figs. B-28 to B-36. Note that only simulation results are presented.

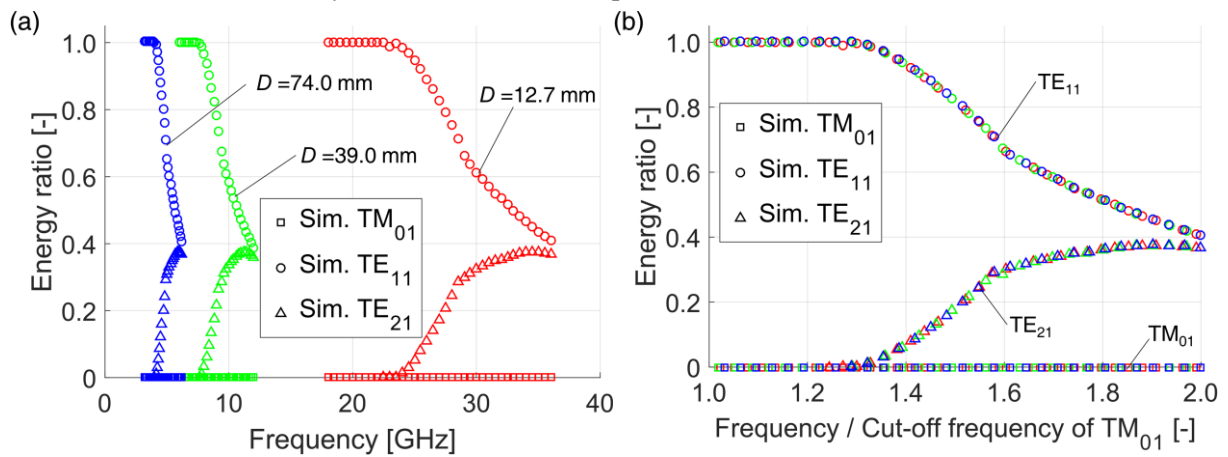


Fig. B-28 Mode conversion of TE₁₁ mode microwaves under vertical polarization at a bend ($r/D = 1$, $\alpha = 90^\circ$), (a) simulated fractional energy for $D = 12.7, 39.0$, and 74.0 mm, (b) normalized simulation results.

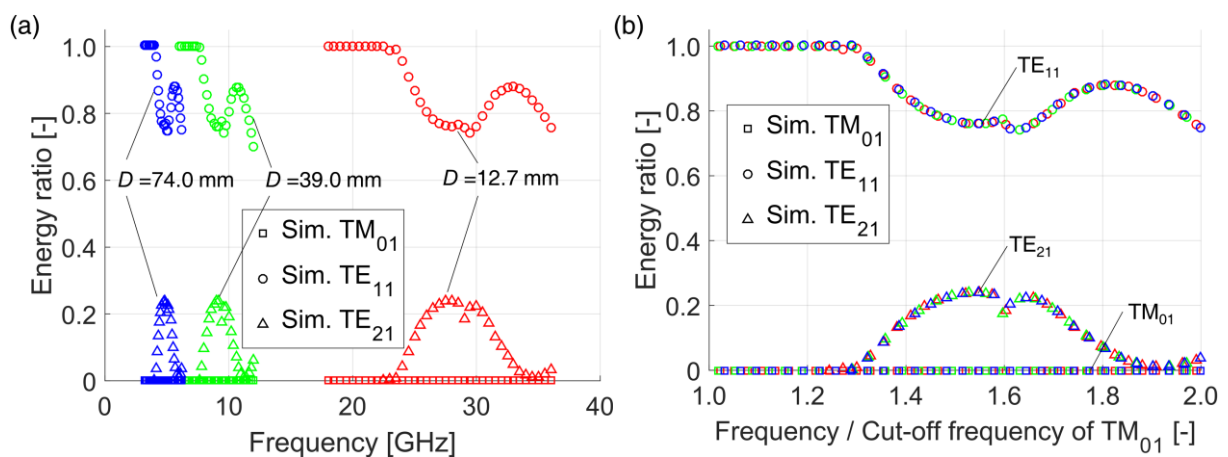


Fig. B-29 Mode conversion of TE₁₁ mode microwaves under vertical polarization at a bend ($r/D = 1$, $\alpha = 180^\circ$), (a) simulated fractional energy for $D = 12.7, 39.0$, and 74.0 mm, (b) normalized simulation results.

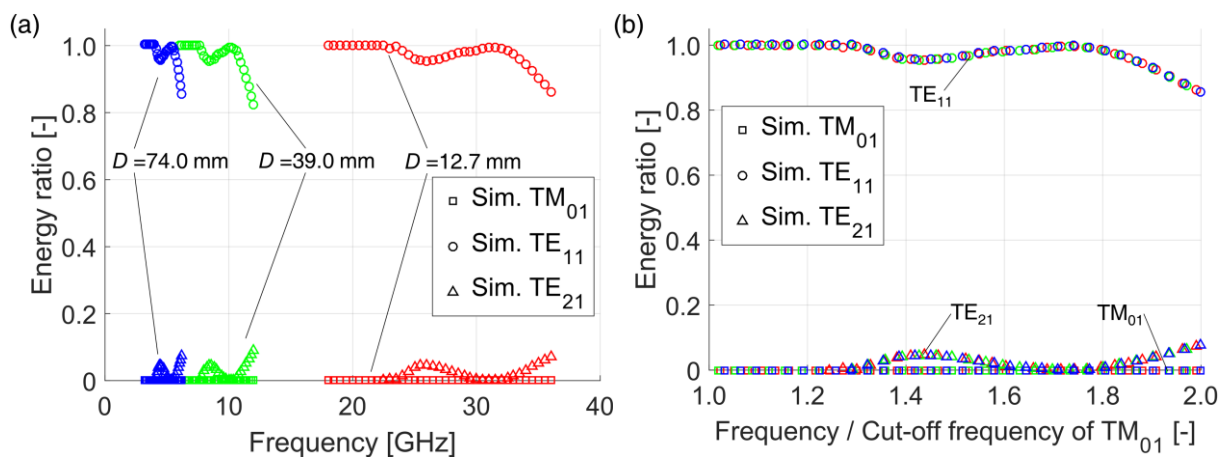


Fig. B-30 Mode conversion of TE₁₁ mode microwaves under vertical polarization at a bend ($r/D = 2$, $\alpha = 90^\circ$), (a) simulated fractional energy for $D = 12.7, 39.0$, and 74.0 mm, (b) normalized simulation results.

= 90°), (a) simulated fractional energy for $D=12.7, 39.0,$ and 74.0 mm, (b) normalized simulation results.

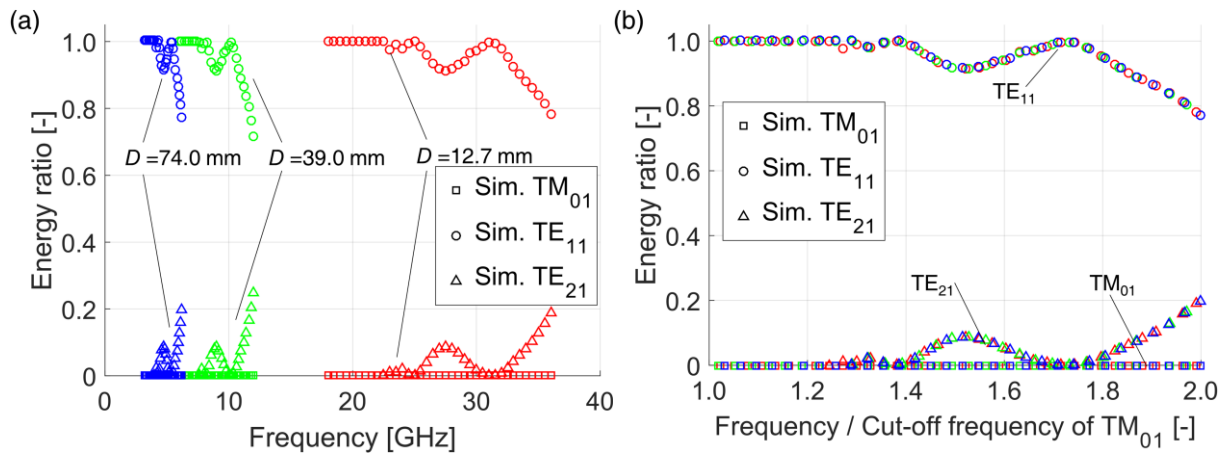


Fig. B-31 Mode conversion of TE_{11} mode microwaves under vertical polarization at a bend ($r/D = 2, \alpha = 180^\circ$), (a) simulated fractional energy for $D = 12.7, 39.0,$ and 74.0 mm, (b) normalized simulation results.

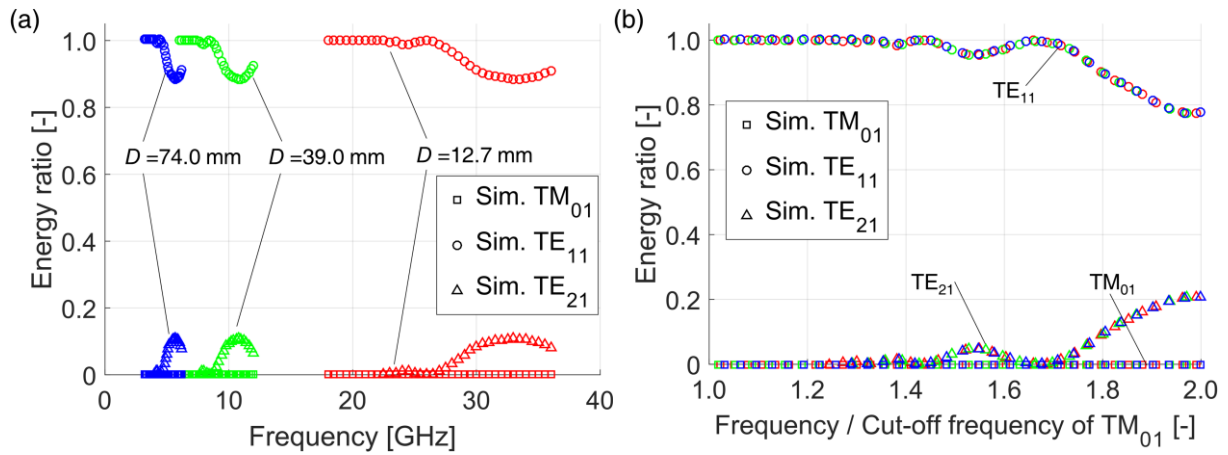


Fig. B-32 Mode conversion of TE_{11} mode microwaves under vertical polarization at a bend ($r/D = 3, \alpha = 180^\circ$), (a) simulated fractional energy for $D = 12.7, 39.0,$ and 74.0 mm, (b) normalized simulation results.

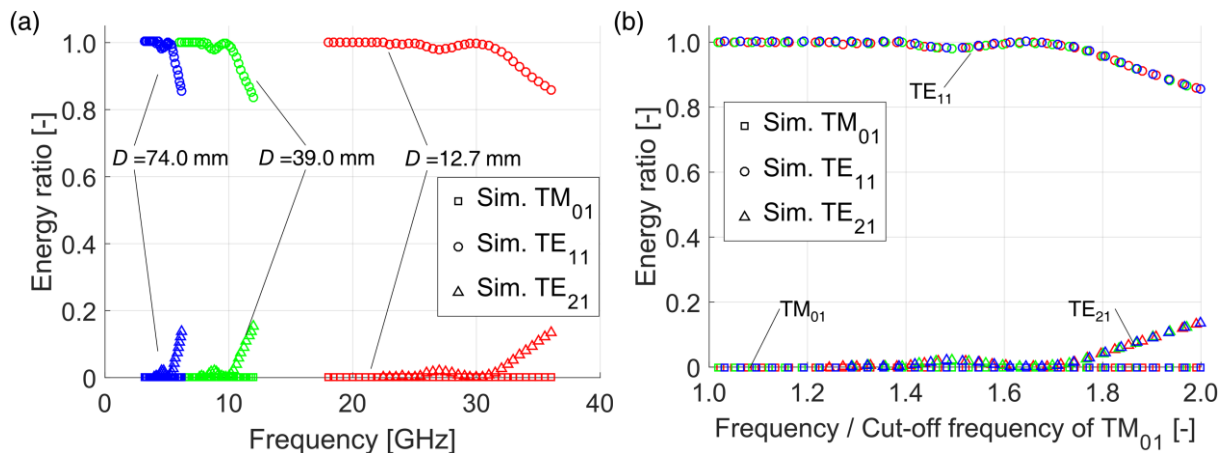


Fig. B-33 Mode conversion of TE_{11} mode microwaves under vertical polarization at a bend ($r/D = 4, \alpha = 90^\circ$), (a) simulated fractional energy for $D = 12.7, 39.0,$ and 74.0 mm, (b) normalized simulation results.

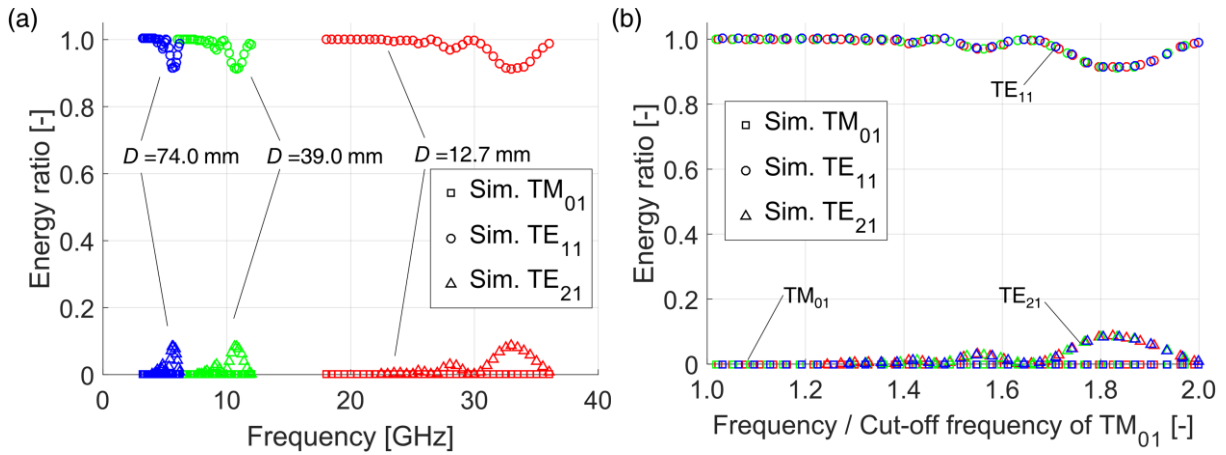


Fig. B-34 Mode conversion of TE_{11} mode microwaves under vertical polarization at a bend ($r/D = 4$, $\alpha = 180^\circ$), (a) simulated fractional energy for $D = 12.7$, 39.0 , and 74.0 mm, (b) normalized simulation results.

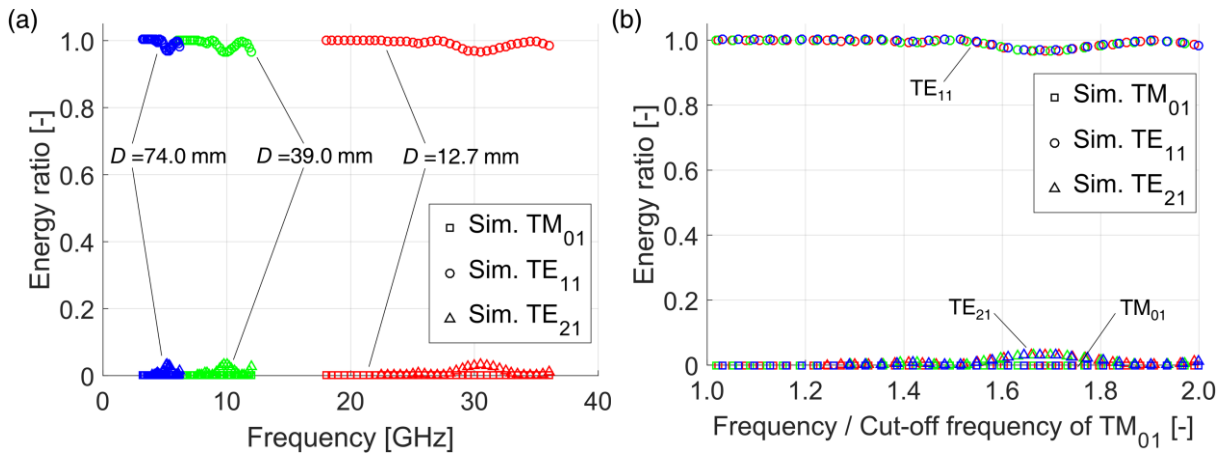


Fig. B-35 Mode conversion of TE_{11} mode microwaves under vertical polarization at a bend ($r/D = 5$, $\alpha = 90^\circ$), (a) simulated fractional energy for $D = 12.7$, 39.0 , and 74.0 mm, (b) normalized simulation results.

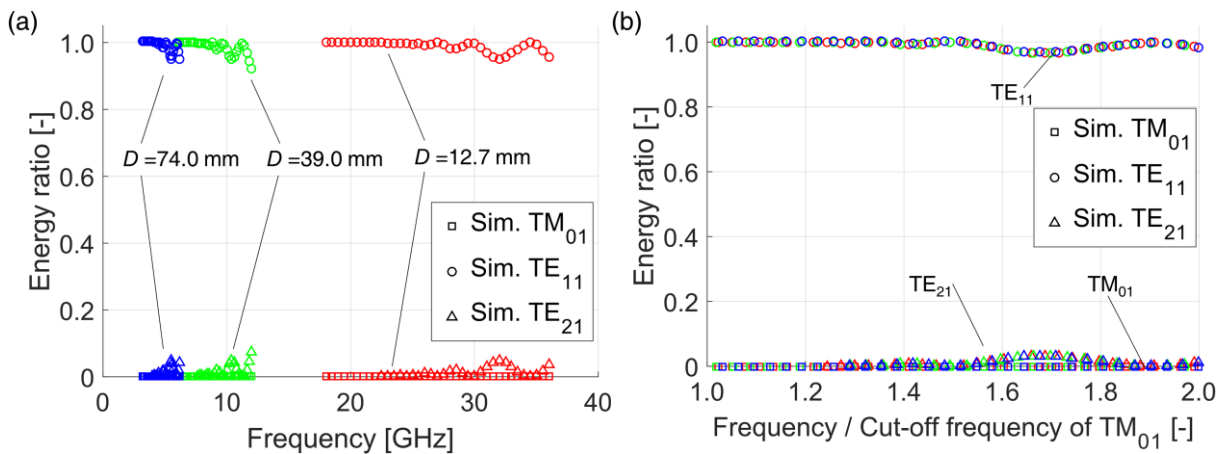


Fig. B-36 Mode conversion of TE_{11} mode microwaves under vertical polarization at a bend ($r/D = 5$, $\alpha = 180^\circ$), (a) simulated fractional energy for $D = 12.7$, 39.0 , and 74.0 mm, (b) normalized simulation results.

C. Additional test of the dual-port, side-incident probe using partial pipe wall thinning

The detectability of the two dual-port, side-incident microwave probes was additionally examined by detecting partial pipe wall thinning. The structure of the partial pipe wall thinning as well as the photograph of the short pipes is illustrated in Fig. C-1, and the dimensions are itemized in Table C-1.

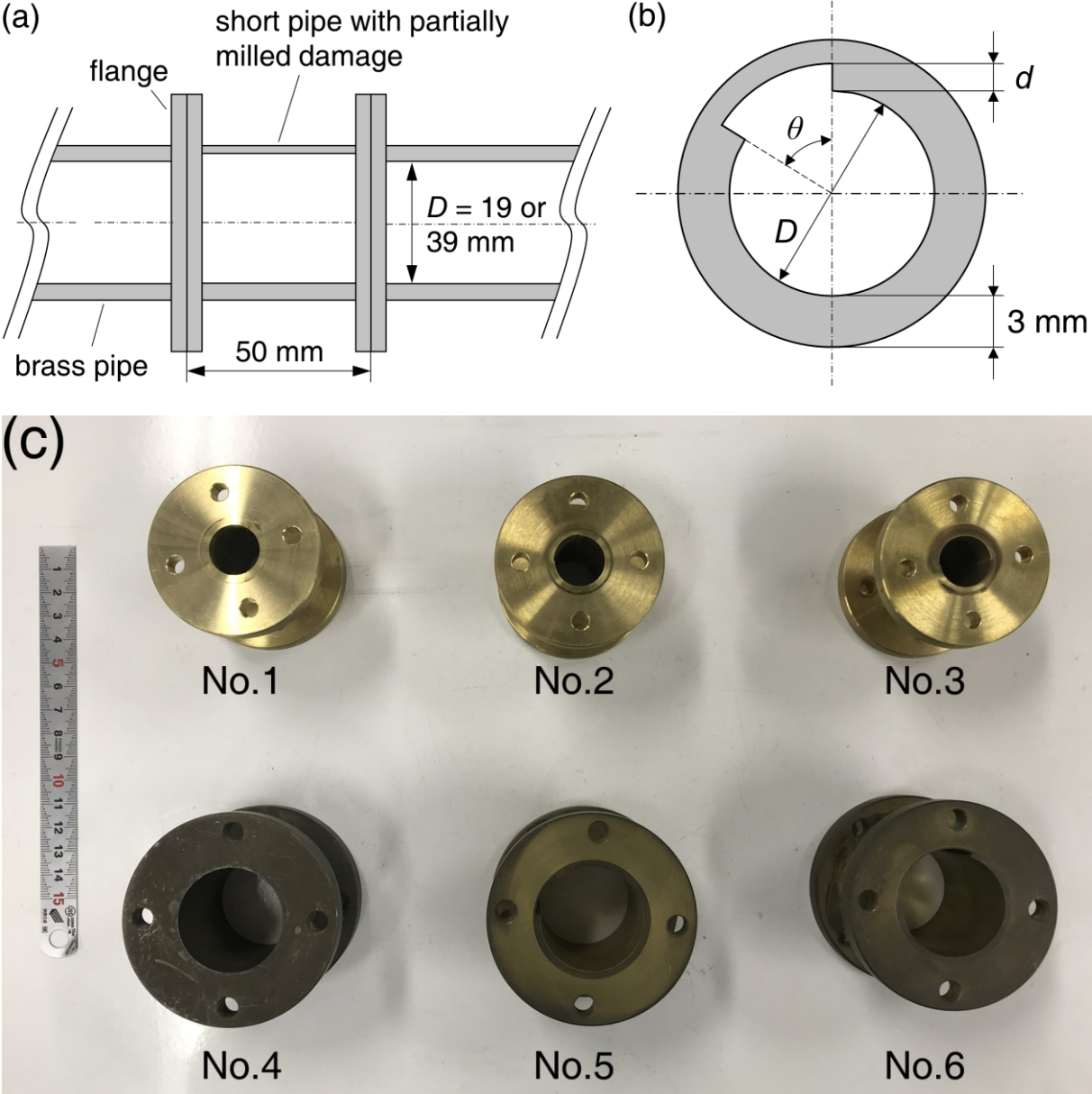


Fig. C-1 Illustration of the short pipe with partial pipe wall thinning, (a) side view, (b) cross-section (not to scale), and (c) photograph of short pipes with partial pipe wall thinning.

Table C-1 Dimensions of the short pipes used in the experiment.

No.	D (mm)	d (mm)	θ (deg.)
1	19.0	0	0
2	19.0	0.5	90
3	19.0	0.5	180
4	39.0	0	0
5	39.0	2	45
6	39.0	2	90

The experimental system is the same as Fig. 5-16. The experimental results are shown in Figs. C-2 to C-5. Although the reflections become smaller compared to the results in Section 5.3.2, the proposed side-incident probes still reflect good detection directivity.

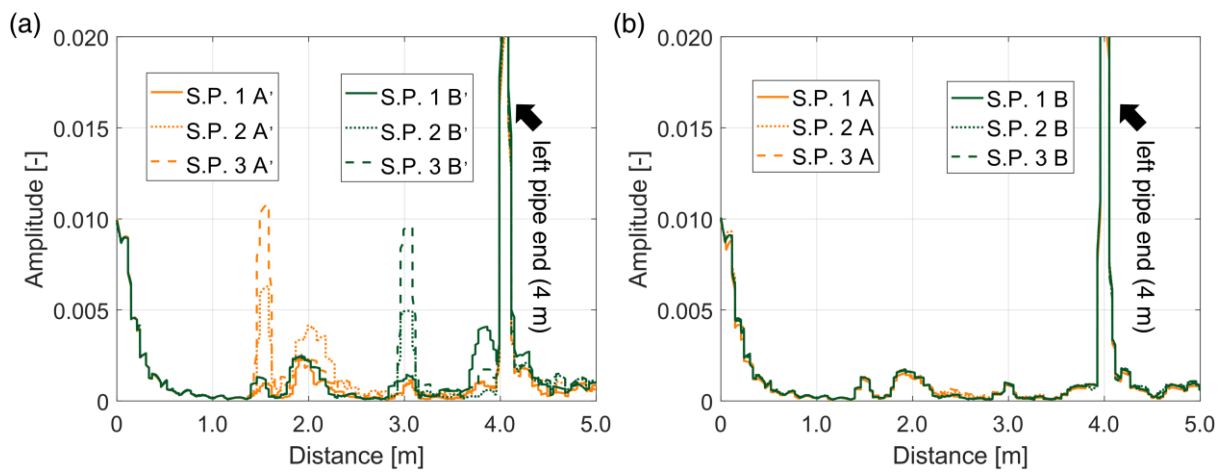


Fig. C-2 Reflection signals from the partial pipe wall thinning deployed at (a) points A' and B' and (b) points A and B when $D = 19$ mm and port L of the probe was used. The left pipe was 4 m in length and the right pipe was 4.5 m. (S.P. = short pipe)

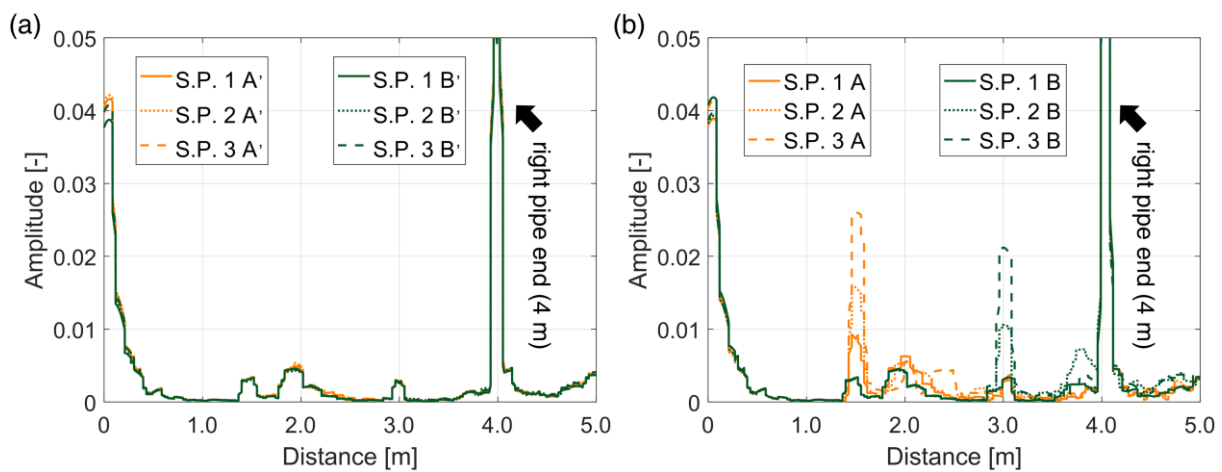


Fig. C-3 Reflection signals from the partial pipe wall thinning deployed at (a) points A' and B' and (b) points A and B when $D = 19$ mm and port R of the probe was used. The right pipe was 4 m in length and the left pipe was 4.5 m. (S.P. = short pipe)

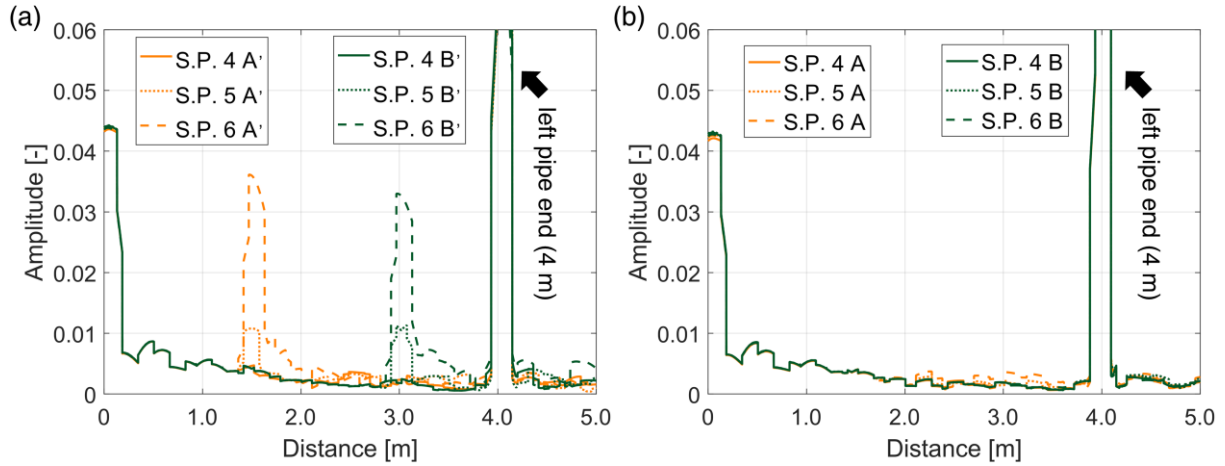


Fig. C-4 Reflection signals from the partial pipe wall thinning deployed at (a) points A' and B' and (b) points A and B when $D = 39$ mm and port L of the probe was used. The left pipe was 4 m in length and the right pipe was 4.5 m. (S.P. = short pipe)

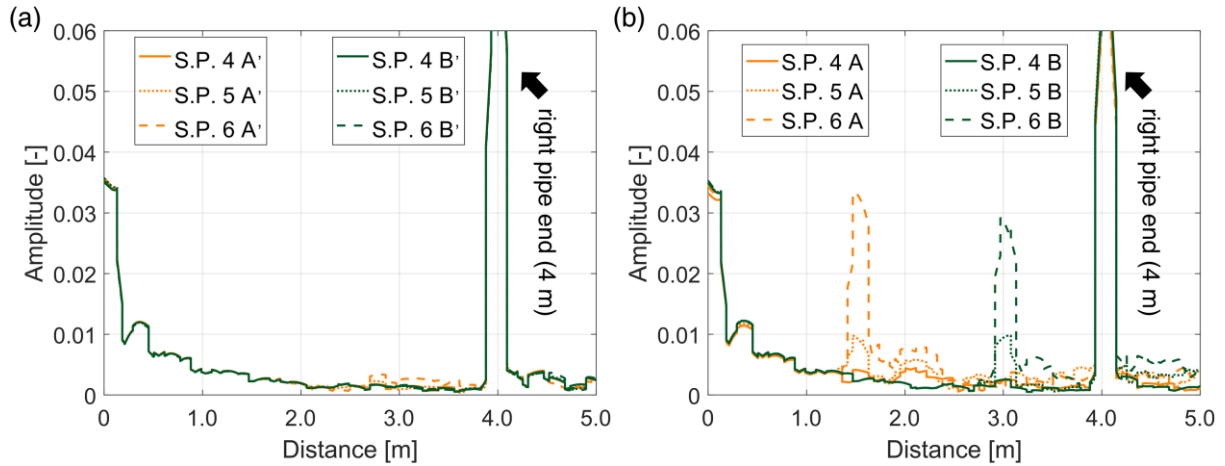


Fig. C-5 Reflection signals from the partial pipe wall thinning deployed at (a) points A' and B' and (b) points A and B when $D = 39$ mm and port R of the probe was used. The right pipe was 4 m in length and the left pipe was 4.5 m. (S.P. = short pipe)

Reference

(The format of reference is 'Vancouver'.)

- [1] Kobayashi H, Steam Eruption from Nuclear Power Plant Cooling System, Failure Knowledge Database, August 9th, 2004, Mihama, Fukui.
- [2] プレスリリース 071212_女川2号機HTR調査結果プレスF I X改(合本). 東北電力株式会社, 2007.12.18.
- [3] Bill Borchardt, Steam Generator Tube Degradations, U.S. Nuclear Regulatory Commission (NRC) commission meeting, February 7th, 2013.
- [4] Wade KC. Steam generator degradation and its impact on continued operation of pressurized water reactors in the United States. Energy Information Administration/Electric Power Monthly. 1995 Aug;66.
- [5] MacDonald PE, Shah VN, Ward LW, Ellison PG. Steam generator tube failures. Nuclear Regulatory Commission; 1996.
- [6] James Benson, Overview and Analysis of Historical Steam Generator Degradation Mechanisms, U.S. Nuclear Regulatory Commission (NRC) commission meeting, February 7th, 2013.
- [7] Airey GP, Vaia AR, Aspden RG. A Stress Corrosion Cracking Evaluation of Inconel 690 for Steam Generator Tubing Applications. Nuclear Technology. 1981 Nov 1;55(2):436-48.
- [8] Briceño DG, Castano ML, García MS. Stress corrosion cracking susceptibility of steam generator tube materials in AVT (all volatile treatment) chemistry contaminated with lead. Nuclear engineering and design. 1996 Aug 2;165(1-2):161-9.
- [9] Kim UC, Kim KM, Choi BS, Maeng WY. Electrochemical behaviors of alloy 690 in caustic solutions containing Pb at 300 C. Corrosion. 2010 Jan;66(1):015002.
- [10] Lucan D. Degradations of Incoloy 800 Steam Generator Tubing. In Steam Generator Systems: Operational Reliability and Efficiency 2011 Mar 16. IntechOpen.
- [11] Li N, Shi SQ, Luo J, Lu J, Wang N. Lead-induced stress corrosion cracking behavior of mechanically surface-treated alloy 690. Materials Research Letters. 2016 Jul 2;4(3):180-4.
- [12] Pietralik JM. The role of flow in flow-accelerated corrosion under nuclear power plant conditions. Japan Society of Maintenance, E-Journal of Advanced Maintenance. 2012;4(2):63-78.
- [13] Rani HP, Divya T, Sahaya RR, Kain V, Barua DK. CFD study of flow accelerated corrosion in 3D elbows. Annals of Nuclear energy. 2014 Jul 1;69:344-51.
- [14] Li R, Mori M, Ninokata H. A calculation methodology proposed for liquid droplet impingement erosion. Nuclear engineering and design. 2012 Jan 1;242:157-63.
- [15] Naitoh M, Okada H, Uchida S, Yugo H, Koshizuka S. Evaluation method for pipe wall thinning due to liquid droplet impingement. Nuclear Engineering and Design. 2013 Nov 1;264:195-202.
- [16] IEEE Standard Letter Designations for Radar-Frequency Bands," in IEEE Std 521-1984, vol., no., pp.1-8, 30 Nov. 1984, doi: 10.1109/IEEESTD.1984.81588.
- [17] Kharkovsky S, Zoughi R. Microwave and millimeter wave nondestructive testing and evaluation- Overview and recent advances. IEEE Instrumentation & Measurement Magazine. 2007 May 29;10(2):26-38.
- [18] Dobmann G, Altpeter I, Sklarczyk C, Pinchuk R. Non-destructive testing with micro-and MM-

- waves—Where we are—Where we go. *Welding in the World*. 2012 Jan 1;56(1-2):111-20.
- [19] Mubarak K, Bois KJ, Zoughi R. A simple, robust, and on-site microwave technique for determining water-to-cement ratio (w/c) of fresh Portland cement-based materials. *IEEE Transactions on Instrumentation and Measurement*. 2001 Oct;50(5):1255-63.
- [20] Bois KJ, Benally A, Nowak PS, Zoughi R. Microwave nondestructive determination of sand-to-cement ratio in mortar. *Journal of Research in Nondestructive Evaluation*. 1997 Jan 1;9(4):227-38.
- [21] Bois KJ, Benally AD, Nowak PS, Zoughi R. Cure-state monitoring and water-to-cement ratio determination of fresh Portland cement-based materials using near-field microwave techniques. *IEEE transactions on Instrumentation and Measurement*. 1998 Jun;47(3):628-37.
- [22] Peer S, Case JT, Gallaher E, Kurtis KE, Zoughi R. Microwave reflection and dielectric properties of mortar subjected to compression force and cyclically exposed to water and sodium chloride solution. *IEEE Transactions on Instrumentation and Measurement*. 2003 Apr 2;52(1):111-8.
- [23] Rashidi M, Knapp MC, Hashemi A, Kim JY, Donnell KM, Zoughi R, Jacobs LJ, Kurtis KE. Detecting alkali-silica reaction: A multi-physics approach. *Cement and Concrete Composites*. 2016 Oct 1;73:123-35.
- [24] Sklarczyk C. Microwave, millimeter wave and terahertz (MMT) techniques for materials characterization. In *Materials Characterization Using Nondestructive Evaluation (NDE) Methods 2016* Jan 1 (pp. 125-159). Woodhead Publishing.
- [25] Sklarczyk C, Porsch F, Wolter B, Boller C, Kurz JH. Nondestructive characterization of and defect detection in timber and wood. In *Advanced Materials Research 2013* (Vol. 778, pp. 295-302). Trans Tech Publications Ltd.
- [26] Jiang Y, Ju Y, Yang L. Nondestructive in-situ permittivity measurement of liquid within a bottle using an open-ended microwave waveguide. *Journal of Nondestructive Evaluation*. 2016 Mar 1;35(1):7.
- [27] Hashemi A, Donnell KM, Zoughi R, Knapp MC, Kurtis KE. Microwave detection of carbonation in mortar using dielectric property characterization. In *2014 IEEE International Instrumentation and Measurement Technology Conference (I2MTC) Proceedings 2014* May 12 (pp. 216-220). IEEE.
- [28] Li Z, Haigh A, Soutis C, Gibson A, Sloan R. Dielectric constant of a three-dimensional woven glass fibre composite: analysis and measurement. *Composite Structures*. 2017 Nov 15;180:853-61.
- [29] Li Z, Haigh A, Soutis C, Gibson A. X-band microwave characterisation and analysis of carbon fibre-reinforced polymer composites. *Composite Structures*. 2019 Jan 15;208:224-32.
- [30] Yakubov VP, Sklarczyk KG, Pinchuk RV, Sukhanov DY, Bulavinov AN, Bevetkii AD. Radio-wave tomography of hidden objects for safety systems. *Russian Physics Journal*. 2008 Oct 1;51(10):1064-82.
- [31] Sklarczyk C, Dobmann G, Melev V, Mayer K. Standoff Detection and Imaging of Suspicious and Concealed Objects with Electromagnetic Waves in the Centimetre and Millimetre Range.
- [32] Moll J, Krozer V, Zimmermann R, Rolef B, Salman R, Jaeschke T, Pohl N. Luggage scanning at 80 GHz for harbor environments. In *EUSAR 2014; 10th European Conference on Synthetic Aperture Radar 2014* Jun 3 (pp. 1-4). VDE.
- [33] Sheen DM, McMakin DL, Hall TE. Three-dimensional millimeter-wave imaging for concealed weapon detection. *IEEE Transactions on microwave theory and techniques*. 2001 Sep;49(9):1581-92.
- [34] Hughes D, Zoughi R, Austin R, Wood N, Engelbart R. Near-Field Microwave Detection of Corrosion Precursor Pitting under Thin Dielectric Coatings in Metallic Substrate. In *AIP Conference Proceedings 2003* Mar 27 (Vol. 657, No. 1, pp. 462-469). American Institute of Physics.
- [35] Ghasr M, Carroll B, Kharkovsky S, Zoughi R, Austin R. Size Evaluation of Corrosion Precursor Pitting Using Near-Field Millimeter Wave Nondestructive Testing Methods. In *AIP Conference Proceedings 2005* Apr 9 (Vol. 760, No. 1, pp. 547-553). American Institute of Physics.

- [36] Maftooli H, Karami HR, Sadeghi SH, Moini R. Output signal prediction of an open-ended coaxial probe when scanning arbitrary-shape surface cracks in metals. *IEEE Transactions on Instrumentation and Measurement*. 2012 Jun 1;61(9):2384-91.
- [37] Zhang H, He Y, Gao B, Tian GY, Xu L, Wu R. Evaluation of Atmospheric Corrosion on Coated Steel Using K-Band Sweep Frequency Microwave Imaging. *IEEE Sensors Journal*. 2016 Jan 28;16(9):3025-33.
- [38] Donnell KM, Zoughi R. Detection of corrosion in reinforcing steel bars using microwave dual-loaded differential modulated scatterer technique. *IEEE Transactions on Instrumentation and Measurement*. 2012 Jun 12;61(8):1-6.
- [39] Buhari MD, Tian GY, Tiwari R. Microwave-based SAR technique for pipeline inspection using autofocus range-doppler algorithm. *IEEE Sensors Journal*. 2018 Nov 2;19(5):1777-87.
- [40] Dvorsky M, Al Qaseer MT, Zoughi R. Detection and Orientation Estimation of Short Cracks Using Circularly-Polarized Microwave SAR Imaging. *IEEE Transactions on Instrumentation and Measurement*. 2020 Mar 4.
- [41] Zhang H, Gao B, Tian GY, Woo WL, Bai L. Metal defects sizing and detection under thick coating using microwave NDT. *NDT & E International*. 2013 Dec 1;60:52-61.
- [42] Gallion JR, Zoughi R. Millimeter-wave imaging of surface-breaking cracks in steel with severe surface corrosion. *IEEE Transactions on Instrumentation and Measurement*. 2017 Aug 29;66(10):2789-91.
- [43] Case JT, Ghasr MT, Zoughi R. Optimum two-dimensional uniform spatial sampling for microwave SAR-based NDE imaging systems. *IEEE Transactions on Instrumentation and Measurement*. 2011 Oct 17;60(12):3806-15.
- [44] Ghasr MT, Case JT, Zoughi R. Novel reflectometer for millimeter-wave 3-D holographic imaging. *IEEE Transactions on Instrumentation and Measurement*. 2014 Jan 21;63(5):1328-36.
- [45] Ghasr MT, Horst MJ, Dvorsky MR, Zoughi R. Wideband microwave camera for real-time 3-D imaging. *IEEE Transactions on Antennas and Propagation*. 2016 Nov 17;65(1):258-68.
- [46] Wu B, Gao Y, Ghasr MT, Zoughi R. Resolution-based analysis for optimizing subaperture measurements in circular SAR imaging. *IEEE Transactions on Instrumentation and Measurement*. 2018 May 15;67(12):2804-11.
- [47] Horst MJ, Ghasr MT, Zoughi R. Design of a compact V-band transceiver and antenna for millimeter-wave imaging systems. *IEEE Transactions on Instrumentation and Measurement*. 2019 Jan 16;68(11):4400-11.
- [48] Kharkovsky S, McClanahan A, Zoughi R, Palmer DD. Microwave dielectric-loaded rectangular waveguide resonator for depth evaluation of shallow flaws in metals. *IEEE Transactions on Instrumentation and Measurement*. 2011 May 31;60(12):3923-30.
- [49] Brinker K, Ghasr MT, Zoughi R. A new dual-loaded aperture probe for near-field millimeter wave imaging. In 2017 IEEE International Instrumentation and Measurement Technology Conference (I2MTC) 2017 May 22 (pp. 1-5). IEEE.
- [50] Salski B, Gwarek W, Korpas P. Electromagnetic inspection of carbon-fiber-reinforced polymer composites with coupled spiral inductors. *IEEE transactions on microwave theory and techniques*. 2014 Jun 2;62(7):1535-44.
- [51] Salski B, Gwarek W, Korpas P, Reszewicz S, Chong AY, Theodorakeas P, Hatzioannidis I, Kappatos V, Selcuk C, Gan TH, Kouj M. Non-destructive testing of carbon-fibre-reinforced polymer materials with a radio-frequency inductive sensor. *Composite Structures*. 2015 Apr 1;122:104-12.
- [52] Li Z, Haigh AD, Soutis C, Gibson AA, Sloan R, Karimian N. Damage evaluation of carbon-fibre

reinforced polymer composites using electromagnetic coupled spiral inductors. *Advanced Composites Letters*. 2015 May;24(3):096369351502400303.

[53] Li Z, Haigh A, Soutis C, Gibson A, Sloan R, Karimian N. Detection and evaluation of damage in aircraft composites using electromagnetically coupled inductors. *Composite Structures*. 2016 Apr 15;140:252-61.

[54] Li Z, Haigh AD, Saleh MN, McCarthy ED, Soutis C, Gibson AA, Sloan R. Detection of impact damage in carbon fiber composites using an electromagnetic sensor. *Research in Nondestructive Evaluation*. 2018 Jul 3;29(3):123-42.

[55] Li Z, Wang T, Haigh A, Meng Z, Wang P. Non-contact detection of impact damage in carbon fibre composites using a complementary split-ring resonator sensor. *Journal of Electrical Engineering*. 2019 Dec 1;70(6):489-93.

[56] Mukherjee S, Shi X, Udpa L, Udpa S, Deng Y, Chahal P. Design of a split-ring resonator sensor for near-field microwave imaging. *IEEE Sensors Journal*. 2018 Jul 3;18(17):7066-76.

[57] Abbasi Z, Niazi H, Abdolrazzaghi M, Chen W, Daneshmand M. Monitoring pH Level Using High-Resolution Microwave Sensor for Mitigation of Stress Corrosion Cracking in Steel Pipelines. *IEEE Sensors Journal*. 2020 Mar 3;20(13):7033-43.

[58] Hosoi A, Yamaguchi Y, Ju Y, Sato Y, Kitayama T. Detection and quantitative evaluation of defects in glass fiber reinforced plastic laminates by microwaves. *Composite Structures*. 2015 Sep 15;128:134-44.

[59] Mukherjee S, Tamburrino A, Udpa L, Udpa S. NDE of composite structures using microwave time reversal imaging. In *AIP Conference Proceedings 2016 Feb 10 (Vol. 1706, No. 1, p. 100002)*. AIP Publishing LLC.

[60] Mukherjee S, Tamburrino A, Haq M, Udpa S, Udpa L. Far field microwave NDE of composite structures using time reversal mirror. *NDT & E International*. 2018 Jan 1;93:7-17.

[61] Li Z, Haigh A, Soutis C, Gibson A. Principles and applications of microwave testing for woven and non-woven carbon fibre-reinforced polymer composites: a topical review. *Applied Composite Materials*. 2018 Aug 1;25(4):965-82.

[62] Li Z, Haigh A, Soutis C, Gibson A, Sloan R. Microwaves sensor for wind turbine blade inspection. *Applied Composite Materials*. 2017 Apr 1;24(2):495-512.

[63] Li Z, Haigh A, Soutis C, Gibson A, Sloan R, Karimian N. Delamination detection in composite T-joints of wind turbine blades using microwaves. *Advanced Composites Letters*. 2016 Jul;25(4):096369351602500401.

[64] Moll J, Arnold P, Mälzer M, Krozer V, Pozdniakov D, Salman R, Rediske S, Scholz M, Friedmann H, Nuber A. Radar-based structural health monitoring of wind turbine blades: The case of damage detection. *Structural Health Monitoring*. 2018 Jul;17(4):815-22.

[65] Sutthaweekul R, Tian GY, Buhari MD. Detection of impact damage and fibre texture on CFRP using open-ended waveguide probe. In *2016 13th International Conference on Electrical Engineering/Electronics, Computer, Telecommunications and Information Technology (ECTI-CON) 2016 Jun 28 (pp. 1-6)*. IEEE.

[66] Sutthaweekul R, Tian G, Wang Z, Ciampa F. Microwave open-ended waveguide for detection and characterisation of FBHs in coated GFRP pipes. *Composite Structures*. 2019 Oct 1;225:111080.

[67] Zoughi R, Gallion JR, Ghasr MT. Accurate microwave measurement of coating thickness on carbon composite substrates. *IEEE Transactions on Instrumentation and Measurement*. 2016 Feb 19;65(4):951-3.

[68] Zoughi R, Arias-Monje PJ, Gallion J, Sarkar S, Wang PH, Gulgunje P, Verghese N, Kumar S.

Microwave dielectric properties and Targeted heating of polypropylene nano-composites containing carbon nanotubes and carbon black. *Polymer*. 2019 Sep 28;179:121658.

[69] Arunachalam K, Udpa L, Udpa SS. A computational investigation of microwave breast imaging using deformable reflector. *IEEE Transactions on Biomedical Engineering*. 2008 Jan 16;55(2):554-62.

[70] Mukherjee S, Udpa L, Udpa S, Rothwell EJ, Deng Y. A time reversal-based microwave imaging system for detection of breast tumors. *IEEE Transactions on Microwave Theory and Techniques*. 2019 Mar 22;67(5):2062-75.

[71] Gao Y, Zoughi R. Millimeter wave reflectometry and imaging for noninvasive diagnosis of skin burn injuries. *IEEE Transactions on Instrumentation and Measurement*. 2016 Nov 9;66(1):77-84.

[72] Gao Y, Ghasr MT, Nacy M, Zoughi R. Towards accurate and wideband in vivo measurement of skin dielectric properties. *IEEE Transactions on Instrumentation and Measurement*. 2018 Jul 16;68(2):512-24.

[73] Li C, Yu X, Lee CM, Li D, Ran L, Lin J. High-Sensitivity Software-Configurable 5.8-GHz Radar Sensor Receiver Chip in 0.13- μm CMOS for Noncontact Vital Sign Detection. *IEEE Transactions on Microwave Theory and Techniques*. 2010 Mar 25;58(5):1410-9.

[74] Kao TY, Yan Y, Shen TM, Chen AY, Lin J. Design and analysis of a 60-GHz CMOS Doppler micro-radar system-in-package for vital-sign and vibration detection. *IEEE Transactions on Microwave Theory and Techniques*. 2013 Mar 6;61(4):1649-59.

[75] Han J, Kim JG, Hong S. A compact Ka-band Doppler radar sensor for remote human vital signal detection. *Journal of electromagnetic engineering and science*. 2012 Dec;12(4):234-9.

[76] Zoughi R, Ghasr MT, Bishop T, Cataldo A, De Benedetto E, Grieco A. Millimeter wave imaging as a tool for traceability and identification of tattooed markers in leather. In 2018 IEEE International Instrumentation and Measurement Technology Conference (I2MTC) 2018 May 14 (pp. 1-5). IEEE.

[77] Shinde S, Jothibasu S, Ghasr MT, Zoughi R. Wideband microwave reflectometry for rapid detection of dissimilar and aged ICs. *IEEE Transactions on Instrumentation and Measurement*. 2017 Apr 4;66(8):2156-65.

[78] Li Z, Haigh A, Soutis C, Gibson A, Sloan R. Evaluation of water content in honey using microwave transmission line technique. *Journal of Food Engineering*. 2017 Dec 1;215:113-25.

[79] Chen Z, Yusa N, Miya K. Enhancements of eddy current testing techniques for quantitative nondestructive testing of key structural components of nuclear power plants. *Nuclear engineering and design*. 2008 Jul 1;238(7):1651-6.

[80] Cheng W. Pulsed eddy current testing of carbon steel pipes' wall-thinning through insulation and cladding. *Journal of Nondestructive evaluation*. 2012 Sep 1;31(3):215-24.

[81] Alobaidi WM, Alkuam EA, Al-Rizzo HM, Sandgren E. Applications of ultrasonic techniques in oil and gas pipeline industries: A review. *American Journal of Operations Research*. 2015;5(04):274.

[82] Tua PS, Quek ST, Wang Q. Detection of cracks in cylindrical pipes and plates using piezo-actuated Lamb waves. *Smart materials and structures*. 2005 Oct 17;14(6):1325.

[83] Shi Y, Zhang C, Li R, Cai M, Jia G. Theory and application of magnetic flux leakage pipeline detection. *Sensors*. 2015 Dec;15(12):31036-55.

[84] Liu B, He LY, Zhang H, Cao Y, Fernandes H. The axial crack testing model for long distance oil-gas pipeline based on magnetic flux leakage internal inspection method. *Measurement*. 2017 Jun 1;103:275-82.

[85] Jiles DC. Theory of the magnetomechanical effect. *Journal of physics D: applied physics*. 1995 Aug 14;28(8):1537.

[86] Shi P, Su S, Chen Z. Overview of Researches on the Nondestructive Testing Method of Metal

- Magnetic Memory: Status and Challenges. *Journal of Nondestructive Evaluation*. 2020 Jun;39:1-37.
- [87] Cheong YM, Lee DH, Jung HK. Ultrasonic guided wave parameters for detection of axial cracks in feeder pipes of PHWR nuclear power plants. *Ultrasonics*. 2004 Apr 1;42(1-9):883-8.
- [88] Siqueira MH, Gatts CE, Da Silva RR, Rebello JM. The use of ultrasonic guided waves and wavelets analysis in pipe inspection. *Ultrasonics*. 2004 May 1;41(10):785-97.
- [89] Alleyne DN, Vogt T, Cawley P. The choice of torsional or longitudinal excitation in guided wave pipe inspection. *Insight-Non-Destructive Testing and Condition Monitoring*. 2009 Jul 1;51(7):373-7.
- [90] Niu X, Duan W, Chen HP, Marques HR. Excitation and propagation of torsional T (0, 1) mode for guided wave testing of pipeline integrity. *Measurement*. 2019 Jan 1;131:341-8.
- [91] Lowe MJ, Alleyne DN, Cawley P. The mode conversion of a guided wave by a part-circumferential notch in a pipe. *Journal of applied mechanics*. 1998;65(3):649-56.
- [92] Tang L, Wu B. Excitation mechanism of flexural-guided wave modes F (1, 2) and F (1, 3) in pipes. *Journal of Nondestructive Evaluation*. 2017 Sep 1;36(3):59.
- [93] Aristegui C, Lowe MJ, Cawley P. Guided waves in fluid-filled pipes surrounded by different fluids. *Ultrasonics*. 2001 Aug 1;39(5):367-75.
- [94] Leinov E, Lowe MJ, Cawley P. Investigation of guided wave propagation and attenuation in pipe buried in sand. *Journal of Sound and Vibration*. 2015 Jul 7;347:96-114.
- [95] Demma A, Cawley P, Lowe M, Pavlakovic B. The effect of bends on the propagation of guided waves in pipes. *Journal of pressure vessel technology*. 2005;127(3):328-35.
- [96] Hayashi T, Kawashima K, Sun Z, Rose JL. Guided wave propagation mechanics across a pipe elbow. In *ASME Pressure Vessels and Piping Conference 2003* Jan 1 (Vol. 16974, pp. 43-47).
- [97] Nishino H, Tanaka T, Katashima S, Yoshida K. Experimental investigation of mode conversions of the T (0, 1) mode guided wave propagating in an elbow pipe. *Japanese Journal of Applied Physics*. 2011 Apr 20;50(4R):046601.
- [98] Sanderson RM, Hutchins DA, Billson DR, Mudge PJ. The investigation of guided wave propagation around a pipe bend using an analytical modeling approach. *The journal of the acoustical society of america*. 2013 Mar;133(3):1404-14.
- [99] Salzburger HJ, Niese F, Dobmann G. EMAT pipe inspection with guided waves. *Welding in the world*. 2012 May 1;56(5-6):35-43.
- [100] Pei C, Xiao P, Zhao S, Chen Z, Takagi T. A flexible film type EMAT for inspection of small diameter pipe. *Journal of Mechanical Science and Technology*. 2017 Aug 1;31(8):3641-5.
- [101] Nakamura N, Ogi H, Hirao M. EMAT pipe inspection technique using higher mode torsional guided wave T (0, 2). *Ndt & E International*. 2017 Apr 1;87:78-84.
- [102] Sugawara K, Hashizume H, Kitajima S. Development of NDT method using electromagnetic waves. *JSAEM Stud. Appl. Electromagn. Mech*. 2001;10:313-6.
- [103] Hashizume H, Shibata T, Yuki K. Crack detection method using electromagnetic waves. *International Journal of Applied Electromagnetics and Mechanics*. 2004 Jan 1;20(3-4):171-8.
- [104] Shibata T, Hashizume H, Kitajima S, Ogura K. Experimental study on NDT method using electromagnetic waves. *Journal of materials processing technology*. 2005 Apr 10;161(1-2):348-52.
- [105] Liu L, Ju Y. A high-efficiency nondestructive method for remote detection and quantitative evaluation of pipe wall thinning using microwaves. *NDT & E International*. 2011 Jan 1;44(1):106-10.
- [106] Liu L, Ju Y, Chen M. Optimizing the frequency range of microwaves for high-resolution evaluation of wall thinning locations in a long-distance metal pipe. *NDT & E International*. 2013 Jul 1;57:52-7.
- [107] Sasaki K, Katagiri T, Yusa N, Hashizume H. Demonstration of the applicability of nondestructive

microwave testing to the long-range inspection of inner-surface cracks in tubes. *Materials Transactions*. 2017 Apr 1;58(4):692-6.

[108] Katagiri T, Sasaki K, Song H, Yusa N, Hashizume H. Proposal of a TEM to TE 01 mode converter for a microwave nondestructive inspection of axial flaws appearing on the inner surface of a pipe with an arbitrary diameter. *International Journal of Applied Electromagnetics and Mechanics*. 2019 Jan 1;59(4):1527-34.

[109] Jones RE, Simonetti F, Lowe MJ, Bradley IP. Use of microwaves for the detection of water as a cause of corrosion under insulation. *Journal of Nondestructive Evaluation*. 2012 Mar 1;31(1):65-76.

[110] Sasaki K, Katagiri T, Yusa N, Hashizume H. Experimental verification of long-range microwave pipe inspection using straight pipes with lengths of 19–26.5 m. *NDT & E International*. 2018 Jun 1;96:47-57.

[111] Sasaki K, Yusa Katagiri T, Hashizume H. Long-Range Inspection of a Pipe Using a Microwave Emitted by a Probe Attached to the Pipe Wall. *Journal of the Japan Society of Applied Electromagnetics and Mechanics*. 2017;25(2):266-72. (In Japanese)

[112] Abbasi K, Motlagh NH, Neamatollahi MR, Hashizume H. Detection of axial crack in the bend region of a pipe by high frequency electromagnetic waves. *International Journal of Pressure Vessels and Piping*. 2009 Nov 1;86(11):764-8.

[113] Uoshita S, Sasaki K, Katagiri T, Yusa N, Hashizume H. Long-range inspection of a pipe with a bend using microwaves. *International Journal of Applied Electromagnetics and Mechanics*. 2019 Jan 1;59(4):1519-26.

[114] Jones RE, Simonetti F, Lowe MJ, Bradley IP. The effect of bends on the long-range microwave inspection of thermally insulated pipelines for the detection of water. *Journal of Nondestructive Evaluation*. 2012 Jun 1;31(2):117-27.

[115] Sasaki K. Development of long-range nondestructive testing technology using microwave for defects in pipes Doctoral dissertation Tohoku University; 2016.

[116] Orfanidis SJ. *Electromagnetic waves and antennas*, 2002.

[117] Pozar DM. *Microwave engineering (Third Edition)*. John Wiley & sons; 2005.

[118] Chang K. *Encyclopedia of RF and microwave engineering*. Wiley J, editor. Wiley-Interscience; 2005 Apr.

[119] The RF Module User's Guide, COMSOL v5.4.

[120] <https://www.microwaves101.com/> (accessed on July 21st, 2020).

[121] Rumiantsev A, Ridler N. VNA calibration. *IEEE Microwave magazine*. 2008 May 14;9(3):86-99.

[122] Sakai Y, Yusa N, Hashizume H. Nondestructive evaluation of wall thinning inside a pipe using the reflection of microwaves with the aid of signal processing. *Nondestructive Testing and Evaluation*. 2012 Jun 1;27(2):171-84.

[123] Katagiri T, Sasaki K, Yusa N, Hashizume H. Development of long-range inspection using TE mode microwaves for detecting axial cracks. *Transactions of the JSME*. 2018;84(859):17-00375. (In Japanese)

[124] Miller SE. Notes on methods of transmitting the circular electric wave around bends. *Proceedings of the IRE*. 1952 Sep;40(9):1104-13.

[125] Morgan SP. Theory of curved circular waveguide containing an inhomogeneous dielectric. *Bell System Technical Journal*. 1957 Sep;36(5):1209-51.

[126] Thumm M. High-power millimetre-wave mode converters in overmoded circular waveguides using periodic wall perturbations. *International Journal of Electronics*. 1984 Dec 1;57(6):1225-46.

[127] Li H, Thumm M. Mode conversion due to curvature in corrugated waveguides. *International*

journal of electronics. 1991 Aug 1;71(2):333-47.

[128] Kumrić H, Thumm M. Optimized overmoded TE₀₁-to-TM₁₁ mode converters for high-power millimeter wave applications at 70 and 140 GHz. *International journal of infrared and millimeter waves*. 1986 Oct 1;7(10):1439-63.

[129] Chen G, Takuya Katagiri, Noritaka Yusa, Hidetoshi Hashizume, Evaluation of factors influencing modal conversion at bend in the light of pipe inspection using microwave NDT. 6th JSNDI Tohoku branch symposium. Japan: Sendai; 2018/04. p. 3.

[130] Chen G, Takuya Katagiri, Noritaka Yusa, Hidetoshi Hashizume, Evaluation of general applicability of microwave NDT to pipes with a bend focusing on mode conversion. 15th Japan society of maintenology conference: student session, Japan: Fukuoka. 2018/07. p. 277–80.

[131] Sasaki K, Liu L, Yusa N, Hashizume H. Optimized microwave excitation probe for general application in NDT of wall thinning in metal pipes of arbitrary diameter. *NDT & E International*. 2015 Mar 1;70:53-9.

[132] Yang S, Li H. Optimization of novel high-power millimeter-wave TM₀₁-TE₁₁ mode converters. *IEEE transactions on microwave theory and techniques*. 1997 Apr;45(4):552-4.

[133] Ling GS, Zhou JJ. Design of mode converters for generating the TE₁₁ mode from TM₀₁ vircator at 4GHz. *International journal of electronics*. 2003 Dec 31;89(12):925-30.

[134] Yuan CW, Zhong HH, Qian BL. Tri-bend TM₀₁-TE₁₁ mode converter with input-output aligned on the same axis. *High Power Laser and Particle Beams*. 2006 Nov 15;18(11):1864-8.

[135] Niu XJ, Zhu XN, Liu YH, Yu XH, Li HF. Study of Ka-band TM₀₁ to TE₁₁ mode converters with parallel input and output waveguides. *Journal of Infrared, Millimeter, and Terahertz Waves*. 2014 Feb 1;35(2):179-86.

[136] Ni J, Zhou S, Zhang P, Li Y. Effect of pipe bend configuration on guided waves-based defects detection: An experimental study. *Journal of Pressure Vessel Technology*. 2016 Apr 1;138(2).

[137] Qi M, Zhou S, Ni J, Li Y. Investigation on ultrasonic guided waves propagation in elbow pipe. *International Journal of Pressure Vessels and Piping*. 2016 Mar 1;139:250-5.

[138] El-Gammal M, Mazhar H, Cotton JS, Shefski C, Pietralik J, Ching CY. The hydrodynamic effects of single-phase flow on flow accelerated corrosion in a 90-degree elbow. *Nuclear engineering and design*. 2010 Jun 1;240(6):1589-98.

[139] Pietralik JM, Schefski CS. Flow and mass transfer in bends under flow-accelerated corrosion wall thinning conditions. *Journal of engineering for gas turbines and power*. 2011 Jan 1;133(1).

[140] Ishimoto J, Akiba S, Tanji K, Matsuura K. Integrated super computational prediction of liquid droplet impingement erosion. *Progress in Nuclear Science Technology*. 2011 Oct 15;2:498-502.

[141] Dhanasekaran TS, Wang T. Numerical model validation and prediction of mist/steam cooling in a 180-degree bend tube. *International journal of heat and mass transfer*. 2012 Jun 1;55(13-14):3818-28.

[142] Fujisawa N, Wada K, Yamagata T. Numerical analysis on the wall-thinning rate of a bent pipe by liquid droplet impingement erosion. *Engineering Failure Analysis*. 2016 Apr 1;62:306-15.

[143] Anritsu Company, Precision RF & Microwave Components, Catalog No. 11410–00236, 2011.

Statement of reuse of materials

Some contents of this doctoral thesis have been previously published or submitted for review, the detailed information and the corresponding parts of this thesis are given below:

[1] Guanren Chen, Takuya Katagiri, Haicheng Song, Noritaka Yusa, Hidetoshi Hashizume, Detection of cracks with arbitrary orientations in a metal pipe using linearly-polarized circular TE₁₁ mode microwaves, *NDT&E International* 107 (2019), 102125. <https://doi.org/10.1016/j.ndteint.2019.102125>
(Corresponding to Sections 4.1, 4.2, and 4.3)

[2] Guanren Chen, Takuya Katagiri, Haicheng Song, Noritaka Yusa, Hidetoshi Hashizume, Investigation of the Effect of a Bend on Pipe Inspection Using Microwave NDT, *NDT&E International* 110 (2020), 102208. <https://doi.org/10.1016/j.ndteint.2019.102208>
(Corresponding to Sections 3.1, 3.2, 3.3, 3.4 in partial, and Appendix A)

[3] Guanren Chen, Takuya Katagiri, Noritaka Yusa, Hidetoshi Hashizume, In-pipe crack detection for multiple diameters using TE₁₁ mode microwaves, *International Journal of Applied Electromagnetics and Mechanics*, accepted on March 4th, 2020. In press.
(Corresponding to Section 4.5 in partial)

[4] Guanren Chen, Takuya Katagiri, Noritaka Yusa, Hidetoshi Hashizume, Design of A Dual-port, Side-incident Microwave Probe for Detection of In-Pipe Damage, *Measurement Science and Technology*, accepted on June 9th, 2020. Available at: <https://doi.org/10.1088/1361-6501/ab9acc>
(Corresponding to Sections 5.2, 5.3.1, and Appendix C)

[5] Guanren Chen, Takuya Katagiri, Noritaka Yusa, Hidetoshi Hashizume, Experimental Investigation on Bend-Region Crack Detection Using TE₁₁ Mode Microwaves, submitted to *Nondestructive Testing and Evaluation* (April 17th, 2020), under review.
(Corresponding to Section 4.6 in partial)

The reuse of the above materials strictly abides by the copyright policy or permissions for authors of the publishers (Elsevier, IOS Press, IOP Publishing, and Taylor & Francis)

-Elsevier: <https://www.elsevier.com/about/policies/copyright/permissions>

-IOS Press: <https://www.iospress.nl/service/authors/permission-to-post-pre-print-post-print-and-publishers-pdf-articles/>

-IOP Publishing: <https://publishingsupport.iopscience.iop.org/questions/quick-check-guide-current-author-rights-policy/>

-Taylor & Francis: <https://authorservices.taylorandfrancis.com/copyright-and-you/>

The above weblinks were accessed on August 19th, 2020.